STELLINGEN

1. De waterbeweging in een getijdehaven en de daarmee gepaard gaande uitwisseling van massa tussen de haven en de rivier waaraan zij gelegen is, zijn sterk afhankelijk van de vormgeving van de havenmond.

2. De constanten van het standaard k-ε turbulentie model, zoals gegeven door Launder en Spalding, zijn bij het gebruik van standaard wandfuncties nabij wanden niet consistent met een waarde van de Von Kármán constante gelijk aan 0,4.

   Launder, B.E., and Spalding, D.B. (1974). "The numerical computation of turbulent flows." *Comp. Meth. in Appl. Mech. and Engrg.*, 3, 269–289.

3. De bewering van Chu en Babarutsi dat de breedte van de ondiepe menglaag constant wordt boven een zekere waarde van de parameter S, die de invloed van de bodemweerstand vertegenwoordigt, is fysisch onjuist.

   Chu, V.H., and Babarutsi, S. (1988). "Confinement and bed-friction effects in shallow turbulent mixing layers." *J. Hydr. Engrg.*, 114(10), 1257–1274.

4. Voor het verkrijgen van de beste numerieke resultaten voor de gemiddelde waterbeweging wordt de benodigde zwaarte van het turbulentiemodel bepaald door de verhouding tussen de maaswijdte van het rekenrooster en de lengteschaal van de turbulentie.

5. Gezien de subjectiviteit in het bepalen van de kwaliteit van een numeriek stromingsmodel die in de civieltechnische praktijk gebruikelijk is, verdient het aanbeveling om bij publicatie van rekenresultaten de verschillen met meetresultaten of een exacte oplossing te kwantificeren.

6. De lezer kan bij het interpreteren van rekenresultaten misleid worden door de grafische presentatie er van.

7. De militaire dienstplicht dient van haar discriminerende karakter ontdaan te worden door het invoeren van een dienstplicht, niet enkel militair, voor ieder individu.

8. De sportieve prestaties van de ons land vertegenwoordigende nationale sportteams kunnen worden verhoogd door de teamleden het volkslied te leren meezingen.

9. Gezien de onafhankelijke aard van de Nederlandse bevolking, is het carpoolen als oplossing voor het fileprobleem tot mislukken gedoemd.

10. De afscheiding van enkele voormalige republieken van voorheen communistische staten in Oost Europa brengt niet de gewenste onafhankelijkheid, maar leidt slechts tot een verschuiving naar afhankelijkheid van het democratische Westen.

Stellingen behorende bij het proefschrift FLOW PATTERNS AND TRANSPORT OF DISSOLVED MATTER IN TIDAL HARBOURS door E.J. Langendoen, Delft, 21 december 1992.

Flow patterns and transport of

dissolved matter in tidal harbours

Proefschrift

ter verkrijging van de graad van doctor aan de
Technische Universiteit Delft, op gezag van de
Rector Magnificus, prof. drs. P.A. Schenck, in
het openbaar te verdedigen ten overstaan van een
commissie aangewezen door het College van Dekanen
op maandag 21 december 1992 te 16.00 uur

door

Eddy Johannes Langendoen,
geboren te Oostvoorne,
civiel ingenieur.
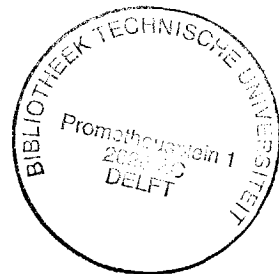
1992

Dit proefschrift is goedgekeurd door de promotor:

prof. dr. ir. J.A. Battjes

Toegevoegd promotor:

dr. ir. C. Kranenburg

Abstract

In the present study the influence of the harbour entrance geometry on the velocity and density fields in the entrance of a tidal harbour is examined by means of laboratory experiments and a field measurement. These experiments have provided a data set through which three numerical models for the flow and transport of dissolved matter in harbour entrances were tested and calibrated.

The three main flow processes that determine the exchange of matter between harbour and river are: a) the velocity difference between the flow in the river and that in the resulting gyre in the harbour entrance, b) a net flow through the entrance (in this study caused by variations in water level), and c) a density-driven exchange flow. These processes and their interactions were examined.

Laboratory experiments with an unstratified oscillatory (tidal) current without water level variations showed that the flow in the harbour entrance and the exchange of matter between harbour and river depend markedly on the geometry of the entrance and the phase of the tide. Especially during slack water a large increase in advective exchange of matter between harbour and river was observed.

A density-driven exchange flow influences the shape of the gyre and the water velocities. Its influence is larger than that of filling and emptying of the harbour basin because of the larger velocities involved.

The depth-averaged numerical models DUCHESS and ESTRA, and the three-dimensional model TRISULA were used to simulate the unstratified flow and the transport of matter in harbour entrances.

The influences of the tidal period, horizontal eddy viscosity and mesh sizes on the computed flow in the harbour were studied with DUCHESS.

The influences of the dispersion formulation and mesh sizes on the computed exchange of matter between harbour and river were studied with ESTRA.

TRISULA was tested and improved for applications to harbour entrances by using the data set obtained from the measurements. The computed flow in the harbour is highly influenced by the resolution of the computational grid, the turbulence modelling (that is, the eddy viscosities), and the boundary conditions at the sidewalls of the harbour.

Samenvatting

Door middel van laboratoriumexperimenten en een veldmeting is in deze studie de invloed van de geometrie van de havenmond op het snelheids- en dichtheidsveld in de mond van een getijdehaven onderzocht. Een dataset is verkregen waarmee drie numerieke modellen voor de waterbeweging en het transport van opgeloste stoffen in havenmonden getoetst en gecalibreerd zijn.

De drie belangrijkste stromingsprocessen die de uitwisseling van stof tussen haven en rivier bepalen zijn: a) het snelheidsverschil tussen de stroming in de rivier en die in de resulterende neer in de havenmond, b) een netto stroming door de havenmond ten gevolge van water-standsvariaties, en c) een door dichtheidsverschillen aangedreven uitwisselingsstroming. Deze stromingsprocessen en hun interacties zijn onderzocht.

Laboratoriumexperimenten met een oscillerende stroming zonder waterstandsvariaties (alleen horizontaal getij) hebben aangetoond dat de stroming in de havenmond en de uitwisseling van stof tussen haven en rivier sterk afhangen van de geometrie van de haven-mond en de getijfase. Vooral tijdens kentering is een grote toename in advective uitwisseling van materie tussen haven en rivier waargenomen.

Een door dichtheidsverschillen aangedreven uitwisselingsstroming beïnvloedt de vorm van de neer en de stroomsnelheden. De invloed is groter dan die ten gevolge van komberging en komlediging, omdat de snelheden in de uitwisselingsstroming groter zijn.

De dieptegemiddelde numerieke modellen DUCHESS en ESTRA, en het drie-dimensionale model TRISULA zijn gebruikt om de ongelaagde waterbeweging en het stoftransport in havenmonden te simuleren.

De invloeden van de getijperiode, horizontale turbulente viscositeit en maaswijdten op de berekende waterbeweging in de haven zijn met DUCHESS onderzocht.

De invloeden van de dispersieformulering en de maaswijdten op de berekende uitwisseling van stof tussen haven en rivier zijn met ESTRA onderzocht.

TRISULA is met behulp van de dataset verkregen uit de metingen getoetst en verbe-terd voor toepassingen op havenmonden. De berekende stroming in de haven wordt sterk beïnvloed door de resolutie van het rekenrooster, de turbulentiemodellering (de turbulente viscositeiten) en de randvoorwaarden aan de wanden van de haven.

Acknowledgements

Contents

- x -

1 Introduction

1.1 Background

Harbours situated on tidal rivers and estuaries usually suffer from siltation of their basins. The routine dredging necessary to sustain the accessibility of the harbour to shipping involves high costs. For example, 23 million cubic meters of silt are dredged annually in Rotterdam (The Netherlands), and in Hamburg, the largest tidal port in Germany, 1 million cubic meters of mud are dredged annually. The accessibility of harbours is essential for, among others, the economy and the employment in the region and in the hinterland. It is important to keep the costs of maintenance of the harbour basins, mainly the costs of routine dredging, as low as possible to insure low prices for the harbour industry, and therefore to be competitive with neighbouring foreign harbours.

Another problem arises from the siltation of the basins besides the costs related to the routine dredging and its impediment to shipping. Certain micro-pollutants are transported with the cohesive sediments, in particular heavy metals which are adsorbed on the clay and silt particles. 10 million cubic meters of the 23 million cubic meters of silt that are dredged annually in Rotterdam is slightly to badly polluted and cannot be dumped in the North Sea. For the disposal of polluted sediment special provisions have to be made, for example dumping sites on land such as the Slufter near Rotterdam. However, these dumping sites are expensive and only temporarily solve the problem.

The presence of pollutants in the harbour water contributes to the deterioration of the water quality in the harbour.

To decrease the amount of routine dredging, the siltation of the harbour basins has to be reduced, for which the mechanisms causing this siltation have to be known. The siltation is induced by the flow in the entrance of the harbour, which is influenced by gyres, changes in tidal level that lead to filling and emptying of the harbour basin, density currents, and the geometry of the harbour entrance. As a result, the water motion in the harbour entrance is complex and of a three-dimensional nature. Detailed knowledge of the water motion, needed

for a reliable prediction of the siltation of harbour basins, then is difficult to obtain.

Most early laboratory research was primarily concentrated on the examination of the process of siltation and the reduction of the siltation in existing harbours, for example Schmucker (1926), Bonnet & Lamoen (1949), Hensen (1953) and Magens (1958). Especially after the Second World War (from 1950 to 1960) an increase in the amount of research was seen, related to the reconstruction and expansion of many harbours in Germany and The Netherlands. One of the first investigations in which a more methodical procedure was used, was carried out by Rohr (1933), who examined the influence of the geometry of the harbour on the amount of siltation. Further extensive research was carried out by Vollmers (1963), Dursthoff (1970) and Booij (1986).

However, most of the research referred to above only considers one mechanism of exchange that causes the siltation of harbour basins, viz. exchange caused by transport of matter through the mixing layer between a gyre in the harbour entrance and a steady river flow. Research in which the influences of other exchange mechanisms and their interactions on the siltation of harbour basins are examined, is scarce. Some work that studies the influence of density differences between river-water and water in the harbour on the exchange of water between harbour and river was carried out by Roelfzema & Van Os (1978) and Delft Hydraulics (1977).

In the seventies and eighties the routine dredging in Rotterdam and Hamburg has increased considerably, which has lead to the initiation of large research projects. Rotterdam Municipal Works and Rijkswaterstaat (Department of Transport and Public Works of The Netherlands) cooperated in the project MKO (Minimization of the Costs of Routine dredging) for a better control of the dredging process and its costs.

1.2 Aim and scope of the present study

The state of affairs outlined above indicates that the exchange of matter between a harbour and a river requires more study, especially concerning the interactions between the different mechanisms of exchange. Too little is known of the complex flow in the harbour entrance to use tools, for example numerical models, to reliably predict the siltation of harbour basins.

Also adequate data are missing to test these models. The study presented in this thesis has two main objectives:

- To obtain a better understanding of the flow pattern in the harbour entrance.

- To generate a data set to test numerical models for the flow in harbour entrances. Such models then can be used to design an optimum harbour entrance to minimize siltation.

The study deals with the exchange between a harbour and a tidal river. Particularly the effects of an unsteady flow along the harbour entrance are studied, whereas in previous research mainly steady flow in the river was considered.

1.3 Approach in the present study

Laboratory and field measurements were carried out to study different mechanisms of exchange, their interactions, and the influence of the geometry of the harbour entrance. The measurements in the laboratory were carried out in scale models in the Hydromechanics Laboratory of the Department of Civil Engineering of the Delft University of Technology (non-stratified flow) and in the Tidal Flume of Delft Hydraulics (stratified flow). The field measurement was carried out in the 1st Petroleum Harbour in Rotterdam (stratified flow).

The data gathered from the measurements were used to test the 3-D computer model TRISULA (made available by Delft Hydraulics). TRISULA can be used for both unsteady and steady flows for which the hydrostatic pressure assumption is valid.

Mechanisms of exchange of matter between harbour and river are discussed in chapter 2. In chapter 3 the laboratory experiments are considered followed by the numerical simulations in chapter 4. The results of the field measurement are presented in chapter 5. Finally a summary and the conclusions of the research are given in chapter 6.

2 Mechanisms of exchange

2.1 Introduction

The water motion in a harbour entrance results in a net transport of sediment to the harbour and siltation of the harbour basins. Three main flow mechanisms inducing an exchange of matter between a harbour and a tidal river can be distinguished, see Booij (1987), Dursthoff (1970), MKO (1983) and Vollmers (1976):

1) Exchange in consequence of a velocity difference between the flow in the river along the harbour entrance and the flow in the harbour.

2) Exchange in consequence of a net flow through the harbour entrance.

3) An exchange flow driven by a density difference between the water in the harbour and the river-water.

Further, less important, mechanisms producing exchange are, for example, shipping and wind.

In sections 2.2 to 2.4 the three main mechanisms of exchange of matter between harbour and river are discussed, and expressions of the magnitudes of the exchanges are given as found in the literature. In section 2.5 the interactions between the three mechanisms are considered. Finally, a discussion follows in section 2.6.

2.2 Flow along the harbour entrance

The water velocity in the river is usually larger than that in the harbour entrance. The velocity difference results from the separation of the flow in the river at the upstream corner of the harbour entrance. The resulting flow pattern is illustrated in Fig. 2.1. The free shear layer at the transition from river to harbour entrance is unstable and a mixing layer develops.
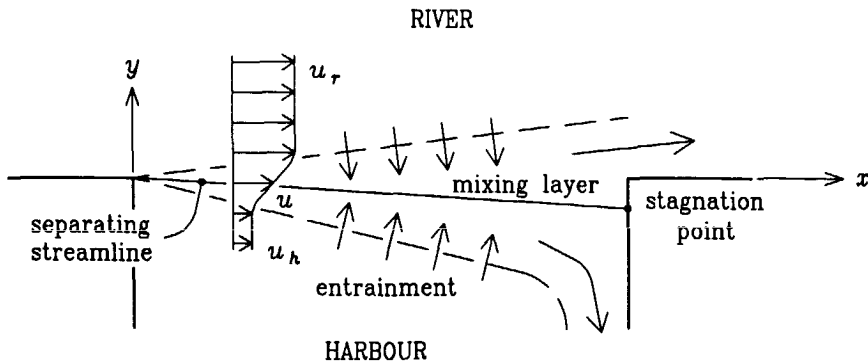
RIVER

Figure 2.1 The mixing layer in the harbour entrance.

Assuming that the water velocity in the river is constant outside the mixing layer and the water velocity in the mixing layer is smaller than that of the river, conservation of mass implies that the separating streamline at the upstream corner of the harbour entrance is directed into the harbour. Part of the water of the mixing layer flows into the river and the other part into the harbour at the stagnation point near the downstream corner of the harbour entrance, that is where the separating streamline encounters the downstream sidewall of the harbour. The location of the stagnation point is determined by the amount of river-water and harbour water that is entrained into the mixing layer. A wider mixing layer, as a consequence of a higher entrainment of river-water and harbour water, results in a location of the stagnation point further into the harbour. In the harbour a circulating flow, a gyre, arises as a result of the entrainment of harbour water into the mixing layer and the supply of water from the mixing layer to the harbour at its downstream sidewall.

For the transport of matter from the river to the harbour and in the harbour itself two phenomena are important: (1) the mixing layer at the transition from harbour to river, and (2) the gyre in the harbour entrance.

2.2.1 The mixing layer

As discussed above, the flow in the river separates from the bank at the upstream corner of

the harbour entrance. A marked transition then is present from the flow in the river to the flow in the harbour near the separation point. Because a system of two parallel streams with different flow velocities is subject to Kelvin-Helmholtz instability, wave-like disturbances arise that grow in the downstream direction and roll-up to become vortices that form a mixing layer. The width of the mixing layer increases as a result of vortex pairing and the growth of the large coherent eddies, see Winant & Browand (1974) and Brown & Roshko (1974).

It is found from experiments, see Fig. 2.2, that a plane mixing layer between two uniform parallel streams spreads linearly. This corresponds to theory that the flow in the mixing layer approaches self-similarity after some distance downstream of the separation point. Brown & Roshko (1974) give for a two-dimensional mixing layer (that is, for infinite depth in the present case)

$$\frac{\mathrm{d}\delta}{\mathrm{d}x} = 0.181 \frac{u_r - u_h}{u_r + u_h} = 0.181\lambda, \tag{2.1}$$

where the width of the mixing layer δ is defined by the velocity-profile maximum-slope thickness

$$\delta = \frac{u_r - u_h}{(\partial u / \partial y)_{max}}. \tag{2.2}$$

Here λ is the relative velocity difference between river-water and harbour water, x is the longitudinal coordinate, y is the transverse coordinate, u is the velocity-component in x-direction, and the subscripts r and h denote river and harbour, respectively.

An analytical solution of the Reynolds equations can be given for the free mixing layer under the assumption of self-similarity of the flow in the mixing layer after some distance downstream of the separation point and using the boundary-layer approximation. This assumption can be shown to imply that $\mathrm{d}\delta/\mathrm{d}x$ is constant. The distributions of mean quantities retain the same functional forms, merely changing their transverse length scale and the scales of the mean value quantities, as in $M = m_0 f(y/l_0)$ where m_0 is a scale of the quantity, and l_0 is a lateral length scale. Both m_0 and l_0 are functions of x alone. A second assumption is that the eddy viscosity is constant in the transverse direction, $\nu_t =$
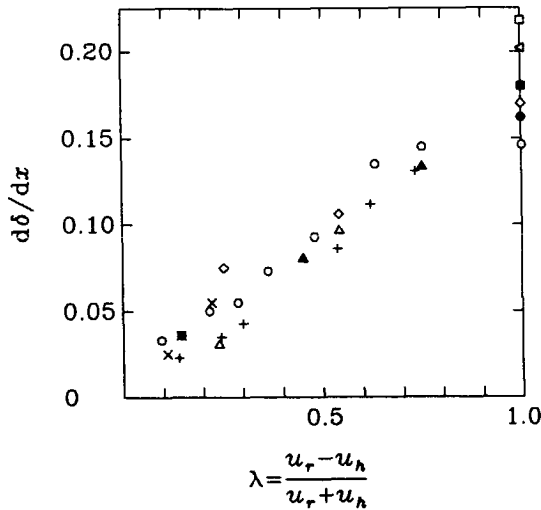
Figure 2.2 Dependence of spreading rate on velocity-difference parameter. Results of various investigators: ▲, Brown & Roshko (1974); ●, Liepmann & Laufer (1947); ○, Miles & Shih (1968); ◇, Mills (1968); ■, Patel (1973); ×, Pui (1969); ⊙, Reichardt; +, Spencer & Jones (1971); ◁, Sunyach (1971); □, Wygnanski & Fiedler (1970); △, Yule (1972). (From Brown & Roshko, 1974.)

$\beta |(u_r - u_h)| \, l_0$, with β the entrainment parameter. The relation between l_0 and the width of the mixing layer according to equation (2.2) is $\delta = \sqrt{2\pi} \, l_0$. The profile of the mean longitudinal velocity in a plane mixing layer then is given by a cumulative normal distribution function or an error integral, see Townsend (1976):

$$u(y) = u_h + (u_r - u_h) f(\eta) = u_h + (u_r - u_h)(2\pi)^{-1/2} \int_{-\infty}^{\eta + \eta_0} e^{-x^2/2} \, dx, \qquad (2.3)$$

where $\eta = y/l_0$. Using the condition of overall conservation of momentum it is found that the lateral position ($\eta = -\eta_0$) of the centre-line of the mixing layer, where the velocity equals $(u_r + u_h)/2$, must satisfy

$$\eta_0 = \frac{\sqrt{2} - 1}{\sqrt{2\pi}} \left[\frac{u_h}{u_r - u_h} + \frac{1}{2} \right]^{-1}.$$

The centre-line is shifted towards the low-speed side of the mixing layer. For square

harbours and relative large depths, η_0 is about 0.22 and y_0 is approximately $0.012x$.

Observations of Sabin, see Townsend (1976), have indicated that

$$\beta = \frac{1}{2\lambda}\frac{dl_0}{dx} = 0.028 \qquad (2.4)$$

over a wide range of velocity ratios. However, substitution of equation (2.1) in equation (2.4) yields a somewhat larger value of β:

$$\beta = \frac{(2\pi)^{-1/2}}{2\lambda}\frac{d\delta}{dx} = \frac{(2\pi)^{-1/2}}{2\lambda}0.181\lambda = 0.036.$$

Rivers and harbours are mostly shallow. The bed friction, not included above, then becomes important. Measurements of Chu & Babarutsi (1988) show that the bed friction reduces the turbulent motion in the shallow mixing layer. Fig. 2.3 shows that the turbulence, produced by the transverse shear, diminishes with increasing values of the bed-friction number S, defined as

$$S = \frac{c_f\delta}{4h}\frac{1}{\lambda},$$

where h is the water depth, and c_f is the bed-friction coefficient ($\tau_b = \frac{1}{2}\rho c_f \bar{u}^2$, where τ_b is the bottom shear-stress, and $\bar{u}$ the depth-averaged velocity). Chu & Babarutsi determined the bed-friction coefficient from

$$\frac{1}{\sqrt{c_f}} = -4\log\left[\frac{1.25}{Re\sqrt{c_f}}\right],$$

where the Reynolds number $Re = 4uh/\nu$ in which ν is the kinematic viscosity coefficient. In Fig. 2.3 the transverse component of the turbulent motion is represented by the rms velocity excess, u'_e, in the mixing layer. The rms velocity excess is the difference between the peak value of the rms velocity in the mixing layer and the average of the rms velocities in the ambient streams, which are generated by bed friction alone as followed from the measurements.

Chu & Babarutsi (1988), see Fig. 2.4, found an initial spreading rate of the shallow mixing layer that is twice as large as the rate of the plane mixing layer (equation (2.1))

$$\frac{d\delta}{dx} = 2\lambda_0\frac{d\delta^*}{dx^*} = 0.36\lambda_0$$
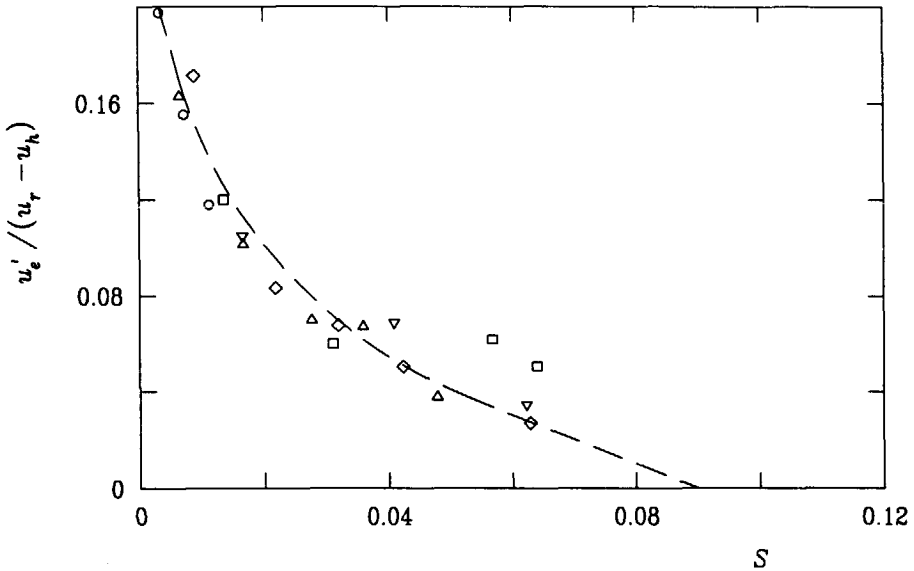
Figure 2.3 Variation of the transverse component of turbulence with bed-friction number. Results of five tests: $\bigcirc$, $h/c_f = 8.67$ m; $\triangle$, $h/c_f = 4.59$ m; $\triangledown$, $h/c_f = 4.00$ m; $\diamondsuit$, $h/c_f = 3.72$ m; $\square$, $h/c_f = 2.89$ m. (From Chu & Babarutsi, 1988.)

for the near field region where the distance from the separation point is small compared with a bed-friction length scale defined as h/c_f. Here $\delta^* = c_f \delta / 2 h \lambda_0$ and $x^* = c_f x / h$, where λ_0 is the relative velocity difference at 0.01 m downstream of the separation point. According to Chu & Babarutsi the water depth limits the growth of the vortices in the vertical direction. The transfer of turbulent energy from a horizontal motion toward a vertical motion then is reduced in a shallow mixing layer, resulting in a larger initial spreading rate.

The transverse spreading rate of the mixing layer reduces as the bed friction becomes more important in the far field region. Chu & Babarutsi (1988) found from their experiments

$$\frac{d\delta}{dx} = 0.36\lambda \left[1 - \frac{S}{0.09} \right], \qquad \text{for } S < 0.09$$

$$\frac{d\delta}{dx} = 0, \qquad \text{for } S > 0.09$$
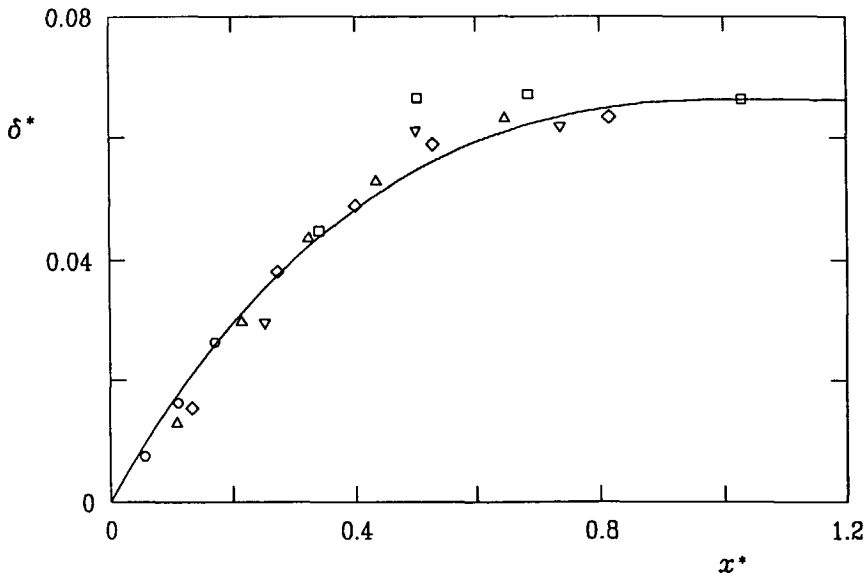
Figure 2.4 Width of the mixing layer. Results of five tests: $\bigcirc$, $h/c_f = 8.67$ m; $\triangle$, $h/c_f = 4.59$ m; $\triangledown$, $h/c_f = 4.00$ m; $\diamondsuit$, $h/c_f = 3.72$ m; $\square$, $h/c_f = 2.89$ m. ———— = equation 2.5. (From Chu & Babarutsi, 1988.)

The result that the spreading rate is zero for $S > 0.09$ is questionable. The turbulence in the mixing layer is as large as that in the ambient streams for $S > 0.09$. The width of the mixing layer should increase, because water from the ambient streams is entrained in the mixing layer.

Assuming that the average of the velocities in the ambient streams remains constant in x-direction the following relation between δ^* and x^* can be obtained

$$\delta^* = 0.18x^* e^{-x^*}, \qquad (x^* < 1)$$
$$\delta^* = 0.18e^{-1} = 0.066, \qquad (x^* \geq 1)$$

(2.5)

The derivation of equation (2.5) is shown in appendix A.

The entrainment coefficient β is not a constant for a shallow mixing layer. Substitution of equation (2.5) in equation (2.4) gives

$$\beta = \frac{e^{-c_f x/h}}{(2\pi)^{1/2}} \left[0.1845 - 0.18 \frac{c_f x}{h} \right].$$

The difference in spreading rates can also be caused by different initial conditions at the point of separation in the experiments of Brown & Roshko (1974) and Chu & Babarutsi (1988). The spreading of the mixing layer is very sensitive to these initial conditions, see for example Oster & Wygnanski (1982). A difference in spreading rate of a free mixing layer is for example caused by differences in turbulence level in both streams, the structure and the level of turbulent fluctuations in the boundary layer at the wall upstream of the separation point, and the curvature of the merging streams and the angle between them. The ambient streams are nearly turbulent free for a free shear layer, but are turbulent for a shallow mixing layer as a result of bed friction.

All causes discussed above can be observed in the flow in the entrance of a harbour. The flow in the harbour is curved due to the gyre in the entrance, and it encounters the flow in the river at an angle. With varying discharge in the river the turbulence levels in the harbour and river also vary.

Dursthoff (1970) found that for a water depth of 0.35 m and λ varying from about 0.7 to 0.8, the boundaries of a mixing layer between a harbour and a river are given by (unit is metre):

$$\delta_r = 0.189 x^{0.6} - 0.011, \qquad y > 0$$
$$\delta_h = 0.211 x^{0.49} - 0.016, \qquad y < 0$$

where $y = \delta_r$ is the boundary of the mixing layer that is located in the river and $y = -\delta_h$ the boundary that is located in the harbour.

The higher spreading rate in the river is probably due to a higher turbulence intensity in the river. The spreading rate is not constant but decreases in the downstream direction. This agrees with the experiments of Chu & Babarutsi (1988), who showed that the spreading rate decreases in the downstream direction due to the bed friction. However, the bed-friction length scale in the experiments of Dursthoff was about 75 m. So, the influence of the bed friction should be small for entrance widths of the order of 1 m. The decrease in spreading rate of the mixing layer in the downstream direction can also be a result of the increase in magnitude of the velocity in the harbour, u_h, towards the downstream sidewall, through which λ decreases and, according to equation (2.1), the spreading rate too.

Dursthoff visually determined the boundaries of the mixing layer from photographs

of dye injected in the mixing layer. This gives an over-estimation of the width of the mixing layer as defined by equation (2.2), not only because the diffusion of matter (dye) is higher than that of momentum, but also because the boundaries of the mixing layer are convoluted. Brown & Roshko (1974), for example, visually overestimated the width of the mixing layer by a factor two.

Booij (1986) measured a width of the mixing layer varying from $b = 0.11x$ to $b = 0.19x$, where b is the distance between the points where the velocity in the mixing layer differs a factor $(u_r - u_h)/2e$ from u_r and u_h. Assuming that the velocity distribution in the mixing layer is an error integral, the distance b is related to δ as: $\delta = 1.39b$. Expressed in terms of δ, the width of the mixing layer varies from $\delta = 0.15x$ to $\delta = 0.26x$. The value of δ depends strongly on the geometry of the harbour entrance and was determined for a water depth of 0.105 m and λ approximately 0.8. In his experiments Booij did not find a distinct influence of the bottom. The bed-friction length scale h/c_f was approximately 20 m, which is large compared with the entrance widths of the harbours studied by Booij, which are of the order of 1 m. Hence, the influence of the bottom is rather small.

Dursthoff (1970) found from his experiments that the velocity profile in the mixing layer at the transition from harbour to river is given by an error integral. Thus, a limited depth has no influence on the shape of the velocity profile in the mixing layer. The length to width ratios of the harbour, L/B, varied from 0.4 to 2, and various magnitudes of the water velocity in the river have been applied.

In contrast with theory and experiments of plane mixing layers, the measurements of Dursthoff show that the centre-line of the mixing layer is shifted to the river. According to Dursthoff this is due to the rather large boundary layer upstream of the separation point. As a result, the velocity in the river in front of the harbour must increase to conserve mass. However, Booij (1986) observed in his experiments that the centre-line of the mixing layer was shifted into the harbour, but was curved. This does not comply with the rectilinear centre-line of a plane mixing layer.

2.2.2 Flow in the harbour

The gyre in the harbour is induced by the entrainment of harbour water into the mixing layer and the supply of water from the mixing layer into the harbour near the stagnation point. Conservation of mass requires that the amount of water entrained into the mixing layer is equal to that transported back to the harbour again. Several gyres and dead zones can be present in a harbour. The pattern and number of gyres depend strongly on the geometry of the harbour. Primary, secondary, and more gyres occur in harbours with a length to width ratio $L/B > 2$. A definition sketch is shown in Fig. 2.5. For harbours with a length to width ratio $1/2 < L/B < 2$ only one gyre is present in the harbour, see Dursthoff (1970) and Booij (1986). Booij observed that the length of the primary gyre does not become much larger than $1.5B$ for harbours with $L/B > 2$ and their entrances perpendicular to the river axis. The length of the primary gyre will be larger for entrances oriented at an angle α less than 90 degrees with respect to the river axis and smaller for entrances oriented at an angle larger than 90 degrees with respect to the river axis.

According to Dursthoff (1970) the width of the flow from the mixing layer into the harbour is about 20 percent of the width of the harbour. The flow increases in width in the flow
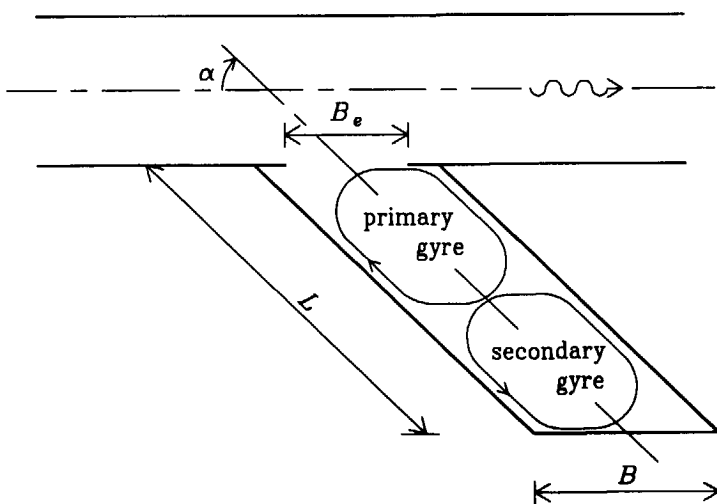
Figure 2.5 Flow pattern in the harbour and definition sketch.

direction of the gyre. Measurements, among others of Booij (1986) and Nece & Falconer (1989), show that the water velocity in the gyre, which is largest near the downstream sidewall, decreases in the flow direction of the gyre. This is displayed in Fig. 2.6.

Dursthoff (1970) observed that the average maximum velocity of the gyre, $\overline{u_{g,\max}}$, is about 33 per cent of the velocity in the river for square harbours and $B_e/B = 1$, where B_e is the width of the entrance. Measurements of the average velocity of the gyre showed that $\overline{u_g} \approx 0.22 u_r$.

Booij (1986) measured somewhat lower values: $\overline{u_{g,\max}} \approx 0.25 u_r$ and $\overline{u_g} \approx 0.17 u_r$. The discrepancy between the results of Booij and Dursthoff is probably caused by a smaller water depth in the experiments of Booij, 0.105 m compared to 0.35 m in the experiments of Dursthoff. This results in a larger influence of the bed friction in the harbour. The bed-friction coefficients are $c_f \approx 0.005$ (Booij) and $c_f \approx 0.0045$ (Dursthoff). For harbours with $B_e/B < 1$ the velocities in the gyre are smaller as a consequence of the reduction in entrance width.

Booij developed an analytical model assuming that there is an equilibrium between the transport of momentum from the river to the harbour through the mixing layer and the friction at the harbour sidewalls; and thus obtained $\overline{u_{g,\max}} \approx 0.3 u_r$ ($L/B > 1.5$) to $0.4 u_r$ ($L/B = 1$) and $\overline{u_g} \approx 0.67 \overline{u_{g,\max}} \approx (0.2\text{—}0.27) u_r$.

The transfer of momentum from the primary gyre to the secondary gyre is not well
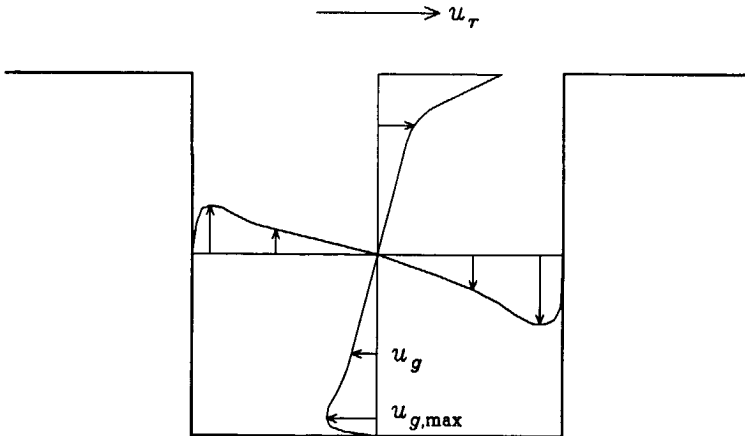
Figure 2.6 Velocity profiles along the central axes of a square harbour.

understood yet. It is sometimes assumed that it is similar to the transfer of momentum from the flow in the river to the primary gyre (Booij, 1986). The velocity in the secondary gyre then is $\overline{u_g} \approx 0.04 u_r$.

The flow in the gyre is highly curved, as a consequence of which a secondary flow exists the strength of which depends on the water depth. The secondary current was already observed by Rohr (1933). The secondary current consists of a flow towards the centre of the gyre near the bottom, and a flow in the opposite direction near the free surface. The secondary current is important for the sediment transport in the harbour. Small sediment particles will spiral towards the centre of the gyre and deposit because the water velocities near the centre are small. The secondary current also transfers momentum and therefore may be important for the development of secondary gyres in the harbour. This can possibly account for the fact that most depth-averaged numerical models are not able to predict secondary gyres.

2.2.3 Exchange of matter

The exchange of matter between a harbour and a river as a consequence of a steady flow along the entrance takes place through the mixing layer. As a result of the roll-up of the wave-like disturbances and the amalgamation of neighbouring vortices, fluid from the harbour and the river is entrained into the mixing layer, see Fig. 2.7. The entrained fluid is homogenized in the core of the shear layer by the small-scale turbulence. When the water in the shear layer flows against the downstream sidewall of the harbour part of it flows into

Figure 2.7 Schematic diagram of entrainment process as a function of the downstream distance, or alternatively, as a function of time while riding with the mean speed. (From Winant & Browand, 1974.)

the river and part of it into the harbour. In this way water from the harbour is transported into the river and river-water is transported into the ha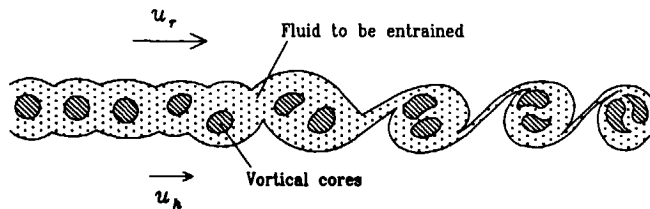rbour. Consequently, exchange of matter occurs if the entrained fluid contains solutes or constituents. The exchange process can be conceived as a diffusion process, the diffusivity of which is the eddy viscosity coefficient ν_t (transport of momentum) or eddy diffusion coefficient D_t (transport of matter). These coefficients are related to each other by the turbulent Schmidt or Prandtl number, $\sigma_t = \nu_t/D_t$. The value of σ_t depends on the quantity being transported and the way the turbulence is produced ($\sigma_t \approx 0.9$ for wall turbulence, and $\sigma_t \approx 0.5$ (mixing layer) and $\sigma_t \approx 0.7$ (round jet) for free turbulence). The eddy diffusion coefficient in a mixing layer is usually expressed as

$$D_t = \beta'(u_r - u_h)\delta/\sigma_t \approx 0.8\beta'u_r\delta/\sigma_t, \qquad (2.7)$$

with $\beta' = \beta/\sqrt{2\pi}$. Thus, the exchange of matter between a harbour and a river increases with u_r and δ. Various values of β' are mentioned in the literature. According to equation (2.4) β' equals 0.011. Equation (2.1), Brown & Roshko (1974), yields $\beta' = 0.014$. According to Rodi (1984) β' equals 0.019 (assuming that the velocity distribution in the mixing layer can be represented by an error integral, the width of the mixing layer as defined by Rodi is $4.653l_0$).

Dimensional considerations give the exchange volume flow rate of water between a harbour and a river as

$$Q_{ex} = Cu_r B_e h,$$

where C is a coefficient that depends on the geometry of the harbour. Booij (1986) obtained $C \approx 0.032$ for harbours with α equal to 90 degrees. Dursthoff (1970) found $C \approx 0.05$, and Obrazovskij (see Dursthoff) $C \approx 0.04$.

The exchange of water between a harbour and a river depends, among other things, on the orientation of the harbour entrance. Experiments of Booij (1986) show that $C \approx 0.05$ for $\alpha = 45$ degrees, and $C \approx 0.02$ for $\alpha = 135$ degrees. Spâtaru & Mârculescu (see Dursthoff) found a smaller influence of the orientation of the harbour entrance: $C \approx 0.035$ for $\alpha = 45$ degrees, and $C \approx 0.025$ for $\alpha = 135$ degrees. The influence of the angle α can be explained by examining the behaviour of the mixing layer. It is observed that in the experiments of Booij the width of the mixing layer is larger for $\alpha = 45$ degrees, and the

width of the mixing layer is smaller for $\alpha = 135$ degrees, with respect to the width for $\alpha = 90$ degrees. A wider mixing layer indicates a larger entrainment of river-water and harbour water into the mixing layer. Consequently, the exchange of water between harbour and river is larger.

For steady flow conditions the exchange of matter is caused by lateral turbulent fluctuations of velocity in the presence of a concentration gradient in the transverse direction of the mixing layer. According to Westrich (1977b) the volume-averaged concentration of dissolved matter in the harbour, $\bar{c}$, can be expressed as

$$\frac{\bar{c}}{\bar{c}_0} = f\left[\frac{h}{B}, \frac{B}{L}, \frac{u_r t}{B}, \frac{u_*}{u_r}, \text{ geometry harbour entrance}\right], \tag{2.8}$$

where $\bar{c}_0$ is the initial concentration at $t = 0$, t is time, and u_* is the bottom shear velocity in the river. The first two dimensionless parameters represent the geometry of the harbour. The third parameter is a dimensionless time, and the fourth parameter is a measure of the turbulence level in the river. The geometry of the harbour entrance can be expressed by the dimensionless parameter B_e/B, and the angle α at which the harbour is oriented with respect to the river axis. Other aspects of the entrance geometry are: the steepness of the sidewalls of the entrance, and the position of a narrowed entrance relative to the harbour basin.

Assuming that the transport of matter from harbour to river is governed by diffusion only, an expression for the function f can be derived from the diffusion equation

$$\frac{\partial c}{\partial t} = \frac{\partial}{\partial x_i}\left[D_t \frac{\partial c}{\partial x_i}\right]. \tag{2.9}$$

Integrating equation (2.9) over the harbour volume V_h yields with the use of the theorem of Gauss and assuming that the volume of water in the harbour is constant in time

$$\frac{\partial}{\partial t}\int_{V_h} c\, dV = \int_\Omega D_t \frac{\partial c}{\partial n}\, d\Omega, \tag{2.10}$$

where n is the direction normal to the boundary, Ω, of the harbour. The concentration gradient in the entrance can be approximated by $(c_r - c_h)/\delta$, where c_r and c_h are the concentrations at the boundaries of the mixing layer, in the river and harbour respectively.

Assuming that the concentration gradients at the closed boundaries and the free surface are zero, and the average concentration in the entrance due to internal mixing in the basin is proportional to the volume-averaged concentration in the harbour, $\overline{c_e} = \varkappa \tilde{c}$, substituting equation (2.7) in the right hand side of equation (2.10) gives

$$V_h \frac{d\tilde{c}}{dt} = -\mu B_e h u_r \tilde{c}. \tag{2.11}$$

The concentration in the river is set to zero so that equation (2.11) characterizes the flushing of a harbour basin. The coefficient μ is given by

$$\mu = \frac{\beta \varkappa (1 - u_h / u_r)}{\sigma_t \sqrt{2\pi}}.$$

Equation (2.11) can be rewritten as

$$\frac{d\tilde{c}}{dt} = -\mu \frac{B_e u_r}{BL} \tilde{c}. \tag{2.12}$$

For the initial condition $\tilde{c}(t=0) = \tilde{c}_0$ the solution of equation (2.12) is:

$$\frac{\tilde{c}}{\tilde{c}_0} = \exp\left[-\mu \frac{B_e}{B} \frac{B}{L} \frac{u_r t}{B}\right]. \tag{2.13}$$

The dimensionless parameters h/B and u_*/u_r are incorporated implicitly in equation (2.13), namely in the coefficient μ. The entrainment parameter β and the ratio u_h/u_r depend on the turbulence level in the river and the bed friction.

Measurements of Westrich (1977a), see Fig. 2.8, confirm equation (2.13).

The parameter B/L becomes important if $L \gtrsim 2B$. The primary gyre then drives a secondary gyre. Replacing, in equation (2.7), u_r by u_h the diffusivity of the mixing layer between the primary and the secondary gyre is much smaller than that of the mixing layer in the harbour entrance. The overall diffusion in the harbour decreases. Consequently, the exchange of matter between harbour and river is reduced because a part of the harbour contributes to the exchange process to a much lesser extent.

Westrich & Clad (1979) observed, see Fig. 2.9, that a single-gyre system has a greater exchange intensity than the corresponding double-gyre system of the same dimension. The single-gyre system was obtained by making a narrowed entrance at the downstream side
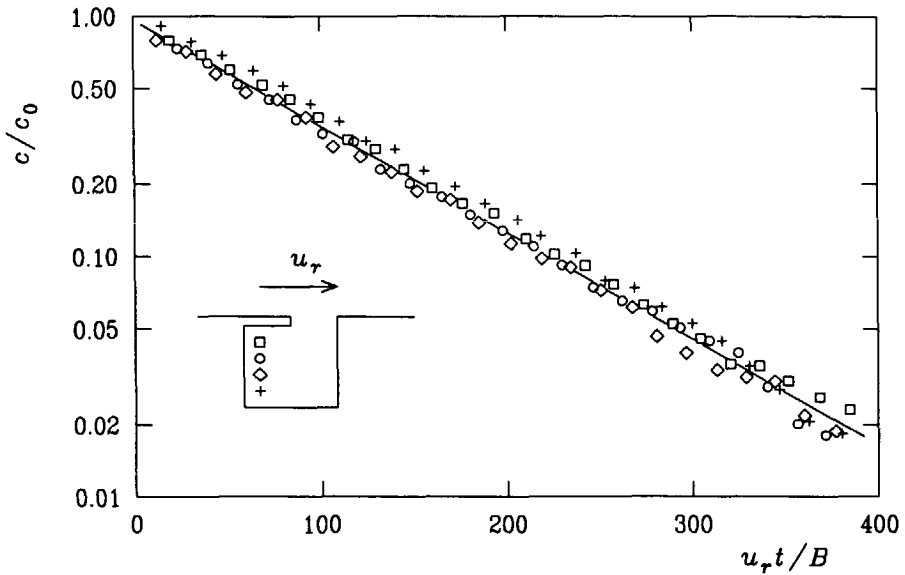
Figure 2.8 The concentration of dissolved matter in progress of time at four points in a harbour. (From Westrich, 1977a.)

of the harbour basin, whereas the double-gyre system occurred when the narrowed entrance was moved to the upstream side of the harbour basin.

Fig. 2.9 also shows the influence of the relative depth on the exchange of water between harbour and river, which is represented by the coefficient μ. Here μ is rewritten as

$$\mu = \ln 2 \frac{B}{B_e} \frac{L}{u_r t_{1/2}}, \qquad (2.14)$$

where $t_{1/2}$ is the half-life of the average concentration in the harbour.

The half-life of the average concentration in the harbour is, according to equation (2.14), proportional to

$$t_{1/2} \propto \frac{B}{B_e} \frac{L}{u_r}.$$

A similar result is obtained by dimensional analysis. Equation (2.9) shows that $t_{1/2}$ is proportional to BL/D_t. When the turbulence in the harbour basin is mainly due to production

B_e/B	one gyre			two gyres	
B/L	1/1	1/2	1/4	1/2	1/4
1.6/1.6	×				
0.8/0.8	■	◫	□	◪	◪
0.4/0.4	o	◐	o	◪	◪
0.2/0.2	◆	◈	◇	◪	◪
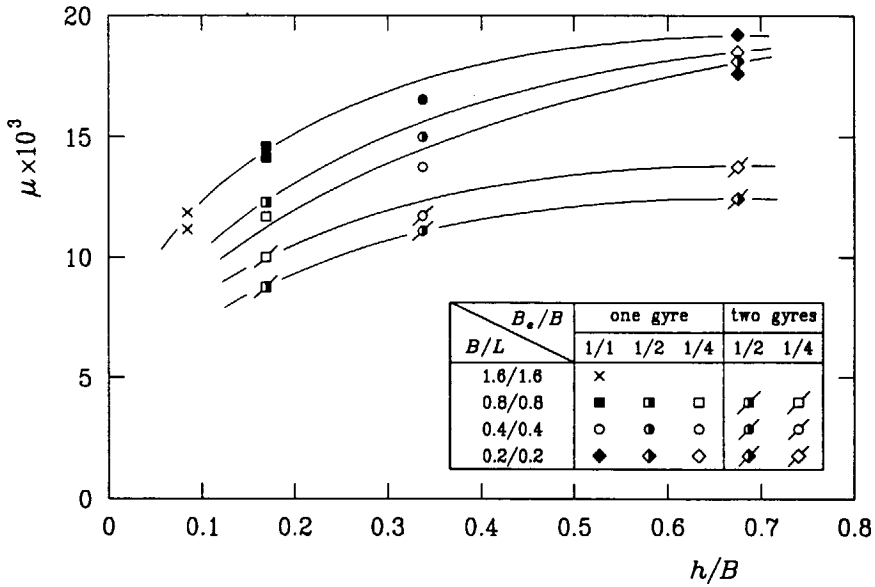
Figure 2.9 Influence of the parameters h/B and B_e/B on the exchange between harbour and river $u_*/u_r = 0.058$. (From Westrich & Clad, 1979.)

in the mixing layer, the diffusivity increases linearly with distance downstream of the separation point (for relatively deep harbours) and the flow velocity in the river. The average diffusivity in the harbour then is proportional to $u_r B_e$.

McGuirk & Rodi (1979) found, see Fig. 2.10.a, that the parameter $t_{1/2} u_r/L$ varied strongly with the water depth at small depths, but approached a constant value at larger depths. In their experiments B_e/B was constant. This agrees with the work of Westrich & Clad (1979), which was shown in Fig. 2.9. The variation of $t_{1/2} u_r/L$ is caused by the influence of bed friction at small depths. Therefore, the diffusion coefficient depends on the water depth. McGuirk & Rodi (1979) assumed the eddy diffusivity to be proportional to $u_r h$, which leads to

$$t_{1/2} \propto \frac{B}{h} \frac{L}{u_r}.$$

The parameter $t_{1/2} u_r h/BL$ varied much less with h than the parameter $t_{1/2} u_r/L$ did, see Fig. 2.10.b, particularly so at small depths where the turbulence is mainly bottom generated.

Figure 2.10 Variation of dimensionless half-life parameters with depth.
O——— = calculation of McGuirk & Rodi (1979), and × = experiments of Nestmann (1977).

As a result, the flushing rate of a harbour basin can be increased by increasing the flow in the river, decreasing the surface area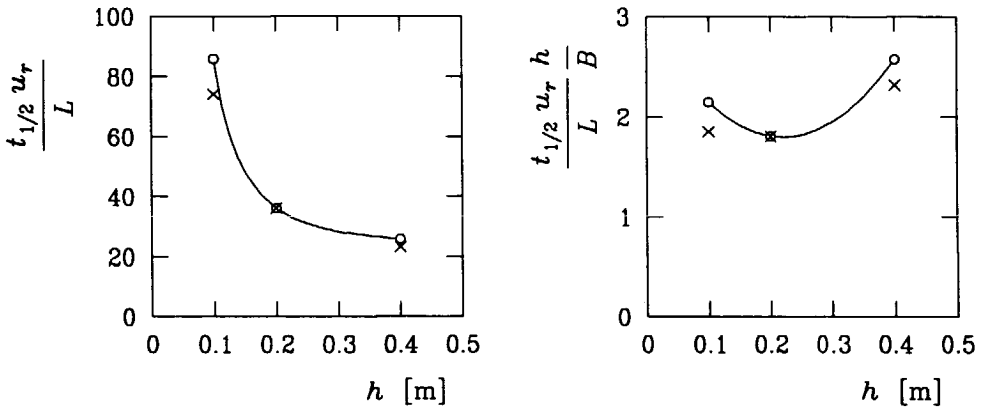 of the harbour basin, increasing the water depth, or increasing the entrance width. This agrees with observations of Westrich & Clad (1979). They found a decrease in exchange between harbour and river with decreasing B_e/B. Also, decreasing h/B led to a decrease in exchange. In deep water the mixing process is more or less three-dimensional, whereas in shallow water the horizontal mixing is weak with respect to the vertical mixing. Therefore, it takes more time to mix the central part of the gyre, giving a smaller exchange of matter between harbour and river.

Equation (2.8) is concerned with dissolved material. For sediment or silt further parameters must be introduced. The fall velocity of the sediment then is important. For cohesive sediments the fall velocity depends on the sizes of the flocs. The flocculation is determined by the turbulence level, the concentration, and the salinity. Furthermore, the critical shear-stress of erosion of cohesive sediments is larger than that of deposition. The rheological characteristics of silt are important for the amount of erosion. The strength of the silt bed increases in time due to the consolidation of the bed.

Rohr (1933) and Vollmers (1963) studied the siltation of harbours as a consequence of a steady river-flow along the harbour entrance. Rohr (1933), see Fig. 2.11, gave an
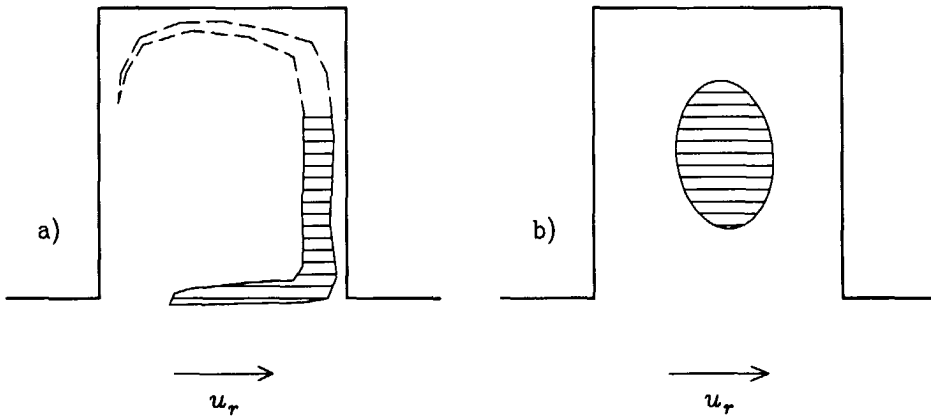
Figure 2.11 Deposition patterns of sediments in a harbour as a consequence of: a) bed-load transport, and b) suspended transport. (From Rohr, 1933.)

illustration of the deposition patterns of coarse (bed-load transport) and fine (suspended transport) sediments.

Rohr (1933) mentioned that the deposition of sediment in a harbour as a consequence of bed-load transport, at constant width of the harbour, increases with the length of the harbour to attain eventually a constant value. This applies also to suspended sediment transport.

Measures to reduce the siltation of harbour basins owing to a uni-directional flow in the river were extensively studied by among others Vollmers (1963) and Dursthoff (1970). Because the gyre in the entrance determines the amount of siltation, they tried to alter its shape and characteristics by changing the geometry of the harbour entrance. Another possibility is to build devices in the entrance to change the shape and characteristics of the gyre.

The most promising of the different measures is that of a deflection wall near the upstream corner of the harbour entrance, see Kirby (1991). A current is generated along the upstream sidewall of the harbour, its direction being opposite to that of the gyre, which annihilates the gyre in the entrance. In the Köhlfleet harbour in Hamburg a reduction in the amount of siltation of approximately 35 per cent has been obtained in this way.

The exchange of matter between a harbour and a river due to an unsteady flow in the river

is discussed only in combination with water level changes at the river, which is discussed in section 2.5.

2.3 A net flow through the harbour entrance

A net flow through the entrance can be caused by: variations in water level at the river; withdrawal of water from or discharge of water to the harbour basin.

Although water level changes are partly caused by variations in the discharge of the river, for example during a peak flow flood wave, variations in tidal level are the most significant cause of a net flow through the entrance. During flood the increase in water level results in a filling of the basin, and during ebb the decrease in water level results in an emptying of the basin, see Fig. 2.12. The water enters or leaves the harbour over the entire depth and width of the harbour entrance.

The tidal motion in a harbour can be computed by the one-dimensional shallow water equations

$$B \frac{\partial \zeta}{\partial t} + \frac{\partial Q}{\partial x} = 0, \qquad (2.15.a)$$

$$\frac{\partial Q}{\partial t} + \frac{\partial}{\partial x} \left[\frac{Q^2}{A} \right] + gA \frac{\partial \zeta}{\partial x} + \frac{g}{C^2} \frac{Q|Q|}{AR} = 0, \qquad (2.15.b)$$
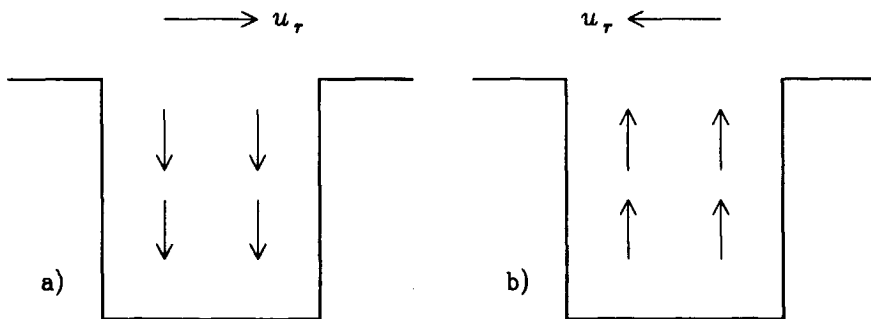

Figure 2.12 Flow pattern in the harbour as a consequence of tide level changes at the river: a) during flood, and b) during ebb.

where ζ is the local water level elevation, Q is the flow rate, A is the area of the cross-section of the harbour, x is the direction parallel to the harbour axis, g is the acceleration due to gravity, C is the Chézy coefficient, and R is the hydraulic radius. At the back wall of the harbour $Q = 0$. Equation (2.15.b) then simplifies to $\partial \zeta/\partial x = 0$. This applies approximately for the entire harbour if the length of the harbour is smaller than about 5 per cent of the tidal wave length, as is usually the case. Integrating equation (2.15.a) to x then yields for the flow rate through the entrance due to tide level changes

$$Q_s = A_h \frac{d\zeta}{dt},$$ (2.16)

where A_h is the storage area of the harbour.

The flow rate of water entering the harbour and the duration of filling of the basin increase as a consequence of withdrawal of water from the harbour. This leads to a larger volume of river-water entering the harbour during a tide. Discharge of water to the harbour decreases the volume of river-water entering the harbour during a tide.

2.4 Density-driven exchange flow

Exchange flows between harbour and river are driven by density differences between the water in the harbour and the river-water. These density differences are associated with differences in salinity, temperature, silt content, or a combination of the three factors. Generally, the difference in salinity is the most important factor that induces the exchange flow. Measurements of Roelfzema & Van Os (1978) showed that, when the three flow mechanisms occur simultaneously, the exchange due to density differences can be 75 per cent of the total exchange of water between harbour and river.

If the density of the river-water is larger than that of the water in the harbour, river-water enters the harbour along the bottom, while water from the harbour leaves the harbour near the surface. The process is reversed if the density of the river-water is lower than that of the water in the harbour, see Fig. 2.13.
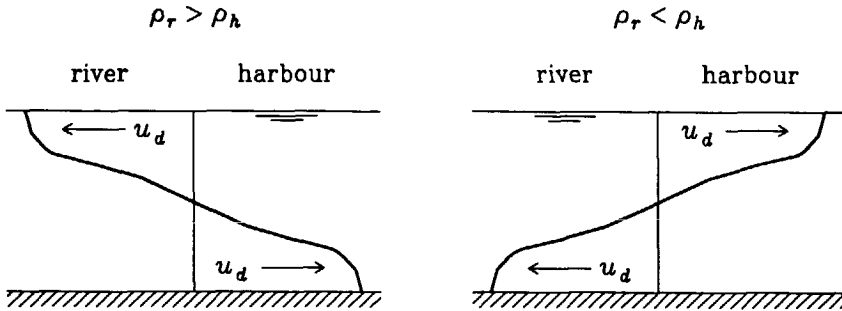
Figure 2.13 Density-driven exchange flow in the harbour entrance.

At the transition from harbour to river a double critical flow establishes itself (Fig. 2.13). Neglecting friction losses at the interface between fresh and salt water, the exchange discharge is given by (Schijf & Schönfeld, 1953):

$$Q_{ex} = \frac{1}{4} B_e h \sqrt{\varepsilon g h} \, , \qquad (2.17)$$

where ε is the relative density: $|\rho_r - \rho_h|/\rho_h$. Assuming that the layer depths are half the water depth, the water velocity in both layers is $u_d = \frac{1}{2}\sqrt{\varepsilon g h}$.

Usually, the exchange discharge will be smaller because of energy losses due to circulating flows in the fresh and salt layers, friction between the layers, mixing between the layers, and contraction of the flow into the harbour. Empirically determined exchange discharges are about 10 per cent smaller than given by equation (2.17).

For a constant density of the river-water, the density of the harbour water approaches the density of the river-water. The density difference between harbour water and river-water then decreases in time. Consequently, the exchange discharge decreases. The exchange discharge also decreases because the flow at the transition from harbour to river does not remain double-critical after reflections of internal waves in the harbour. The flow at the transition from harbour to river then is just critical.

However, the densities in the harbour and river are not constant in space and time. For harbours on estuaries the density of the river-water changes as a consequence of the tide. Fresh water is present in front of the harbour during ebb, whereas salt water is present in front of the harbour during flood. As a result, the direction of the density-driven exchange

flow in the harbour entrance continually reverses. The degree of mixing between salt and fresh water in the river, and thus the density distribution in the river in space and time, is also determined by the tide (see section 2.5).

The salinity of the water influences the siltation of harbour basins. It has a large effect on the flocculation of silt and thus on the fall velocity of the flocs. Harbours situated on estuaries at the transition from fresh river-water to salt sea-water have to deal with large problems concerning the siltation of their basins, because every tidal cycle a large volume of harbour water is renewed.

2.5 Interactions of the flow mechanisms

Generally, the exchange of matter between harbour and river is not caused by only one of the three flow mechanisms discussed in the preceding sections, but by a combination of these flow mechanisms. In some situations one of the three mechanisms can be neglected with respect to the other two mechanisms. For a harbour situated directly on the sea coast or upper river, the exchange flow due to a density difference between harbour water and river-water is usually negligible. For harbours situated along estuaries the exchange of matter between harbour and river is determined often by a combination of all flow mechanisms.

The flow mechanisms will interact when they occur simultaneously, for example see Booij (1986), Delft Hydraulics (1977), and Roelfzema & Van Os (1978). The flow rate through the harbour entrance is sometimes assumed to be simply the sum of the flow rates due to the three mechanisms separately, MKO (1983). Measurements of Booij (1986) show that this concept is not valid for a combination of flow along the harbour entrance and a net flow through the harbour entrance.

If nevertheless superposition of the three flow mechanisms is allowed, the consequences are (MKO, 1983):

1) For the condition that the density-driven exchange flow can be neglected and the velocity u_s of the net flow into the harbour is less than the velocity $\overline{u_{g,max}}$ of the
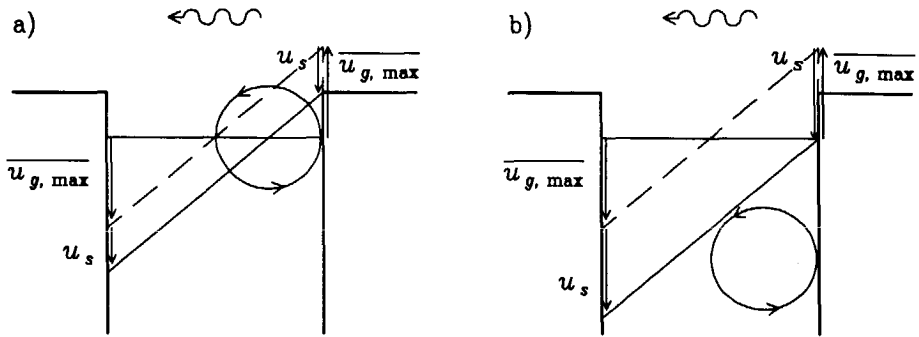
Figure 2.14 Superposition of a flow filling the basin and a gyre, according to MKO (1983).

gyre in the entrance, the water motion in the entrance is shown in Fig. 2.14.a concerning a filling of the harbour basin. The resulting gyre at the upstream corner of the harbour entrance has been observed in field measurements. River-water enters the harbour at the downstream sidewall of the entrance.

The gyre is located at the downstream corner of the entrance if an emptying of the harbour basin occurs, while harbour water leaves the harbour at its upstream sidewall.

2) As condition 1), except that the velocity of the net flow is larger than the maximal velocity of the gyre. Fig. 2.14.b shows that a small gyre, which does not take part in the exchange process, then is present further into the harbour.

3) The presence of all three flow mechanisms results in different locations of the gyre in the upper and lower layers, see Fig. 2.15. In the case shown the river-water has a higher density than the harbour water, and the basin is being filled.

Booij (1986) studied the exchange as a consequence of a flow along the mouth of the harbour in combination with discharge and withdrawal of water, to and from the harbour respectively. The mixing layer is shifted towards the river by discharging water to the harbour basin. As a consequence less river-water will flow into the harbour, which results in a weaker gyre. Withdrawal of water from the harbour results in a stronger gyre. These results indicate that in a quantitative sense superposition is not correct.
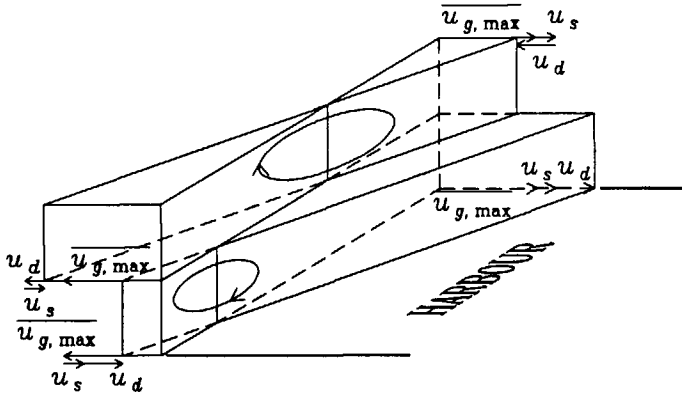
Figure 2.15 Superposition of the three flow mechanisms, according to MKO (1983).

Dursthoff (1970) asserts that the three flow mechanisms interact. The gyre in the entrance can be suppressed or hindered by the density-driven exchange flow. Furthermore, he states that if a gyre and a density-driven exchange flow occur simultaneously, the gyre causes mixing between the upper and lower layers, through which the density-driven exchange flow can be reduced.

Christiansen (1987) states that the effect of the gyre in the harbour entrance is a narrowing of the stream filling the basin during rising tide, see Fig. 2.16.a, resulting in a higher flow velocity and consequently a larger transport of sediment into the basin. Because of the lower
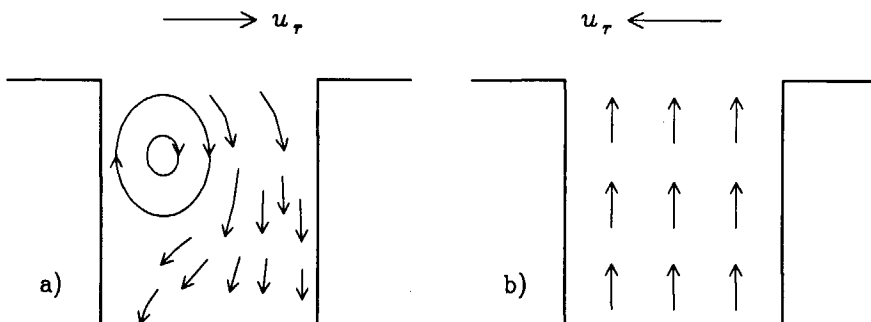
Figure 2.16 Currents in a tidal harbour: a) during flood, and b) during ebb. (From Christiansen, 1987.)

velocities further into the harbour the sediment is deposited. After flood slack tide the gyre is pushed out of the harbour by the emptying of the basin. The emptying of the basin during ebb suppresses the gyre, see Fig. 2.16.b. As a result, the lower velocities in the harbour basin are not sufficient to resuspend all the deposited sediment. Continuous sedimentation of the harbour then ensues.

The suppression of the gyre during ebb was observed in field measurements in a harbour in Rotterdam, MKO (1987).

Westrich (1977b) and Brinkmann (1990) studied the exchange between a harbour and a river due to an unsteady flow in the river and water level variations at the river.

Westrich (1977b) assumed the exchange between harbour and river to be the sum of the exchange due to a flow along the harbour entrance (see section 2.2, equation 2.13) and the exchange due to water level variations separately. Assuming that the concentration in the river is zero, the volume- and tide-averaged concentration of dissolved matter in the harbour is given by:

$$\frac{\bar{c}}{\bar{c}_0} = \exp\left[-(\mu u_r + \gamma \bar{w})\frac{\bar{A}}{\bar{V}}t\right], \qquad (2.18)$$

where γ, $0 \leq \gamma \leq 1$, is a constant describing the degree of internal mixing in the harbour basin, $\bar{w}$ is the cross-sectional average mean lateral velocity in the entrance during the filling and emptying of the basin, $\bar{A}$ is the average area over one tidal cycle of the entrance cross-section, and $\bar{V}$ is the average harbour volume over one tidal cycle. For steady flow conditions, $\mu u_r/\gamma \bar{w} \gg 1$, equation (2.18) reduces to equation (2.13). For large water level variations in the river, $\mu u_r/\gamma \bar{w} \ll 1$, equation (2.18) reduces to

$$\frac{\bar{c}}{\bar{c}_0} = \exp\left[-\gamma \bar{w}\frac{\bar{A}}{\bar{V}}t\right].$$

The mass exchange coefficient for the unsteady situation then is

$$\mu = \frac{\ln 2}{t_{1/2}\dfrac{\bar{A}\bar{w}}{\bar{V}}} = \frac{2\ln 2}{\dfrac{t_{1/2}}{T}\dfrac{\Delta V}{\bar{V}}},$$

where T is the tidal period, and ΔV is the tidal prism.

Figure 2.17 shows the influence of the tidal period and range on the exchange of water between harbour and river. The flushing rate of the harbour increases by increasing the tidal prism and period. For the extreme situation that $\Delta V/\overline{V} \to 0$ or $L/u_r T \to 0$ the flow in the harbour entrance is quasi-steady and the exchange is caused by turbulent diffusion only. Thus, $t_{1/2} u_r/L$ is constant for relatively deep harbours, see section 2.2 and Fig. 2.17. In the limit that $L/u_r T \to \infty$ the exchange is determined only by the tidal range and the surface area of the harbour.

Westrich (1977b) only considered unsteady flow in one direction. Consequently, his results cannot be applied to tidal flow. Measurements of Brinkmann (1990) show that during slack water the exchange of water between harbour and river increases because of changes in flow direction in the river. Fig. 2.18 shows that this exchange is mainly convective, the gyre in
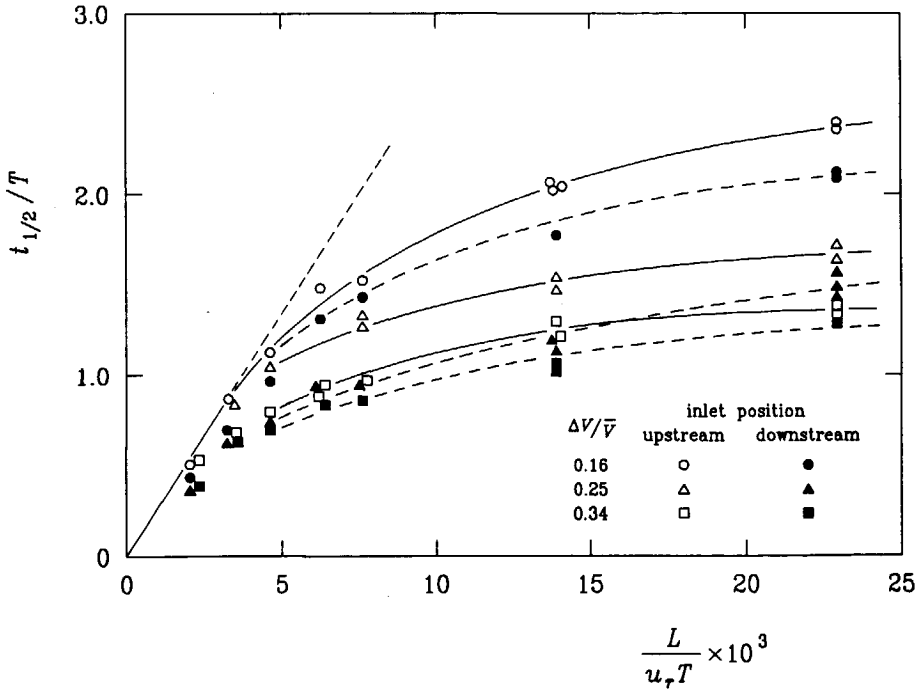

Figure 2.17 Influence of the tidal range and period on the exchange of water between harbour and river: $B_e/B = 0.25$, $h/L = 0.16$. (From Westrich, 1977b.)
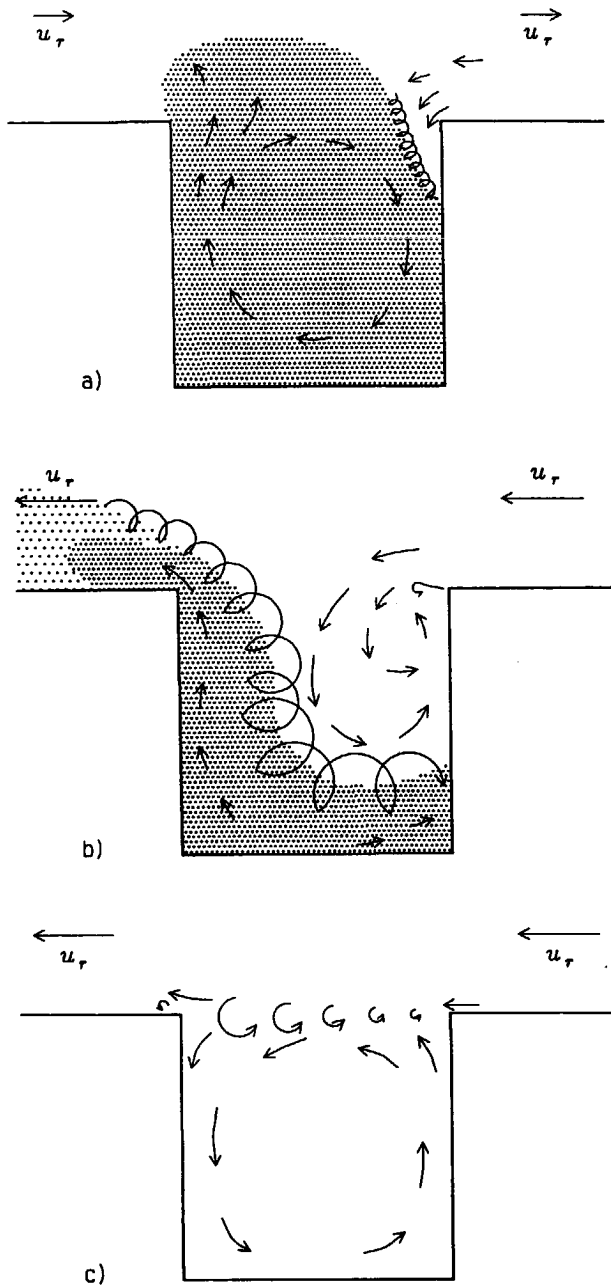
Figure 2.18 Flow pattern in a harbour on a tidal river (tidal period is 900 s): a) 10 s before ebb slack tide, b) 85 s after ebb slack tide, and c) 145 s after ebb slack tide. (From Brinkmann, 1990.)

the harbour entrance moves into the river, and after slack water is replaced by a new gyre containing river-water. About 60 per cent of the total exchange of water over a tidal cycle occurs during both slack waters.

Brinkmann (1990) carried out experiments in a harbour on a tidal river to determine the relationship between the magnitude of the exchange of water between harbour and river and the water depth, the tidal range, the velocity in the river, the tidal period, the size of the harbour basin, and the width of the harbour entrance. Two related dimensionless parameters were found. One, $\Pi_1 = u_{r,max} T/h$, describing the influence of the maximum velocity in the river and the water depth, the other, $\Pi_2 = L^5/B^4 h$, describing the influence of the ratio of the length and the width of the harbour basin. The percentage of water of the harbour volume, Q_{ex}, that is exchanged per tidal cycle between harbour and river is given by (see Fig. 2.19)

$$Q_{ex} \Pi_2^{0.1} = 67.48 \, \Pi_1^{0.081}. \tag{2.19}$$

The exchange must be multiplied by $\sqrt{B_e/B}$ for entrances smaller than the width of the harbour. The exchange then is given by

Figure 2.19 The exchange of water between a harbour and a tidal river.
———— = equation (2.19). (From Brinkmann, 1990.)

$$Q_{ex} = 67.48 \left[\frac{u_{r,\max} T}{h} \right]^{0.081} \left[\frac{B_e^5 h}{BL^5} \right]^{0.1}.$$

Density-driven exchange flow through the harbour entrance usually occurs simultaneously with tidal flow in the river. The density of the river-water in front of the harbour then is 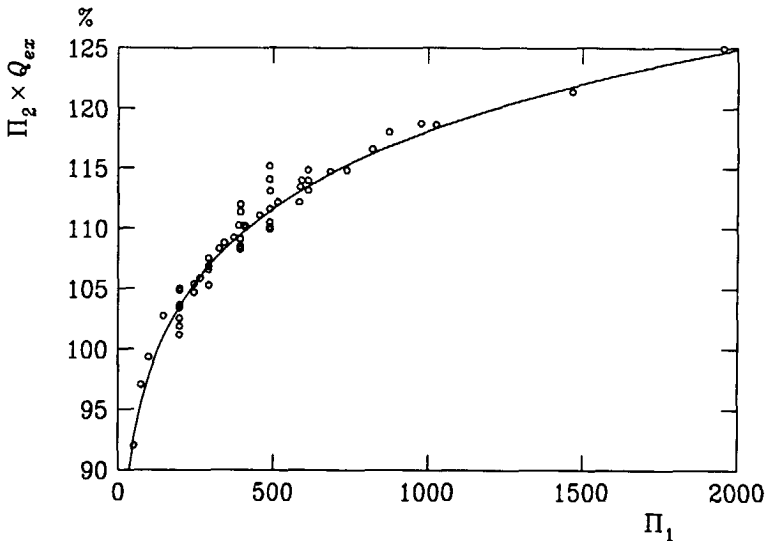not constant in space and time due to the tidal flow in the river. There will be a time lag between the variations in density of harbour water and in the density of river-water. The density of harbour water follows that of the river-water. The magnitude of the time lag is determined by the rate at which harbour water is exchanged by river-water, which depends on the width of the harbour entrance, the volume of the harbour, the velocity of the exchange flow and the period of the tide. Consequently, the density variation of harbour water is smaller than that of river-water. The density of harbour water equals about the tide-averaged density of the river-water. Then, $\left| \rho_r - \overline{\rho_r} \right| / \overline{\rho_r}$ can be used as relative density difference in equation (2.17).

The layer depths of the density-driven exchange flow change when a net flow is present in the harbour entrance. Assuming that the flow at the transition from harbour to river is critical the layer depths can be determined.

The tidal flow in the river has an influence on the degree of mixing of the fresh river-water and the salt sea-water, and thus the density distribution in front of the harbour. The degree of mixing in the estuary can be expressed by the estuarine Richardson number Ri_E, Fischer et al. (1979):

$$Ri_E = \frac{\Delta \rho \, g \, Q_f}{\rho \, W u_t^3}, \tag{2.20}$$

where $\Delta \rho$ is the density difference between sea-water and fresh river-water, Q_f is the fresh water discharge, W is the channel width at the mouth, and u_t is the rms tidal velocity at the mouth. Observations of real estuaries suggest that, very approximately, the transition from a well mixed to a strongly stratified estuary occurs for Ri_E in the range 0.08 (well mixed: $Ri_E < 0.08$) to 0.8 (stratified: $Ri_E > 0.8$).

Model experiments, Delft Hydraulics (1977), showed that the largest exchange of water between harbour and river occurred at well mixed conditions at the river.

2.6 Summary and discussion

In this chapter the main mechanisms that cause siltation of harbour basins were considered. The exchange between a harbour and a tidal river is caused by the water motion in the entrance. Three main flow mechanisms can be distinguished in the water motion: (1) a mixing layer at the transition from harbour to river as a consequence of a velocity difference between the flows in the river and in the harbour, (2) a net flow through the entrance, and (3) an exchange flow as a consequence of a density difference between harbour water and river-water.

These mechanisms usually occur simultaneously, and they will interact. Thus, a superposition of the exchanges caused by the individual flow mechanisms is not correct. Generally, when the flow mechanisms coincide, the density-driven exchange flow gives the largest exchange of water between harbour and river.

The exchange of water between harbour and river then can be decreased largely by influencing the density-driven exchange flow. The exchange of water between harbour and river will decrease by decreasing the density difference between harbour water and river-water. However, the density of river-water is a fixed quantity. The mixing between the fresh and the salt layers in the harbour entrance then has to be increased to reduce the density difference between harbour water and river-water, for example by an air bubble curtain at the transition from harbour to river (see Delft Hydraulics, 1975).

Studies of the influence of mechanism 3 on the exchange of water between harbour and river are scarce in literature . Not only because mechanism 3 cannot be modified, but also because laboratory experiments require large and complex facilities.

However, many harbours are situated directly on sea coasts or upper rivers, or the ports are separated from the estuaries by locks. Mechanism 3 then is not important and the exchange of water between harbour and river is largely determined by mechanism 1.

Extensive research concerning mechanism 1 has been carried out to quantify the exchange of water between harbour and river, and to find measures to decrease this exchange. The magnitude of the exchange caused by the mixing layer is governed by the flow pattern in the

harbour, which is determined by the geometry of the harbour entrance. Measures to decrease the exchange of water between harbour and river concern the altering of the entrance geometry, through which the gyre in the entrance disappears or its size decreases (Vollmers (1963), Dursthoff (1970), and Christiansen (1987)).

Mechanism 2 is mostly caused by variations in tidal level. The exchange between harbour and river due to mechanism 2 can be decreased only by decreasing the surface area of the harbour. However, the surface area of a harbour is mostly a fixed condition when designing a harbour. Mechanism 2 can be used to influence mechanism 1. For example, a net flow directed towards the river can prevent the development of a gyre in the harbour entrance. Consequently, the siltation of the harbour basin then is reduced.

Generally, the exchange is reduced by decreasing the cross-section of the harbour entrance, decreasing the water depth, decreasing the water velocity in the river (as a result of which the velocity difference between the flows in the river and in the harbour is decreased), increasing the length to width ratio of the harbour (or in general inducing several gyres in the harbour, through which only a part of the harbour contributes to the exchange process), and decreasing the density difference between river-water and harbour water.

3 Laboratory experiments

3.1 Introduction

In the previous chapter the mechanisms, which cause exchange of matter between a harbour and a tidal river, were discussed. Three flow mechanisms were considered to be the main causes, namely: (1) a flow along the entrance of the harbour; (2) a net flow through the harbour entrance; and (3) a density-driven exchange flow, generally due to differences in salinity between the river-water and the water in the harbour. Parameters and quantities were determined that influence the flow in harbour basins and the exchange of mass between a harbour and a tidal river. It was shown that the geometry of the entrance has a substantial effect on the exchange of mass between harbour and river. Therefore, the influence of the entrance geometry on the velocity and density fields in the entrance of a tidal harbour is examined by using physical models.

The experiments had a two-fold goal: a) qualitatively, to increase our insight into the interactions between the three mechanisms; and b) quantitatively, to generate a data set with which numerical models can be tested for the flow in harbour entrances. This chapter considers goal (a), while goal (b) is discussed in chapter 4. The data files containing the generated data set are available on floppy disk (see Langendoen, 1990).

Because the flow pattern in the entrance is quite complicated owing to interactions of the three flow mechanisms, experiments with an unstratified and with a stratified tidal flow in the river were carried out.

Two facilities were used to carry out the experiments: a model in the Hydromechanics Laboratory (Department of Civil Engineering, Delft University of Technology) for the experiments with homogeneous density, and the Tidal Flume of Delft Hydraulics for the experiments with stratified flow.

The model at the Delft University of Technology consists of a basin, area 4 m × 2 m, in which harbour entrances of different geometry can be built, and an adjacent straight flume,
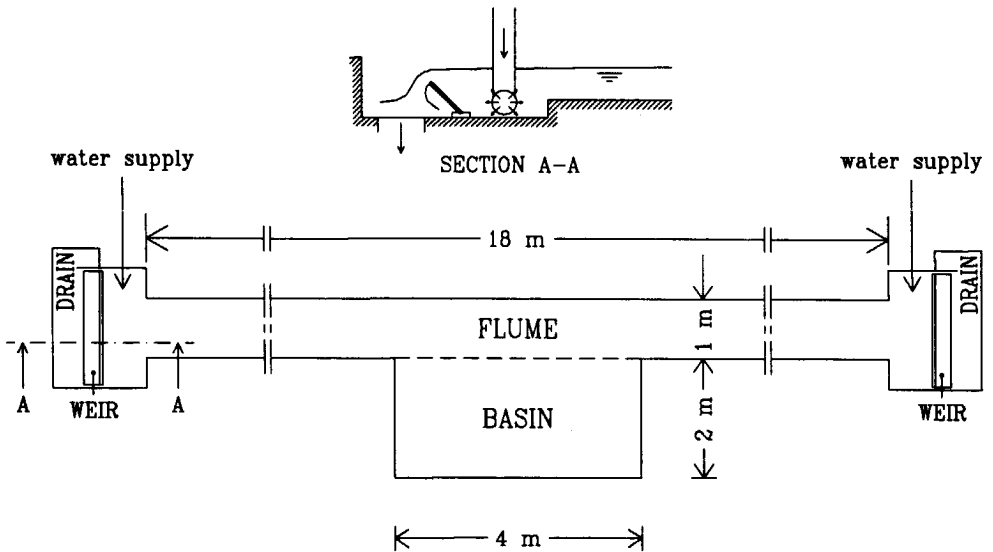
Figure 3.1 Physical model at the Delft University of Technology.

length 18 m and width 1 m, representing a river in which a uniform time-varying (tidal) current can be generated, either with or without tide level variations, see Fig. 3.1. The model is built up from brick sidewalls covered with a thin layer of mortar, and a bottom of mortar. The bottom of the model is horizontal and the sidewalls are vertical. The various harbour geometries were constructed using plaster elements. The flow in the flume is generated by a constant water supply and an adjustable sharp-crested weir at each end of the flume.

In this facility depth-averaged velocities, vertical distributions of time-mean velocities and the exchange of heat between harbour and river were measured to determine the influence of the geometry on the flow pattern in the harbour entrance and the exchange of water between harbour and river.

Depth-averaged velocities were measured by determining the paths of floats that drew almost until the bottom. Mean horizontal flow components were measured at some tens of locations using electromagnetic velocimeters, diameter 0.033 m. The instantaneous velocities were averaged using a triangular filter with a width of 20 s. The exchange of heat between harbour and river was determined by mixing the water in the harbour with hot water, which

resulted in a rise in temperature of approximately 2 degrees centigrade, when the current in the river was near maximum. This water was sprayed into the water inside the harbour to obtain a horizontally and vertically uniform temperature distribution while disturbing the flow as little as possible. Subsequent time histories of temperature were measured using thermistors at several locations in the harbour.

For a more detailed discussion of model and measurements see Langendoen (1989,1990).

A sketch of the Tidal Flume is shown in Fig. 3.2. The two major sections of the Tidal Flume are a basin with a surface area of 120 m^2, representing a sea, and a flume with a width of 1 m and a length of 130 m, representing a river. A rectangular harbour basin of 3.60 m × 2.76 m, in which various geometries of the harbour entrance were examined, was situated at 24.5 m from the transition from sea to flume.

The following quantities were measured at various locations in the harbour entrance and an adjacent section of the river: salinity, temperature, water velocity, and water elevation.

The salinity was measured using a conductivity probe (eight points in the water column), and the horizontal flow components were measured using an electromagnetic velocimeter (five points in the water column for the unstratified flow and eight points for the stratified flow).

An extensive description of the Tidal Flume is given by Delft Hydraulics (1986). For a detailed discussion of model and measurements see Langendoen & Karelse (1990).
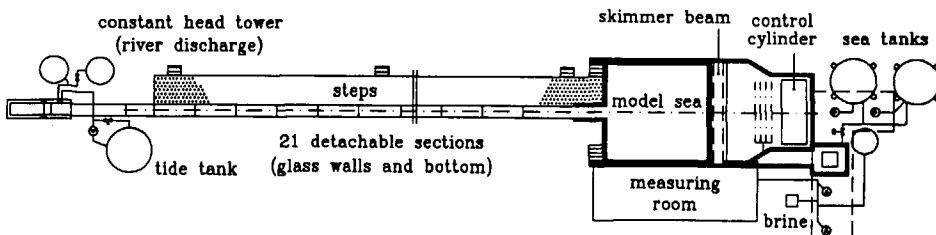

Figure 3.2 Plan of the Tidal Flume of Delft Hydraulics (harbour basin not shown).

Three series of experiments were carried out: (1) experiments with an oscillatory current in the river without variations in water level, (2) experiments with an oscillatory current in the river with variations in water level, and (3) experiments with a stratified tidal flow. Experiment series (1) are discussed in section 3.2, experiment series (2) in section 3.3, and experiment series (3) in section 3.4, followed by a discussion in section 3.5.

Simulations of the measured flow in the harbour and the measured exchange of matter between harbour and river were carried out with computer models for two model harbours from experiment series (1), see Chapter 4. When the results of the measurements that were simulated are presented in section 3.2, their corresponding simulations are referred to. In this way the measurements and their simulations can be viewed simultaneously.

3.2 Experiments with an oscillatory current in the river

A flow along the mouth of the harbour produces an exchange of water between harbour and river, because a mixing layer is present at the transition from harbour to river due to the velocity difference between the flow in the river and the gyre in the harbour entrance. Transport of matter occurs from harbour to river and vice versa through the mixing layer. The exchange due to a steady flow in the river has been studied extensively as is shown in chapter 2. However, the exchange between harbour and river and the flow pattern in the entrance due to an oscillatory flow in the river has hardly been studied, despite the fact that for tidal harbours the flow along the entrance is usually oscillatory. Brinkmann (1990) examined the exchange of water between a harbour and a tidal river. However, studies of the velocity field in the entrance, which can lead to a better understanding of the exchange mechanisms and the way they interact, are lacking.

The exchange of water between harbour and river due to an oscillatory flow in the river without variations in water level, is a function of the following dimensionless parameters (see chapter 2): B/L, B_e/B, h/B, $\hat{u}T/B$, $u_*/\hat{u}$, the Reynolds number, and the angle α the harbour entrance makes with the river axis. Here $\hat{u}$ is the amplitude of the tidal current velocity. A

definition sketch is shown in Fig. 2.5. The influences of these parameters on the exchange of water between harbour and river and the flow in the harbour entrance were studied in the model at the Delft University of Technology.

Four geometries of the harbour were considered, see Fig. 3.3. Three harbours had their length axes perpendicular to the length axis of the river, namely: (1) a square harbour of 1 m × 1 m, (2) a rectangular harbour of 1 m × 2 m and (3) a square harbour of 1 m × 1 m with a narrowed entrance of 0.5 m; one harbour, (4), of 1 m × 1 m and an entrance width of 1 m had its length axis at an angle of 45 degrees to the length axis of the flume. The sidewalls of the harbours were vertical and the bottoms of river and harbours were at the same horizontal level. Table 3.1 lists the experiments made and the values of the dimensionless parameters for the model harbours. The mean water depth was 0.11 m in all experiments.

If the model harbours are supposed to represent a harbour of width 200 m and depth 20 m, which is the size of a typical basin in the Rotterdam harbour area, the length scales are of the order 200. Assuming a maximum water velocity in the field of 1 m/s conventional Froude law scaling to obtain the velocity scale would yield a maximum Reynolds number in the model harbours of 2750. To maintain turbulent flow in the model harbours the Froude
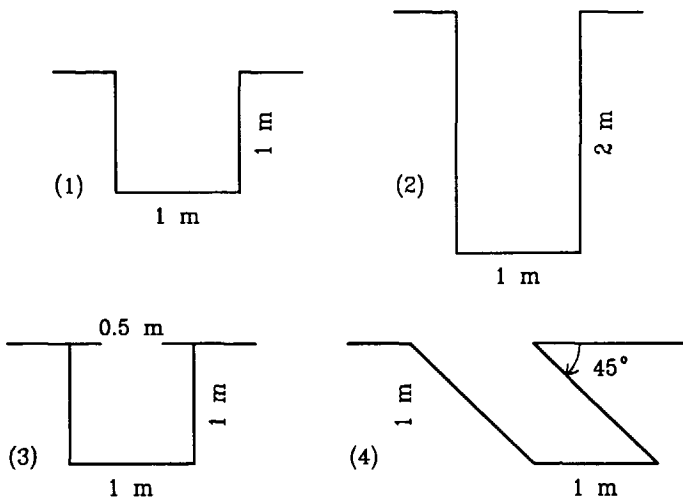

Figure 3.3 Top view of model harbours.

Table 3.1   Values of the dimensionless parameters for the model harbours
examined at the Delft University of Technology.

	exp. no.	$\dfrac{\hat{u}T}{B} \cdot \dfrac{B_e}{B}$	$\dfrac{B}{L}$	$\dfrac{h}{B}$	$\dfrac{B_e}{B}$	α
Harbour 1	1A	95				
	1B	190	1	0.11	1	90
	1C	380				
Harbour 2	2A	95				
	2B	190	0.5	0.11	1	90
	2C	380				
Harbour 3	3	95	1	0.11	0.5	90
Harbour 4	4	190	1	0.11	1	45

number criterion was dropped, which is allowed because free surface deformations are not important here. Scaling according to the Reynolds criterion would yield a maximum Froude number in the flume of 170. As a compromise a velocity scale of 2.5 was chosen. The related maximum Reynolds number in the model harbours was about 15000, and the maximum Froude number in the flume was 0.36. The corresponding amplitude of the velocity in the flume was 0.37 m/s.

A characteristic time scale of the tide, t_t, is the tidal period T. The time scale of the flow in the harbour entrance (a developing gyre), t_g, is proportional to $L_g B / \hat{u} B_e$, with L_g the length of the primary gyre. This time scale is based on experiments in steady flow by Booij (1986). It can be assumed that the length of the gyre is proportional to the width of the harbour. The ratio $t_t/t_g = \hat{u}TB_e/B^2$ which then results, should be equal in the field and the experimental model. For a diurnal tide the model period would become 590 s. To speed up the experiments a little, a period of 500 s was selected. The flow rate in the flume in front of the harbour is shown in Fig. 3.4.

The influence of the tidal period on the flow in the harbour entrance and the exchange
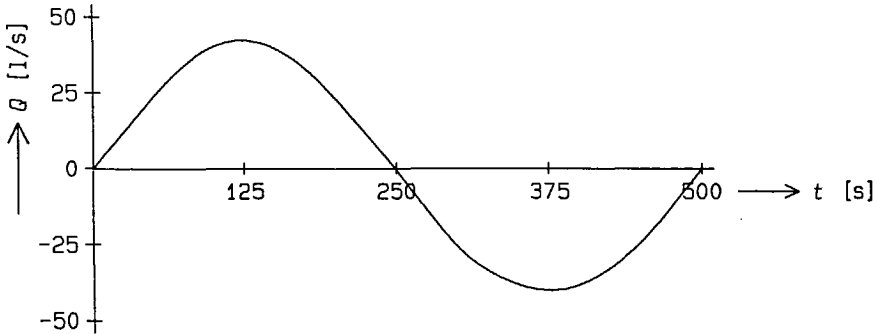
Figure 3.4 Flow rate in the flume in the experiments with model harbours 1
to 4.

of water between harbour and river has been examined in model harbours 1 and 2. Periods
of 250 s (experiments 1A en 2A) and 1000 s (experiments 1C and 2C) have been studied.

The measurements made in model harbours 1 to 4 —viz. depth-averaged flow patterns,
vertical distributions of velocity, and the exchange of water between harbour and river— are
discussed below.

3.2.1 Depth-averaged flow patterns

To limit the amount of figures to demonstrate the time-dependence of the flow, the depth-
averaged flow patterns in harbours 1 to 4 are shown only at four times. These times are
chosen to show (a) the mechanisms which determine the exchange of mass between harbour
and river, (b) the influence of the entrance geometry on the flow in the entrance, and (c) the
differences with a steady flow along the entrance.

Depth-averaged flow patterns in harbour 1, experiment 1B, at four time levels are shown in
Fig. 3.5. The results of the simulation of the depth-averaged flow are presented in section
4.3.3. The measured flow patterns were found to reproduce well from one cycle to another.
The patterns shown in Fig. 3.5 therefore have been composed of several recordings. Around
maximum current (t = 125 s and 375 s) a single, quasi-steady gyre exists in the harbour
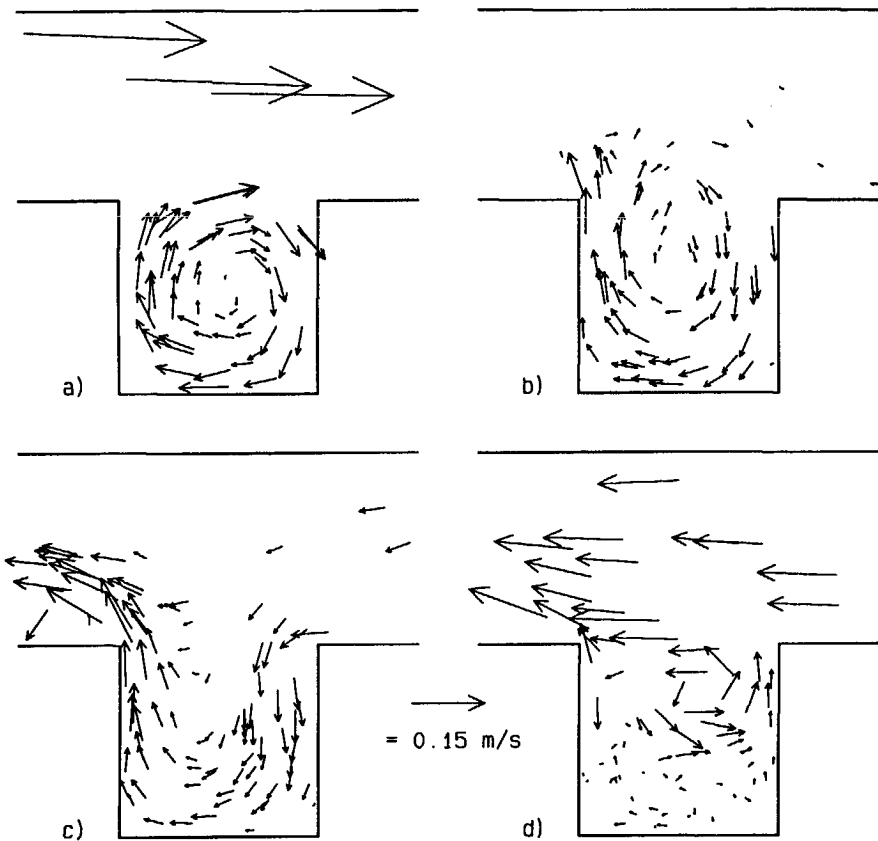
Figure 3.5 Depth-averaged flow patterns in harbour 1: a) $t = 150$ s, b) $t = 250$ s, c) $t = 260$ s, and d) $t = 280$ s.

(Fig. 3.5.a). When the velocity in the river decreases to that in the harbour, the gyre starts to increase in size and its centre moves towards the river (Fig. 3.5.b, slack water). After slack water the direction of the river flow reverses, and the flow in the river is guided into the harbour by the rotating gyre while water is flowing out of the harbour at its downstream side, see Fig. 3.5.c ($t = 260$ s) and Photo 1 ($t = 10$ s). A new gyre starts to develop at the upstream corner of the entrance, and the old gyre is squeezed and breaks up in two parts. One part is advected with the river flow, and the other part is pushed to the back of the harbour while decaying, see Fig. 3.5.d ($t = 280$ s) and Photo 2 ($t = 50$ s). The new gyre grows, moves towards the downstream corner, and after some time occupies the complete
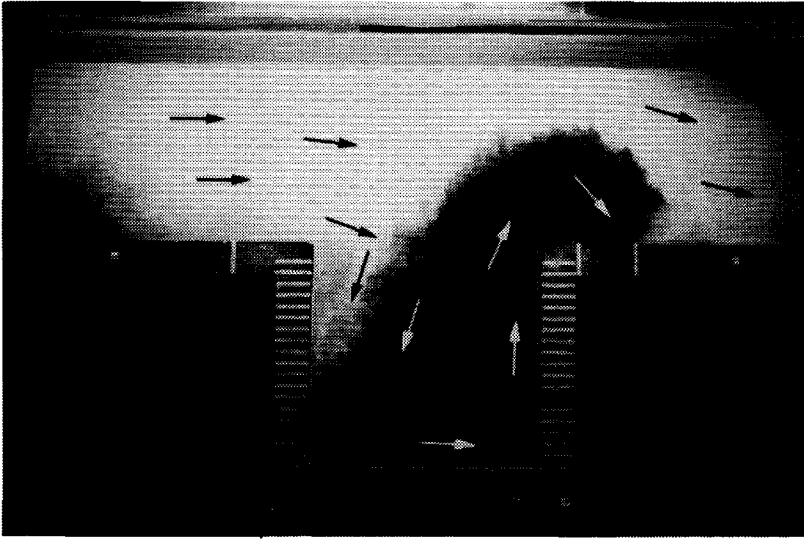
Photo 1   Exchange of dyed water from harbour 1 and limpid river-water shortly after slack water (t = 10 s, experiment 1B).
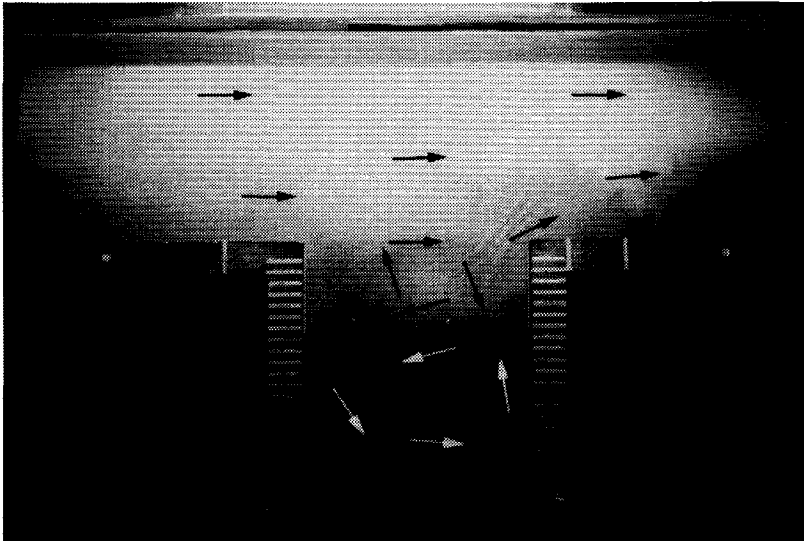
Photo 2   Exchange of dyed water from harbour 1 and limpid river-water at t = 50 s (experiment 1B).

harbour. A flow pattern then arises that is the reverse of that shown in Fig. 3.5.a.

The influence of the parameter $\hat{u}TB_e/B^2$ on the flow pattern in the entrance was studied by varying the magnitude of the period. Periods of 250 s (experiment 1A) and 1000 s (experiment 1C) were used in addition to the period of 500 s. It was observed that the gyre in the harbour was not fully quasi-steady near maximum current for a period of 250 s. Based on experiments in steady flow, Booij (1986) gives for the time the flow pattern in the harbour needs to adapt to a change in velocity in the river:

$$t_g \approx 50 C^2 \frac{L_g B}{u_r B_e}, \tag{3.1}$$

where C is a constant varying from 0.4 to 1 depending on the harbour geometry. For a square harbour with $B_e = B = L_g = 1$ m, $u_r = 0.37$ m/s, and $C = 0.6$, t_g equals about 50 s. This means that a period of 200 s should be sufficient to obtain quasi-steady flow at maximum current. However, in the present experiments the flow in the river continually changed its direction, which apparently results in a larger adaptation time.

The development of the gyre is about equally fast in experiments 1A ($T = 250$ s) and 1C ($T = 1000$ s) as it is for a period of 500 s. Consequently, decreasing the parameter $\hat{u}TB_e/B^2$ results in an increase of the phase difference between the developing flow of the gyre and the accelerating flow in the river.

The influence of the parameter $\hat{u}TB_e/B^2$ on the flow pattern in the entrance of model harbour 2 was studied, as in the experiments in model harbour 1, by varying the period (250 s, 500 s and 1000 s). A period larger than 250 s was necessary to obtain a quasi-steady flow in model harbour 1 at maximum current in the river. It can be expected that a period of at least 500 s is needed to obtain a quasi-steady flow in model harbour 2, because the time the flow in the harbour needs to adapt to the flow in the river is proportional to the length of the primary gyre in the harbour, see equation (3.1).

In harbour 2, experiment 2B, a second, counter rotating gyre exists at the back of the harbour around maximum current (see Fig. 3.6.a). This gyre spans the width of the harbour, and its breadth gradually increases from about 0.25 m at maximum current to 0.5 m during slack water (see Fig. 3.6.b). The flow near the entrance at slack water resembles that in
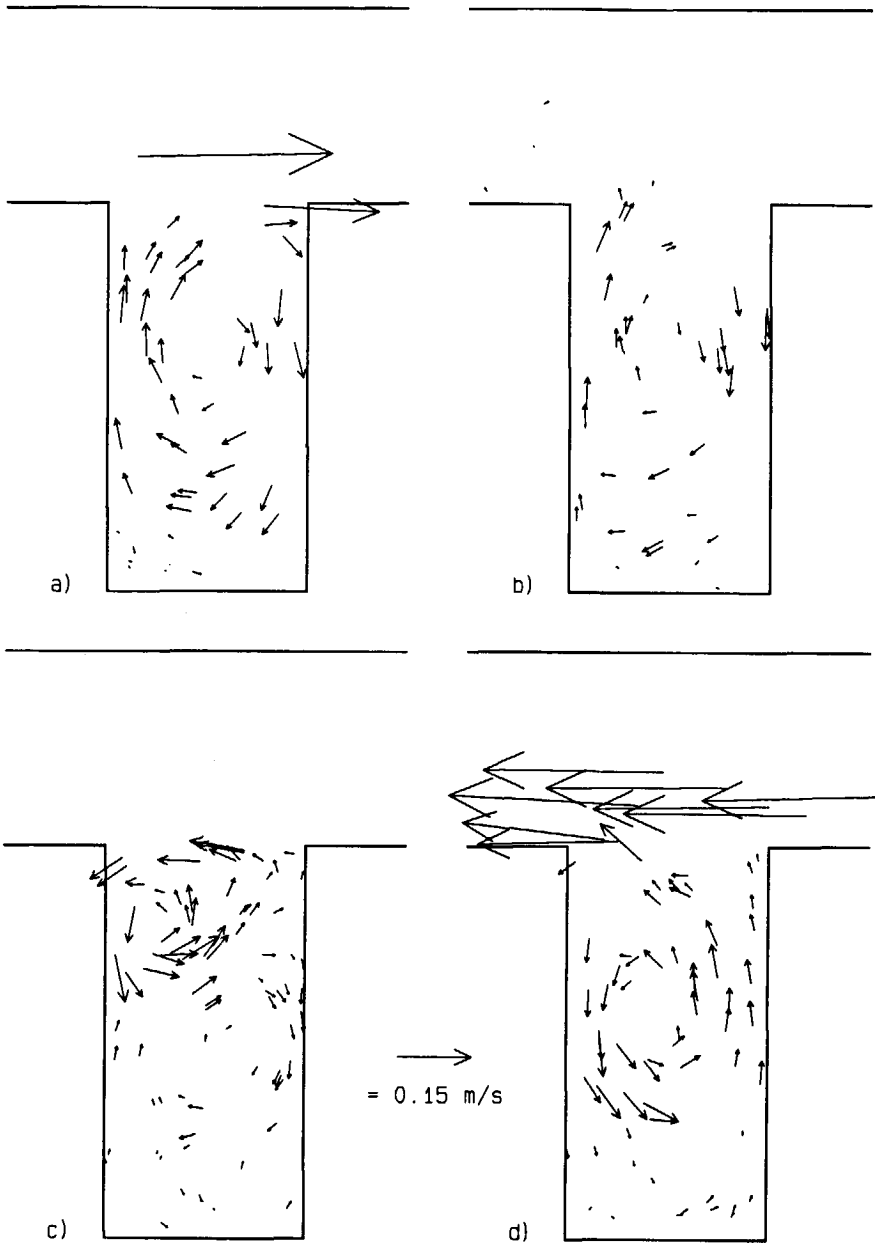
Figure 3.6 Depth-averaged flow patterns in harbour 2: a) $t = 140$ s, b) $t = 250$ s, c) $t = 300$ s, and d) $t = 360$ s.

harbour 1. The primary gyre moves to the river, but not to the same extent as in model harbour 1. The old primary gyre is broken into two parts, one part is transported with the flow in the river and the other part is pushed to the back of the harbour by the developing new gyre, see Fig. 3.6.c ($t = 300$ s) and Photo 3 ($t = 50$ s). The old primary gyre decays, after which the old secondary gyre is assimilated by the new gyre, because they have the same direction of rotation, see Fig. 3.6.d ($t = 360$ s) and Photo 4 ($t = 110$ s). A new secondary gyre comes into existence just at the next maximum current in the river.

The counter rotating secondary gyre did not come into existence at maximum current in the river in experiment 2A ($T = 250$ s). Thus, a quasi-steady flow in model harbour 2 is not obtained for a period of 250 s. Experiments 2A ($T = 250$ s) and 2C ($T = 1000$ s) show that the development of the new gyre after slack water is equally fast as in experiment 2B. Thus, decreasing the parameter $\hat{u} T B_e / B^2$ causes an increase in the phase difference between the developing flow of the gyre and the accelerating flow in the river.

The observed depth-averaged flow patterns in model harbour 3 are shown in Fig. 3.7. Fig. 3.7.a shows that in harbour 3 a single gyre exists around maximum current as observed in
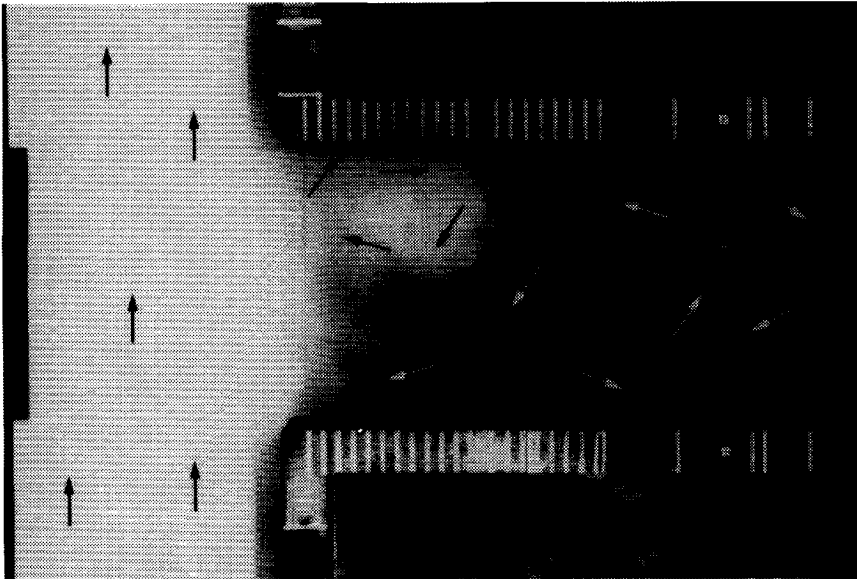
Photo 3 Exchange of dyed water from harbour 2 and limpid river-water at t = 50 s (experiment 2B).
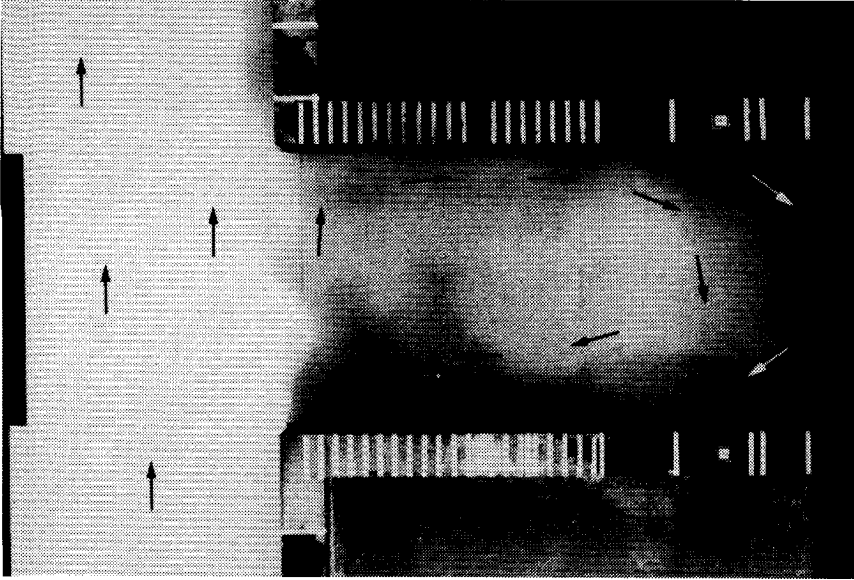
Photo 4 Exchange of dyed water from harbour 2 and limpid river-water at t = 110 s (experiment 2B).
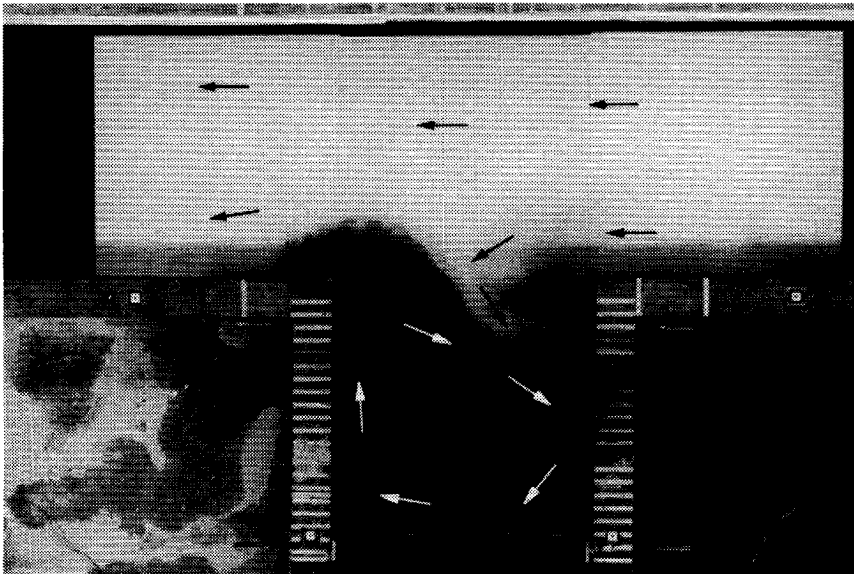
Photo 5 Exchange of dyed water from harbour 3 and limpid river-water at t = 260 s (experiment 3).
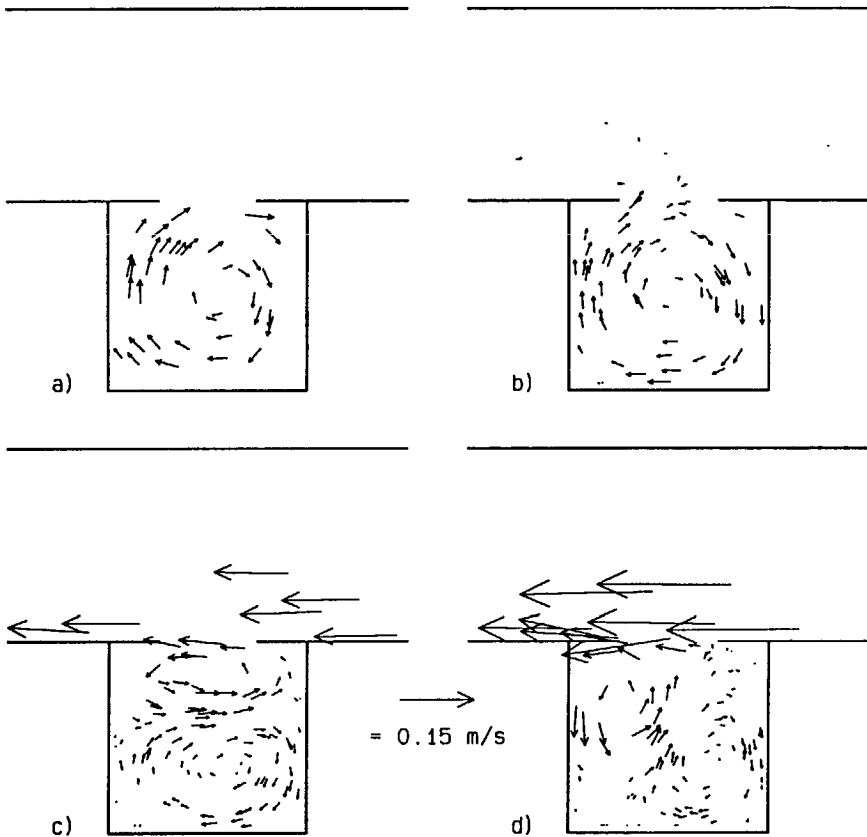
Figure 3.7 Depth-averaged flow patterns in harbour 3: a) $t = 180$ s, b) $t = 250$ s, c) $t = 290$ s, and d) $t = 320$ s.

model harbour 1. However, the water velocities are less by approximately 40 per cent. The gyre remains completely within the harbour at slack water, see Fig. 3.7.b. As a result, the exchange of water between harbour and river will be smaller during slack water than in model harbours 1 and 2. Photo 5 pictures the flow in the harbour just after slack water ($t = 260$ s).

The new gyre initially grows mainly in a direction parallel to the river, see Fig. 3.7.c, and the old gyre is more long-lived than that in harbour 1 (experiment 1B), see Fig. 3.7.d. As a result of a smaller entrance width and consequently the small exchange at slack water the gyre can persist almost unchanged.

Quasi-steady flow in the harbour was obtained just around maximum current. In model harbour 1 a period slightly higher than 250 s was sufficient to obtain a quasi-steady flow in the harbour at maximum current, while in model harbour 3 with half the entrance width the period must be at least 500 s. This was to be expected because, see equation (3.1), the time the harbour flow needs to adapt to the flow in the river is inversely proportional to the entrance width.

The observed depth-averaged flow patterns in model harbour 4 are shown in Fig. 3.8. When the flow in the river is from left to right at maximum current ($t = 125$ s), a large gyre, almost occupying the entire harbour area, and a small gyre in the corner on the right at the

Figure 3.8 Depth-averaged flow patterns in harbour 4: a) $t = 120$ s, b) $t = 260$ s, c) $t = 290$ s, and d) $t = 370$ s.

back of the harbour are present in the harbour, see Fig. 3.8.a. The water velocities in the gyre are as large as the water velocities in the gyre in experiment 1B at maximum current. The results of simulations of the depth-averaged flow in harbour 4 are presented in section 4.3.3.
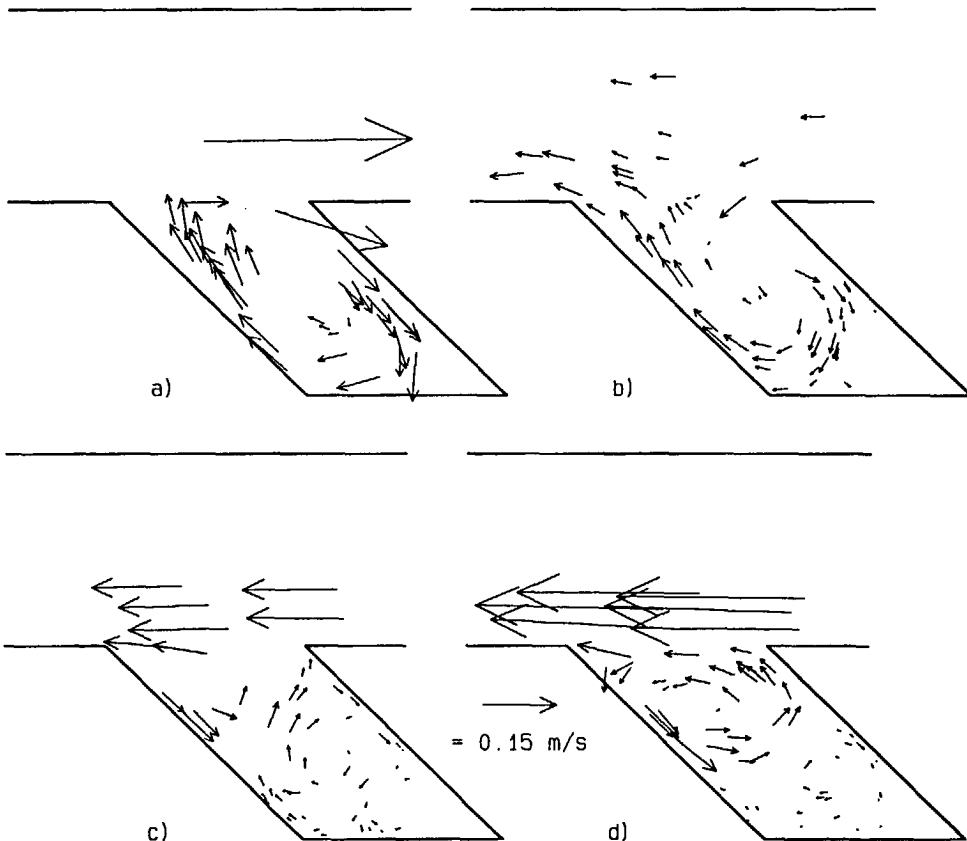
Fig. 3.8.b shows that the same phenomena are observed in harbour 4 as in the previous experiments during slack water ($t = 250$ s). Three gyres are present in the harbour after slack water, see Fig. 3.8.c. In contrast with the previous experiments the old gyre does not decay, see Fig. 3.8.d. At $t = 375$ s the water velocities in the primary gyre are approximately 50 per cent of those at the previous maximum current ($t = 125$ s).

The differences in the sizes of the gyres and the water velocities in the gyres are probably caused by the geometry of the downstream sidewall of the entrance. The angle between the downstream wall of the entrance and the river has a marked influence on the velocities in the gyre and the size of the gyre. A small angle was found to imply large velocities in the gyre and a large size of the gyre. Booij (1986) found a decrease in the velocities of 40 per cent for an angle of 135 degrees with respect to those for an angle of 90 degrees.

At the next slack water the primary gyre moves into the river again and after slack water a new large gyre comes into existence.

3.2.2 Vertical distribution of the velocity

In chapter 2 it was stated that the flow in the gyre is three-dimensional. A secondary current exists in the gyre. The direction of the velocity vector varies in the vertical direction, implying velocity components perpendicular to the direction of the the depth-averaged velocity. The associated flow is usually designated as the secondary current. Measurements were made to examine the depth dependence of the velocity field.

Fig. 3.9 shows the flow patterns at four levels for experiment 1B at $t = 375$ s (maximum current). (The results of the simulation of the three-dimensional flow in the harbour are presented in section 4.3.3.) Two notable processes can be observed. Firstly, a secondary
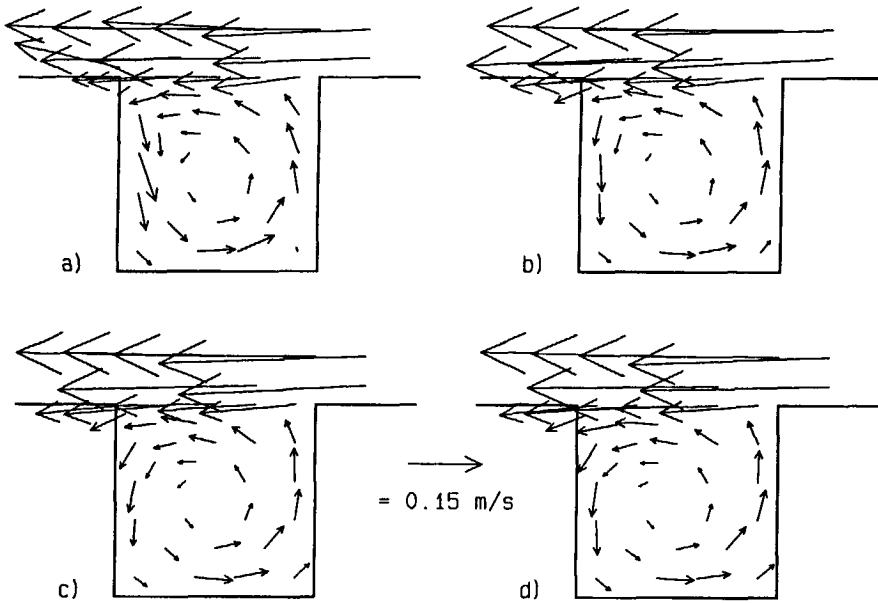
Figure 3.9 Flow patterns for experiment 1B at maximum current ($t = 375$ s) at four levels: a) 0.015 m, b) 0.04 m, c) 0.06 m, and d) 0.08 m above the bottom, respectively.

current with the velocities directed towards the centre of the gyre at 0.015 m above the bottom (Fig. 3.9.a), and a flow in opposite direction near the free surface occurs. The angle between the flow direction near the bottom and the flow direction near the surface is about 20 degrees. The ratio of the maximum velocities of the secondary current and the main flow, v_s/U, varies between 0.14 and 0.18 at 0.10 m from the harbour sidewalls. Secondly, the near-bottom velocities close to the downstream sidewall of the entrance are clearly larger (approximately 50 per cent) than those higher in the water column. This phenomenon commences when the new gyre has moved towards the downstream sidewall of the harbour, and it continues to exist almost until the next slack water. Visualization of the flow near the stagnation point at the downstream sidewall showed that high-momentum fluid from the mixing layer between harbour and river water flows from close to the water surface towards the bottom and further into the harbour.

Figures 3.10 to 3.14 show the vertical distributions of the velocity for the case that the

positions of the weirs were fixed at maximum current. Consequently, a steady flow developed in the river and in the harbour.

The velocity distribution in the water column at a location 0.1 m from the downstream harbour sidewall and 0.4 m into the harbour is shown in Fig. 3.10 for harbour 1.

Fig. 3.11 shows that in model harbour 2 the same processes occur as in model harbour 1. The velocity distribution in the water column at a location 0.10 m from the downstream harbour sidewall and 0.75 m into the harbour shows the presence of a secondary current and larger water velocities near the bottom than higher in the water column. The ratio of the maximum velocities of the secondary current and the main flow is approximately 0.23. The water velocities near the bottom are about 50 per cent larger than those higher in the water column.

In model harbour 3, as in harbours 1 and 2, the water velocities near the bottom close to the
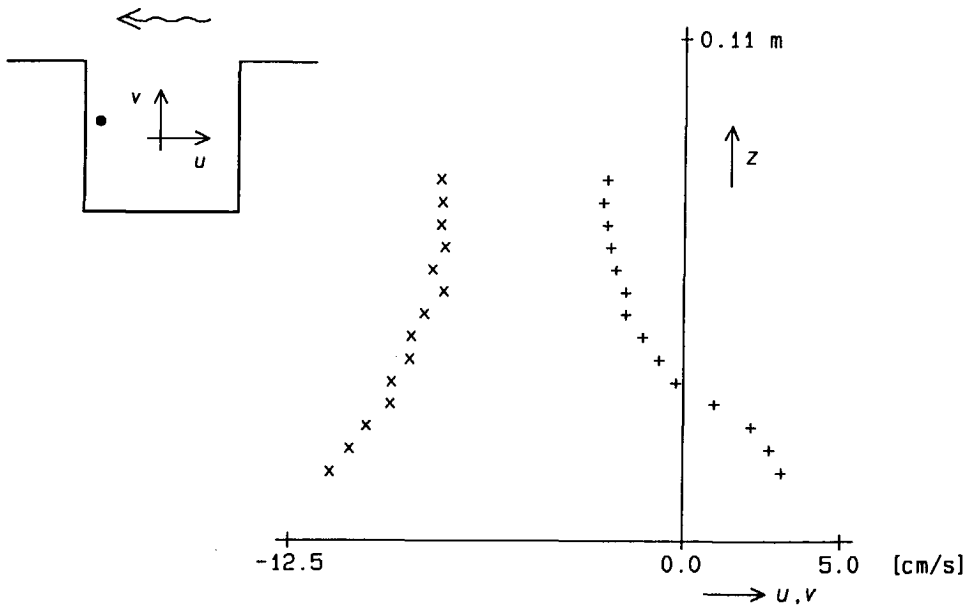
Figure 3.10 Velocity distribution in the water column in harbour 1: $+ = u$ velocity component and $\times = v$ velocity component.
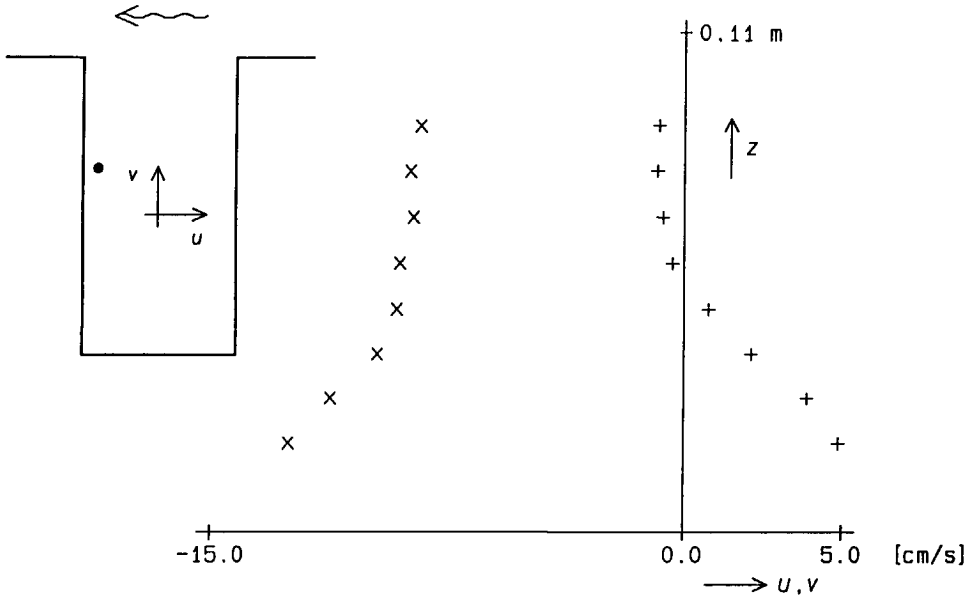
Figure 3.11 Velocity distribution in the water column in harbour 2: $+ = u$ velocity component and $\times = v$ velocity component.

stagnation point are larger, about 35 per cent, than those higher in the water column (see Fig. 3.12). The secondary current is weak and can be observed only at verticals 3 and 4 ($v_s/U \approx 0.05$).

Larger water velocities near the bottom close to the stagnation point are observed in model harbour 4 as well, both when the flow in the river is from left to right (Fig. 3.13) and when the flow in the river is from right to left (Fig. 3.14). When the flow is from left to right the velocities near the bottom are approximately 20 per cent larger, and when the flow is from right to left approximately 50 per cent larger than those higher in the water column.

When the flow is from left to right the ratio v_s/U is 0.07 at vertical 2 and 0.22 at vertical 3. When the flow is from right to left the ratio v_s/U is 0.22 at vertical 1 and 0.09 at vertical 2.
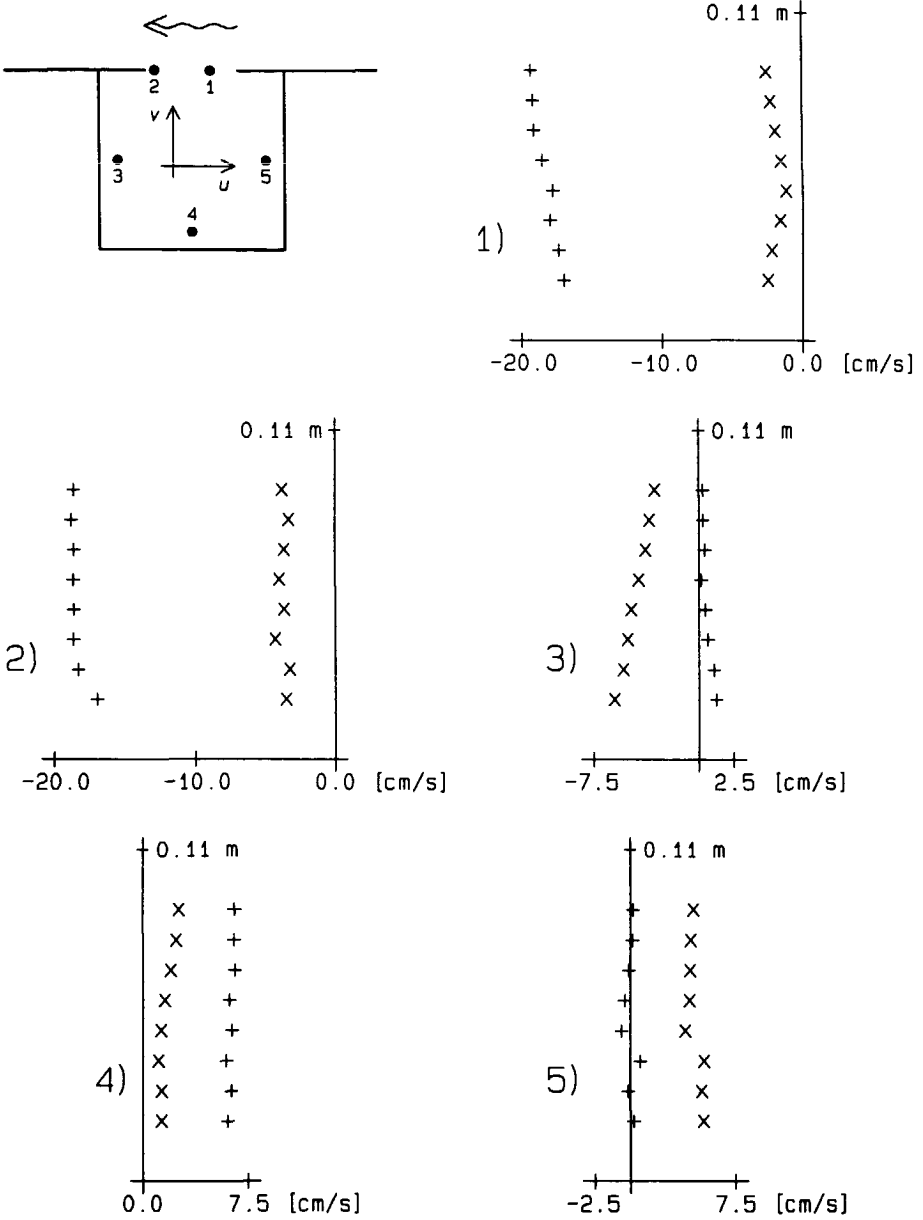
Figure 3.12 Velocity distributions in the water column in harbour 3: + = *u* velocity component and × = *v* velocity component.
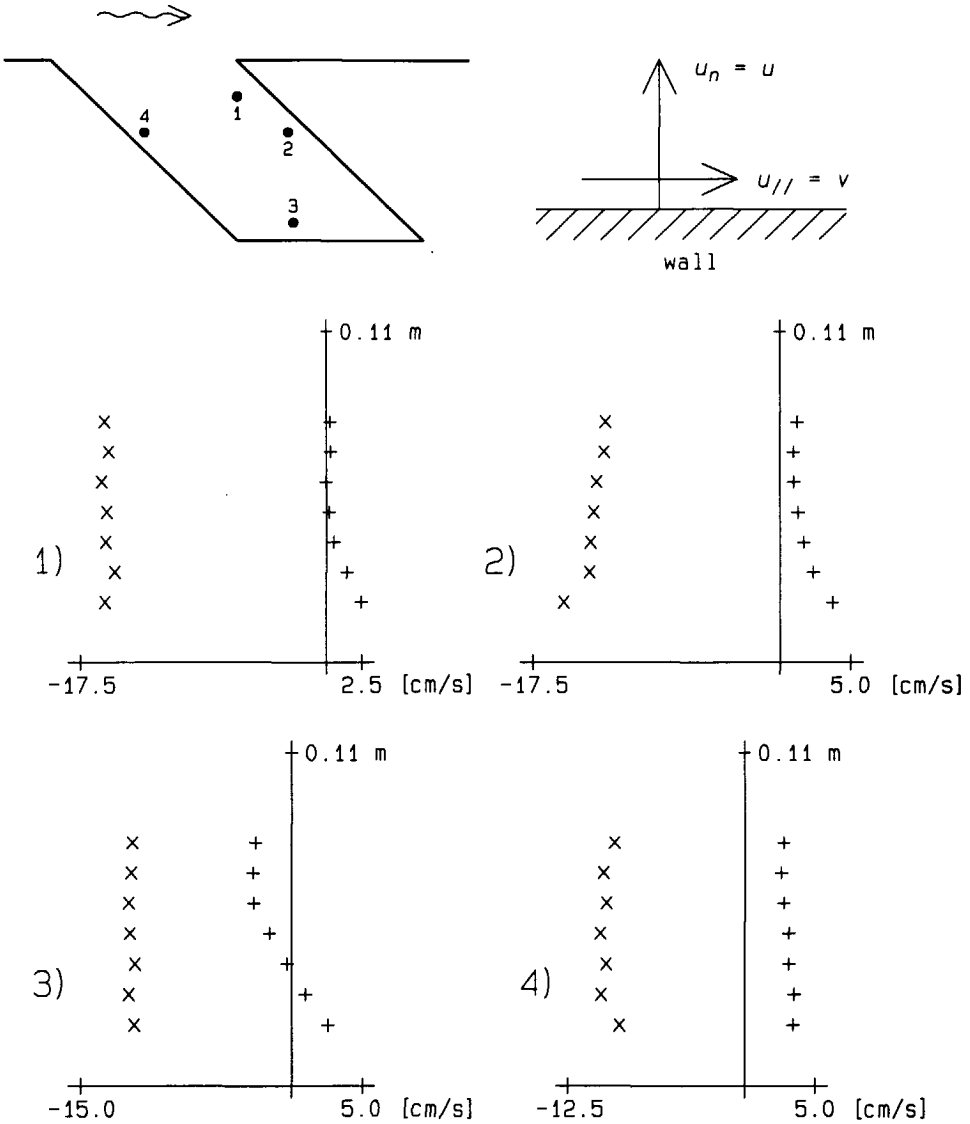
Figure 3.13 Velocity distributions in the water column in harbour 4: $+$ = u velocity component and $\times$ = v velocity component.
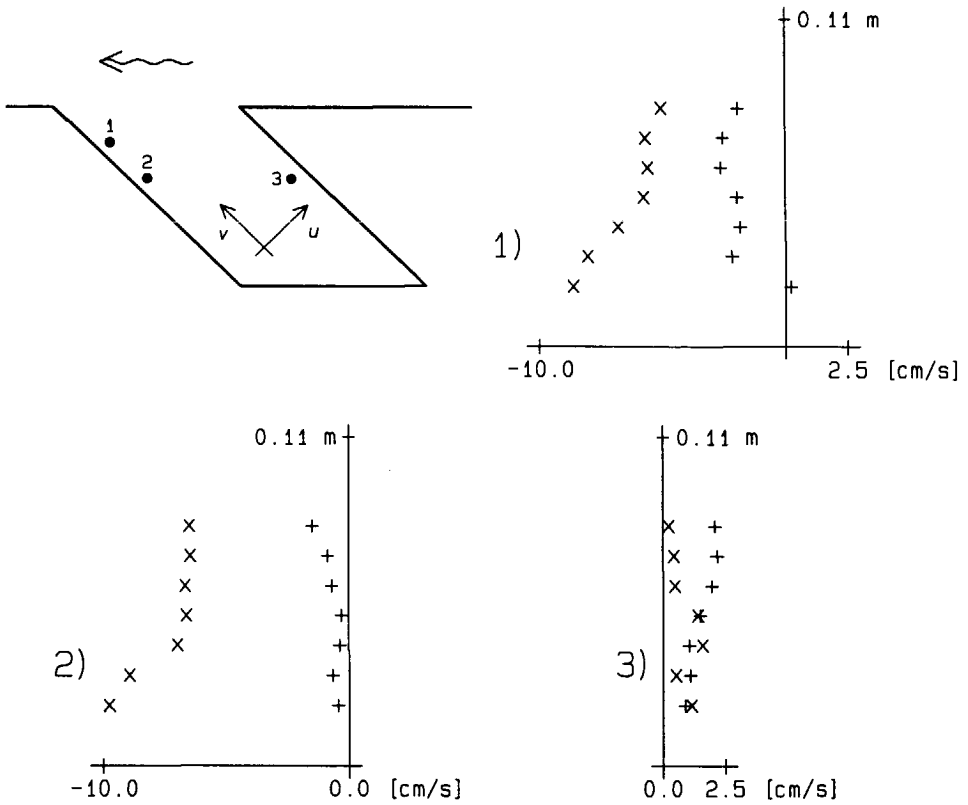
Figure 3.14 Velocity distributions in the water column in harbour 4: $+ = u$ velocity component and $\times = v$ velocity component.

3.2.3 Exchange of water between harbour and river

Heated water is used as a tracer to examine the exchange of water between harbour and river. The heat transport Q_θ through the entrance of the harbour can be determined from the evolution of the mean temperature of the water in the harbour (see Langendoen, 1990):

$$Q_\theta(t) = -\rho c V_h \frac{d\tilde{\theta}}{dt},$$

where ρ is the density of water, c is the specific heat, V_h is the volume of the harbour, and $\tilde{\theta}$ is the volume-averaged excess temperature of the harbour water with respect to the river-water. A normalized heat transport, λ, is defined according to

$$\lambda(t) \; = \; \frac{Q_\theta(t)}{\rho c A_e \, \hat{u} \, \tilde{\theta}(t)} \; = \; - \frac{V_h \dfrac{\mathrm{d}\tilde{\theta}}{\mathrm{d}t}}{A_e \, \hat{u} \, \tilde{\theta}(t)} \, , \qquad\qquad (3.2)$$

where A_e is the cross-sectional area of the harbour entrance.

The thermistor measurements were used to obtain $\tilde{\theta}(t)$. This signal was low-pass filtered and numerically differentiated with respect to time.

Figures 3.15 and 3.16 show the time histories of $\lambda(t)$ for model harbours 1 to 4. The evolution of λ for the various harbour geometries can be explained from the flow pattern in the harbour entrance and the geometry of the harbour.

The results of computations with the 2-D computer model ESTRA to determine the exchange rate of dissolved matter between harbour and river are presented in section 4.3.2 concerning harbour 1.

For model harbour 1 the large peaks around slack water evidently result from the pronounced advective exchange which then occurs. The gyre is moving into the river and guides, by its rotation, river-water into the harbour. The second peak is lower than the first, since water that is less easily exchanged remains in the harbour after the first slack water.

The dip after slack water results from the fact that the new gyre has not yet developed. The new gyre is moving towards the downstream sidewall of the harbour. As a consequence of which only new water, with the same temperature as the river-water, is present near the entrance and the exchange of heat is low.

The subsequent rise is caused by the arrival at the entrance of warmer water, the remnants of the old primary gyre, from the back of the harbour, which is advected by the new gyre.

The gradual decrease in λ during the quasi-steady phase, when diffusion governs the exchange process, is caused by the decreasing velocity difference between the flow in the river and the flow in the gyre. As a result, the turbulence generated in the mixing layer at the transition from harbour to river will also decrease and consequently the turbulent exchange does so too.
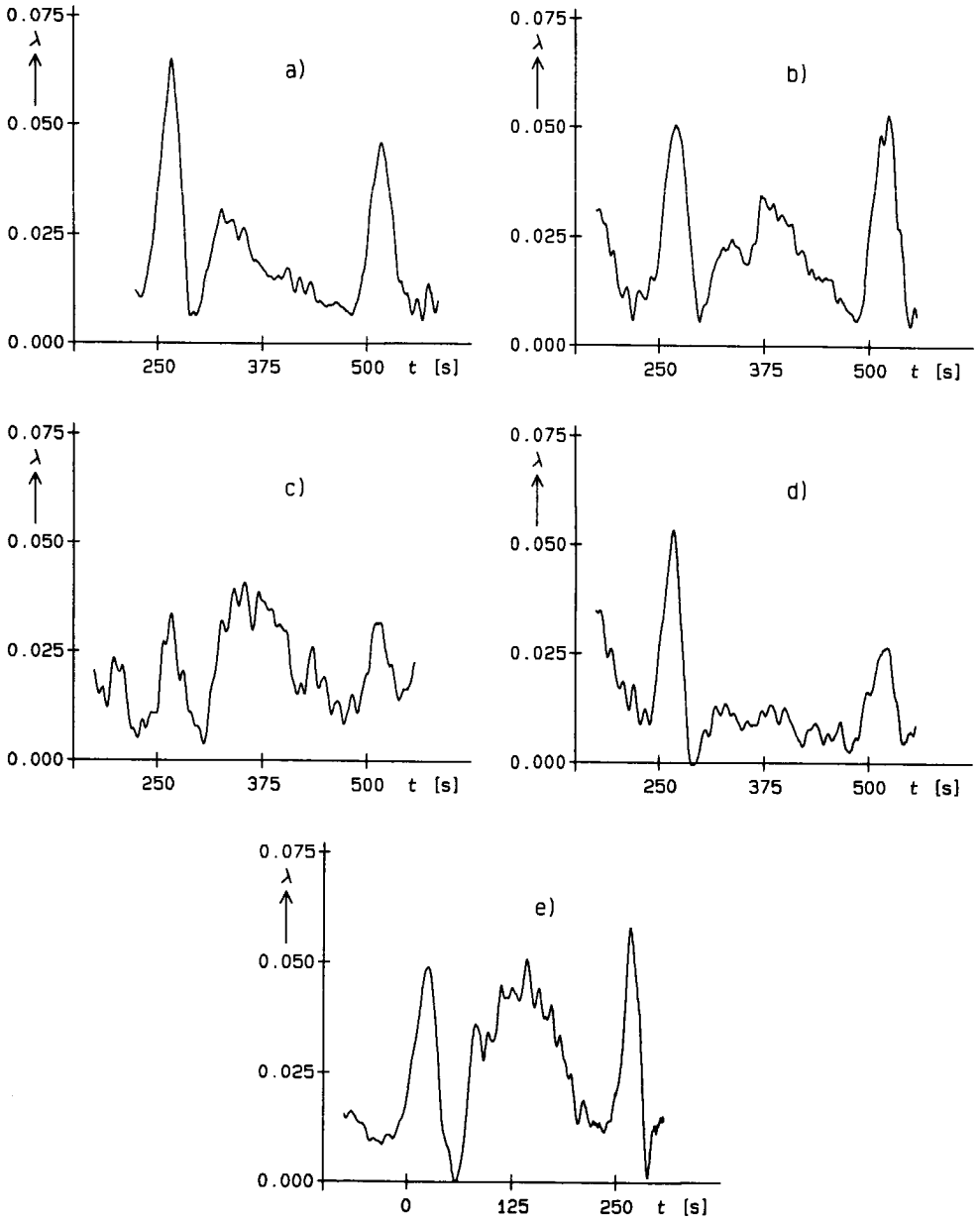
Figure 3.15 Normalized heat transport through the entrance: a) harbour 1; b) harbour 2; c) harbour 3; d) harbour 4, flow from right to left along the entrance; and e) harbour 4, flow from left to right along the entrance.
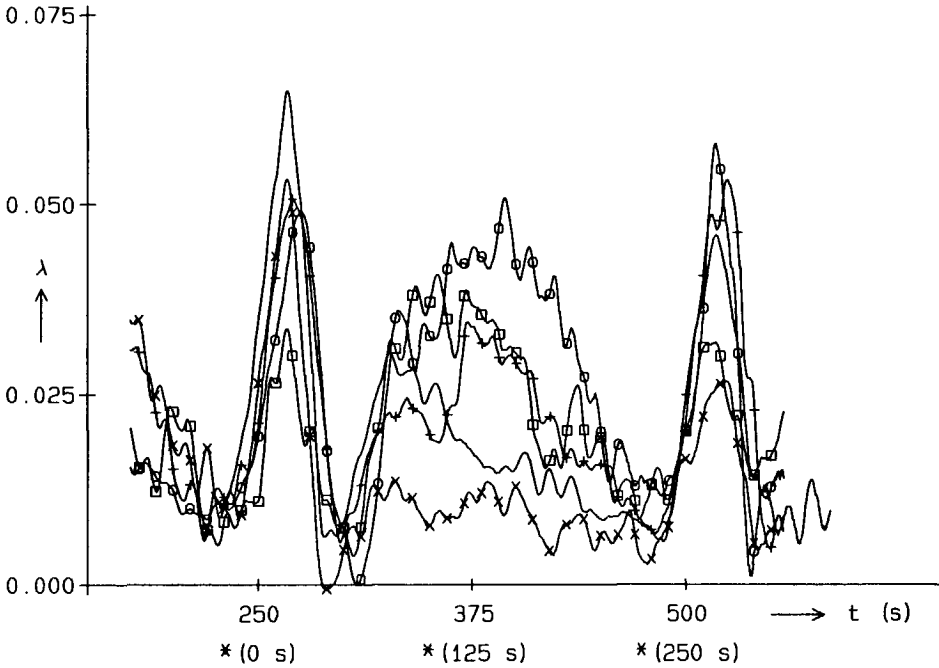
Figure 3.16 Normalized heat transport through the entrance: ———— ,
harbour 1; —+—+—, harbour 2; —⊟—⊟—, harbour 3; —⊖—⊖—, harbour 4
(time indicated by ∗); and —✕—✕—, harbour 4.

The first peak for harbour 2 is lower than that for harbour 1, since the secondary gyre does
not contribute to the exchange process. However, the second peak is relatively high because
more old water is present near the entrance.

The increase in λ, starting at $t = 300$ s, is caused by the arrival of the remnants of
the old primary gyre at the entrance. When the developing new gyre spans the entire width
of the harbour λ is more or less constant for some time. The sudden increase at $t = 370$ s
is caused by the arrival of the remnants of the old secondary gyre at the entrance.

The peaks at slack water in the case of harbour 3 are low, since the gyre does not move into
the river. Between the slack periods, however, λ is about twice as large as that for harbour
1. Consequently, the ratio $\frac{1}{\tilde{\theta}} \frac{d\tilde{\theta}}{dt}$ is about the same for model harbours 1 and 3 during the
quasi-steady phase of the flow.

There is a distinct difference in the evolution of λ between both maximum currents in the case of harbour 4. This is caused by the different orientations of the harbour entrance with respect to the river flow, as can be observed from the behaviour and the shape of the mixing layer at the transition from harbour to river. When the angle between the downstream sidewall of the harbour entrance and the river-bank is 45 degrees the mixing layer is rather wide with large vortices resulting in a large exchange of water between harbour and river, see Photo 6. When this angle is 135 degrees the mixing layer is narrow with small vortices, resulting in a much smaller exchange of water between harbour and river, see Photo 7.

The tide-averaged values of λ are 0.019 for harbour 1, 0.022 for harbour 2, 0.023 for harbour 3, and 0.020 for harbour 4, respectively. These values are remarkably close to each other, although the flow conditions are widely different. The value of λ in steady-flow conditions ($\hat{u}$ now being the constant water velocity in the river) is about 0.032 (Booij, 1986), which is also about the value near maximum current in the present experiments.

Normalizing Q_θ with the tide-averaged absolute value of the velocity of the tidal
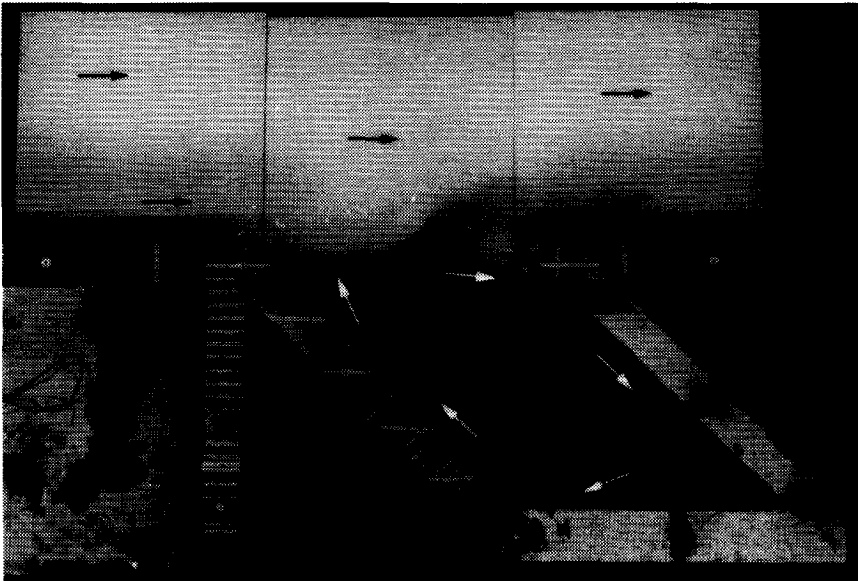
Photo 6 Exchange of dyed water from harbour 4 and limpid river-water at maximum current ($t = 125$ s).
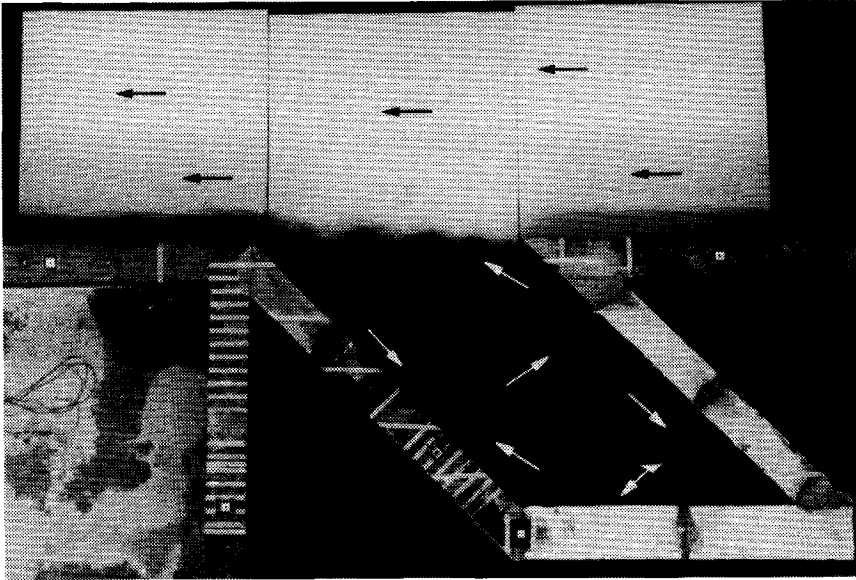
Photo 7 Exchange of dyed water from harbour 4 and limpid river-water at maximum current ($t = 375$ s).

current ($\bar{u} = 2\hat{u}/\pi$) or with the rms tidal velocity ($u_{rms} = \hat{u}/\sqrt{2}$) results in tide-averaged values of λ of the same magnitude as found by Booij (1986) for steady flow conditions.

The conclusions concerning the experiments discussed above are given in section 3.5.

3.3 Experiments with a tidal flow in the river with changes in water level

In addition to the dimensionless parameters given in the previous section the phase difference between the velocity of the tidal current and the tidal level, and the dimensionless parameter $\Delta V/\bar{V}_h$ influence the exchange of water between harbour and river. Here ΔV is the tidal prism of the harbour and $\bar{V}_h$ is the tide-averaged volume of the harbour. The parameter $\Delta V/\bar{V}_h$ is equal to the ratio $\hat{h}/\bar{h}$, where $\hat{h}$ is the amplitude of the tide level and $\bar{h}$ the tide-averaged water depth, because the surface areas of the harbours used in this study are constant during a tidal cycle.

Two experiments with an oscillatory current in the river with variations in water level were carried out: one in the model at the Delft University of Technology, and one in the Tidal Flume of Delft Hydraulics.

The goal of the experiment at the Delft University of Technology was to enlarge our insight into the interactions between a net flow through the harbour entrance and the gyre in the entrance.

In the Tidal Flume experiments with stratified tidal flow in the river were carried out. The length, velocity and time scales differed from those used at the Delft University of Technology. Consequently, the parameters that determine the exchange of mass between harbour and river also differed. To determine the influence of stratification on the flow in the harbour entrance, an experiment with unstratified tidal flow was carried out.

The geometry of the harbour for the experiment at the Delft University of Technology is shown in Fig. 3.17. The harbour is designated as harbour 5 and the experiment as experiment 5. The harbour geometry of the experiment in the Tidal Flume is shown in Fig. 3.18. The harbour is designated as harbour 6.

To obtain the correct velocity of the net flow through the harbour entrance, the parameter $\Delta V/\bar{V}_h$ should be the same in the field as in the experiment. However, to determine the correct influence of the net flow on the gyre in the entrance, the ratio $u_s/\overline{u_g}$ between the velocity of the net flow and the velocity of the gyre should be the same in the field and in the experiment. Equation (3.3) shows that the ratio $u_s/\overline{u_g}$ scales as $\hat{h}/\bar{h}$, if the ratio t_t/t_g is
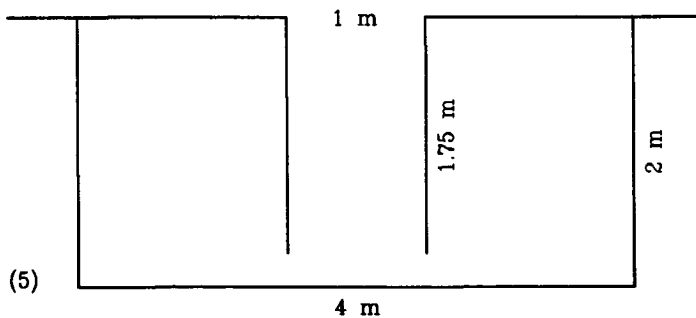
Figure 3.17 Top view of model harbour 5.
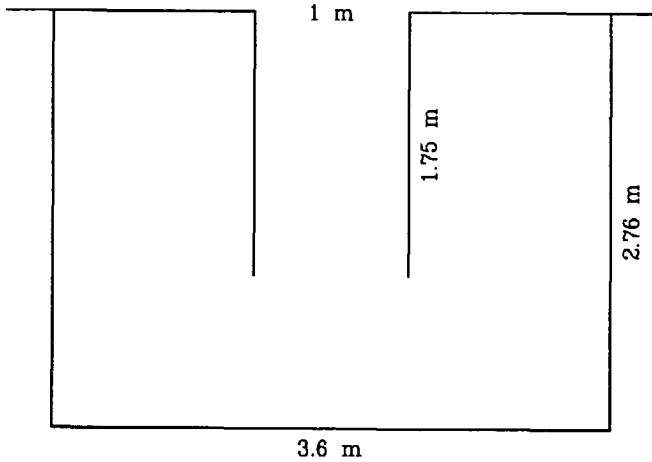
Figure 3.18 Top view of model harbour 6.

the same in the experiment and in the field:

$$\frac{u_s}{\overline{u_g}} \approx \frac{\dfrac{A_h}{A_e}\dfrac{d\zeta}{dt}}{\hat{u}} \approx \frac{\dfrac{BL}{B_e h}\dfrac{\hat{h}}{T}}{\hat{u}} \approx \frac{B^2}{B_e \hat{u} T}\frac{\hat{h}}{h} = \frac{t_g}{t_t}\frac{\hat{h}}{h}. \tag{3.3}$$

The ratio $u_s/\overline{u_g}$ is approximately 0.15 to 0.20 for the harbours in the Rotterdam Harbour Area. This yields a velocity of the net flow in experiment 5 of 0.010 to 0.015 m/s. This is obtained by producing a tidal current with an amplitude of the variation in tidal level of 0.02 m, and by using the entire area of the basin.

The values of the various parameters for model harbour 5 are: $\hat{u} T B_e/B^2$ equals 140 at high tide and 115 at low tide, $\overline{h}/B = 0.11$, $\hat{h}/\overline{h} = 0.18$, $B_e/B = 1$, and $\alpha = 90$ degrees. The discharge in the flume varied from 36 ℓ/s ($\hat{u} = 0.28$ m/s) at high tide to 21 ℓ/s ($\hat{u} = 0.23$ m/s) at low tide. Fig. 3.19 shows the discharge and the tidal level in the flume in front of the harbour during a tidal cycle.

The dimensions of model harbour 6 in the Tidal Flume are based on the tidal system Rotterdam Waterway—Botlek Harbour in The Netherlands. The Rotterdam Waterway, near the Botlek Harbour, has a width of about 600 m and a depth of 15 m. The mean water depth in the flume was 0.2 m. This leads to the following scales: the length scale is 600, the depth
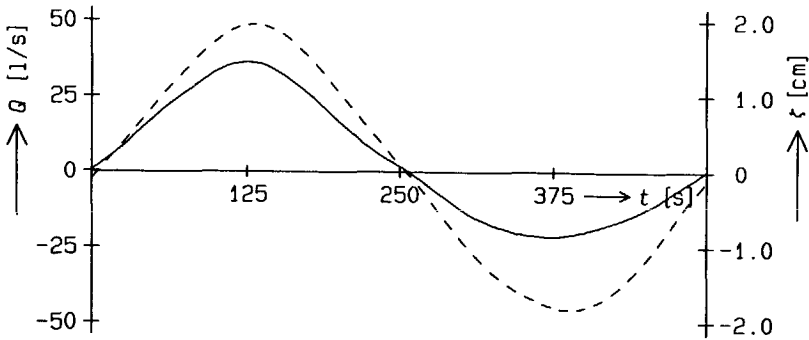
Figure 3.19 Time-histories of discharge and water level in the river in experiment 5: ———, discharge; and – – –, water level elevation.

scale is 75, the velocity scale is 8.66 (using Froude law scaling), and the time scale is 69.3. As a result, the model period is 650 s for a diurnal tide. The Botlek Harbour has a surface area of 3.5 km^2, resulting in a surface area of the harbour in the experimental model of 10 m^2. The geometry of the harbour entrance is the same as that of model harbour 5.

The flow in the flume was generated by introducing a sinusoidal water level elevation with an amplitude of 0.025 m at the transition from sea to flume. The maximum water velocity of the tidal current was about 0.20 m/s. Fig. 3.20 shows the discharge and the tidal level in the flume in front of the harbour during a tidal cycle.

The values of the various dimensionless parameters are: $\hat{u} T B_e / B^2 = 130, \bar{h}/B = 0.2$,
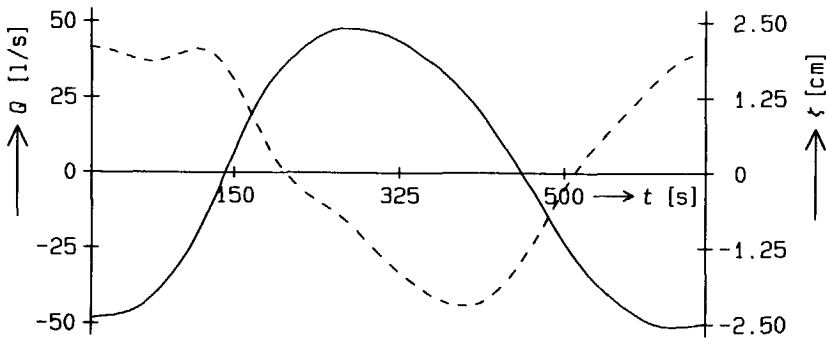
Figure 3.20 Time-histories of the discharge and the water level in the river in front of the harbour (experiment 6): ———, discharge; and – – –, water level elevation.

$\hat{h}/\bar{h} = 0.125$, $B_e/B = 1$, and $\alpha = 90$ degrees.

The main differences between experiments 5 (Delft University of Technology) and 6 (Delft Hydraulics) are: (1) the water depth in experiment 6 is twice as large as in experiment 5, consequently the influence of the bottom is less; (2) the influence of the net flow through the entrance on the gyre is smaller in experiment 6 than in experiment 5, because of a relative smaller variation in tidal level; and (3) there is a phase difference of about 60 s between the discharge in the flume and the tidal level in experiment 6, see Fig. 3.20.

3.3.1 Experiment 5

Measurements of mean horizontal velocities at 0.02, 0.04 and 0.06 m above the bottom were carried out. The results are discussed for high tide and low tide (no net flow through the entrance), and slack water after high tide and low tide (no flow along the entrance).

HIGH TIDE

At high tide ($t = 125$ s, Fig. 3.21) a large primary gyre is present in the harbour entrance, as is to be expected. The flow pattern is similar to that in the experiment without water level variations and the same geometry of the harbour entrance (experiment 2B).

The two processes observed at maximum current in the experiments with only an oscillatory current are noticeable too. Near the bottom (Fig. 3.21.a) the flow in the gyre is directed towards the centre of the gyre and half-way down the water column (Fig. 3.21.c) the flow in the gyre is directed away from the centre of the gyre. At the downstream sidewall of the harbour entrance the water velocity near the bottom is larger than higher in the water column. Fig. 3.22 shows the development of the gyre after slack water. It is faster than in experiment 2B. The gyre is quasi-steady 70 s after slack water as opposed to 125 s after slack water in experiment 2B.

Figure 3.21 Flow patterns for experiment 5 at high tide (t = 125 s) at three levels: a) 0.02 m, b) 0.04 m, and c) 0.06 m above the bottom, respectively.

SLACK WATER AFTER HIGH TIDE

At slack water after high tide (t = 250 s, see Fig. 3.23), when the net flow through the entrance due to the emptying of the basin is at its maximum, it can be observed that the gyre moves into the river. At this phase of the tide the cross-sectional averaged velocity u_s, of the net flow through the entrance, is about 0.015 m/s.

LOW TIDE

At low tide (t = 375 s, Fig. 3.24) the flow pattern in the entrance is rather indeterminate and the velocities are low. Although the rate of filling or emptying of the basin at low tide is
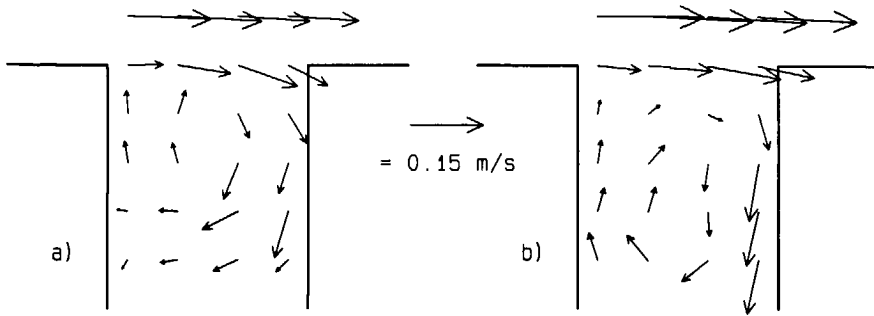
Figure 3.22 Development of the gyre towards high tide. Flow pattern at 0.04 m above the bottom in experiment 5: a) $t = 50$ s, and b) $t = 70$ s.

negligible, a gyre in the entrance cannot be observed. This is due to the emptying of the harbour basin preceding the low tide, which hindered the development of the gyre, see Fig. 3.25.
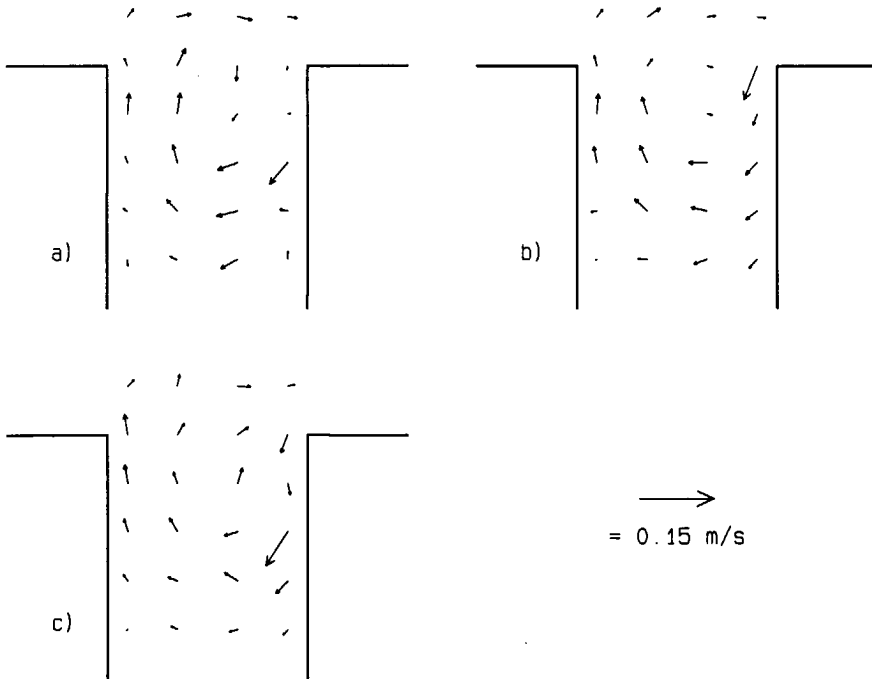
Figure 3.23 Flow patterns for experiment 5 at slack water after high tide ($t = 250$ s) at three levels: a) 0.02 m, b) 0.04 m, and c) 0.06 m above the bottom, respectively.

Figure 3.24 Flow patterns for experiment 5 at low tide ($t = 375$ s) at three levels: a) 0.02 m, b) 0.04 m, and c) 0.06 m above the bottom, respectively.
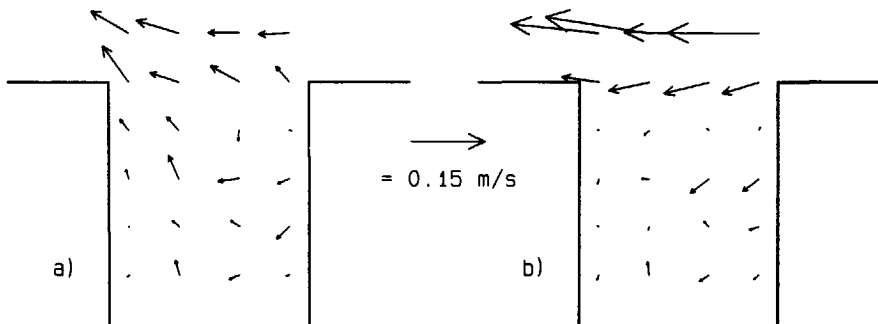
Figure 3.25 Development of the gyre towards low tide. Flow pattern at 0.04 m above the bottom in experiment 5: a) $t = 280$ s, and b) $t = 325$ s.

<u>SLACK WATER AFTER LOW TIDE</u>

At slack water after low tide ($t = 500$ s, see Fig. 3.26) when the net flow through the entrance due to the filling of the basin is at its maximum, the gyre remains in the harbour. The filling of the basin prevents the gyre from moving into the river. The average velocity of the net flow through the entrance, u_s, now is about 0.014 m/s.

3.3.2 Experiment 6

In the harbour entrance horizontal mean velocities in 25 verticals (at 0.02, 0.04, 0.08, 0.12, and 0.16 m above the bottom) and the water level elevation were measured.
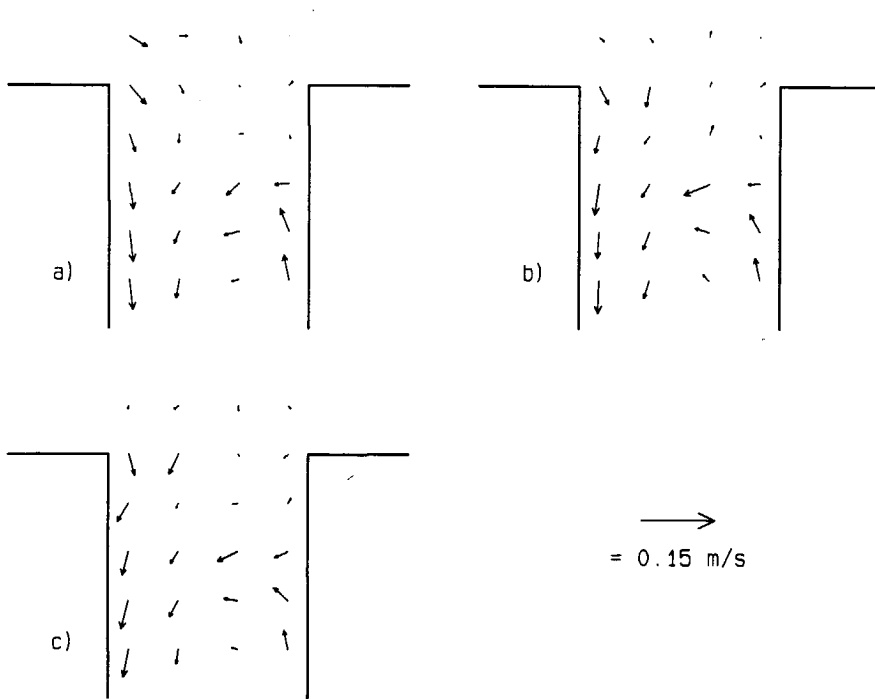
Figure 3.26 Flow patterns for experiment 5 at slack water after low tide ($t = 500$ s) at three levels: a) 0.02 m, b) 0.04 m, and c) 0.06 m above the bottom, respectively.

HIGH TIDE

Fig. 3.27 shows the flow patterns at four levels above the bottom at high tide ($t = 65$ s). A gyre is present in the harbour entrance. The centre of the gyre is located about 0.75 m into the harbour. The length of the gyre then is about 1.5 the width of the harbour. Near the bottom the flow in the gyre is directed inward, Fig. 3.27.a, and close to the surface it is directed outward (Fig. 3.27.d). At the downstream sidewall of the harbour entrance the water velocity near the bottom is larger than higher in the water column. These phenomena were also observed in the experiments described previously. The development of the gyre is similar to that observed in experiment 5.

SLACK WATER AFTER HIGH TIDE

Fig. 3.28 shows the influence of the emptying of the harbour basin on the gyre in the
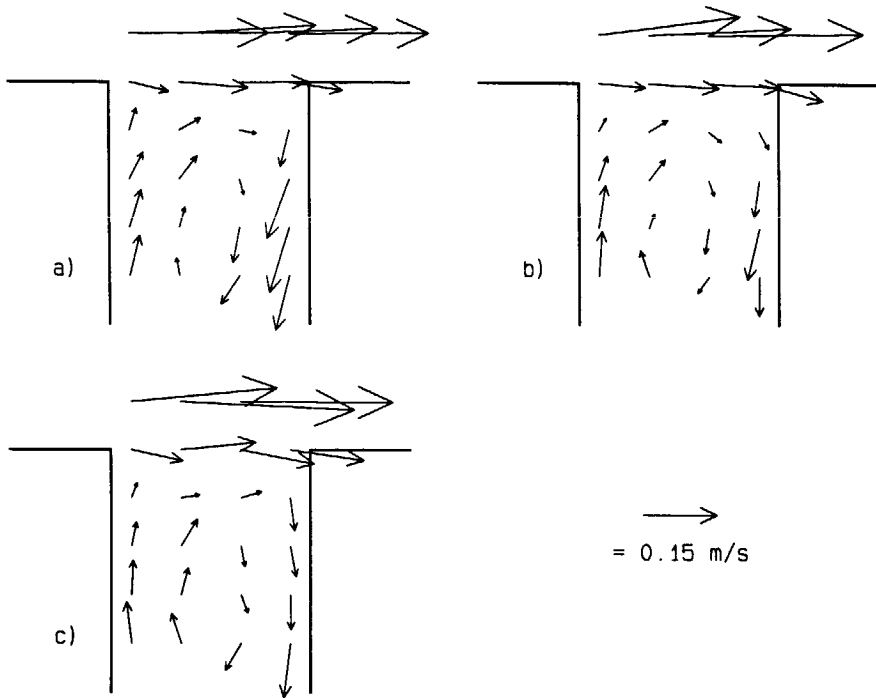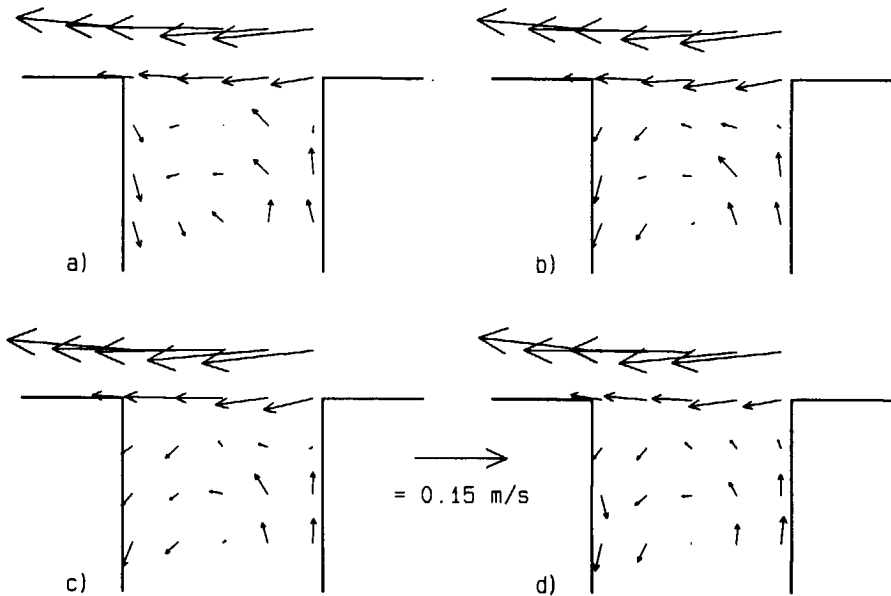

Figure 3.27 Flow patterns for experiment 6 at high tide ($t = 65$ s) at four levels: a) 0.02 m, b) 0.04 m, c) 0.08 m, and d) 0.16 m above the bottom, respectively.
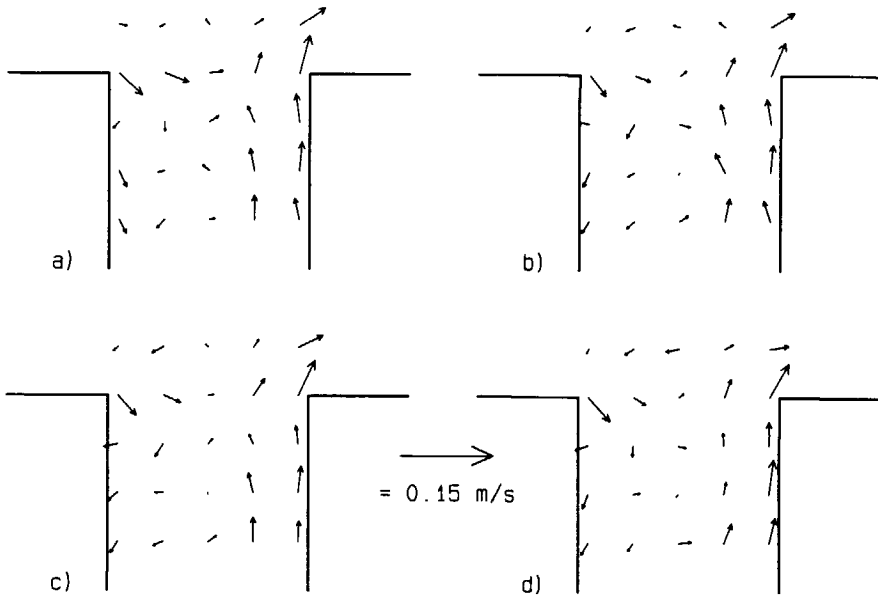
Figure 3.28   Flow patterns for experiment 6 at slack water after high tide
($t = 143$ s) at four levels: a) 0.02 m, b) 0.04 m, c) 0.08 m, and d) 0.16 m
above the bottom, respectively.

entrance during slack water after high tide. The velocity of the net flow through the entrance is about 0.009 m/s. The emptying of the basin results in a decrease in magnitude of the velocities in the gyre where the flow in the gyre is directed into the harbour, and an increase in magnitude where the flow in the gyre is directed towards the flume. The gyre has moved a little into the river.

LOW TIDE

Fig. 3.29 shows the flow patterns at four levels above the bottom at low tide ($t = 390$ s). A gyre is present as opposed to low tide in experiment 5 at the Delft University of Technology. The velocity of the net flow through the entrance preceding low tide is about 0.007 m/s, which is twice as small as the velocity of the net flow preceding low tide in experiment 5 at the Delft University of Technology. Hence, the development of a new gyre after slack water is less hindered by the emptying of the basin. Nevertheless, the develop-
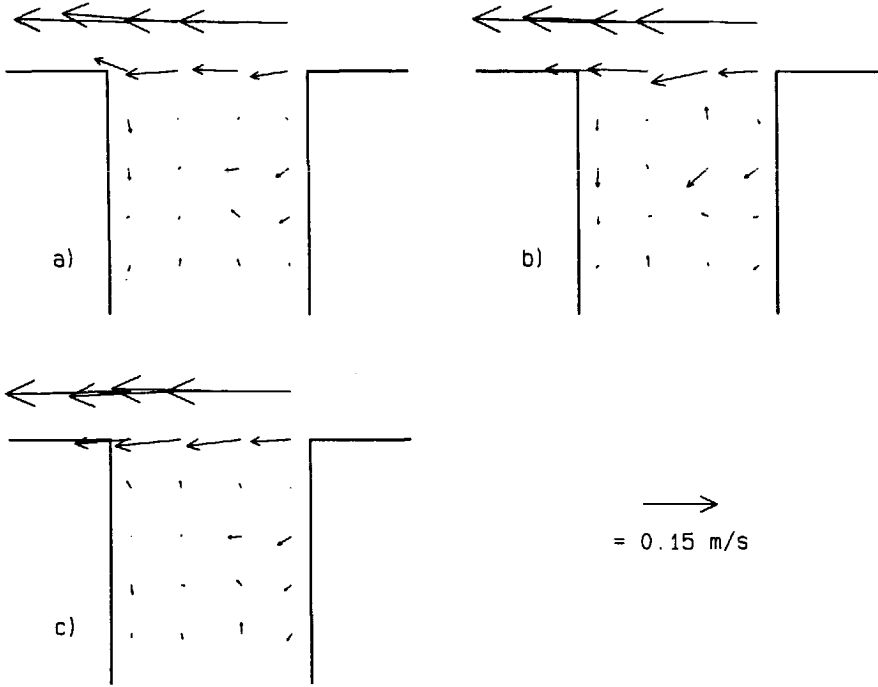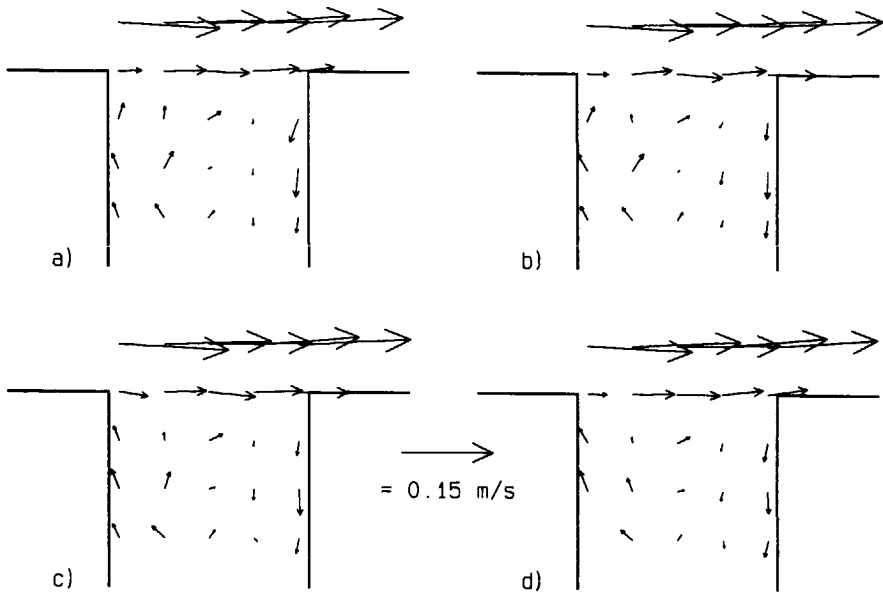
Figure 3.29 Flow patterns for experiment 6 at low tide ($t = 390$ s) at four levels: a) 0.02 m, b) 0.04 m, c) 0.08 m, and d) 0.16 m above the bottom, respectively.

ment of the gyre takes longer than in the experiments without variations in tidal level. Also, the shape of the gyre at low tide is more irregular than that at high tide.

SLACK WATER AFTER LOW TIDE

The influence of the filling of the harbour basin on the water velocities in the gyre during slack water after low tide, see Fig. 3.30, is an increase in magnitude where the flow in the gyre is directed into the harbour and a decrease in magnitude where the flow in the gyre is directed towards the flume. The velocity of the net flow through the entrance is about 0.01 m/s. The gyre has moved to the back of the harbour entrance (its centre is not visible).

The conclusions concerning the experiments discussed above are given in section 3.5.
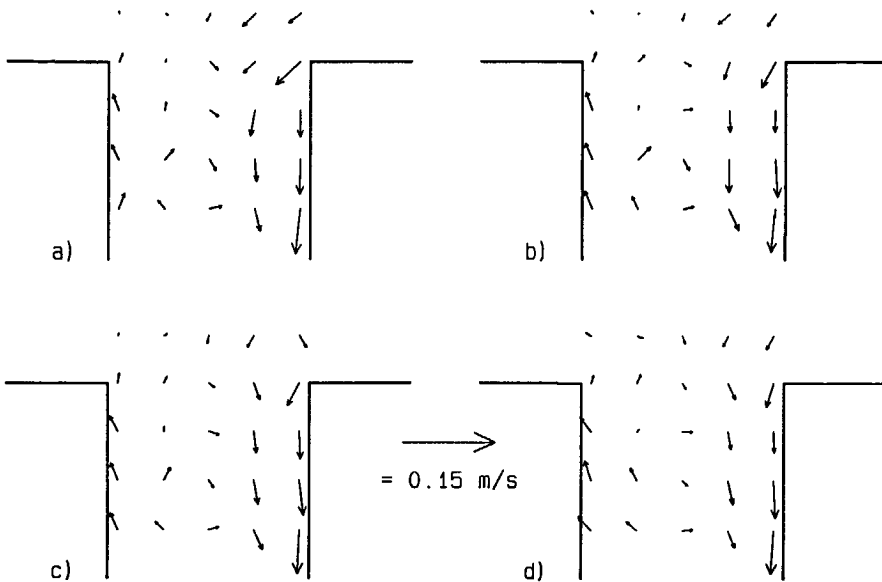
Figure 3.30 Flow patterns for experiment 6 at slack water after low tide ($t = 461.5$ s) at four levels: a) 0.02 m, b) 0.04 m, c) 0.08 m, and d) 0.16 m above the bottom, respectively.

3.4 Experiments with a stratified tidal flow in the river

The study of the influence of the harbour entrance geometry on the velocity and density fields due to a stratified tidal flow in the river has been carried out in the Tidal Flume of Delft Hydraulics.

Two more parameters then influence the exchange of mass between harbour and river: the estuarine Richardson number, see equation (2.20), which indicates the rate of stratification of the river-water; and the ratio, $T/t_i = T\sqrt{\varepsilon g h}/L$, between the tidal period and a time scale t_i of internal-wave propagation from the harbour entrance to the back of the harbour.

The length, depth, velocity, and time scales are the same as in experiment 6 with the unstratified flow (see section 3.3). A fresh water discharge of 0.0044 m³/s is introduced at the upstream end of the flume, corresponding to a river discharge of 1700 m³/s in the Rotterdam Waterway. The flow in the flume is generated by introducing a sinusoidal water
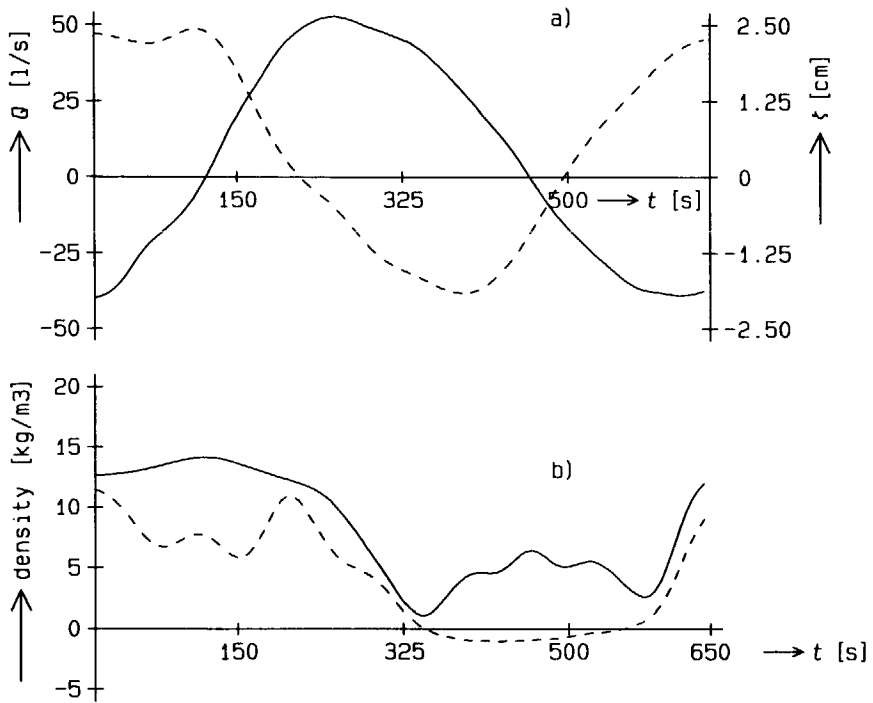
Figure 3.31 Time-histories of the discharge, the water level, and the density in the river in front of the harbour: a) ————, discharge and — — —, water level elevation; b) ————, density at 0.047 m above the bottom; — — —, density at 0.14 m above the bottom (1000 kg/m^3 is substracted from the density).

level elevation with an amplitude of 0.025 m at the transition from sea to flume. The water velocity of the fresh water discharge then is about 0.022 m/s and the maximum water velocity of the tidal current about 0.30 m/s. The density difference between the sea water and the fresh river water is 20 kg/m^3. The estuarine Richardson number then equals 0.09. Thus the flow in the flume is partially mixed, see Fischer et al. (1979). The salt intrusion extended from 24 m at ebb slack tide to 65 m at flood slack tide from the transition from flume to sea. Consequently, the harbour entrance (at 24.5 m from the transition from sea to flume) is situated near the location of minimum salt intrusion. The water level elevation, the discharge and the density at two levels above the bottom in the river in front of the harbour are shown in Fig. 3.31.
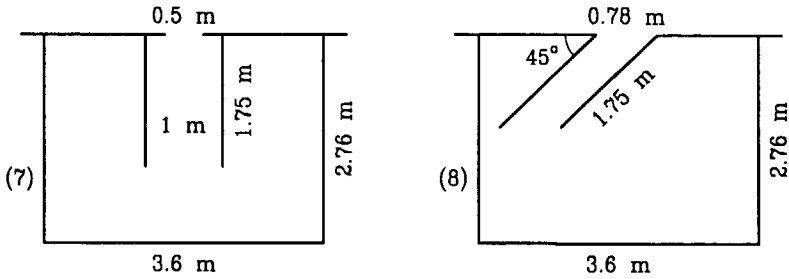
Figure 3.32 Top views of model harbours 7 and 8.

Besides the harbour geometry shown in Fig. 3.18, harbour 6, two other harbour geometries have been examined (see Fig. 3.32): a) a harbour, designated as harbour 7, with its length axis perpendicular to the flume and a width of 1 m but with an entrance width of 0.5 m; and b) a harbour, designated as harbour 8, with its length axis at an angle of 45 degrees to the length axis of the flume and an entrance width of 0.78 m. The values of the parameters that determine the exchange of mass between harbour and river are listed in Table 3.2.

The salinity, temperature and velocity were measured in several verticals in the harbour entrance. The two horizontal velocity components were measured at 0.02, 0.04, 0.06, 0.08, 0.10, 0.12, 0.14, and 0.16 m above the bottom. The densities were determined at 0.023, 0.047, 0.070, 0.094, 0.117, 0.140, 0.164, and 0.187 m above the bottom.

Table 3.2 Values of the dimensionless parameters for the model harbours examined at Delft Hydraulics.

	$\dfrac{\hat{u}\,T}{B} \cdot \dfrac{B_e}{B}$	$\dfrac{B}{L}$	$\dfrac{\bar{h}}{B}$	$\dfrac{\hat{h}}{\bar{h}}$	$\dfrac{B_e}{B}$	α	T/t_i
Harbour 6	160	-	0.2	0.11	1	90	45
Harbour 7	80	-	0.2	0.11	0.5	90	45
Harbour 8	200	-	0.26	0.11	1	45	45

The results of the three experiments are discussed for high tide, flood slack tide, low tide, and ebb slack tide. These times are chosen because the flow patterns could be interpreted more easily at these times, primarily because one of the three mechanisms of exchange then is absent. For example, at high and low tides there is no net flow through the harbour entrance. The flow pattern in the harbour entrance then is governed by a gyre, driven by the tidal current, and a density-driven exchange flow.

3.4.1 Harbour 6

<u>HIGH TIDE</u>

At high tide the flow in the harbour entrance is a combination of a density-driven exchange flow and a gyre driven by the flood current.

Figures 3.33 and 3.34 show the density and velocity distributions in the water column in harbour 6 at high tide. The profiles of the velocity component v along transect 3 show the presence of a density-driven exchange flow in the entrance. Water with a higher density is entering the harbour near the bottom over almost the complete entrance width, see profile d, while water with a lower density is leaving the harbour near the surface.
    The velocity of the density-driven exchange flow is determined from the vertical distributions of the velocity component v along transect 3 (see Fig. 3.34), because the velocities in the gyre only contribute to the velocity component u along this transect.

Fig. 3.35 shows the presence of a gyre in the entrance. Half-way down the water column (0.10 m above the bottom, Fig. 3.35.c), here the velocity of the density-driven exchange flow is approximately zero, the gyre spans the entire width of the harbour entrance. The water velocities in the gyre at the upstream sidewall of the harbour are approximately three times as small as those at the downstream harbour sidewall.
    In the lower layer, Fig. 3.35.a, the size of the gyre is much smaller than half-way
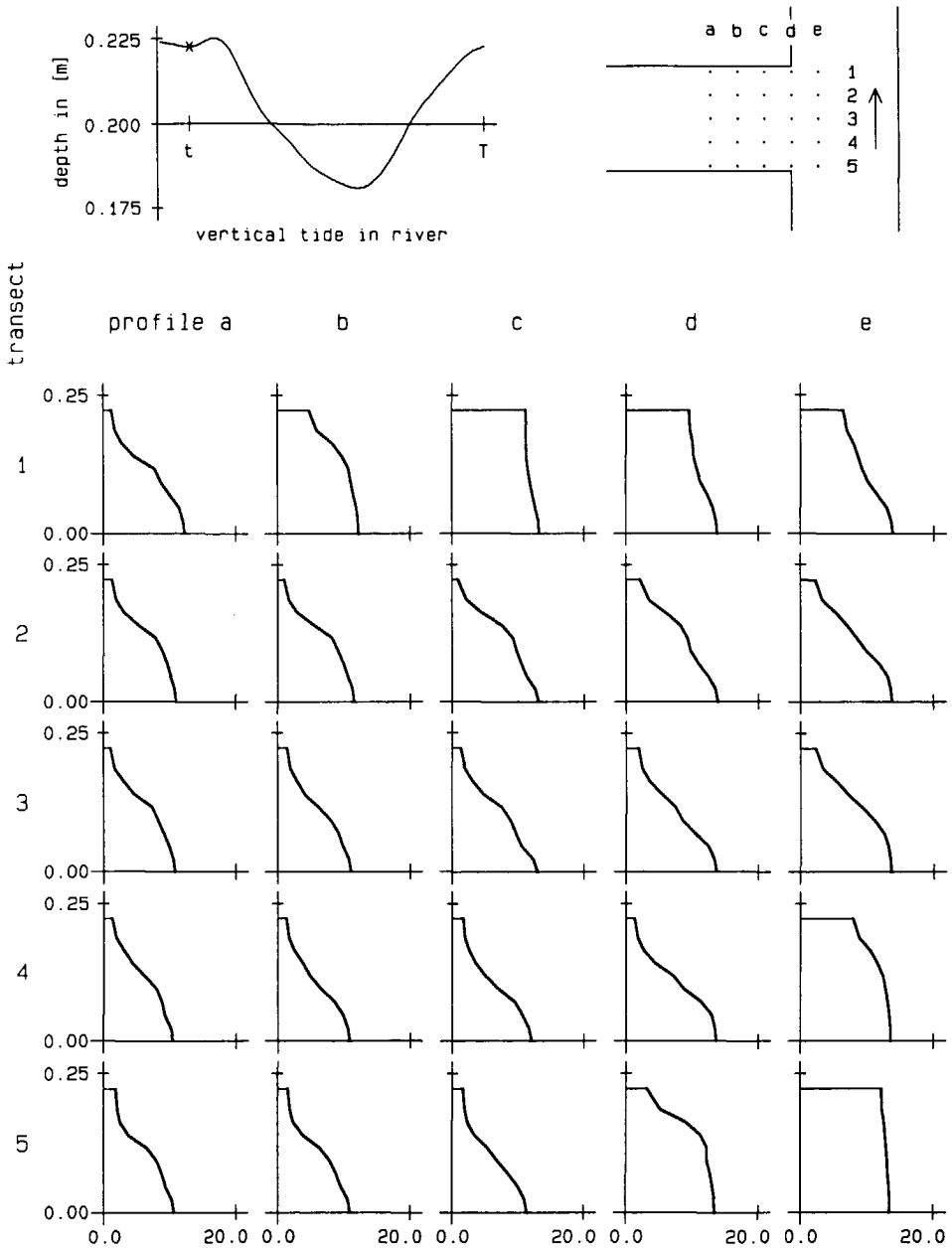
Figure 3.33 Density distributions in the water column in harbour 6 at high tide ($t = 65$ s): ————, ρ - 1000 kg/m^3.

Figure 3.34 Velocity distributions in the water column in harbour 6 at high
tide ($t = 65$ s): ————, u in m/s; and $-\ -\ -$, v in m/s.

Figure 3.35 Flow patterns in harbour 6 at high tide (t = 65 s) at four levels: a) 0.04 m, b) 0.08 m, c) 0.10 m, and d) 0.14 m above the bottom, respectively.

down the water column and the gyre is located near the upstream sidewall of the harbour. In the upper layer, Fig. 3.35.d, a small gyre exists at the downstream sidewall of the harbour. Here, river-water enters the harbour over the entire depth along the downstream sidewall of the harbour entrance, see transect 1 in Fig. 3.34. The density-driven exchange flow primarily occurs along transects 2 to 4. So, an interaction between the gyre and the density-driven exchange flow is observed in the entrance. The density-driven exchange flow causes a gyre of which the axis makes an angle with the vertical. The flow pattern resembles that given by by MKO (1983), see section 2.5 (Fig. 2.15).

The velocity of the density-driven exchange flow can theoretically be determined from (see section 2.4)

$$u_d = 0.45 \sqrt{\varepsilon g h} \ .$$

With ε = 0.01, see Fig. 3.33, and h = 0.225 m, u_d equals 0.07 m/s. This is about the magnitude of v in the upper and the lower layers along transect 3. The maximum water

velocities in the gyre in the abscence of a density-driven exchange flow would be about 0.04 to 0.05 m/s. The velocities in the density-driven exchange flow are of the same magnitude as the water velocities in an undisturbed gyre.

SLACK WATER AFTER HIGH TIDE

At slack water after high tide ($t = 130$ s) the flow pattern in the entrance is a combination of the remainder of the gyre during high tide, a density-driven exchange flow, and a net flow due to the emptying of the basin. Fig. 3.36 portrays the flow pattern in the harbour entrance. A remainder of the gyre can be observed. Half-way down the water column the gyre has decreased in size and moved towards the sidewall at the right of the harbour entrance.

The flow in the entrance is basically a density-driven exchange flow. Near the bottom, Fig. 3.36.a, the flow is into the harbour, and near the surface, Fig 3.36.d, the flow is to the river.

Figure 3.36   Flow patterns in harbour 6 at slack water after high tide ($t = 130$ s) at four levels: a) 0.04 m, b) 0.08 m, c) 0.10 m, and d) 0.14 m above the bottom, respectively.

LOW TIDE

At low tide ($t = 390$ s) the flow pattern in the entrance is a combination of a density-driven exchange flow and a gyre driven by the ebb current in the flume.

Figures 3.37 and 3.38 show the vertical distributions of density and velocity in harbour 6 at low tide. Denser harbour water is leaving the harbour near the bottom along transects 2 to 4, while fresh river-water enters the harbour near the surface over the entire entrance width.

Fig. 3.39 shows the presence of a gyre in the entrance. Half-way down the water column, Figures 3.39.b and c, the length of the gyre is small compared to its width. The centre of the gyre is located more towards the downstream sidewall of the harbour entrance. The flow in the entrance differs from the flow at high tide (Fig. 3.35), where a more circular shaped gyre was present half-way down the water column. As in the experiments with an unstratified tidal flow (experiments 5 and 6) the size and shape of the gyre differ at high and low tides. In the experiments with an unstratified tidal flow this was caused by the emptying of the basin before low tide.

The flow pattern at 0.04 m above the bottom, Fig. 3.39.a, shows a small gyre at the downstream corner of the harbour entrance. This gyre is not driven by the flow along the harbour entrance, because the flow at the transition from harbour to river is parallel to the length axis of the harbour over the entire width of the harbour entrance. The density profiles near the stagnation point at the downstream sidewall of the harbour entrance, verticals 5-b and 5-c in Fig. 3.37, show that fresh river-water flows downwards and meets, close to the bottom, the outgoing exchange flow by which it is guided out of the harbour. This also explains the sudden change in the density distribution from vertical 5-a to 5-b.

The flow pattern near the surface, Fig. 3.39.d shows a small gyre at the upstream sidewall of the harbour entrance, which unlike the gyre near the bottom is driven by the ebb current in the flume.

The density-driven exchange flow at low tide is less distinct than at high tide and slack water after high tide.
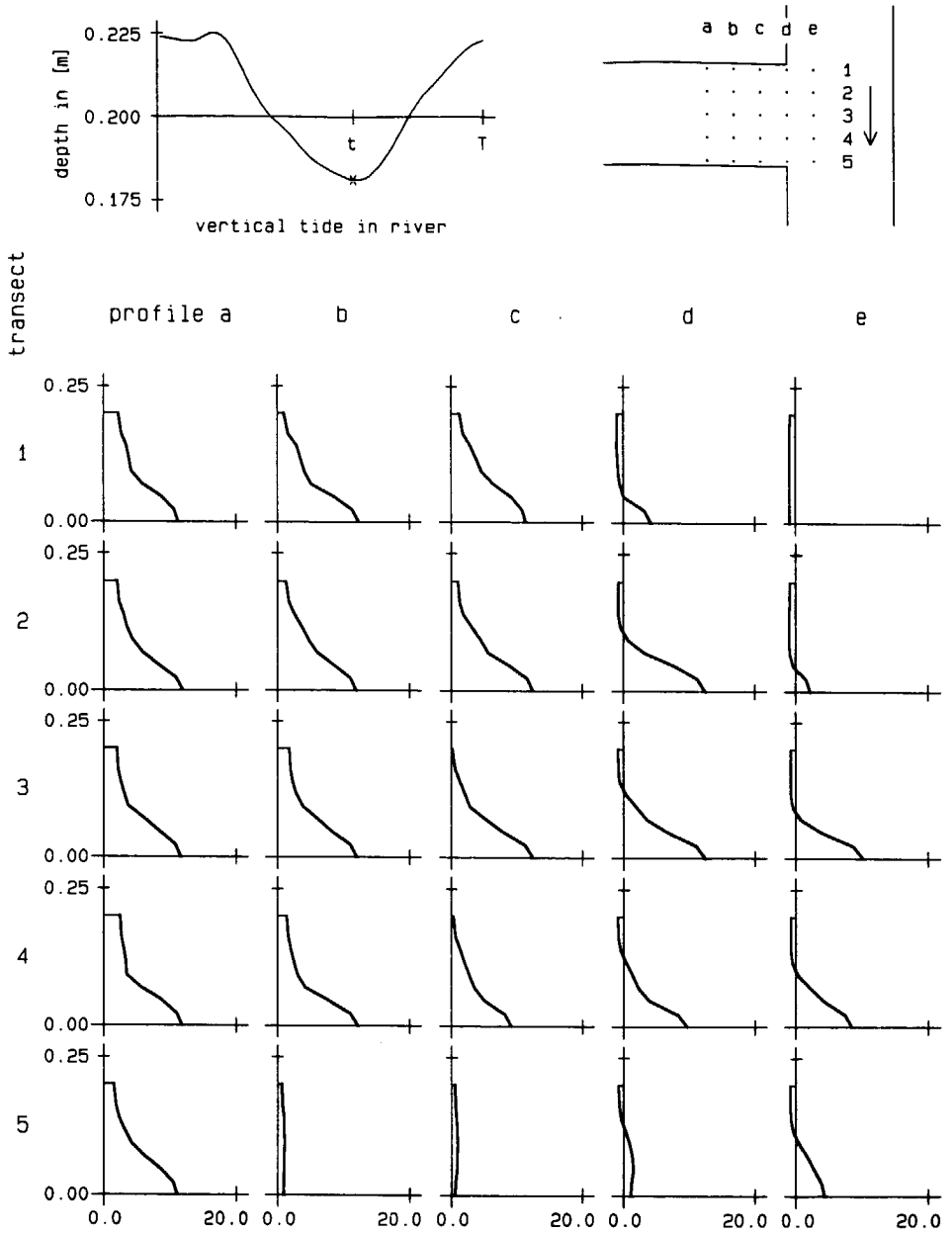
Figure 3.37 Density distributions in the water column in harbour 6 at low tide (t = 390 s): ————, ρ - 1000 kg/m^3.
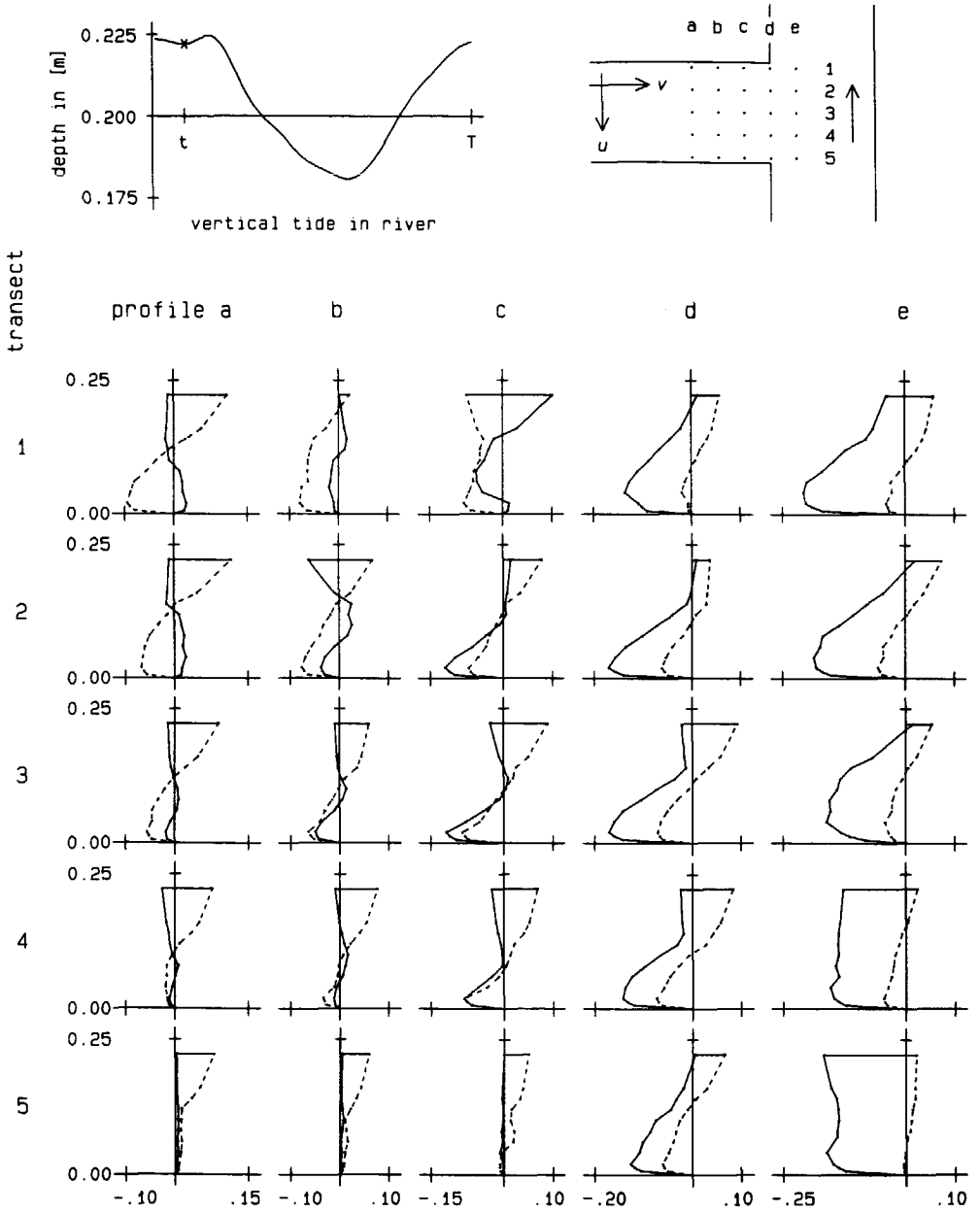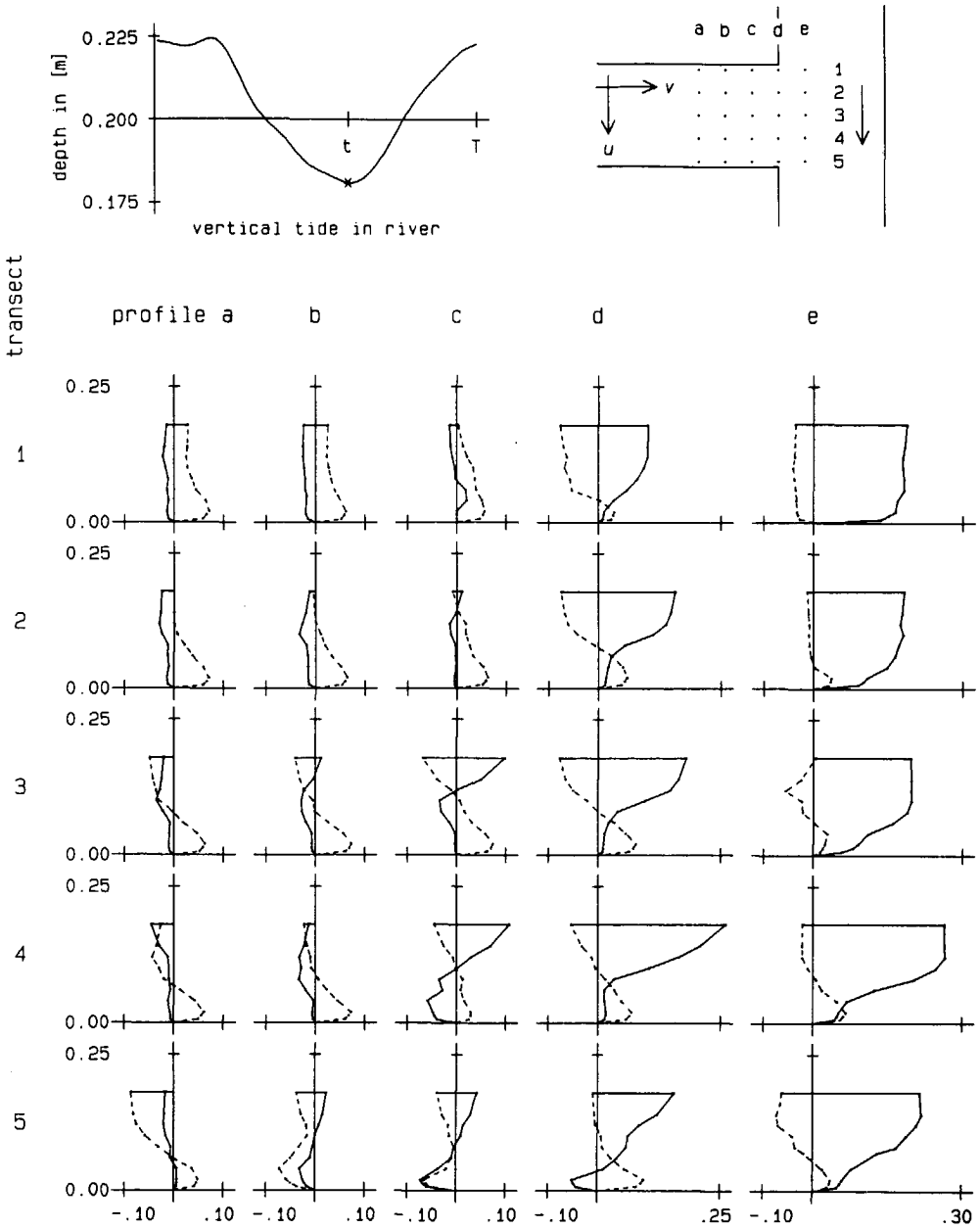
Figure 3.38 Velocity distributions in the water column in harbour 6 at low tide ($t = 390$ s): ———, u in m/s; and $-$ $-$ $-$, v in m/s.
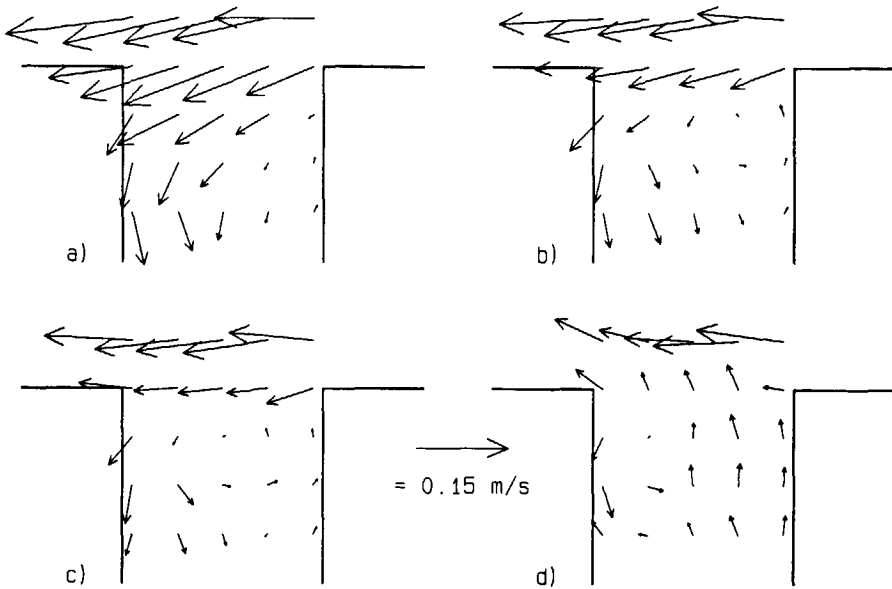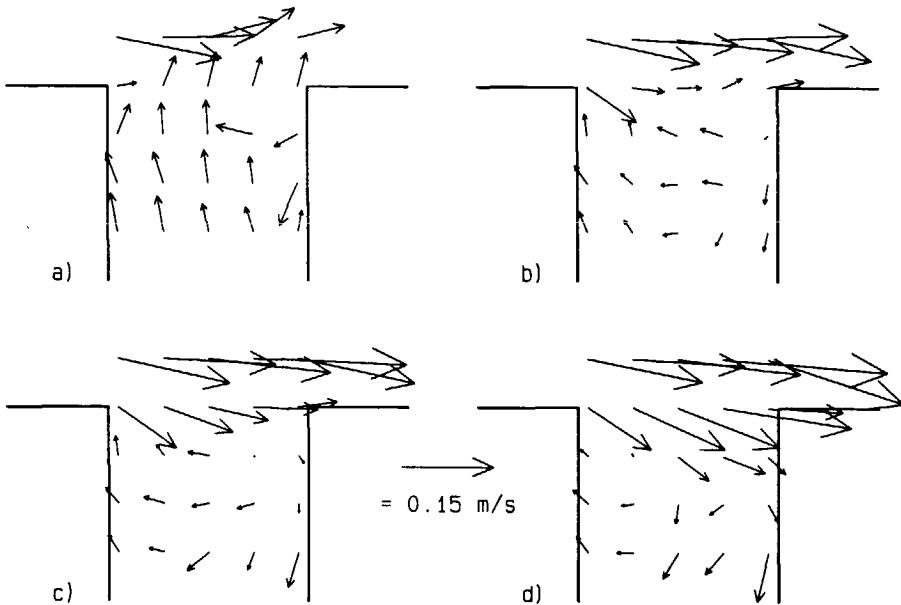
Figure 3.39 Flow patterns in harbour 6 at low tide (t = 390 s) at four levels: a) 0.04 m, b) 0.08 m, c) 0.10 m, and d) 0.14 m above the bottom, respectively.

SLACK WATER AFTER LOW TIDE

At slack water after low tide (t = 461.5 s) the very complex flow pattern near the stagnation point is still present in the harbour entrance, see Fig. 3.40. The gyre at low tide in the upper layer has remained at the sidewall at the left of the harbour entrance. The density-driven exchange flow is the dominant exchange mechanism at this time. Denser harbour water is leaving the harbour near the bottom, Fig. 3.40.a, while fresh river-water enters the harbour near the surface, Fig. 3.40.d.

3.4.2 Harbour 7

The geometry of harbour 7 is shown in Fig. 3.32. The geometry is similar to that of the previous harbour, harbour 6, except that the entrance is narrowed to 0.5 m.
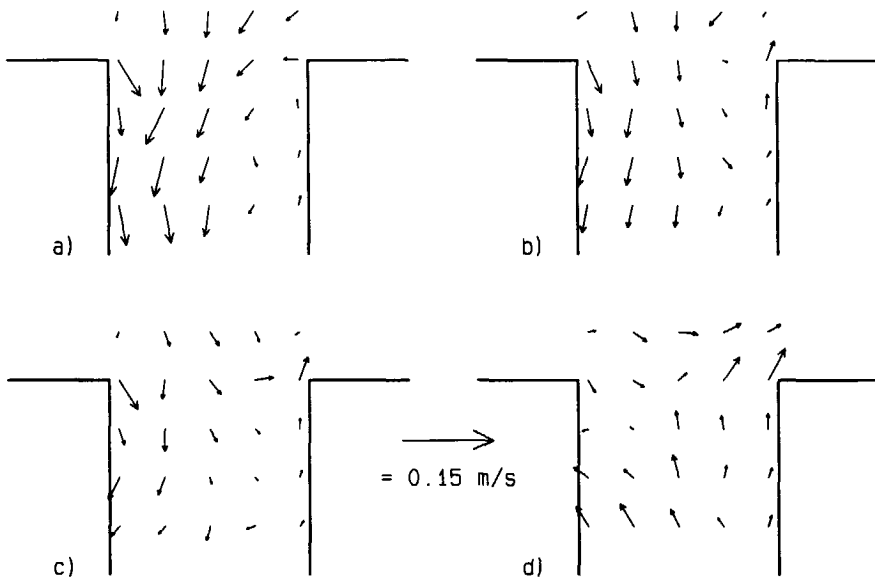
Figure 3.40   Flow patterns in harbour 6 at slack water after low tide
(t = 461.5 s) at four levels: a) 0.04 m, b) 0.08 m, c) 0.10 m, and d) 0.14 m
above the bottom, respectively.

HIGH TIDE

Fig. 3.41 shows the flow patterns at four levels above the bottom in harbour 7 at high tide
(t = 65 s). The flow in the harbour entrance is comparable to that in harbour 6. Denser
river-water enters the harbour near the bottom over the complete entrance width and close
to the downstream sidewall over the entire water depth.

Fig. 3.41.a shows that near the bottom a small gyre exists at the upstream corner of
the harbour entrance. The size of the gyre is somewhat larger than in harbour 6, because the
density-driven exchange flow is situated more towards the downstream section of the
harbour, as a result of the narrowing of the entrance.

Half-way down the water column at 0.10 m above the bottom, Fig. 3.41.c, a gyre
exists that spans the entire width of the entrance. The water velocities in the gyre are much
larger along the downstream sidewall of the harbour than along the upstream sidewall of the
harbour.

The gyre near the surface at the downstream corner of the entrance, see Fig. 3.41.d,

Figure 3.41 Flow patterns in harbour 7 at high tide ($t = 65$ s) at four levels:
a) 0.04 m, b) 0.08 m, c) 0.10 m, and d) 0.14 m above the bottom, respective-
ly.

is not so distinct as in harbour 6.

The velocity of the density-driven exchange flow is about the same as in harbour 6. Consequently, the narrowing of the entrance width and the gyre in the entrance do not influence the velocity of the density-driven exchange flow.

SLACK WATER AFTER HIGH TIDE

The flow at slack water after high tide ($t = 130$ s) is primarily a density-driven exchange flow. Denser river-water is entering the harbour near the bottom, and harbour water is leaving the harbour near the surface. A recirculating flow occurs behind the jetties in the entrance, because the density-driven exchange flow separates at the tips of the jetties. The net flow due to the emptying of the harbour basin is negligible with respect to the density-driven exchange flow.

LOW TIDE

At low tide (t = 390 s) the flow pattern in the entrance is a combination of a gyre driven by the ebb current in the river, and a density-driven exchange flow.

Fig. 3.42 shows that fresh river-water enters the harbour near the surface and denser water from the harbour leaves the harbour over the entire entrance width.

The flow pattern at 0.10 m above the bottom, Fig. 3.42.c, shows a gyre spanning almost the entire width of the harbour. About the same flow pattern exists near the surface (Fig. 3.42.d). The shape of the gyre at 0.10 m above the bottom is more coherent than in harbour 6 at the same time. Furthermore, the water velocities in the harbour are smaller than in harbour 6 as a result of the narrowing of the entrance width.

Just as in harbour 6 fresh river-water flows downwards near the downstream sidewall of the harbour entrance. However, in this case it occurs somewhat further to the back of the
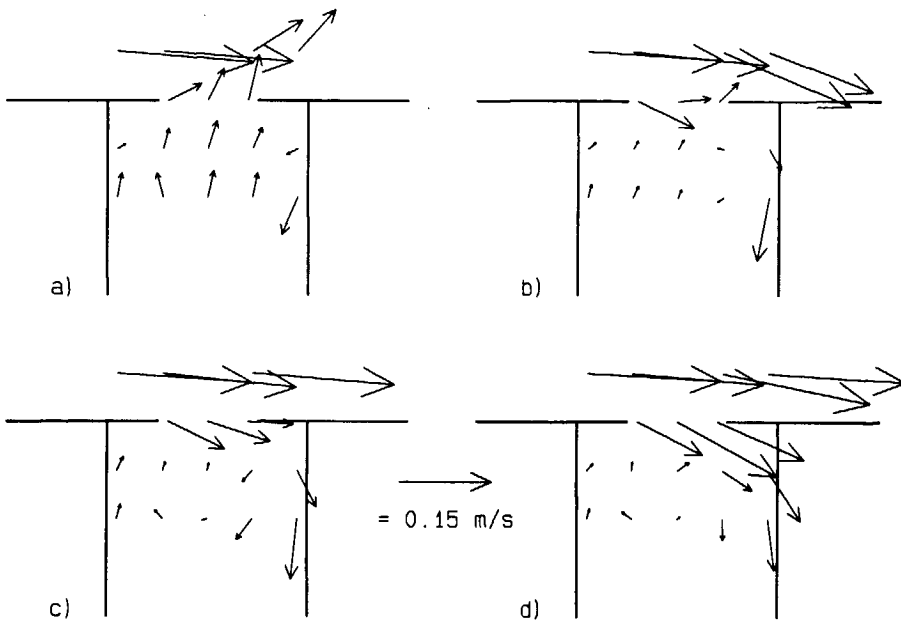
Figure 3.42 Flow patterns in harbour 7 at low tide (t = 390 s) at four levels: a) 0.04 m, b) 0.08 m, c) 0.10 m, and d) 0.14 m above the bottom, respectively.

harbour. This explains the recirculating flow near the bottom.

SLACK WATER AFTER LOW TIDE

Fig. 3.43 shows the influence of the filling of the basin on the density-driven exchange flow in the harbour entrance at slack water after low tide ($t = 468$ s). While in harbour 6 the net flow through the entrance due to the filling of the basin (u_s is about 0.013 m/s) did not influence the density-driven exchange flow, it does affect the density-driven exchange flow in harbour 7 as a consequence of a higher velocity (u_s is about 0.025 m/s) due to the narrowing of the entrance. The influence of this current on the density-driven exchange flow is a decrease in velocity of the density-driven exchange flow near the bottom and an increase in velocity of the density-driven exchange flow near the surface. The density-driven exchange flow is entering the harbour with velocities that are much larger than in harbour 6. The velocities near the bottom are smaller than in harbour 6.
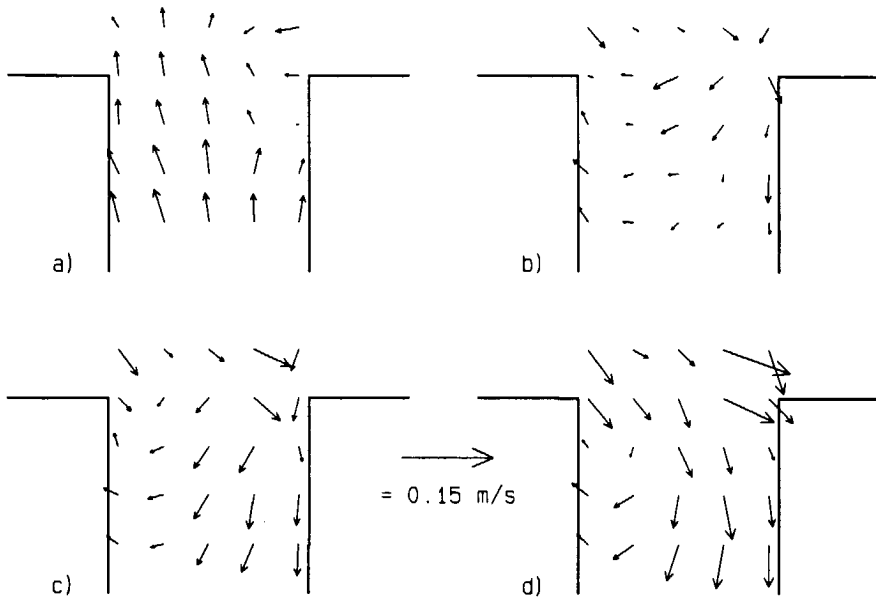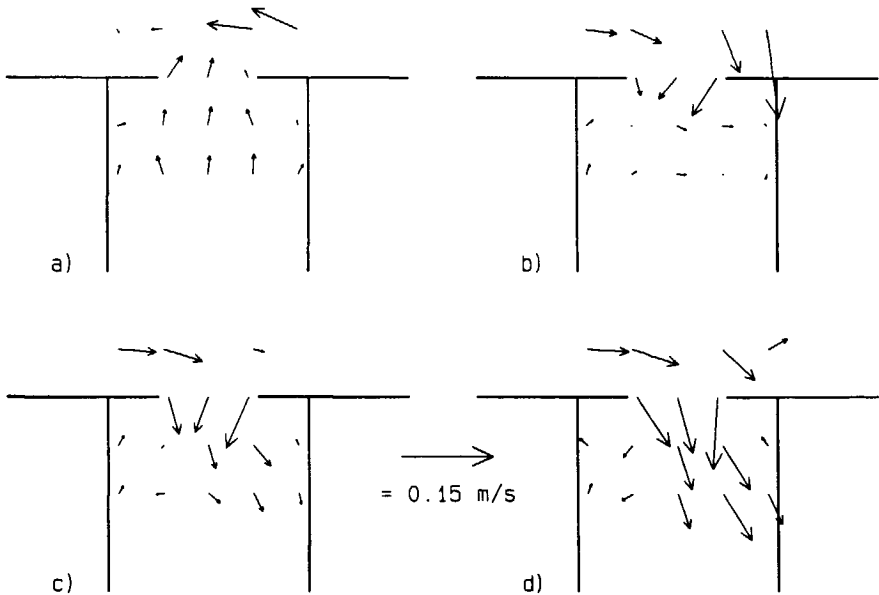
Figure 3.43 Flow patterns in harbour 7 at slack water after low tide ($t = 468$ s) at four levels: a) 0.04 m, b) 0.08 m, c) 0.10 m, and d) 0.14 m above the bottom, respectively.

A gyre develops in the upper layer behind each jetty, see Fig. 3.43.d, because the density-driven exchange flow separates at the tip of each jetty in the entrance.

3.4.3 Harbour 8

The geometry of harbour 8 is shown in Fig. 3.32. The harbour entrance makes an angle of 45 degrees with the river. The width of the harbour ($B = 0.78$ m) is smaller than that of harbours 6 and 7 ($B = 1.0$ m).

HIGH TIDE

At high tide ($t = 65$ s) the flow in the harbour entrance is a combination of a density-driven exchange flow and a gyre driven by the flood current, see Fig. 3.44.

Denser river-water enters the harbour near the bottom and harbour water leaves the
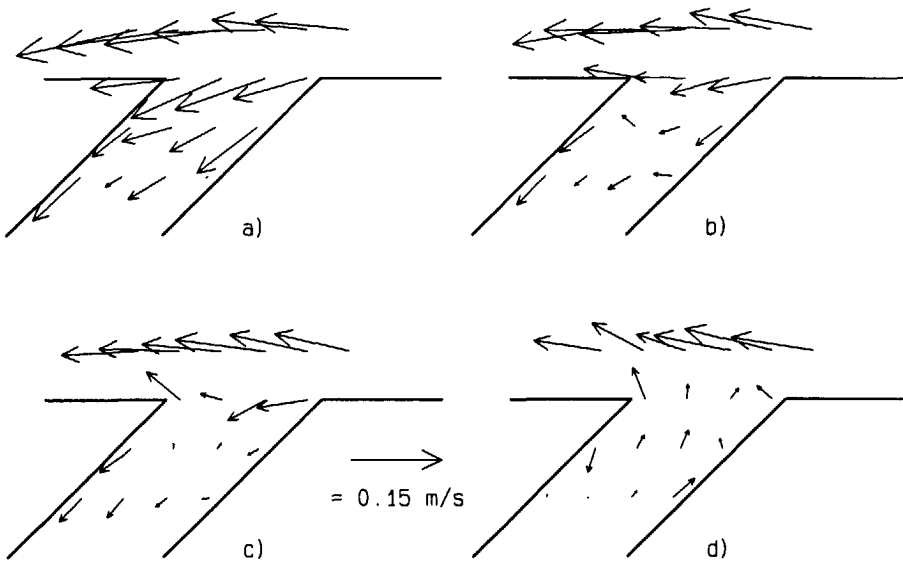
Figure 3.44 Flow patterns in harbour 8 at high tide ($t = 65$ s) at four levels: a) 0.04 m, b) 0.08 m, c) 0.10 m, and d) 0.14 m above the bottom, respectively.

harbour near the surface. The velocity of the density-driven exchange flow is approximately as large as in harbours 6 and 7.

The flow near the bottom, see Fig. 3.44.a, is almost parallel to the length axis of the harbour entrance. A gyre in the lower layer is absent because the flow does not separate at the upstream corner of the harbour entrance.

Near the surface and half-way down the water column a small gyre at the downstream corner of the harbour entrance is present (Figures 3.44.c and d).

SLACK WATER AFTER HIGH TIDE

At slack water after high tide ($t = 130$ s) the flow in the harbour entrance is primarily a density-driven exchange flow as in harbour 7. Denser river-water is entering the harbour near the bottom, and harbour water is leaving the harbour near the surface.

The net flow due to the emptying of the harbour basin is negligible with respect to the density-driven exchange flow. The gyre occurring in the upper layer during high tide has disappeared.

LOW TIDE

At low tide ($t = 360$ s) the flow pattern in the harbour entrance is a combination of a density-driven exchange flow and a gyre driven by the ebb current in the river, see Fig. 3.45.

The velocity of the density-driven exchange flow is about twice as small as in harbour 6 at low tide.

The same phenomena are visible near the stagnation point at the downstream corner of the entrance as in harbours 6 and 7. Fresh river-water flows downwards near the downstream sidewall of the harbour entrance, and leaves the harbour near the bottom.

The exchange of water between harbour and river is small at this moment. Most water from the upper fresh layer that enters the harbour leaves the harbour at the downstream
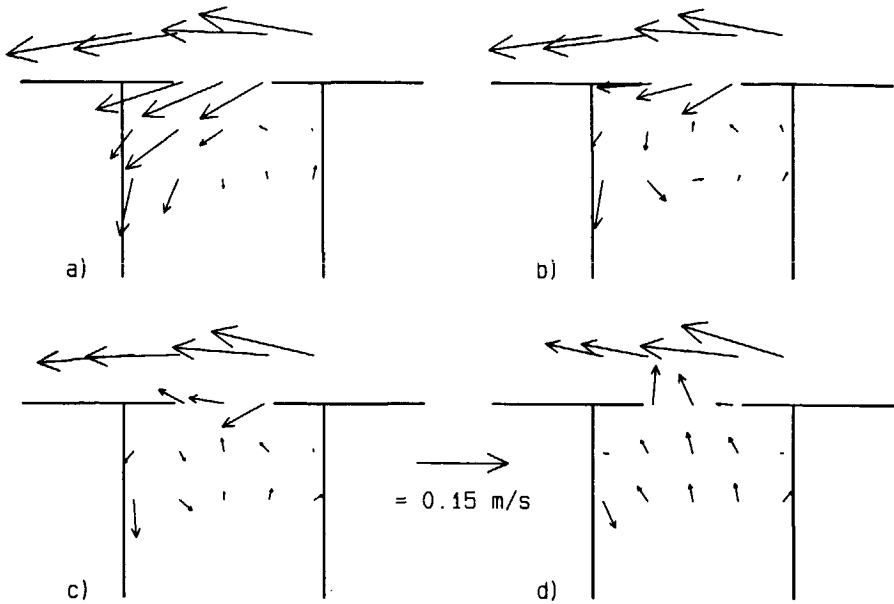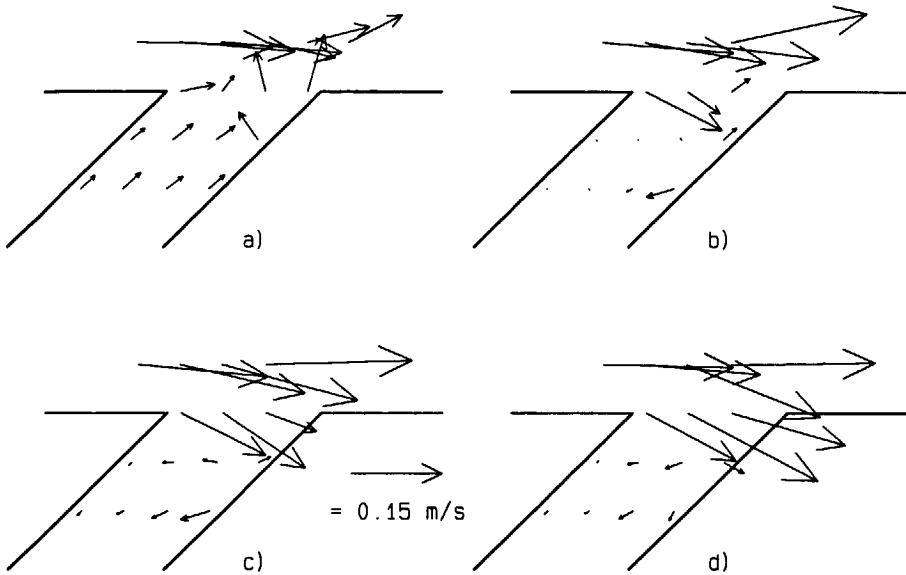
Figure 3.45 Flow patterns in harbour 8 at low tide ($t = 360$ s) at four levels: a) 0.04 m, b) 0.08 m, c) 0.10 m, and d) 0.14 m above the bottom, respectively.

corner of its entrance. This is comparable to the result obtained from the experiments in an oblique harbour at the Delft University of Technology, see Fig. 3.8 section 3.2.1. The exchange of water was much smaller for an angle of 135 degrees between the downstream sidewall of the entrance and the downstream river-bank than for an angle of 45 degrees.

SLACK WATER AFTER LOW TIDE

At slack water after low tide ($t = 481$ s) the influence of the net flow (u_s is about 0.02 m/s) through the entrance due to the filling of the basin on the exchange flow is only small. The flow in the entrance primarily consists of a density driven exchange flow. A circulating flow is absent.

3.5 Summary and discussion

In this chapter the experiments carried out in physical models at the Hydromechanics Laboratory of the Delft University of Technology and at Delft Hydraulics were discussed. In the experiments the influences of various parameters on the flow in the harbour entrance and the exchange of mass between harbour and river were examined. These parameters are: the ratio, t_t/t_g, between the time scales of the flows in the river and harbour; the ratio, B/L, between the width of the harbour and the length of the harbour; the relative water depth h/B; the ratio, $\hat{h}/h$, between the amplitude of the tidal level and the water depth; the ratio, B_e/B, between the widths of the harbour entrance and the harbour; the orientation of the harbour entrance with respect to the river; and the estuarine Richardson number defined by equation (2.20).

Three series of experiments were carried out: (1) experiments with an oscillatory current in the river without variations in water level, (2) experiments with an oscillatory current in the river with variations in water level, and (3) experiments with a stratified tidal flow.

3.5.1 Oscillatory current in the river without variations in water level

When the current in the river is around maximum, the flow is quasi-steady for a quite large duration for the harbours considered. The exchange then takes place through the mixing layer between harbour and river, that is, it is caused by turbulent motions only.

The maximum and average water velocities in the gyre in the square harbour are $0.25\,u_r$ and $0.17\,u_r$ respectively. These results agree with that obtained by Booij (1986) for a steady river flow. A narrowing of the entrance width of 50 per cent yields 40 per cent smaller water velocities in the gyre.

The time-histories of the dimensionless heat transport through the entrance, λ, for the examined harbour geometries show, see Fig. 3.16, that the progress of λ in time is determined by the harbour geometry. If the flow pattern in the harbour comprises various

gyres, for example if the harbour length is larger than twice the harbour width, λ is less because the secondary, tertiary, etc gyres hardly contribute to the exchange process.

The orientation of the harbour entrance influences the flow pattern in the harbour and consequently the exchange of mass between harbour and river. The angle between the downstream wall of the harbour entrance and the river influences the velocities in the gyre and the size of the gyre. When the flow in the harbour is quasi-steady the exchange of mass between harbour and river is much larger for an angle of 45 degrees than for an angle of 135 degrees. It was observed that the spreading rate of the mixing layer was much larger for an angle of 45 degrees than for an angle of 135 degrees.

A good explanation for this phenomenon is lacking at the moment. A tentative explanation for this phenomenon is as follows. When the vortices in the mixing layer arrive at the downstream corner of the harbour entrance, some of them flow into the river and some of them into the harbour. This process induces an exchange of mass between harbour and river, and energy from the river flow is supplied to the flow in the harbour. For an angle of 45 degrees most vortices flow into the harbour, while for an angle of 135 degrees the geometry guides most vortices to the river. Consequently, more water flows into the harbour for an angle of 45 degrees. As a result, more harbour water has to be entrained into the mixing layer to satisfy the mass balance in the harbour, which gives a wider mixing layer (cf. equation 2.4). Because more water flows into the harbour also more energy is supplied to the flow in the harbour. This results in a larger size of the gyre and larger water velocities in the gyre.

For the harbour oriented at 45 degrees to the river the higher entrainment of water into the mixing layer probably arises because the mixing layer is more convoluted than it is for angles larger than 90 degrees. However, more study is required.

The unsteadiness of the flow in the harbour can be observed clearly during both slack waters. The flow observed is similar to that found by Brinkmann (1990), see section 2.3.

It is observed that the gyre in the entrance, present at maximum current in the river, moves into the river at slack water. After slack water the direction of the river flow reverses, and the flow in the river is guided into the harbour by the rotating gyre while water is flowing out of the harbour at its downstream side. A large increase in advective exchange

then takes place around slack water. For a square harbour, $A_h = 9$ m^2, $T = 900$ s, $\hat{h} = 0.02$ m, $\bar{h} = 0.21$ m, and $\hat{u} = 0.046$ m/s, Brinkmann measured that about 60 per cent of the exchange over a tidal cycle occurs around both slack waters when the flow in the harbour is unsteady (about $0.48\,T$). In this study, for the square harbour of 1 m^2, 40 per cent of the exchange over a tidal cycle occurs around both slack waters (here $0.25\,T$).

Thus, the phenomena during slack water determine, to a considerable extent, the exchange of mass between harbour and river due to an oscillatory current in the river. The exchange at slack water can be reduced by narrowing the entrance, as a result of which the gyre cannot move into the river.

The development of a new gyre after slack water does not seem to depend on the tidal period. As a consequence, the phase difference between the development of the gyre and the accelerating flow in the river increases as the period decreases.

Measurements of the velocity distribution in the water column show that, except for the harbour with a narrowed entrance, a quite strong secondary current is present in the gyre. The maximum velocity in the secondary current is on the average 15 per cent of the main velocity in the gyre.

Close to the stagnation point on the downstream sidewall, in all model harbours, larger water velocities (20 to 50 per cent larger) were observed near the bottom than higher in the water column. Near the bed high-momentum fluid from the mixing layer between harbour and river appears to be transported into the harbour.

3.5.2 Oscillatory current flow in the river with variations in water level

From the measurements it follows that a superposition of a net flow through the entrance and a gyre in the entrance, as given by MKO (1983) see section 2.5, is not correct. From the measurements presented in section 3.3 it follows that the gyre at high tide spans the entire width of the harbour, and its centre is situated at the centre-line of the harbour. The water velocities in the gyre are somewhat larger than those in the experiments without water level variations.

This agrees with the work of Booij (1986) for a steady river-flow (u_r = 0.50 m/s). A steady net inflow of water from river to harbour, length 3 m and width 1 m, of 0.005 m/s resulted in larger water velocities in the gyre and a larger length of the gyre. A steady net outflow of water from harbour to river (u_s = 0.005 m/s) resulted in smaller velocities in the gyre and a smaller length of the gyre.

Tidal water level changes cause an acceleration in the development of the new gyre towards high tide as a consequence of the filling of the basin. Towards low tide the development of the new gyre is hindered by the emptying of the basin. At low tide no gyre comes into existence if the magnitude of the net flow through the entrance due to the emptying of the basin is sufficiently large.

At high and low tides (if a gyre is present in the harbour entrance) the same phenomena occur as have been observed during maximum current in the experiments with an oscillatory current in the river. A secondary current is present in the gyre, and close to the downstream harbour sidewall larger water velocities were observed near the bottom than higher in the water column.

3.5.3 Stratified tidal flow in the river

The exchange flow driven by a density difference between harbour water and river-water is present during the complete tidal cycle, and causes the dominant exchange process for all three model harbours examined, especially around slack water.

The density-driven exchange flow influences the size of the gyre considerably. In the layer where the density-driven exchange flow is directed towards the harbour, a small gyre is situated at the upstream corner of the harbour entrance. In the layer where the density-driven exchange flow is directed towards the river, a small gyre is situated at the downstream corner of the harbour entrance. This agrees with the superposition principle of MKO (1983), see section 2.5. It seems that the gyre (its position and size) is influenced by the density-driven

exchange flow because the velocity of the density-driven exchange flow has about the same magnitude as the velocities in the gyre. The velocity of the net flow through the entrance due to the filling and emptying of the basin was an order of magnitude smaller than the water velocities in the gyre.

At low tide the velocity and density profiles in the entrance show that water near the stagnation point at the downstream sidewall of the harbour entrance flows toward the bottom in all model harbours. This is probably the reason of the higher velocities near the bottom around both maximum currents, also in the experiments with unstratified flow.

4 Numerical simulations

4.1 Introduction

The physical model experiments discussed in the previous chapter have shown the influence and the importance of the harbour entrance geometry on the flow in the harbour entrance and the exchange of mass between harbour and river. Interactions between the various exchange mechanisms were shown. The knowledge gained and the data gathered from the physical model experiments can be used to test and improve numerical models for a better prediction of the flow in the entrance and the exchange of mass between harbour and river.

The advantages of numerical models with respect to physical models are that they are cheaper and more adaptable. The disadvantage of a numerical model is that it is a mathematical approximation of reality, in particular the turbulence has to be modelled. The motion of water and the transport of matter are described by a set of differential equations, which in turn are approximated by a set of finite difference equations needed for the numerical model. As a result, while a physical model is a small-scale reproduction of reality, information is lost in a numerical model and the finite-difference approximations may affect the results.

However, numerical models have proven to be useful tools in many fields. In the practice of civil engineering, for example, especially in those cases where the problem is of a nearly two-dimensional nature, such as the flow in rivers, estuaries (unstratified flow) and coastal seas, numerical models are often used. In the case of a complex three-dimensional flow, for example the flow in harbour entrances, further development is required concerning the way the finite difference equations are constructed and solved efficiently, and the type of turbulence model that is to be used.

In this work existing numerical models were used to compute the depth-averaged flow in the harbour (DUCHESS and TRISULA), the flushing of a harbour basin (ESTRA), and the three-dimensional flow in the harbour (TRISULA). The purpose is to examine whether these models are suited to predict the flow in harbour entrances with arbitrary geometry, and the

exchange of matter between harbour and river, by comparing computational results with the results of the measurements presented in the previous chapter. The emphasis is on the resolution of the computational grid and the parameterizations of the eddy viscosity and diffusivity.

In section 4.2 the three numerical models are discussed. In section 4.3 the results of simulations of the depth-averaged flows in two model harbours (harbours 1 and 4, see section 3.2), the simulation of the 3-D flow in model harbour 1, and the flushing of model harbour 1 are examined. Finally in section 4.4 some conclusions are given.

4.2 Characteristics of the numerical models

Three numerical models were used to simulate the flow (DUCHESS and TRISULA) and the transport of matter (ESTRA) in a harbour. DUCHESS (see Booij, 1990) and ESTRA (see Booij & Sokolewicz, 1990) were developed by the Hydromechanics Group (Department of Civil Engineering, Delft University of Technology) and TRISULA was developed by Delft Hydraulics (see Delft Hydraulics, 1988).

The first model, DUCHESS, solves the two-dimensional shallow water equations and the second, ESTRA, solves the depth-averaged convection-diffusion equation. The velocity field computed by DUCHESS is used as input for ESTRA. The third model, TRISULA, solves the three-dimensional shallow water equations. The models are discussed below.

4.2.1 DUCHESS

"DUCHESS" is short for Delft University Computer program for two-dimensional Horizontal Estuary and Sea Surges. It is intended to perform two-dimensional tidal and storm surge computations. The program is based on a finite difference approximation of the two-dimensional shallow water equations, i.e. the momentum and continuity equations integrated over the water depth, which apply only to flows with negligible vertical accelerations. The vertical pressure distribution is approximately hydrostatic. The mass balance equation reads

$(i = 1,2)$:

$$\frac{\partial \zeta}{\partial t} + \frac{\partial q_i}{\partial x_i} = 0.$$

The momentum equation reads $(i, k = 1,2)$:

$$\frac{\partial q_i}{\partial t} + \frac{\partial q_i q_k / h}{\partial x_k} + g h \frac{\partial (\zeta + p_a)}{\partial x_i} + c_f |q| q_i / h^2 + f_{ik} q_k - W_i = \frac{\partial}{\partial x_k} \left[h \nu_t \frac{\partial q_i / h}{\partial x_k} \right].$$

Here ζ is the water level elevation, q_i is the volume flux per unit width, p_a is the atmospheric pressure divided by the water density and the acceleration of gravity, c_f is a dimensionless friction factor, f_{ik} is the coriolis coefficient, and W_i is the component of the wind stress on the surface in x_i-direction. The summation convention is employed, that is summation is understood to be performed over any subscript appearing twice in the same term.

The eddy viscosity ν_t is modelled as the sum of a constant part and a part depending on the volume flux

$$\nu_t = C_1 + C_2 |q| + C_3 |q|^2, \tag{4.1}$$

where C_1, C_2, and C_3 are constants.

The model uses a rectangular computational grid, with alternating points for the calculation of water level and current, see Fig. 4.1. Central difference approximations are used for the spatial derivatives. The discretization in time is according to the Alternating Direction Implicit Method. Apart from some details the solution method is similar to the one developed by Leendertse (1967) and further developed by Stelling (1983). An extensive description of
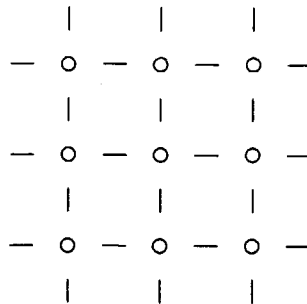
Figure 4.1 Computational grid used in DUCHESS: O, ζ- and h-point; —, q_1-point; and |, q_2-point.

the numerical scheme is given by Booij (1990). The accuracy of the scheme is of second order in space and approximately second order in time.

At closed boundaries the velocity component perpendicular to the wall is set equal to zero, and a partial-slip condition can be applied so that the wall exerts the proper shear stress on the fluid. At open boundaries the discharge or water level is imposed. Open boundaries can be made weakly reflective so that disturbances in the computational domain, for example those initiated by the start of the model, will be absorbed for the larger part at the open boundary.

4.2.2 ESTRA

"ESTRA" is short for Estuarine and Sea Transport Model, and needs as input the flow field computed by DUCHESS. The model is based on the vertically integrated conservation equation for the mass of a certain material. The model can be used for a variety of environmental problems. Among these are problems involving dissolved oxygen, biological oxygen demand, and transport of silt and oil. Four modes of transport are available in the model, viz. well-mixed, suspended, buoyant, and immobile material. The last mode represents a situation with zero transport and is used for the modelling of a bottom layer.

The transport model is formulated so that it can be used for the four transport modes. The mass balance equation reads ($i = 1,2$):

$$\frac{\partial M}{\partial t} + \frac{\partial S_i}{\partial x_i} = P,$$

where M is the integral of the concentration c over depth, S_i is the transport of a material in x_i-direction, and P is a production term.

For each transport mode the mass transport can be written as a sum of the convective and the dispersive transport

$$S_i = u_i M - D_t h \frac{\partial M/h}{\partial x_i}.$$

The expression for the transport velocity u_i depends on the transport mode. The four

expressions are given in Booij & Sokolewicz (1990). The dispersion coefficient is either constant or the product of a dimensionless coefficient, the friction velocity and the water depth.

The multi-component system used in the ESTRA-model, allows up to ten materials to interact with each other. The transports of these materials are computed simultaneously. The interactions are modelled as contributions of these materials to the production term for a particular material. A number of production terms for non-conservative materials is available in ESTRA.

The numerical aspects of the ESTRA model are similar to those of DUCHESS. The computational grid is shown in Fig. 4.2. As in DUCHESS, central difference approximations are used for the spatial derivatives and the discretization in time is according to the Alternating Direction Implicit Method.

    The scheme has a very low numerical damping, which in regions with strong gradients in the flow or concentration field can lead to oscillations of the computed concentrations. A smoothing procedure is applied, which prevents the concentration to become negative. As an option, a first order upstream approximation of the convective terms can be used.

    Conditions for the concentration and the transport of the material must be imposed at the boundaries. At open boundaries the following conditions are imposed: a) when the flow is out of the model, the gradients of the concentration and the transport components S_1 and
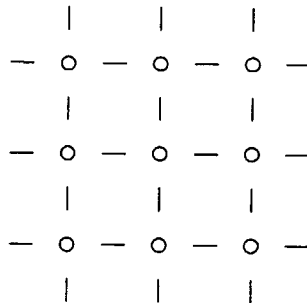
Figure 4.2 Computational grid used in ESTRA: $\bigcirc$, M-point; —, S_1-point; and $|$, S_2-point.

S_2 are zero; and b) when the flow is into the model, the concentration and the transport component perpendicular to the boundary must be given.

At closed boundaries the transport component perpendicular to the wall and the gradients normal to the wall of the concentration and the transport component parallel to the wall are zero.

4.2.3 TRISULA

The TRISULA programme system for three-dimensional flow simulations is also based on the assumption of a hydrostatic pressure distribution. The basic mathematical description of TRISULA deals with water level elevation, flow velocity in three dimensions and density. The density is a function of salinity and temperature. It is coupled dynamically with the flow equations to simulate density driven flow. This approach results in a set of non-linear equations for free surface flow, conservation of heat, salt and, in addition, dissolved constituents.

GOVERNING EQUATIONS

TRISULA uses a so-called sigma-coordinate system, introduced by Phillips (1957) for atmospheric numerical models. The computational problems which arise in the vicinity of bathymetric irregularities are hereby overcome. The σ-coordinate is defined by $\sigma = (z - \zeta)/h$, where z is the cartesian vertical coordinate. In this system σ ranges from $\sigma = 0$ at the free surface ($z = \zeta$) to $\sigma = -1$ at the bottom ($z = -d$). The number of vertical grid points is constant over the entire computational field. In the horizontal plane orthogonal curvilinear coordinates ξ and η are used to make a more accurate schematization of irregular boundaries possible.

The continuity equation is given by

$$\frac{\partial \zeta}{\partial t} + \frac{1}{\sqrt{G_{\xi\xi}} \sqrt{G_{\eta\eta}}} \left[\frac{\partial h u \sqrt{G_{\eta\eta}}}{\partial \xi} + \frac{\partial h v \sqrt{G_{\xi\xi}}}{\partial \eta} \right] + \frac{\partial \omega}{\partial \sigma} = 0,$$

where u is the velocity component in ξ-direction, v is the velocity component in η-direction, ω is the velocity component in σ-direction relative to a σ-plane, $G_{\xi\xi}$ and $G_{\eta\eta}$ are components of the covariant metric tensor. The velocity component ω is given by

$$\omega = w - \frac{u}{\sqrt{G_{\xi\xi}}} \left[\sigma \frac{\partial h}{\partial \xi} + \frac{\partial \zeta}{\partial \xi} \right] - \frac{v}{\sqrt{G_{\eta\eta}}} \left[\sigma \frac{\partial h}{\partial \eta} + \frac{\partial \zeta}{\partial \eta} \right] - \left[\sigma \frac{\partial h}{\partial t} + \frac{\partial \zeta}{\partial t} \right],$$

where w is the velocity component in z-direction.

The momentum equations in ξ- and η-directions read

$$\frac{\partial u}{\partial t} + \frac{u}{\sqrt{G_{\xi\xi}}} \frac{\partial u}{\partial \xi} + \frac{v}{\sqrt{G_{\eta\eta}}} \frac{\partial u}{\partial \eta} + \frac{\omega}{h} \frac{\partial u}{\partial \sigma} + \frac{uv}{\sqrt{G_{\xi\xi}} \sqrt{G_{\eta\eta}}} \frac{\partial \sqrt{G_{\xi\xi}}}{\partial \eta} +$$

$$- \frac{v^2}{\sqrt{G_{\xi\xi}} \sqrt{G_{\eta\eta}}} \frac{\partial \sqrt{G_{\eta\eta}}}{\partial \xi} - fv + \frac{1}{\rho \sqrt{G_{\xi\xi}}} \frac{\partial p}{\partial \xi} +$$

$$- \frac{1}{\sqrt{G_{\xi\xi}}} \frac{\partial A}{\partial \xi} + \frac{1}{\sqrt{G_{\eta\eta}}} \frac{\partial F}{\partial \eta} - \frac{\nu_t^v}{h^2} \frac{\partial^2 u}{\partial \sigma^2} = 0,$$

$$\frac{\partial v}{\partial t} + \frac{u}{\sqrt{G_{\xi\xi}}} \frac{\partial v}{\partial \xi} + \frac{v}{\sqrt{G_{\eta\eta}}} \frac{\partial v}{\partial \eta} + \frac{\omega}{h} \frac{\partial v}{\partial \sigma} + \frac{uv}{\sqrt{G_{\xi\xi}} \sqrt{G_{\eta\eta}}} \frac{\partial \sqrt{G_{\eta\eta}}}{\partial \xi} +$$

$$- \frac{u^2}{\sqrt{G_{\xi\xi}} \sqrt{G_{\eta\eta}}} \frac{\partial \sqrt{G_{\xi\xi}}}{\partial \eta} + fu + \frac{1}{\rho \sqrt{G_{\eta\eta}}} \frac{\partial p}{\partial \eta} +$$

$$- \frac{1}{\sqrt{G_{\eta\eta}}} \frac{\partial A}{\partial \eta} - \frac{1}{\sqrt{G_{\xi\xi}}} \frac{\partial F}{\partial \xi} - \frac{\nu_t^v}{h^2} \frac{\partial^2 v}{\partial \sigma^2} = 0,$$

where p is the water pressure, ν_t^v is the eddy viscosity in the vertical direction, and A and F are given by

$$A = \frac{\nu_t^h}{\sqrt{G_{\xi\xi}}\,\sqrt{G_{\eta\eta}}} \left[\frac{\partial\, u\sqrt{G_{\eta\eta}}}{\partial \xi} + \frac{\partial\, v\sqrt{G_{\xi\xi}}}{\partial \eta} \right],$$

$$F = \frac{\nu_t^h}{\sqrt{G_{\xi\xi}}\,\sqrt{G_{\eta\eta}}} \left[\frac{\partial\, v\sqrt{G_{\eta\eta}}}{\partial \xi} - \frac{\partial\, u\sqrt{G_{\xi\xi}}}{\partial \eta} \right],$$

where ν_t^h is the eddy viscosity in the horizontal plane.

The shallow-water approximation is used to model the flow. The vertical momentum equation then reduces to the hydrostatic pressure relation, which upon integration gives

$$p = p_{\text{atm}} + gh \int_\sigma^0 \rho(\xi, \eta, \sigma', t)\, \mathrm{d}\sigma',$$

where p_{atm} is the pressure at the free surface.

The shallow water approximation imposes the main restriction on the applicability of the approach: vertical accelerations due to buoyancy effects and due to sudden variations in the bottom topography cannot be taken into account. TRISULA can be used for applications with predominantly horizontal motion, such as wind-generated currents in lakes, tidal flow in coastal seas and estuaries, salt intrusion in estuaries, far-field cooling-water dispersion, and large-scale pollutant dispersion.

TURBULENCE MODELS

In the applications for which TRISULA is intended a distinct difference is present between the horizontal and vertical scales of the flow and the distributions of salt and temperature . As a result, the grid size in the horizontal plane and the time step are much larger than the typical length and time scales of those turbulent motions of which the length scales are correlated with the water depth. This turbulence is referred to as three-dimensional turbulence, and is usually simulated by a turbulence model (for example a k-ε model). The large-scale turbulence, at scales one order of magnitude larger than the horizontal grid sizes,

is computed directly by the numerical model. The fluctuating motions at scales between those of 3-D turbulence and the large-scale turbulence are not represented usually in numerical models. These fluctuating motions are nearly horizontal and are referred to as subgrid two-dimensional turbulence. Therefore, eddy viscosities in the horizontal plane and in vertical direction are distinguished according to: $\nu_t^h = \nu_t^{2D} + \nu_t^v$ and $\nu_t^v = \nu_t^{3D}$.

Several turbulence models have been implemented in TRISULA to predict the effects of three-dimensional turbulence, which is mainly generated by velocity gradients with typical length scales equal to the water depth or smaller. The version which was made available for use in the present study by Delft Hydraulics (to be called the DH-version hereafter) contains three such models: a) a so-called algebraic eddy viscosity model, b) a k-L model, and c) a k-ε model. Here k is the turbulent kinetic energy per unit mass, L is the mixing length, and ε is the dissipation. In the course of this study, a number of modifications and alternative formulations were implemented. These will be described in section 4.3.3.

An extensive description of the implementation of the turbulence models in the DH-version of TRISULA is given in Uittenbogaard et al. (1991). A summary of these turbulence models is given here. At the moment the turbulence models are only implemented for non-equidistant rectangular meshes in the horizontal plane.

The eddy viscosity is usually expressed as the product of a velocity and a length scale, which are connected with the measures of velocity and length of the larger eddies that are responsible for the transport of momentum and matter. In the algebraic eddy viscosity model and the k-L model the length scale is given by a mixing length, L, and the velocity scale is given by the square root of the turbulent kinetic energy, $\sqrt{k} = \sqrt{\frac{1}{2}\overline{u_i' u_i'}}$, where u_i' is the velocity fluctuation. The eddy viscosity then is given by the Kolmogorov-Prandtl expression:

$$\nu_t = c_\mu' L \sqrt{k} , \tag{4.2}$$

where c_μ' is a constant. For the k-ε model the length scale is defined as $L = c_D k^{3/2}/\varepsilon$, where c_D (= $c_\mu'^3$) is a constant. The eddy viscosity then is given by:

$$\nu_t = c_\mu \frac{k^2}{\varepsilon} , \tag{4.3}$$

where c_μ is a constant.

a) algebraic eddy viscosity model

The algebraic eddy viscosity model is the simplest of the three turbulence models. Here both L and k are prescribed. The turbulent kinetic energy is given by:

$$k = -3u_{*,b}^2 \sigma + 3u_{*,w}^2(1+\sigma),\qquad(4.4)$$

where $u_{*,b}$ is the friction velocity at the bottom, $u_{*,w}$ is the friction velocity at the surface due to the wind shear stress. The mixing-length profile is given by the Bakhmetev distribution

$$L = \kappa h(1+\sigma)(-\sigma)^{1/2},\qquad(4.5)$$

where κ is the constant of Von Karman.

In the absence of wind ($u_{*,w} = 0$) a parabolic viscosity profile is obtained across the water depth by substituting equations (4.4) and (4.5) in equation (4.2). Its maximum is $hu_{*,b}/9$. A parabolic viscosity profile yields a logarithmic velocity profile.

In this study spatially constant horizontal and vertical eddy viscosities are categorized in the group of algebraic eddy viscosity models.

b) k-L turbulence model

A more advanced eddy viscosity model is the k-L model. Here k is solved from a transport equation, which reads

$$\frac{\partial k}{\partial t} + u\frac{\partial k}{\partial x} + v\frac{\partial k}{\partial y} + \frac{\omega}{h}\frac{\partial k}{\partial \sigma} = D_k + P_k + B_k - \varepsilon_k,\qquad(4.6)$$

where D_k is the diffusion of k, P_k is the production of k, B_k is the buoyancy flux, and ε_k is the dissipation of k.

The diffusion of k in equation (4.6) is given by

$$D_k = \frac{\partial}{\partial x}\left[\left(\nu+\frac{\nu_t}{\sigma_k}\right)\frac{\partial k}{\partial x}\right] + \frac{\partial}{\partial y}\left[\left(\nu+\frac{\nu_t}{\sigma_k}\right)\frac{\partial k}{\partial y}\right] + \frac{1}{h^2}\frac{\partial}{\partial \sigma}\left[\left(\nu+\frac{\nu_t}{\sigma_k}\right)\frac{\partial k}{\partial \sigma}\right],$$

where σ_k is the turbulent Schmidt number for k. The horizontal diffusion terms are kept in cartesian coordinates to avoid artificial creeping of k along inclined σ-planes, see Van Kester

& Uittenbogaard (1990).

Assuming that the gradients of the vertical velocity w can be neglected with respect to the gradients of the horizontal velocity components u and v, the production of k is given by

$$P_k = 2\nu_t \left[\left(\frac{\partial u}{\partial x} \right)^2 + \left(\frac{\partial v}{\partial y} \right)^2 + \frac{1}{2} \left(\frac{\partial u}{\partial y} + \frac{\partial v}{\partial x} \right)^2 + \frac{1}{2} \left(\frac{\partial u}{\partial z} \right)^2 + \frac{1}{2} \left(\frac{\partial v}{\partial z} \right)^2 \right].$$

For simplicity the production is given in cartesian coordinates here.

The buoyancy flux, which represents the conversion of k into potential energy or vice versa, is given by

$$B_k = \frac{\nu_t}{\sigma_t} \frac{g}{\rho h} \frac{\partial \rho}{\partial \sigma}.$$

Using equation (4.2) the dissipation of k in the k-L model is given by

$$\varepsilon = c_D \frac{k^{3/2}}{L} = c'_\mu c_D \frac{k^2}{\nu_t}.$$

As in the algebraic eddy viscosity model, the mixing length L is prescribed according to equation (4.5).

c) k-ε turbulence model

The most advanced eddy viscosity model implemented in TRISULA is the k-ε model. The eddy viscosity is expressed, see equation (4.3), in the quantities k and ε. The turbulent kinetic energy is given by equation (4.6). The dissipation ε is solved from a transport equation, which reads

$$\frac{\partial \varepsilon}{\partial t} + u \frac{\partial \varepsilon}{\partial x} + v \frac{\partial \varepsilon}{\partial y} + \frac{\omega}{h} \frac{\partial \varepsilon}{\partial \sigma} = D_\varepsilon + P_\varepsilon + B_\varepsilon - \varepsilon_\varepsilon, \tag{4.7}$$

where D_ε is the diffusion of ε, P_ε is the production of ε, B_ε is the buoyancy flux, and ε_ε is the destruction of ε.

The diffusion of ε is given by

$$D_\varepsilon = \frac{\partial}{\partial x} \left[\left(\nu + \frac{\nu_t}{\sigma_\varepsilon} \right) \frac{\partial \varepsilon}{\partial x} \right] + \frac{\partial}{\partial y} \left[\left(\nu + \frac{\nu_t}{\sigma_\varepsilon} \right) \frac{\partial \varepsilon}{\partial y} \right] + \frac{1}{h^2} \frac{\partial}{\partial \sigma} \left[\left(\nu + \frac{\nu_t}{\sigma_\varepsilon} \right) \frac{\partial \varepsilon}{\partial \sigma} \right],$$

where σ_ε is the turbulent Schmidt number for ε. The horizontal diffusion terms are kept in cartesian coordinates to avoid artificial creeping of ε along inclined σ-planes.

The production of ε is given by

$$P_\varepsilon = c_{1\varepsilon} \frac{\varepsilon}{k} P_k = c_\mu c_{1\varepsilon} \frac{k}{\nu_t} P_k,$$

where $c_{1\varepsilon}$ is a constant, and use has been made of equation (4.3).

The buoyancy flux is given by

$$B_\varepsilon = c_{1\varepsilon} \frac{\varepsilon}{k} (1 - c_{3\varepsilon}) B_k = \frac{c_\mu c_{1\varepsilon}}{\sigma_t} k (1 - c_{3\varepsilon}) \frac{g}{\rho h} \frac{\partial \rho}{\partial \sigma},$$

where $c_{3\varepsilon}$ is a constant, and use has been made of equation (4.3).

The destruction of ε is given by

$$\varepsilon_\varepsilon = c_{2\varepsilon} \frac{\varepsilon^2}{k},$$

where $c_{2\varepsilon}$ is a constant.

The constants, see Table 4.1, that occur in the standard k-ε model are determined from experiments with free turbulent flows, see Launder & Spalding (1974).

Table 4.1 Values of the empirical constants of the standard k-ε model.

c_μ	$c_{1\varepsilon}$	$c_{2\varepsilon}$	$c_{3\varepsilon}$	σ_k	σ_ε
0.09	1.44	1.92	1.0	1.0	1.3

SOLUTION TECHNIQUE

In TRISULA the computational domain is covered by a two-dimensional horizontal mesh of curvilinear orthogonal grids of variable size. Such a mesh makes possible a more accurate schematization of complicated irregular geometries and an increased computational efficiency. As in the horizontal mesh, the vertical grid may have a variable size (non-equidistant distribution of interfaces), which facilitates a more detailed reproduction of features in zones of particular interest, for example near the surface or the bottom. This is important to resolve

steep gradients near stratifications, the surface (heat exchange problems) and near the bottom (sediment transport).

The computational grid is staggered both in the horizontal and vertical planes, see Fig. 4.3. The time integration employs a two step method, which is a combination of a modified ADI-scheme for the depth-averaged continuity and momentum equations and a fully implicit scheme in the vertical for the momentum equations per layer.

In the first step the momentum equation in η-direction for all layers is solved to compute v in each layer, the depth-averaged momentum equation in ξ-direction and the depth-averaged continuity equation are solved to compute the water levels after which u and ω in each layer are computed from the momentum equation in ξ-direction and the continuity equation for each layer respectively. In the second step, the directions and velocity components are interchanged in the solution procedure.

The finite difference scheme for the velocity components per layer and the water level is of second order accuracy in space and time. The calculation of the vertical velocity ω is only first order accurate.

At the open boundaries, the following quantities can be imposed: a) water level, b) velocity profile, c) discharge, and d) the incoming Riemann-invariant, $\overline{u} + 2\sqrt{gh}$, where $\overline{u}$ is the depth-averaged velocity. Conditions a), b), and c) can be made weakly reflective.

At closed boundaries the velocity component perpendicular to the wall is zero. The law of the wall is applied for the velocity parallel to the boundary.
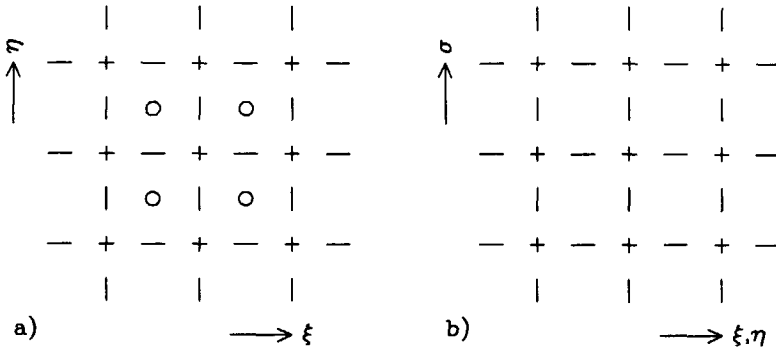
Figure 4.3 Computational grid of TRISULA: a) $+$ = ζ and c, $-$ = u, $|$ = v, and $\bigcirc$ = d; b) $+$ = c, $-$ = u or v, and $|$ = ω.

The turbulent kinetic energy and the dissipation are imposed in the bottom layer, according to $k = 3u_*^2$ and $\varepsilon = u_*^3/\kappa\Delta z_b$, where Δz_b is half the bottom layer thickness. In absence of wind the boundary conditions in the top layer are given by $\partial k/\partial\sigma = 0$ and $\partial\varepsilon/\partial\sigma = 0$. At open boundaries the turbulent kinetic energy and the dissipation are prescribed according to $k = -3\sigma u_*^2$ and $\varepsilon = \dfrac{c_\mu^{3/4}}{\kappa}\left(k_s^{3/2}/z_s - k_b^{3/2}/z_b\right)$, where k_s and k_b are the turbulent kinetic energies in the top and bottom layers, z_s is the distance to the water surface, and z_b is the distance to the bottom. At closed boundaries the same conditions are applied as at the bottom.

4.3 Results

Simulations of the depth-averaged flow pattern in a harbour were performed with the models DUCHESS and TRISULA. Simulations of the three-dimensional flow in a harbour were carried out with TRISULA. The flushing of a harbour basin is examined with ESTRA using flow fields computed with DUCHESS.

The computations with DUCHESS and ESTRA were performed prior to the experiments in the physical models, which were discussed in chapter 3. These computations were carried out mainly to get an impression of the flow and the transport of matter in the model harbours examined. The computations with TRISULA were carried out after the experiments in the physical models.

Only the flows in two harbour geometries were examined. The examined harbours are the square harbour with a surface area 1 m^2, that is model harbour 1 in chapter 3 (see Fig. 3.3), and the oblique harbour oriented at 45 degrees with the river and a surface area of 1 m^2, that is model harbour 4 in chapter 3. The flow and the transport of matter in the square harbour is studied with all three models, whereas the flow in the oblique harbour is only studied with TRISULA.

4.3.1 DUCHESS

The depth-averaged flow in a square harbour of 1 m^2, model harbour 1 in section 3.2, was computed (see also Langendoen, 1989). Because the computations were made prior to the experiments, some differences exist between the discharge in the river and the water depth in the physical and numerical models. The water depth in the computations equalled 0.10 m and the amplitude of the discharge in the flume was 50 ℓ/s ($\hat{u}$ = 0.50 m/s). In the experiments in the physical model the water depth was 0.11 m and the amplitude of the discharge in the flume was 42 ℓ/s ($\hat{u}$ = 0.37 m/s).

Eight runs have been made with DUCHESS in which the period, eddy viscosity, and grid size were varied to examine their influences on the computed flow in the harbour. The selected values of these parameters are listed in Table 4.2. The open boundaries in the flume, at 2 m from the centre-line of the harbour, were represented as velocity boundaries and were weakly reflective. The friction factor c_f was set at 0.004.

Table 4.2 Values of parameters in runs with DUCHESS.

	run 1	run 2	run 3	run 4	run 5	run 6	run 7	run 8
period [s]	500	500	500	500	250	375	750	500
eddy viscosity [m^2/s]	5E-4	1E-3	5E-3	$u_* h$ [1]	5E-4	5E-4	5E-4	5E-4
grid size [m]	0.10	0.10	0.10	0.10	0.10	0.10	0.10	0.05

INFLUENCE OF THE EDDY VISCOSITY

The influence of the eddy viscosity on the flow in the harbour is examined in runs 1 to 4.

---

[1] A so-called $u_* h$ formulation is used for this run.

According to calculations with a depth-averaged k-ε model and measurements in a physical model of the flow in a square harbour (surface area of 1 m^2, water depth 0.10 m, and velocity of the steady river-flow u_r equal to 0.5 m/s) by Booij (1991), the turbulence in the harbour is mainly generated in the mixing layer in the harbour entrance and convected into and through the harbour. A constant eddy viscosity can then be applied in depth-averaged flow computations. Booij (1991) determined that $\nu_t = 0.0014 u_r B_e$. This yields an eddy viscosity of 7.0E-4 m^2/s ($u_r = \hat{u} = 0.5$ m/s) for the simulation of the flow in model harbour 1.

Integrating equation (2.7) over the width of the harbour entrance, the average eddy viscosity in the mixing layer is

$$\overline{\nu}_t = 0.072 \beta' \lambda u_r B_e. \tag{4.8}$$

Substituting $\lambda = 0.67$ (that is $u_h = 0.2 u_r$), $u_r = 0.5$ m/s, and $\beta' = 0.015$ in equation (4.8), yields $\overline{\nu}_t = 3.6$E-4 m^2/s. The maximum eddy viscosity in the mixing layer, $\nu_{t,\text{max}} \simeq 2\overline{\nu}_t = 7.2$E-4 m^2/s, approximately equals the value obtained from Booij (1991).

The eddy viscosity is varied around 7.0E-4 m^2/s to determine its influence on the flow in the harbour. Spatially constant eddy viscosities of 5.0E-4 m^2/s, 1.0E-3 m^2/s, and 5.0E-3 m^2/s were used in runs 1 to 3. In run 4 the eddy viscosity was modelled via a $u_* h$ formulation. The depth-averaged eddy viscosity is $(0.1$ to $0.2) u_* h$ for bottom-generated turbulence (see Fischer et al., 1979). The constants in equation (4.1) then are $C_1 = 1.0$E-5 m^2/s to prevent that $\nu_t = 0$ when $q = 0$, $C_2 = 7.0$E-3, and $C_3 = 0$, which results in $\nu_t = 0.11 u_* h + 1.0$E-5 m^2/s. However, the influence of the mixing layer on ν_t is ignored in this way.

Fig. 4.4 shows the computed flow patterns in the harbour for runs 1 to 4 at $t = 175$ s, which is 50 s after maximum current. At this time the flow in the harbour is quasi-steady.

It is observed that the shape of the gyre and the water velocities in the gyre are almost the same for the constant eddy viscosities of 5.0E-4 m^2/s (Fig. 4.4.a) and 1.0E-3 m^2/s (Fig. 4.4.b).

For the constant eddy viscosity of 5.0E-3 m^2/s (Fig. 4.4.c) the velocities in the gyre are smaller. Also the shape of the gyre is different, and its centre is located more towards the downstream corner of the harbour entrance.
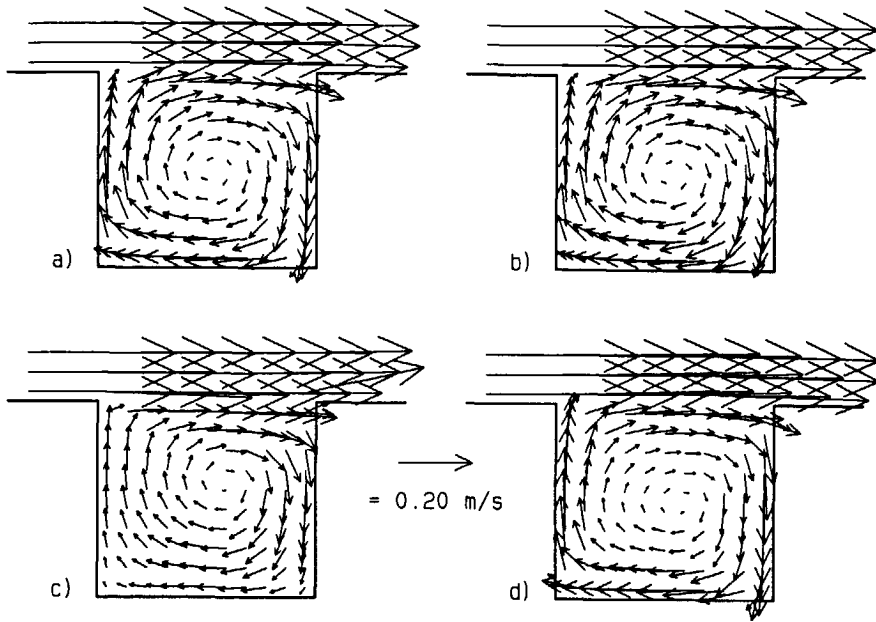
Figure 4.4   Influence of the eddy viscosity on the depth-averaged flow patterns in the harbour at $t = 175$ s: a) $\nu_t = 5.0$E-4 m^2/s, b) $\nu_t = 1.0$E-3 m^2/s, c) $\nu_t = 5.0$E-3 m^2/s, and d) $\nu_t = 0.11u_* h + 1.0$E-5 m^2/s.

For the $u_* h$ formulation, see Fig. 4.4.d, it is observed that the velocities in the grid points nearest to the perimeter of the harbour are much larger than in the other grid points in the harbour. Water that enters the harbour along its downstream sidewall does not spread much in transverse direction, which is caused by a small value of the eddy viscosity. The maximum eddy viscosity along the downstream sidewall is 1.5E-4 m^2/s, which is about three times as small as the eddy viscosity used in run 1. The shape of the gyre is about the same as in runs 1 and 2.

The flow patterns at $t = 325$ s (75 s after slack water) are shown in Fig. 4.5. For the smaller eddy viscosity, the distance that the centre of the gyre has travelled in the harbour is larger. The streamwise increase in width of the flow in the gyre is more rapid for larger eddy viscosities. Consequently the centre of the gyre is located more towards the downstream corner of the entrance for larger eddy viscosities, and the distance that the centre of the gyre has travelled is smaller.
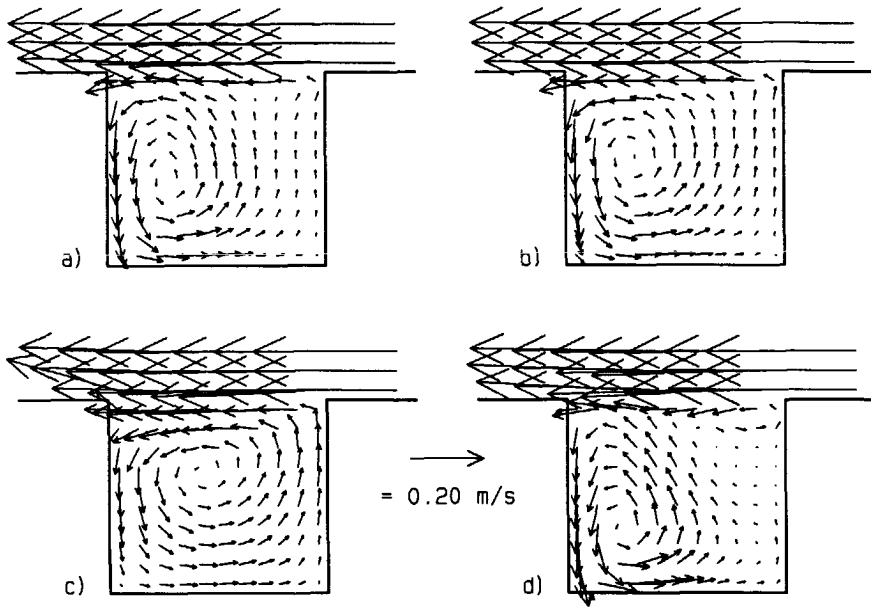
Figure 4.5 Influence of the eddy viscosity on the depth-averaged flow patterns in the harbour at $t = 325$ s: a) $\nu_t = 5.0\text{E-4}$ m^2/s, b) $\nu_t = 1.0\text{E-3}$ m^2/s, c) $\nu_t = 5.0\text{E-3}$ m^2/s, and d) $\nu_t = 0.11u_* h + 1.0\text{E-5}$ m^2/s.

The flow pattern for the $u_* h$ formulation, see Fig. 4.5.d, shows a small gyre near the upstream corner of the entrance, which is often observed in lid-driven cavity flow. Also the mixing layer is oscillating a little. This may be caused by too small values of the eddy viscosity.

From a qualitative comparison with measurements presented in the previous chapter (see Fig. 3.5) it can be concluded that too large an eddy viscosity predicts an incorrect evolution of the gyre after slack water. The position of the centre of the gyre is too close to the downstream sidewall of the harbour and the velocities in the gyre are too small.

Too small an eddy viscosity can give rise to instability of the mixing layer. The distance that the centre of the gyre travels in the harbour is too large.

The best results are obtained with an eddy viscosity based on the turbulence generated in the mixing layer.

INFLUENCE OF THE TIDAL PERIOD

The influence of the duration of the tidal period on the flow pattern in the harbour is examined by runs 1 ($T = 500$ s), 5 ($T = 250$ s), 6 ($T = 375$ s) and 7 ($T = 750$ s).

When the flow in the harbour is quasi-steady there is no difference between the flow patterns in these runs. This behaviour continues until slack water, see Langendoen (1989).

Fig. 4.6 shows the flow patterns at 50 s after slack water for $T = 250$ s and $T = 500$ s. It is observed that the development of the new gyre is faster for smaller tidal periods. This is in contrast with the experiments carried out in this harbour at the Delft University, experiments 1A ($T = 250$ s), 1B ($T = 500$ s), and 1C ($T = 1000$ s) discussed in section 3.2.1. In these experiments it was found that the development of the gyre did not depend on the tidal period.

Fig. 4.7 shows the flow patterns for runs 1, 5, 6, and 7 at equal phases of the tide, $t/T = 0.65$ (slack water occurs at $t/T = 0.5$). At this phase of the tide the new gyre is more developed for larger periods. The gyre has more time to adapt to the flow in the river for larger periods. Decreasing the tidal period T, that is the parameter $\hat{u}TB_e/B^2$ introduced in section 3.2, results in an increase of the phase difference between the developing flow of the gyre and the accelerating flow in the river. This agrees with the measurements of the depth-averaged flow discussed in section 3.2.1.

It can be concluded that the tidal period does not influence the flow in the harbour during
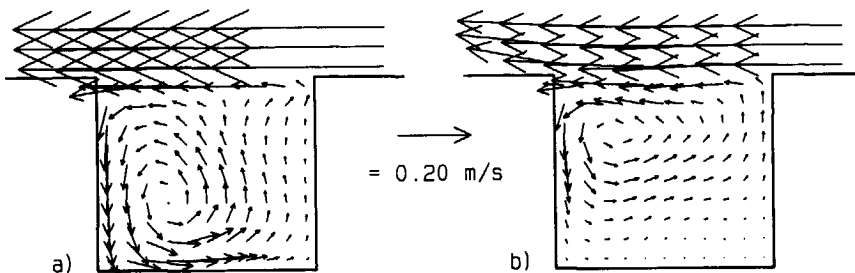
Figure 4.6 Influence of the tidal period on the depth-averaged flow patterns in the harbour at 50 s after slack water: a) $t = 175$ s, and $T = 250$ s; and b) $t = 300$ s, and $T = 500$ s.
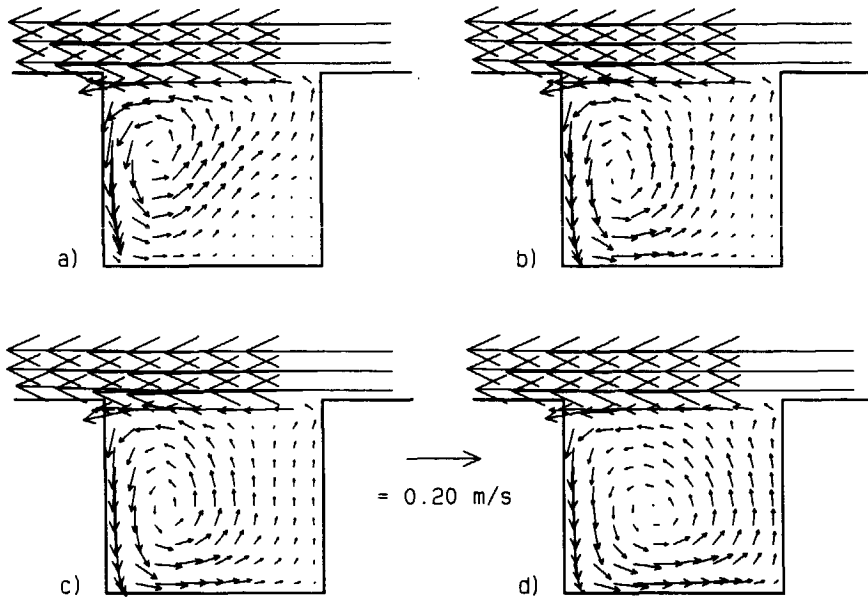
Figure 4.7 Influence of the tidal period on the depth-averaged flow patterns in the harbour at $t/T = 0.65$: a) $T = 250$ s, b) $T = 375$ s, c) $T = 500$ s, and d) $T = 750$ s.

maximum current if the gyre is fully developed. It can be attractive then to choose a smaller period to decrease the computational time. However, this leads to an incorrect phase difference between the developing gyre in the harbour and the flow in the river.

INFLUENCE OF THE GRID SIZE

The influence of the grid size on the flow pattern in the harbour is examined in runs 1 ($\Delta x = \Delta y = 0.10$ m) and 8 ($\Delta x = \Delta y = 0.05$ m).

Fig. 4.8 shows the flow patterns in the harbour at $t = 300$ s (50 s after slack water). It is observed that the development of the new gyre after slack water is faster for the finer grid (run 8, Fig. 4.8.b). Two reasons can be given. Firstly, the numerical dissipation for the finer grid is less than that of the coarse grid. Secondly, numerical viscosity is present at the
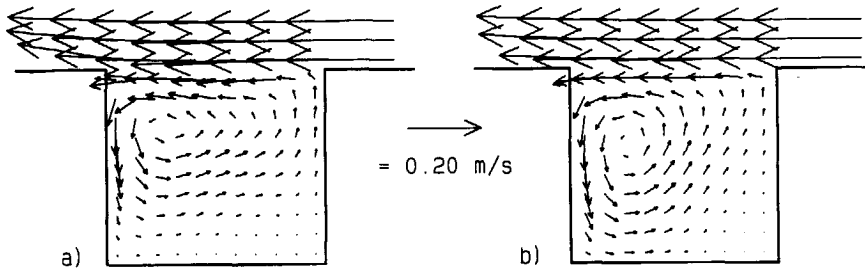
Figure 4.8 Influence of the grid size on the depth-averaged flow patterns in
the harbour at $t = 300$ s: a) $\Delta x = 0.10$ m, and b) $\Delta x = 0.05$ m.

boundaries. The numerical viscosity is larger for the coarser grid. Along the downstream
sidewall of the harbour the normal gradient of the velocity parallel to the wall is about as
large for the fine and coarse grid, see Fig. 4.8. The friction at the downstream sidewall of
the harbour then is larger for the coarse grid, consequently the development of the gyre is
retarded.

Comparing the computed flow patterns with the measured depth-averaged flow patterns (see
Fig. 3.5 in section 3.2.1 and Langendoen, 1989) it is concluded that the grid size of 0.10 m
is too coarse to predict accurately the time scales of the phenomena arising after slack water.

4.3.2 ESTRA

The flushing of the harbour is examined with the numerical model ESTRA. The flow field
of run 8 ($T = 500$ s, $\Delta x = 0.05$ m, and $\nu_t = 5.0\text{E-}4$ m^2/s) is used as input. The flow field
was written to disk every half second, which results in a time step to be used by ESTRA of
1.0 s.

At maximum current in the river, the harbour is instantly and uniformly filled with
a solute with a concentration of 50 g/m^3, and the changes in concentration in the river and
harbour are computed.

Two different formulations to model the dispersion have been considered, namely a constant

isotropic dispersion coefficient and a formulation with a variable, anisotropic dispersion coefficient.

Because the space discretizations are central differences, a dispersion coefficient, D_t, larger than 1.25E-2 m^2/s should be used —the cell Peclet number, $Pe_{\Delta x} = u\Delta x/D_t$, then is always lower than two— to suppress the oscillatory behaviour of the numerical scheme. Such a coefficient would lead to erroneously high dispersion. A dispersion coefficient of 5.0E-3 m^2/s is used, resulting in maximum Peclet numbers of 5 in the river and 2.5 in the mixing layer during maximum current in the river. So, only around maximum current some oscillations are generated in the mixing layer by the numerical scheme. This dispersion coefficient was applied both in the streamwise and transverse directions (isotropic dispersion). The results of the computation with this value are shown in Fig. 4.9.

When the flow in the harbour is quasi-steady, new water from the river enters the harbour at the downstream side of the harbour, and flows along the walls further into the
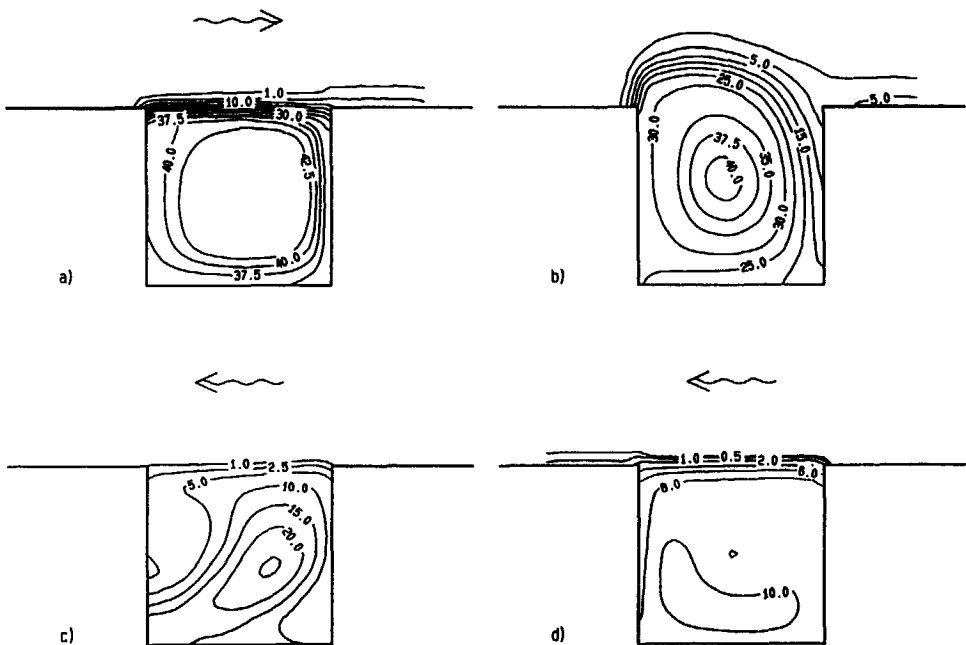
Figure 4.9 Isolines of concentration in g/m^3 (D_t = 5.0E-3 m^2/s): a) t = 175 s, b) t = 250 s (slack water), c) t = 300 s, and d) t = 375 s (maximum current).

harbour (see Fig. 4.9.a, $t = 175$ s). As a consequence of diffusion, the maximum concentration in the harbour has decreased from 50 g/m^3 at maximum current ($t = 125$ s) to 42.5 g/m^3.

During slack water, Fig. 4.9.b ($t = 250$ s), the cloud of solute is advected by the gyre into the river. At this time a large exchange between harbour and river occurs. The solute in the river is washed away by the accelerating river-flow, Fig. 4.9.c ($t = 300$ s). Fig. 4.9.c also shows the contours of the developing new gyre. Fig. 4.9.d ($t = 375$ s, maximum current) shows that new water enters the harbour again along the downstream sidewall of the harbour.

In the second formulation the dispersion is anisotropic. A velocity dependent dispersion coefficient is mostly expressed as: $D_t = \gamma u_* h$, where γ is a constant. For bottom-generated turbulence, the streamwise dispersion coefficient, as given by Elder (1959), is $D_t = 5.93 u_* h$. The transverse dispersion coefficient for bottom-generated turbulence is $0.15 u_* h$ (see Fischer et al., 1979). The cell Peclet number in this computation is approximately:

$$\mathrm{Pe}_{\Delta x} = \frac{u \Delta x}{D_t} \approx \frac{u \Delta x}{6 u_* h} \approx \frac{16 u \Delta x}{6 u h} = \frac{8 \Delta x}{3 h}.$$

For a grid size $\Delta x = 0.05$ m, and a water depth $h = 0.10$ m, $\mathrm{Pe}_{\Delta x}$ is 1.33. This value is less than 2, and hence the numerical solution does not oscillate. The results of the computation are shown in Fig. 4.10.

The dispersion of the solute is about the same as for the isotropic dispersion with $D_t = 5.0\mathrm{E}\text{-}3$ m^2/s. Only during slack water, Fig. 4.10.b, the maximum concentration in the harbour is somewhat smaller, 37.5 g/m^3 with respect to 40.0 g/m^3 in Fig. 4.9.b.

The transverse dispersion coefficient in the mixing layer is about 2.3E-4 m^2/s ($u \approx 0.25$ m/s) around maximum current, which is 22 times as small as that used in the isotropic dispersion formulation. It can be expected then that the decrease in concentration of the solute in the harbour, thus the exchange between harbour and river, is much smaller for the anisotropic dispersion formulation. However, this is not visible in Figures 4.9 and 4.10.

The exchange of matter between harbour and river is given by equation (3.2). In the case of a solute the normalized transport through the harbour entrance reads:
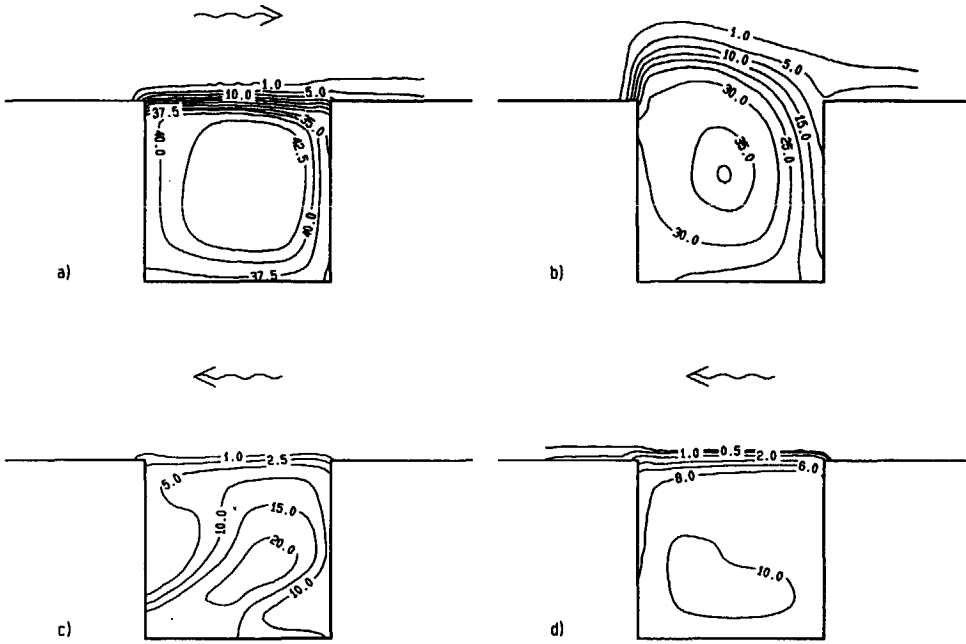
Figure 4.10 Isolines of concentration in g/m^3, anisotropic dispersion (γ = 0.15): a) t = 175 s, b) t = 250 s, c) t = 300 s, and d) t = 375 s.

$$\lambda = -\frac{V_h \dfrac{d\bar{c}}{dt}}{A_e \hat{u}\bar{c}},$$

where $\bar{c}$ is the volume-averaged concentration in the harbour.

Fig. 4.11 shows the computed and measured λ. It is observed that the transport through the harbour entrance for the isotropic dispersion formulation (D_t = 5.0E-3 m^2/s) is as large as for the anisotropic dispersion formulation with a transverse mixing coefficient D_t = 0.15u_*h. Around maximum current, t = 375 s, when diffusion governs the exchange process, the measured normalized rate of exchange between harbour and river is about three times the two computed normalized rates of exchange. Furthermore, during slack water (t = 250 s) the computed normalized transport is approximately 30 per cent too high.

During maximum current the flow in the river is parallel to the harbour entrance. As a consequence, the rate of exchange of matter between harbour and river then is determined
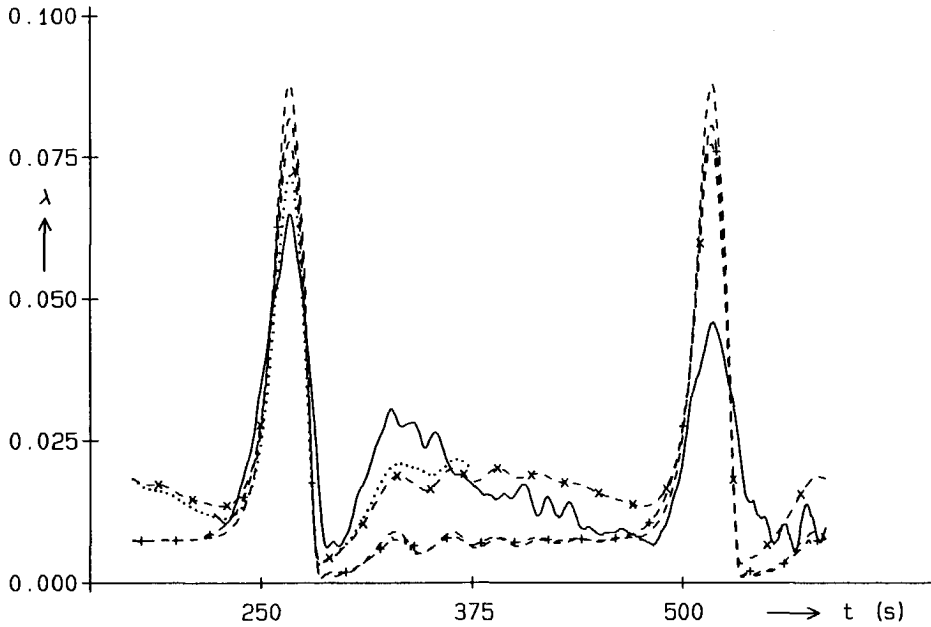
Figure 4.11 Normalized transport through the entrance: measured, ————; computed, — — — = isotropic dispersion (D_t = 5.0E-3 m²/s), -+-+- = anisotropic dispersion (γ = 0.15), -×-×- = anisotropic dispersion (γ = 1.0), and · · · · = anisotropic dispersion (γ = 1.0 and Δx = 0.025 m).

by the magnitude of the transverse dispersion coefficient. In case of the anisotropic dispersion formulation the transverse mixing coefficient $D_t = 0.15u_*h$ is based on bottom-generated turbulence, and is too small to describe the dispersion in a mixing layer. An analytical expression for the transverse dispersion coefficient in a shallow mixing layer is not known. Vertical variations of the water velocity and the concentration of the solute in the mixing layer can considerably enhance the transverse mixing. If the deviation of the velocity normal to the harbour entrance from the depth-averaged velocity is zero, then the transverse dispersion coefficient equals the diffusion coefficient given by equation (2.7), which results in $\gamma \approx 0.5$. The measurements, see Fig. 3.9 (section 3.2.2), only showed a small secondary flow in the mixing layer. Hence, taking γ = 1.0 yields a transverse dispersion coefficient $D_t = u_*h$, which results in a better agreement between computation and measurement during maximum current (see Fig. 4.11). During slack water (t = 250 s) the computed normalized transport agrees somewhat better with the measured normalized transport. This probably

results from a higher rate of exchange during maximum current.

However, the computed normalized transport is still 20 per cent too high at slack water ($t = 250$ s). During slack water the gyre has moved into the river and advects water from the harbour into the river, and guides river-water into the harbour through its rotation. Diffusion is less important at this moment. An improved prediction of the mean-velocity field in the harbour entrance should give better agreement between computation and measurement. Fig. 4.11 shows the result of a computation with a refined grid ($\Delta x = 0.025$ m) for slack water ($t = 250$ s). The computed normalized transport through the entrance is improved at both slack water and maximum current.

Figures 4.12.a and d show that the mixing layer is reproduced much better in the case of the refined grid (cf. Fig. 4.10). The spreading rate of the mixing layer is constant, whereas in Figures 4.9 and 4.10 the width of the mixing layer is constant. As a consequence, with the refined grid the normalized transport through the harbour entrance agrees better with the measured normalized transport at maximum current.
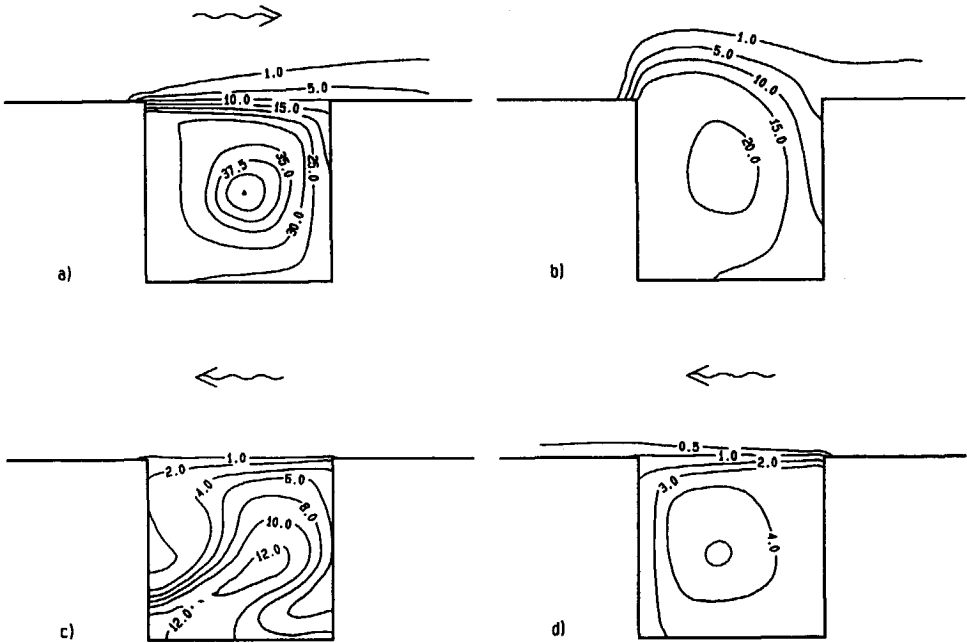
Figure 4.12 Isolines of concentration in g/m^3 ($\gamma = 1$ and $\Delta x = 0.025$ m):
a) $t = 175$ s, b) $t = 250$ s, c) $t = 300$ s, and d) $t = 375$ s.

4.3.3 TRISULA

Both the depth-averaged and the three-dimensional versions of TRISULA were used to compute the flow in the square harbour. The results are compared with the measured depth-averaged and local velocities.

The flow in the oblique harbour is computed with the depth-averaged version of TRISULA only.

THE DEPTH-AVERAGED FLOW

In the computations with DUCHESS it was found that the grid size highly influences the flow pattern in harbour 1, see Fig. 4.8. Hence, also with TRISULA the influence of the grid size on the flow in the harbour was examined. In view of the large number of grid points needed for the calculations of the three-dimensional flow in the harbour, the largest mesh sizes of the computational grid were determined for which the computed flow still agrees with the measured flow in harbour 1.

The harbour and a part of the river with a length of 5 m were schematized. The open boundaries were situated at 2.5 m from the centre-line of the harbour.

Runs were made with the equidistant computational grids used in DUCHESS, grid sizes of 0.10 m and 0.05 m respectively, and with a non-equidistant computational grid shown in Fig. 4.13, in which the grid sizes in the harbour varied between 0.05 m at the sidewalls and 0.075 m in the centre of the harbour. The grid sizes in the river varied between 0.05 m near the harbour sidewalls and 0.16 m at the open boundaries. The ratio between the grid sizes of two adjacent cells is maximally 1.1.

The number of grid points is 1071 (equidistant, $\Delta x = 0.10$ m), 4141 (equidistant, $\Delta x = 0.05$ m), and 1650 (non-equidistant). The number of grid points in the non-equidistant computational grid thus is reduced by a factor 2.5 when compared to the equidistant fine grid.

30

N

1
1   55

——> M
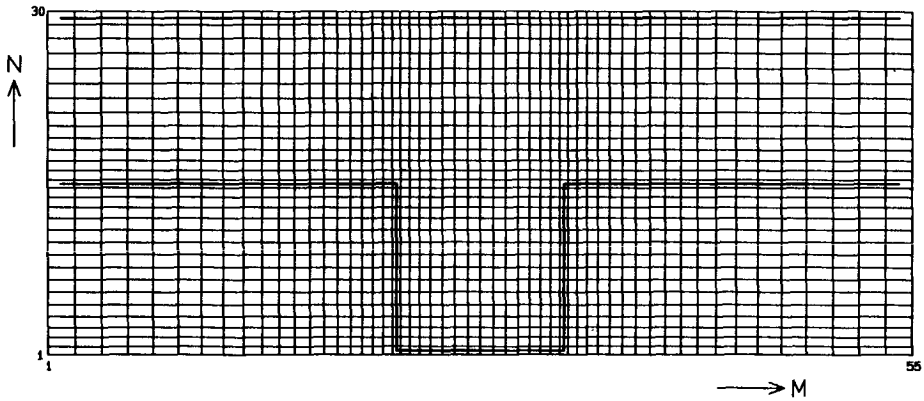
Figure 4.13 Non-equidistant computational grid used by TRISULA.

At the open boundaries a sinusoidal flow rate with an amplitude of 42 ℓ/s was imposed. The open boundaries were weakly reflective to suppress free oscillations initiated at the start of the computation. The water depth was 0.11 m. The eddy viscosity was constant in space and time, and had a value of 5.0E-4 m^2/s. The bed-friction coefficient c_f, determined from the measurements, was 0.005. At the closed boundaries a free-slip condition was imposed, that is $\partial u_{\parallel}/\partial n = 0$, where $u_{\parallel}$ is the velocity component parallel to the wall and n is the direction normal to the wall.

To obtain a quasi-steady solution in which the flow is periodic, it was necessary to compute two tidal cycles.

The results of the computations with the equidistant grids are not shown here. As in the computations with DUCHESS, it was observed that the development of the new gyre after slack water was faster for the finer grid. The computation with the non-equidistant grid produced the same flow in the harbour as that with the equidistant fine grid. Fig. 4.14 shows the computed and measured flow patterns in the harbour at various times. The measured flow patterns were determined from the experiments with floats, see section 3.2.1.

It is observed that the development of the new gyre after slack water is a little too slow. At $t = 310$ s, Fig. 4.14.b, the computed centre of the gyre has travelled a smaller distance than in the measurement. The computed velocity in the new gyre is too small at the initial stage of the development, see Fig. 4.14.a. From $t = 340$ s, Fig.4.14.c, the computed

MEASURED   COMPUTED

a)

b)

c)

≈ 0.15 m/s

d)
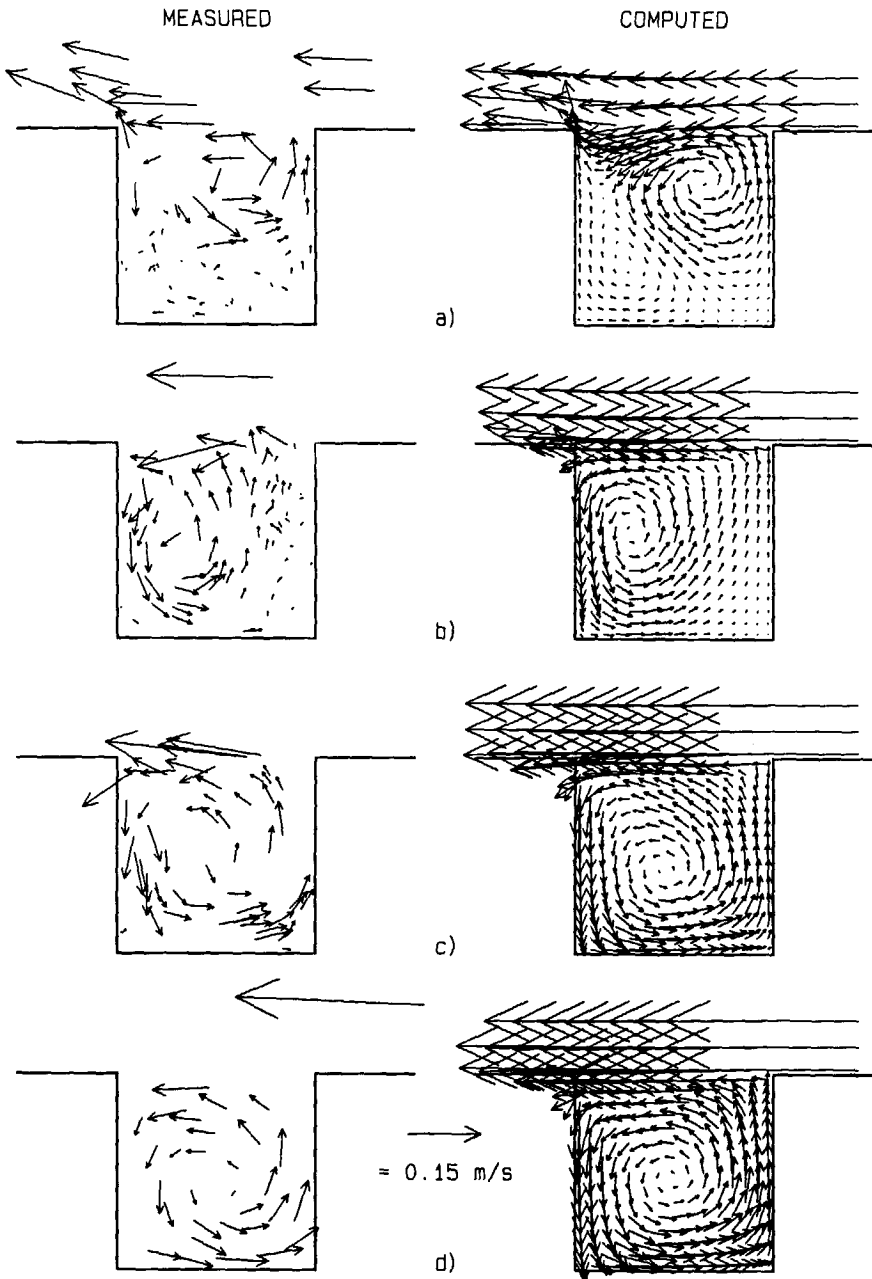
Figure 4.14 Measured and computed flow patterns in the harbour: a) $t = 280$ s, b) $t = 310$ s, c) $t = 340$ s, and d) $t = 375$ s.

location of the centre of the gyre is correct.

In Fig. 4.15 the computed velocities are compared with the measured velocities along two transects through the centre of the computed gyre parallel to the walls of the harbour. The measured depth-averaged velocities were determined from the vertical distribution of the velocities measured with the electromagnetic velocimeter.

The computed velocity profiles are seen to agree quite well with the measured velocity profiles. In the early stages of the development, Figures 4.15.a and b, some differences are present because the centres of the computed and the measured gyres do not have the same

Figure 4.15 Velocity profiles along two transects through the centre of the computed gyre: a) $t = 280$ s, b) $t = 310$ s, c) $t = 340$ s, and d) $t = 375$ s. Measured: + and ×. Computed: ——— (free slip).

location. As already observed in Fig. 4.14.a, the computed velocities in the core of the new
gyre are too small at $t = 280$ s.

Around maximum current, when the flow in the harbour is quasi-steady, the computed
velocities close to the harbour sidewalls are too large, because there is no friction at these
walls. Fig. 4.16 shows the velocity profiles in the harbour for a computation in which a
partial-slip condition is imposed at the closed boundaries. The predicted velocities near the
harbour sidewalls improve, especially during maximum current. However, the development
of the new gyre becomes much slower. Also, the computed velocities are too small during
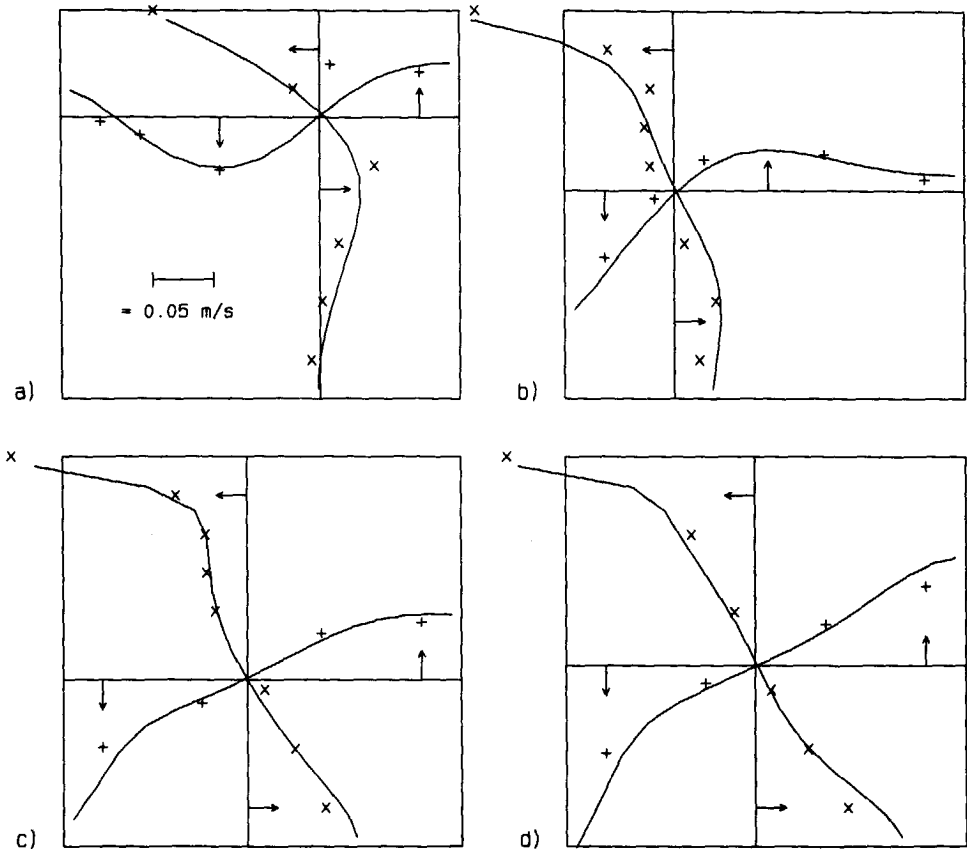the development of the gyre.
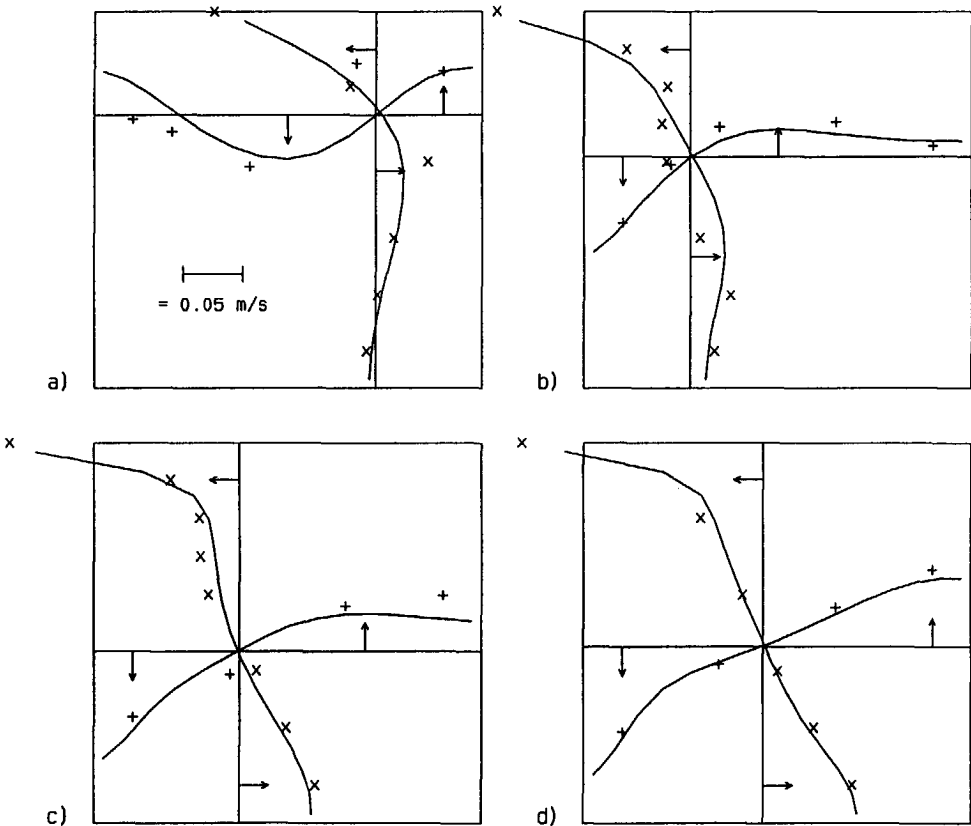
Figure 4.16 Velocity profiles along two transects through the centre of the
computed gyre: a) $t = 280$ s, b) $t = 310$ s, c) $t = 340$ s, and d) $t = 375$ s.
Measured: + and ×. Computed: ————— (partial slip).

The depth-averaged flow in harbour 1 is predicted well with TRISULA. As in computations with a steady river-flow along the harbour entrance (Booij, 1991), a spatially constant eddy viscosity can be applied to compute the flow in a harbour on a tidal river without variations in water level, provided that the harbour is covered by a mesh with a sufficient resolution (about 20×20 grid points). The mesh size of the computational grid is important to calculate the correct time scales of the phenomena after slack water. The time scales of the phenomena that occur after slack water also depend on the friction at the sidewalls.

In the laboratory experiments at the Delft University of Technology a quite different behaviour of the flow in the oblique harbour (model harbour 4) was observed during both maximum currents, see Fig. 3.8 in section 3.2.1. The orientation of the harbour with respect to the flow direction in the river influences the size of the gyre and the water velocities in the gyre. A small angle between the downstream wall of the entrance and the river was found to imply large velocities and a large size of the gyre.

It is examined whether TRISULA is able to predict this different behaviour of the flow in the harbour. The representation of the sidewalls of the harbour needs special attention because the harbour is oriented at 45 degrees with the river. Two computational grids are used: 1) a rectilinear equidistant grid in which the sidewalls of the harbour are represented as "steps" (see Fig. 4.17.a), and 2) a curvilinear non-equidistant grid in which the sidewalls of the harbour are represented as straight lines (see Fig. 4.17.b), except near the corners of the harbour entrance. The eddy viscosity in the computations equalled 5.0E-4 m^2/s.

The computed flows in the harbour during both maximum currents are shown in Fig. 4.18 for both computational grids. They are compared with the measured depth-averaged flows at these times.

At both times the length of the gyre is too small for the rectilinear grid. The representation of the sidewalls of the harbour provides an additional roughness. The friction at the sidewalls of the harbour is then too large to compute the correct flow in the harbour. This is shown by the computation in which a curvilinear grid was used. The lengths of the gyres are much larger because no shear stress is exerted on the fluid at the sidewalls of the harbour.
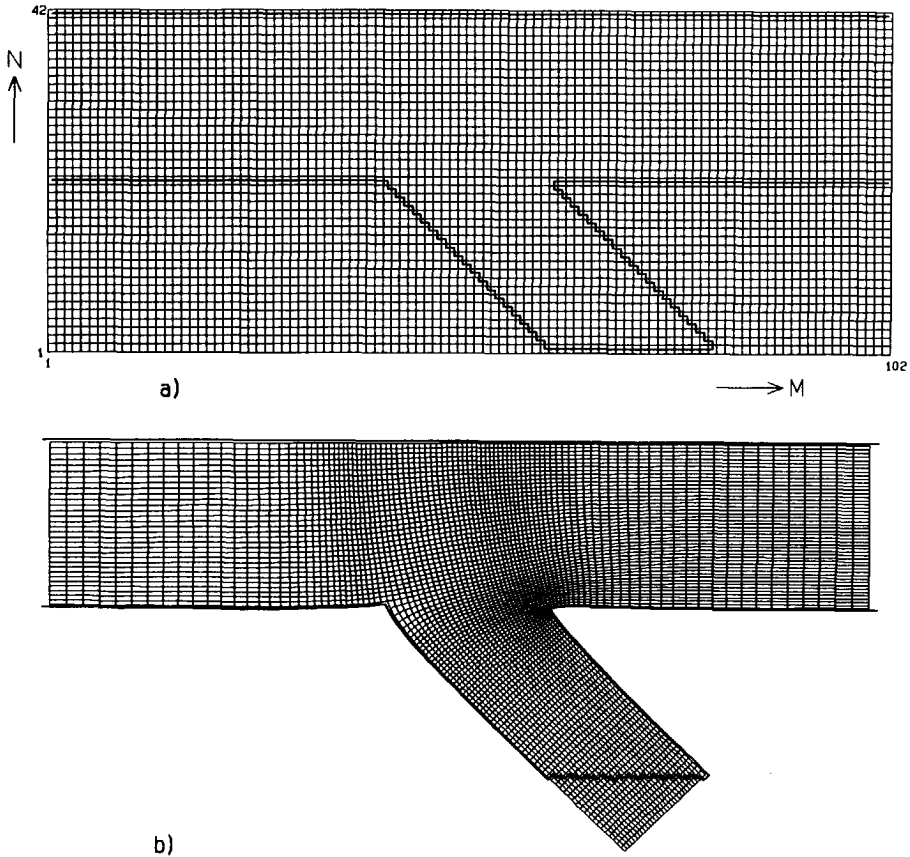
Figure 4.17 Computational grids for the oblique harbour: a) rectilinear equidistant grid, and b) curvilinear non-equidistant grid.

However, at $t = 375$ s the length of the gyre is largely overpredicted with the curvilinear grid, which is caused by the geometry of the downstream corner of the entrance. The flow in the harbour is highly influenced by the orientation of the harbour. A small angle between the downstream sidewall of the entrance and the river was found to imply larger velocities in the gyre and a larger length of the gyre. The angle between the downstream sidewall of the entrance and the river is smaller than 135 degrees, because otherwise the computational grid would not be orthogonal. Consequently, the length of the computed gyre is larger than that of the measured gyre. At $t = 375$ s the water velocities in the gyre are too large, whereas at $t = 125$ s they agree well with the measured velocities in the gyre.
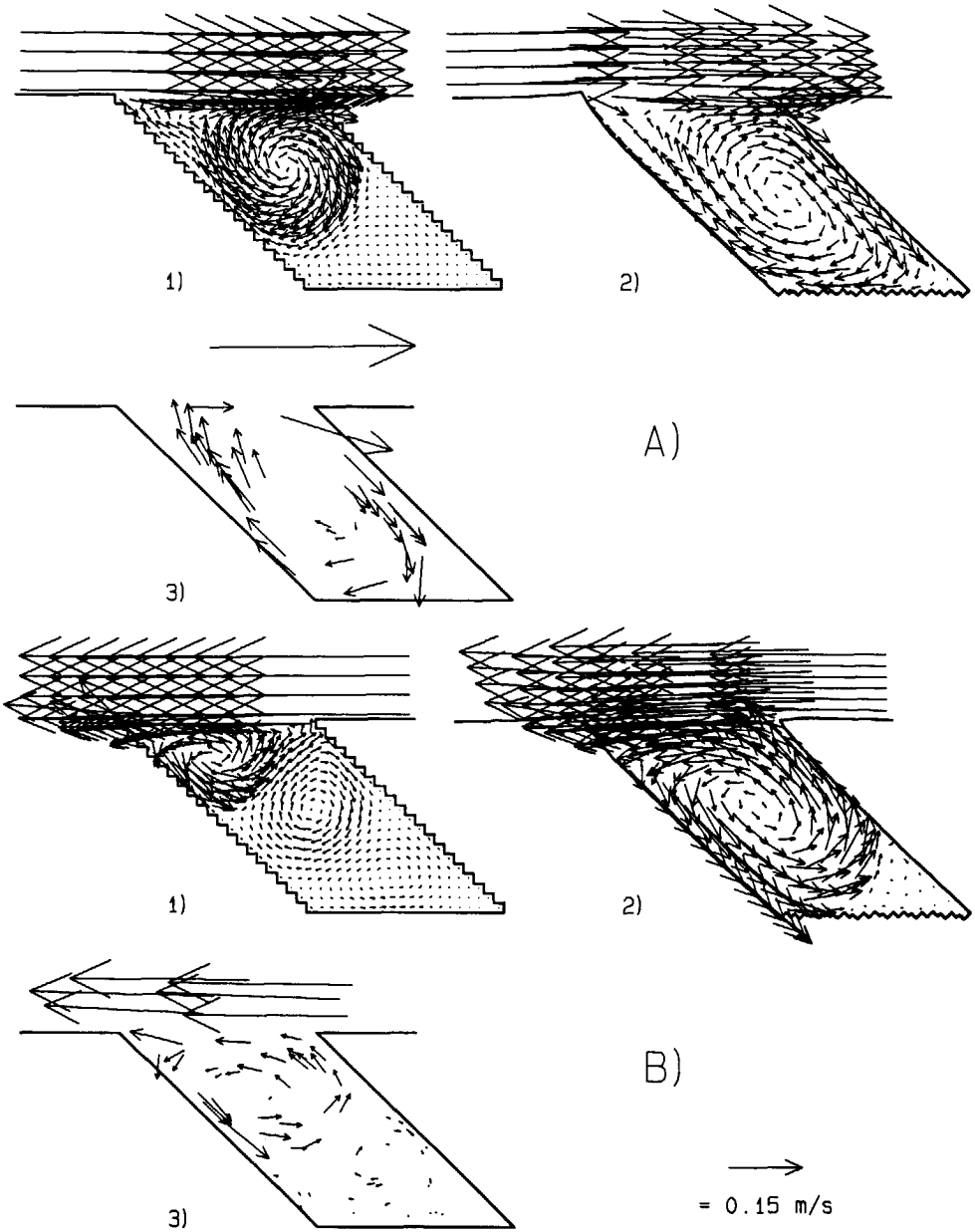
Figure 4.18 Flow patterns in harbour 4 at A) $t = 125$ s and B) $t = 375$ s: 1) computed (rectilinear grid), 2) computed (curvilinear grid), and 3) measured.

THE THREE-DIMENSIONAL FLOW

The flow in the harbour is three-dimensional, as is shown by the measurements discussed in section 3.2.2 (see Figures 3.9 to 3.14). This is important for the siltation of harbour basins. For example, suspended cohesive and non-cohesive sediments, which are transported from the river to the harbour, spiral down to the centre of the gyre and deposit at that location due to the small velocities. Consequently, a continuous siltation of the harbour ensues because the flow in the harbour is not able to erode the deposited sediment.

As opposed to the computations of the depth-averaged flow, the computations of the three-dimensional flow are strongly influenced by the modelling of the turbulence. As discussed in section 4.2.3 three turbulence models are available in the DH-version of TRISULA. All three models were used to simulate the 3-D flow in the harbour. Results of two of these models are presented here.

a) algebraic eddy viscosity model

Computations with spatially constant horizontal and vertical eddy viscosities, and with a variable vertical eddy viscosity were carried out. The horizontal non-equidistant computational grid in these computations was the same as the one used in the computations of the depth-averaged flow in the harbour, see Fig. 4.13. The vertical resolution was five layers. At the open boundaries the flow rate is imposed, and the velocity profile is logarithmic. At the closed boundaries a free-slip condition is applied. For a rough bottom the measured roughness height according to Nikuradse, k_N, equals 4.05E-3 m, which in the depth of 0.11 m is equivalent with a bed-friction coefficient, c_f, of 0.005.

The horizontal eddy viscosity, ν_t^h, is 5.0E-4 m^2/s in all computations. As was shown above (Figures 4.14 to 4.16), this value resulted in computed depth-averaged velocities that agree with the measured depth-averaged velocities. It can be expected that such a value of the horizontal eddy viscosity also yields local velocities in the three-dimensional computations that agree with the magnitudes of the measured local velocities.

The spatially constant vertical eddy viscosity, ν_t^v, is varied from 5.0E-4 m^2/s to 1.0E-4 m^2/s. The results of the computation with an isotropic eddy viscosity of 5.0E-4 m^2/s

are shown in Figures 4.19.a and b at 0.0935 m and 0.044 m above the bottom during maximum current ($t = 375$ s). The magnitudes of the water velocities in the gyre agree with those measured (cf. Fig. 3.9). However, the computed flow patterns at these levels are approximately identical. The secondary current and the larger velocities near the bottom along the downstream sidewall of the harbour are suppressed because the vertical eddy viscosity is too large.

The occurrence of relatively high velocities near the bottom along the downstream sidewall of the harbour during maximum current is better predicted with a vertical eddy viscosity of 1.0E-4 m²/s. The computed velocity of the secondary current is still too small compared to that measured. However, the flow did not become quasi-steady around maximum current, see Figures 4.20.a and b ($t = 405$ s). There is too little friction between the layers in the numerical model. As a result, high-momentum fluid that is entering the harbour near the bottom along its downstream sidewall is hardly affected by the surrounding fluid.

A similar result as was shown in Fig. 4.20, is obtained with an variable vertical eddy viscosity. The eddy viscosity calculated by equations (4.2), (4.4) and (4.5) depends on the local friction velocity at the bottom. As a result, the eddy viscosity in the harbour is small, maximally about 7.5E-5 m²/s, because of the small water velocities in the gyre.

The use of more advanced eddy viscosity models, which include the advection of the turbulence generated in the mixing layer, is necessary.
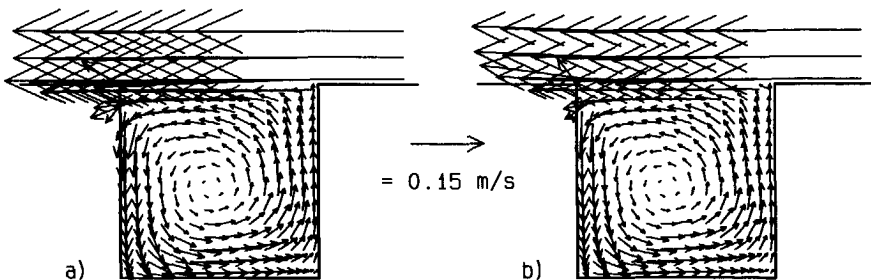
Figure 4.19 Computed flow patterns at $t = 375$ s, $\nu_t^h = \nu_t^v = 5.0E\text{-}4$ m²/s: a) 0.0935 m, and b) 0.044 m above the bottom, respectively.
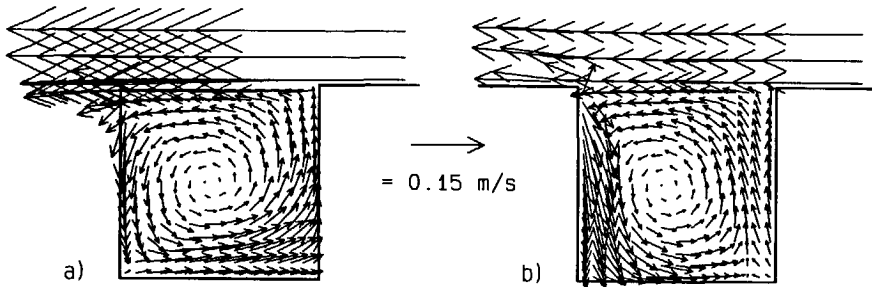
Figure 4.20 Computed flow patterns at $t = 405$ s, $\nu_t^h = 5.0E\text{-}4$ m²/s and $\nu_t^v = 1.0E\text{-}4$ m²/s: a) 0.0935 m, and b) 0.044 m above the bottom, respectively.

b) *k-L* turbulence model

The results obtained with the *k-L* model described in section 4.2.3 were not satisfactory, and are not presented here. No attempts were made to improve the results.

c) *k-ε* turbulence model in DH-version of TRISULA

A computation with the *k-ε* model described in section 4.2.3 was carried out, initially on the same grid as was used above. The flow in the harbour was poorly represented compared with the results obtained from the measurements. This was ascribed to too coarse a grid. The turbulent kinetic energy is produced in the mixing layer at the transition from harbour to river and transported into the harbour along its downstream sidewall. This requires an accurate approximation of the gradients of velocity and turbulent kinetic energy. For this reason a refined non-equidistant grid (7410 points, of which 1681 in the harbour) was used. The mesh sizes in the harbour varied from 0.02 m at the walls and the transition from harbour to river to 0.03 m at the centre of the harbour. The mesh sizes in the river varied from 0.02 m near the harbour to 0.07 m at the open boundaries.

It turned out that the flow in the harbour computed with the *k-ε* model was highly influenced by the boundary conditions of k and ε at the harbour sidewalls. A computation was carried out with the standard set of boundary conditions which is implemented in the DH-version of TRISULA ($k = 3u_*^2$ and $\varepsilon = u_*^3/\kappa\Delta n$, where Δn is the distance normal to the closed

boundary), see model c) in Table 4.3.

Table 4.3 Runs carried out with the k-ε model.

model	Boundary Conditions	
	k	ε
c)	$k = 3u_*^2$	$\varepsilon = u_*^3/\kappa\Delta n$
d)	$\partial k/\partial n = 0$	$\partial\varepsilon/\partial n = 0$
e)	$\partial k/\partial n = 0$	$\varepsilon = c_D k^{3/2}/\kappa\Delta n$

The results of the computation with model c) showed that the computed water velocities close to the harbour sidewalls around maximum current in the river are much larger than those measured, see Fig. 4.21.a. Furthermore, the computed turbulent kinetic energies in the boundary grid points in the harbour are small (about 0.0005 m²/s² along the downstream harbour sidewall), while in the grid points next to the boundary grid points k is much larger (about 0.01 m²/s²). At the boundary k is determined by the shear velocity, which is small. In a grid point next to a boundary point k is determined by the turbulence generated in the mixing layer, which is much larger than the turbulence generated at the harbour sidewalls. Because k and ε at closed boundaries only depend on the local friction velocity, the turbulence generated in the mixing layer does not extend to the sidewalls of the harbour.

Also the computed k, ε and ν_t (about 0.01 m²/s², 0.01 m²/s³ and 0.0017 m²/s) in the mixing layer are much higher than those based on a local equilibrium between production and dissipation of k ($k \approx 0.0025$ m²/s², $\varepsilon \approx 0.001$ m²/s³ and $\nu_t \approx 0.0005$ m²/s).

Ergo, the boundary conditions used in model c) are not suited to compute the flow, the turbulent kinetic energy and its dissipation in this harbour.

d) modified k-ε model I

In view of the conclusion above alternative sets of boundary conditions were implemented by the writer, yielding models d) and e), to obtain better results with the k-ε model. In model
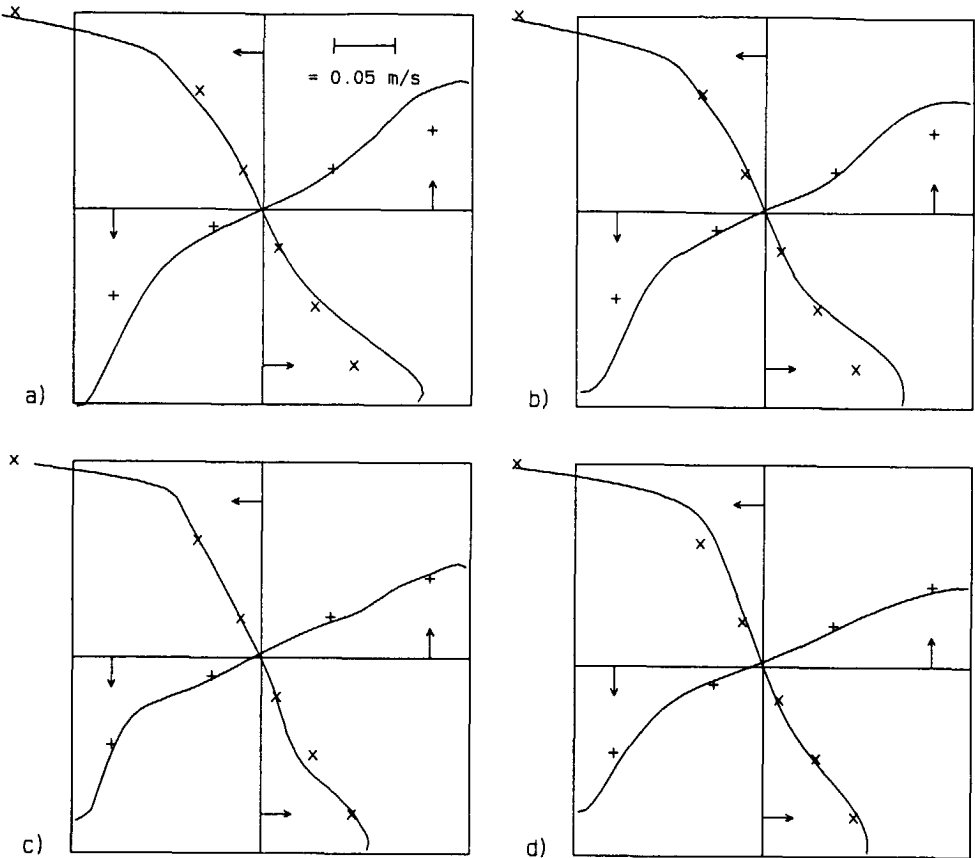
Figure 4.21 Profiles of depth-averaged velocities along two transects through the centre of the computed gyre at maximum current ($t = 375$ s). Measured: + and ×. ———— = computed: a) model c), b) model d), c) model e), and d) mixing-length model (ten layers).

d), see Table 4.3, k and ε were computed in the boundary points to enable the turbulence generated in the mixing layer to extend to the sidewalls of the harbour. The imposed boundary conditions were that the gradients of k and ε normal to the wall are zero. For k this boundary condition is correct if the boundary point is located in the log law region of the wall boundary layer. The boundary condition for the dissipation is incorrect, because the dissipation shows a hyperbolic dependence on the distance from the wall. Consequently, the gradient of the viscosity normal to the wall is also zero according to equation (4.3). As a

result, the eddy viscosity in vertical direction, ν_t^v, will be too large at the closed boundaries.

During the quasi-steady phase of the tide the large vertical eddy viscosity at the boundary suppresses the secondary current and the larger velocities near the bottom along the downstream sidewall of the harbour, see Fig. 4.22. Furthermore, the velocities near the sidewalls of the harbour are still too large, see Fig. 4.21.b.

In model d) the length scale of the turbulence along the sidewalls of the harbour is incorrect. Because both k and ε are mainly determined by the turbulence generated in the mixing layer, the length scale is approximately the width of the mixing layer, and consequently is too large in the regions near the walls. The gradient of L normal to the sidewall of the harbour in model d) is also zero, because it is only a function of k and ε. Strictly, the mixing length must go to zero at the sidewall of the harbour, as a consequence of which the eddy viscosity will go to zero at the wall.

e) modified k-ε model II

To overcome the problems of models c) and d) noted above, TRISULA was modified to compute the turbulent kinetic energy from a transport equation and the mixing length is prescribed in the boundary grid points as $L = \kappa \Delta n$, see model e) in Table 4.3. This yields a Dirichlet type boundary condition for the dissipation of k: $\varepsilon = c_D k^{3/2}/\kappa \Delta n$.

The results of this computation are shown in Figures 4.21.c and 4.22. The computed depth-averaged velocities in the harbour agree very well with the measured depth-averaged velocities. However, as in models c) and d), the vertical distribution of the velocity is not well predicted. Fig. 4.22 shows that the high-momentum fluid that flows into the harbour along the bottom remains closer to the sidewalls of the harbour in the computations. The computed velocity of the secondary flow is too small. Also the velocities near the bottom are too small.

It is clear that the best results are obtained with the boundary conditions used in model e). The boundary conditions of model c) that are usually used with k-ε models are not adequate here. The boundary conditions of model c) can be derived from those of model e) by assuming that at the boundary the production of turbulent kinetic energy is in equilibrium with its dissipation. Therefore, the inclusion of transport of turbulent kinetic energy at the
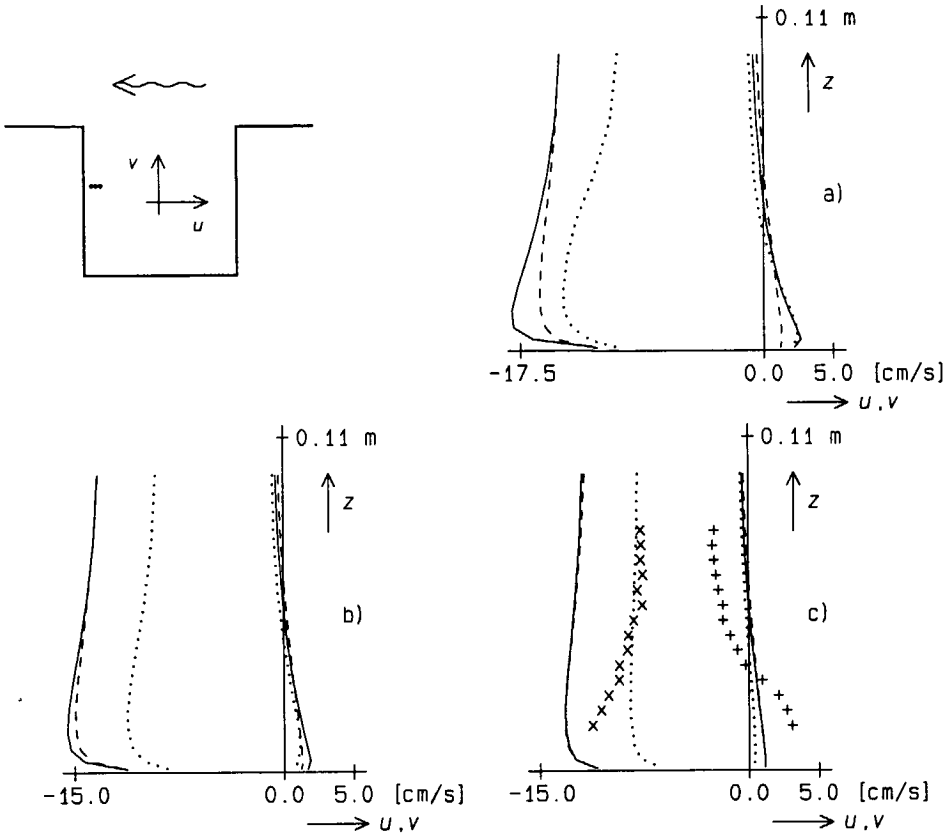
Figure 4.22 Vertical distributions of the horizontal velocity components at maximum current (t = 375 s), 0.4 m into the harbour and varying distance from the downstream harbour sidewall: a) 0.06 m, b) 0.08 m, and c) 0.10 m. Measured: + = u and × = v. Computed: ———— = model c), – – – = model d), and $\cdots$ = model e).

boundary points in the harbour, in particular those near the stagnation point, is necessary.

The k-ε model, however, has the disadvantage that the computation time required for one run is very long. Two tidal cycles have to be simulated to obtain a periodic flow in the harbour, which takes about 50 hours on a CRAY YMP. The time and costs required to study the influence of different harbour geometries, boundary conditions, and model parameters on the siltation of harbour basins then are too large for the k-ε model. A turbulence model is needed

that gives reasonable computation times (a few hours) on work stations.

f) Mixing-length model

A relatively simple turbulence model which is classified as an algebraic eddy viscosity model, is the so-called mixing-length model. The advantage of an algebraic turbulence model is that no differential equations have to be solved to determine the eddy viscosity. The mixing-length model was not discussed in section 4.2.3 because it is not routinely implemented in TRISULA. The mixing-length model is based on the assumption that locally in the flow field an equilibrium exists between the production and the dissipation of turbulent kinetic energy. Equation (4.6) then reduces to $P_k = \varepsilon_k$, or

$$\frac{1}{2} \nu_t \left[\frac{\partial u_i}{\partial x_j} + \frac{\partial u_j}{\partial x_i} \right]^2 = \varepsilon = C_D \frac{k^{3/2}}{L}. \qquad (4.9)$$

The turbulent kinetic energy k can be eliminated by using the expression $\nu_t = c'_\mu \sqrt{k} \, L$. The eddy viscosity then reads:

$$\nu_t = L^2 \left\{ \frac{1}{2} \left[\frac{\partial u_i}{\partial x_j} + \frac{\partial u_j}{\partial x_i} \right]^2 \right\}^{1/2} .$$

The mixing length L is given by equation (4.5).

Four computations with the mixing-length model were carried out, see Table 4.4. The vertical eddy viscosity, ν_t^v, is computed by the mixing-length model in all four runs. The horizontal eddy viscosity, ν_t^h, is constant in runs 1 through 3 (5.0E-4 m^2/s), and is computed by the mixing-length model, assuming isotropy, in run 4.

In runs 1 and 2 only the vertical gradients of the velocity components were implemented in the production term in equation (4.9), in runs 3 and 4 the complete production term was calculated.

The influence of the vertical resolution of the grid was examined by varying the number of layers. The number of layers is five in runs 1 and 4, and ten in runs 2 and 3. The interfaces are not equidistant. Near the bottom the layer thickness is smaller than near the surface. The layer widths in runs 1 and 4 are (from top to bottom): 30, 30, 20, 12, and 8

per cent of the water depth, respectively. The layer widths in runs 2 and 3 are (from top to bottom): 15, 15, 14, 14, 12, 10, 8, 6, 4, and 2 per cent of the water depth, respectively.

Table 4.4 Runs carried out with the mixing length model.

	ν_t^h in [m^2/s]	Velocity gradients in production term	Number of layers
run 1	5.0E-4	only $\partial/\partial z$	5
run 2	5.0E-4	only $\partial/\partial z$	10
run 3	5.0E-4	all	10
run 4	$\nu_t^h = \nu_t^v$	all	5

In the mixing-length model the positions of the vertical eddy viscosity in the vertical computational grid differ from those in the turbulence models implemented in TRISULA. In the DH-version of TRISULA used in this study both the horizontal and the vertical eddy viscosities are computed in a constituent point (see Fig. 4.3), which is at the same level (half-way two sigma planes) as the points of the horizontal velocity components. The vertical diffusion terms are approximated by central differences so that interpolation between two viscosities is needed. In the mixing-length model the vertical eddy viscosity is computed half-way the velocity points, that is at the sigma planes. No interpolation of the viscosities for this level then is needed. Also the discretization of the vertical gradients in the production term is more accurate, because the vertical distance between two velocity points is smaller.

When using the mixing-length model in TRISULA the velocities from three layers are necessary to determine the vertical diffusion, while with the k-L or k-ε model the velocities from five layers are necessary to determine the vertical diffusion terms.

The computed flows in the harbour for runs 1 to 3 differ only little. The depth-averaged flow patterns are identical. Differences are observed in the vertical distribution of the velocity. Fig. 4.23 shows the measured (electromagnetic velocimeter) and the computed depth-
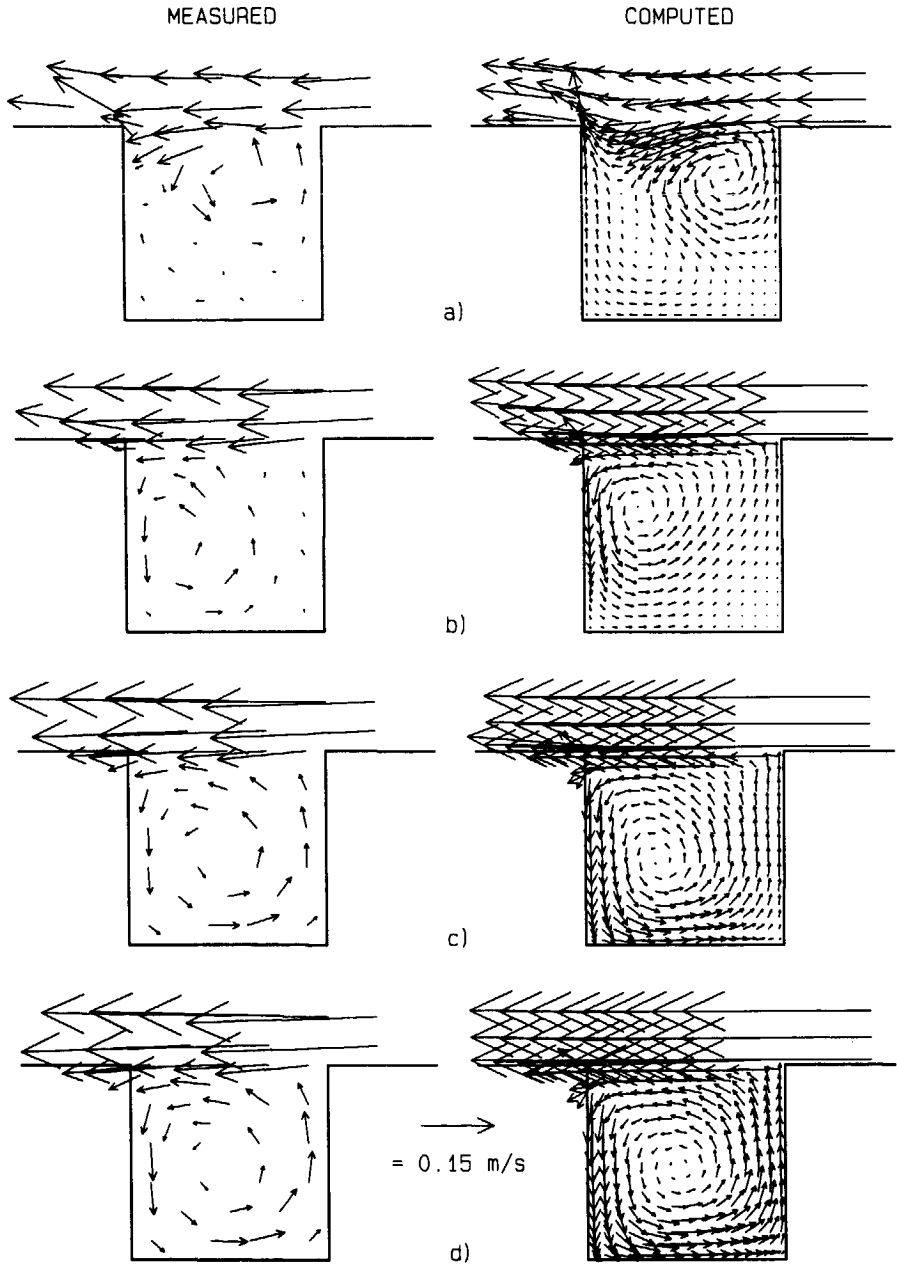
Figure 4.23 Measured and computed depth-averaged flow patterns in the harbour (run 3): a) $t = 280$ s, b) $t = 310$ s, c) $t = 340$ s, and d) $t = 375$ s.

averaged flow (run 3) in the harbour. As in the computations of the depth-averaged flow the development of the gyre is too slow. At $t = 340$ s the measured and the computed centres have almost the same location. Around maximum current the measured and the computed flows agree quite well.

The three-dimensional nature of the flow is shown in Fig. 4.24. The flow patterns of run 2 at maximum current ($t = 375$ s) are plotted at eight levels above the bottom. It is observed, except at the back wall of the harbour, that the flow near the bottom is directed towards the centre of the gyre, whereas the flow near the surface is directed towards the sidewalls of the harbour. Also, along the downstream sidewall of the harbour the velocities near the bottom are larger than those near the surface. These phenomena were also observed in the physical model experiments. However, in these experiments a secondary current existed at the back wall of the harbour, see Fig. 3.9, which is not found in the computations.

The magnitudes of the measured and the computed velocities at $t = 375$ s are compared at 0.015 m, 0.04 m, 0.06 m and 0.08 m above the bottom along two transects through the computed centre of the gyre of run 2, see Fig. 4.25. Generally, the velocities are predicted well. The computed width of the mixing layer is a little too small, and along the upstream sidewall of the harbour the velocities in the upper section of the water column are slightly underpredicted.

The vertical distributions of the horizontal velocity components of the four runs in a vertical at 0.4 m from the transition from harbour to river and 0.1 m from the harbour sidewall are shown in Fig. 4.26 for $t = 375$ s (maximum current). They are compared with the measured velocities in the gyre in the case of a steady river-flow (cf. Fig. 3.10).

The distributions of the velocities are the same for runs 1 (five layers) and 2 (ten layers). The solution does not depend on the number of layers.

Although the depth-averaged flows for runs 2 and 3 were similar, differences exist between the vertical distributions of the velocities. The eddy viscosities predicted in run 3 are somewhat larger than those in run 2, because all the gradients of the velocities are included in the determination of the production of turbulent kinetic energy. As a result, the velocity variations are less pronounced.
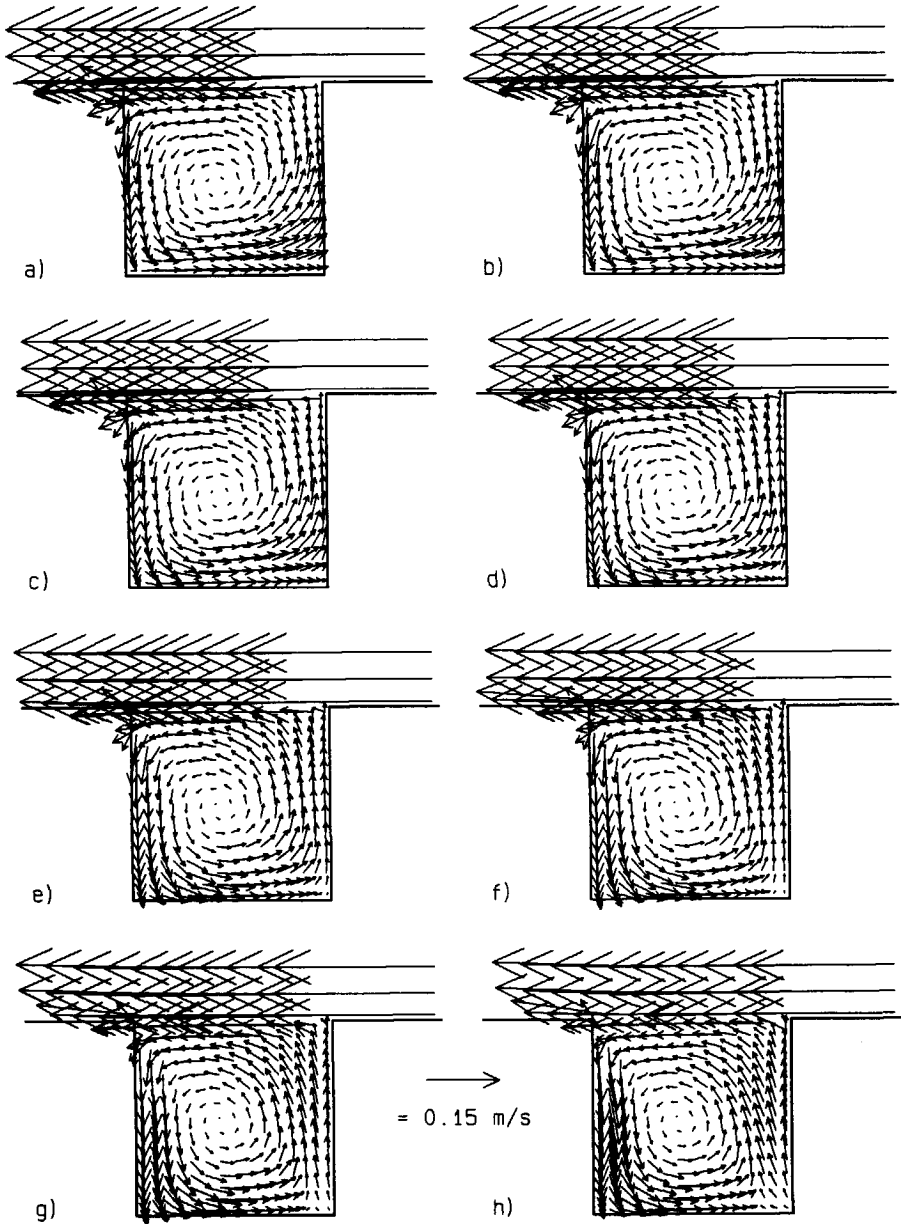
Figure 4.24 The calculated flow patterns at maximum current ($t = 375$ s) at various levels above the bottom (run 2): a) 0.10 m, b) 0.085 m, c) 0.069 m, d) 0.054 m, e) 0.04 m, f) 0.028 m, g) 0.018 m, and h) 0.01 m.
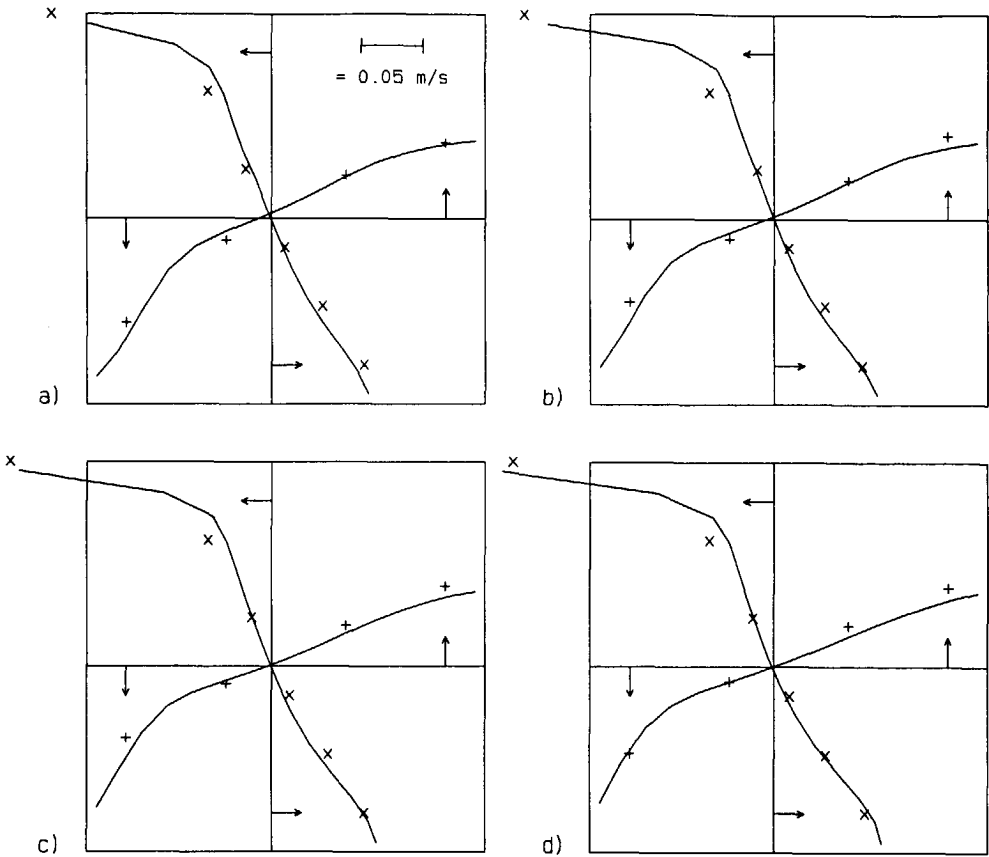
Figure 4.25 Velocity profiles along two transects through the computed centre of the gyre at maximum current ($t = 375$ s): a) 0.015 m, b) 0.04 m, c) 0.06 m, and d) 0.08 m above the bottom, respectively. Measured: + and ×. Computed: —————— (run 2).

Comparing the computed distributions of runs 1 to 3 with the measured distributions, it is observed that the velocity component parallel to the wall is predicted reasonably well (only near the bottom it is too small), but that the velocity component normal to the wall is underpredicted considerably.

Run 4 (isotropic viscosity) predicts larger velocities at this location than the other three runs. However, as is shown in Fig. 4.27, the gyre in the harbour behaves quite differently when compared to the measured flow and the flows computed in runs 1 to 3 (cf.
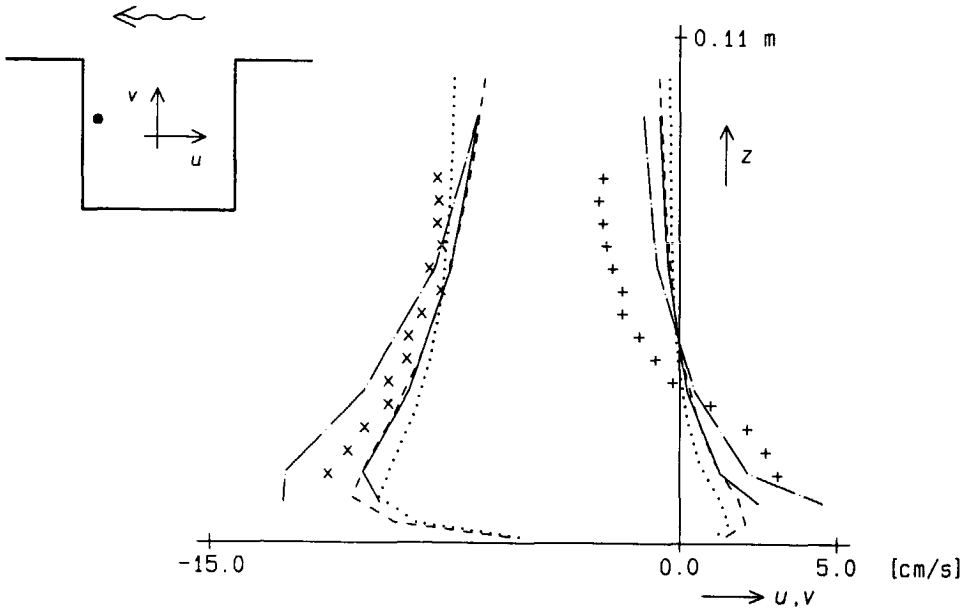
Figure 4.26 Vertical distributions of the horizontal velocity components at maximum current (t = 375 s). Measured: + = u and × = v. Computed: ———— = run 1, — — — = run 2, · · · · = run 3, and —· —· — = run 4.

Fig. 4.23). The development of the gyre is faster than in runs 1 to 3, see Figures 4.27.a and b compared to Figures 4.23.a and b. Around maximum current, Fig. 4.27.d, the flow in the harbour is not yet quasi-steady. The evolution of the flow is similar to that computed with DUCHESS using a $u_* h$ formulation to compute the eddy viscosity, see Figures 4.4.d and 4.5.d. In this case the horizontal eddy viscosity in the harbour is smaller than 5.0E-4 m^2/s, both in the computation with TRISULA and in the computation with DUCHESS. As shown by the computations with DUCHESS, a smaller horizontal eddy viscosity accelerates the development of the new gyre after slack water. Hence, the slower evolution of the gyre in runs 1 to 3 is caused by a value of the horizontal eddy viscosity which is too high, because it is based on the flow in the harbour entrance during maximum current. During maximum current the horizontal eddy viscosity in the harbour is too small in run 4. As a result, the flow in the harbour is unsteady during maximum current, and the water entering the harbour at the downstream corner of its entrance hardly spreads in transverse direction.
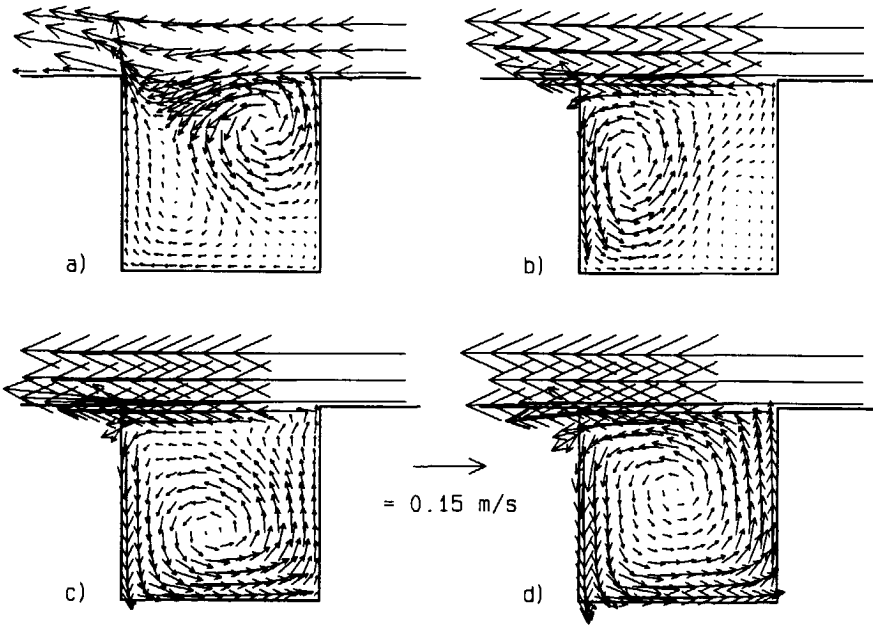
Figure 4.27 Computed depth-averaged flow in the harbour for run 4 (isotropic eddy viscosity): a) $t = 280$ s, b) $t = 310$ s, c) $t = 340$ s, and d) $t = 375$ s.

A computation with the mixing-length model was also carried out on the refined grid that was used in the computations with the k-ε model. The vertical resolution was 10 layers and the horizontal eddy viscosity was 5.0E-4 m²/s. Fig. 4.21.d shows that the computed depth-averaged flow in the harbour agrees well with the measured depth-averaged flow.

The results of the mixing-length model are as satisfactory as those obtained with the k-ε model (compare Figures 4.21.c and d). The computed velocities in the harbour are similar, only the velocities in the mixing layer are predicted better with the k-ε model. The mixing-length model has some advantages with respect to the k-ε model: 1) fewer grid points are needed both in the horizontal and vertical planes to obtain similar results, 2) no differential equations have to be integrated to determine the eddy viscosity, and 3) as a consequence of 1) and 2) the computation time and costs are far less. The computation time for run 1 with the mixing-length model (Table 4.4) was 90 minutes on a CONVEX 240, which approximately corresponds with 20 minutes on a CRAY YMP, and is a factor 150 less then the k-ε model e).

Table 4.5 gives an overview of the computation times on a CRAY YMP with TRISULA concerning the calculations presented in this section. The overview is a little distorted because the computations with a constant eddy viscosity and with the mixing-length model were carried out with a version of TRISULA that was better suited for so-called vector computers like the CONVEX C240 and the CRAY YMP (no indirect addressing and no drying and flooding). The computation time for this version was decreased with a factor 6.

Table 4.5 Estimated CPU times in minutes on a CRAY YMP of runs performed with TRISULA in which the 3-D flow in a square harbour was computed for two tidal cycles.

turbulence model	one layer	five layers	ten layers
constant eddy viscosity	30	45	—
mixing-length model	—	60	90
k-ε model	—	2000	3000

From a practical view point it can be concluded that the use of the mixing-length model is to be preferred to that of the k-ε model. The computation time is far less.

The large computation times with the k-ε have led to changes in the structure of TRISULA to make it more suitable for vector computers, see Van Kester & Stelling (1992). At the moment the computation times with the k-ε model are decreased with a factor 5.

4.4 Summary and discussion

In this chapter three numerical models (DUCHESS, ESTRA, and TRISULA) were tested for the flows in a square harbour (1 m × 1 m, $\alpha = 90$ degrees) and in an oblique harbour (surface area 1 m², $\alpha = 45$ degrees), and for the flushing of a square harbour. The flow in the harbours was driven by an oscillating current in the river without variations in tidal level. Simulation of the flow in other harbours and the interactions between the three exchange mechanisms discussed in chapter 3 are left for future study. After calibration these models

are to be used to determine the optimum harbour entrance geometry to minimize the siltation of the basin.

Both the depth-averaged and the three-dimensional flow in the harbour were computed. Although it is to be expected that three-dimensional numerical models produce better results, because the flow in the harbour is three-dimensional, two-dimensional (depth-averaged) models have the advantage that they are less complicated, therefore use less CPU time and memory, and consequently are much cheaper than a 3-D model.

The mean flow and concentrations in the harbour were calculated and compared with the velocity and temperature measurements that were discussed in section 3.2. The turbulence, which is important not only for the exchange of matter between harbour and river, but also to reproduce the correct mean three-dimensional flow in the harbour, was modelled in the three-dimensional computations. However, turbulence measurements with which to compare the predictions are not available.

4.4.1 DUCHESS and TRISULA (depth-averaged)

The depth-averaged flow in the harbour is predicted well. The resolution of the computational grid is important to compute the correct time scale of the development of the new gyre after slack water. About 20 × 20 grid points in the harbour are needed.

As in computations with a steady river-flow (Booij, 1991), a spatially constant eddy viscosity can be applied inside the harbour. The eddy viscosity influences the time scale of the development of the gyre t_g, and the magnitudes of the velocities in the gyre. A larger eddy viscosity yields a larger time scale and smaller velocities. The eddy viscosity used in the computations was based on the flow during maximum current. As a result, the computed time scale of the development of the gyre was too small, because the eddy viscosity is too large during the other phases of the tide. To meet this difficulty an eddy viscosity which depends on the phase of the tide could be introduced:

$$\nu_t = \nu_{t_0} + \hat{\nu}_t |\sin(\omega t)|, \tag{4.10}$$

where ν_{t_0} is the eddy viscosity at slack water, and $\hat{\nu}_t$ is the amplitude of the eddy viscosity. Reasonable values are: $\nu_{t_0} = 5.0\text{E-}5 \text{ m}^2/\text{s}$ and $\hat{\nu}_t = 4.5\text{E-}4 \text{ m}^2/\text{s}$.

When using a free-slip boundary condition at the closed boundaries, the velocities near the sidewalls of the harbour are too large. Using a partial-slip condition through which the wall friction exerts the correct shear stress on the fluid, these velocities do agree with the measured velocities. However, the computed time scale t_g then becomes too large.

4.4.2 ESTRA

The exchange of matter between harbour and river is predicted well by ESTRA, provided the mean velocity field is accurately reproduced both during maximum current and slack water and a correct dispersion formulation is used. During the quasi-steady phase of the tide when diffusion governs the exchange process, the exchange is best predicted with a velocity dependent dispersion formulation according to $D_t = \gamma u_* h$, where $\gamma = 6$ in the longitudinal direction and $\gamma = 1$ in the transverse direction. With $\gamma = 1$ the transverse dispersion coefficient is about twice as high as the eddy diffusion coefficient.

4.4.3 TRISULA (3-D)

The modelling of the turbulence is important to reproduce the measured three-dimensional flow in the harbour. Using a constant eddy viscosity or the algebraic eddy viscosity model implemented in TRISULA, it was not possible to reproduce the flow in the harbour at all. A more advanced turbulence model is necessary.

A somewhat more advanced algebraic eddy viscosity model (not implemented in the version of TRISULA used), which is able to reproduce the measured flow reasonably well, is the mixing-length model. This mixing-length model is based on the assumption that a local equilibrium exists between the production and dissipation of turbulent kinetic energy.

The predicted time scale of the development of the gyre with the mixing-length model

with an isotropic eddy viscosity agreed reasonably well with that measured. During maximum current the flow in the harbour was not quasi-steady owing to too small a horizontal eddy viscosity. Using the constant horizontal eddy viscosity from the computations of the depth-averaged flow in the harbour, which implies an anisotropic eddy viscosity formulation, resulted in better agreement around maximum current. However, the computed time scale t_g became larger because the eddy viscosity was too large during the development of the gyre. A horizontal eddy viscosity according to equation (4.10) will probably improve the computed time scale.

The magnitude of the velocities parallel to the sidewalls of the harbour were predicted well with the anisotropic eddy viscosity formulation. However, the computed velocities normal to the sidewalls of the harbour were too small by a factor two. This is probably caused by the constant horizontal eddy viscosity, because the isotropic eddy viscosity formulation gave higher velocities.

The most advanced turbulence model implemented in TRISULA is the k-ε model. A computational grid at least twice as fine as that used with the mixing-length model is needed to obtain the same results. The gradients of the turbulent kinetic energy and its dissipation have to be discretized very accurately.

The results of the k-ε model are highly influenced by the boundary conditions of k and ε at the sidewalls of the harbour. The conditions $k = 3u_*^2$ and $\varepsilon = u_*^3/\kappa \Delta n$, which are usually used, are not suitable here. These conditions are based on a local equilibrium between production and dissipation of turbulent kinetic energy. Consequently, in this approximation turbulence generated in the mixing layer and transported into the harbour cannot influence the region near the wall. In this region the transport of turbulent kinetic energy has to be included with the boundary condition $\partial k/\partial n = 0$ at the walls. The mixing length is prescribed as $L = \kappa \Delta n$, yielding the local value of $\varepsilon = c_D k^{3/2}/\kappa \Delta n$.

5 Field measurement

5.1 Introduction

A field measurement was carried out by Rijkswaterstaat and Rotterdam Municipal Works in the 1st Petroleum Harbour situated on the Rotterdam Waterway (The Netherlands), see Fig. 5.1. The main goal of the measurement was to generate a data set to validate the numerical model TRISULA. Furthermore, the results of the field measurement can be compared with the results of the measurements carried out in the Tidal Flume of Delft Hydraulics (see section 3.4). However, this comparison can only be qualitative, because the model harbours had idealized geometries and the resolution of the field observations was too coarse.

The entrance width of the 1st Petroleum Harbour is about 300 m, and the harbour length is about 1600 m. The harbour entrance is oriented at an angle of about 45 degrees to the river. The average water depth during a tidal cycle is about 15 m. The water level elevation, the river-discharge and the density at two levels below the free surface are shown in Fig. 5.2.
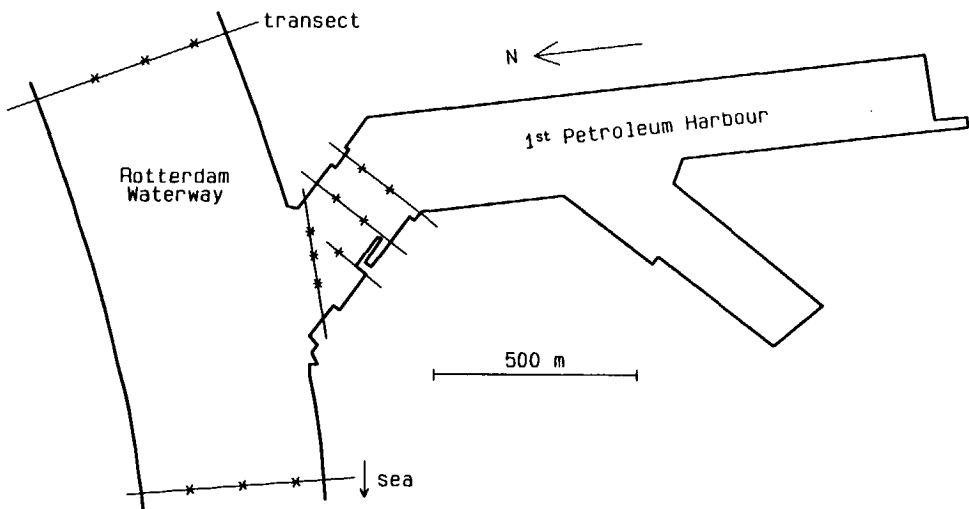
Figure 5.1   Geometry of the 1st Petroleum Harbour in Rotterdam. * = measurement locations.
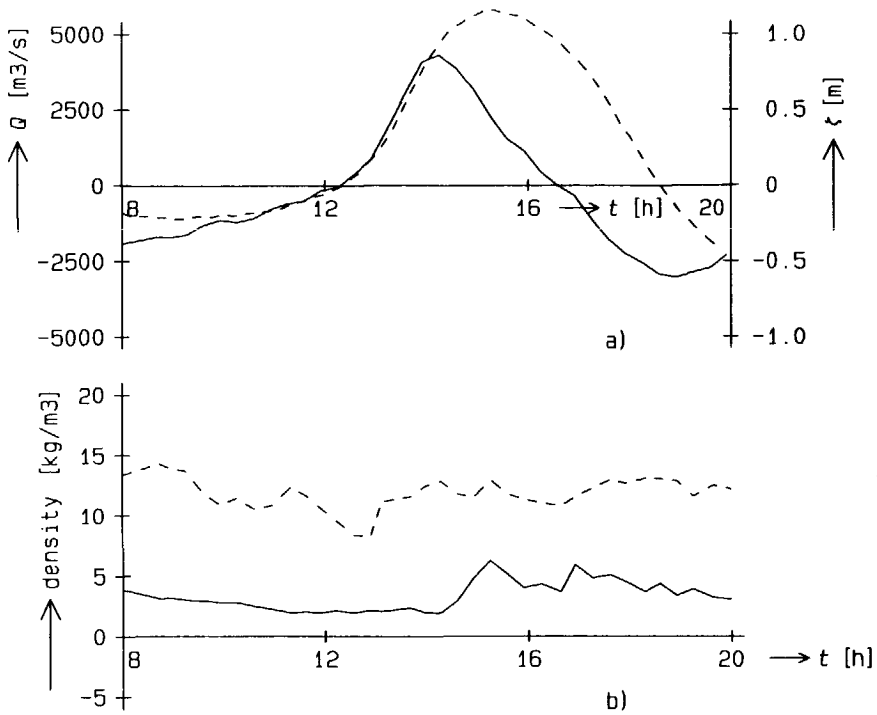
Fig. 5.2 Time histories of discharge, water level elevation, and density in the river in front of the harbour: a) ————, discharge and − − −, water level elevation with respect to NAP; b) ————, density at 6 m below the free surface and − − −, density at 12 m below the free surface.

The various dimensionless parameters (section 3.4) that influence the exchange of mass between harbour and river are listed in Table 5.1.

All three flows that cause exchange between a harbour and a tidal river —a flow along the entrance of the harbour, a net flow through the harbour entrance, and a density-driven exchange flow— were present during the measurement campaign.

At 14 locations in the harbour and river, see Fig. 5.1, vertical distributions of time-mean velocity, salinity and temperature were measured. All quantities were measured 0.5 m from the free surface and the bottom and every two meters in the water column. The velocity was measured by impeller type velocimeters which were vertically dragged through the water column, while recording the magnitude of the velocity and its direction. The salinity was

measured simultaneously with the velocity at the same point using a conductivity probe.

Table 5.1   Values of the dimensionless parameters for the 1st Petroleum Harbour.

$\dfrac{\hat{u}T}{B} \cdot \dfrac{B_e}{B}$	$\dfrac{B}{L}$	$\dfrac{\overline{h}}{B}$	$\dfrac{\hat{h}}{\overline{h}}$	$\dfrac{B_e}{B}$	α	$\dfrac{T}{t_i}$
95	-	0.05	0.05	1	45	48

The results of the field measurement are discussed in section 5.2. A comparison with the experiments in model harbour 8 (section 3.4.3) is made in section 5.3.

5.2 Results

The results of the measurements to be discussed are for low tide, ebb slack tide, high tide, and flood slack tide. These times are chosen because: (1) the flow patterns could be interpreted more easily, primarily because one of the three mechanisms of exchange then was absent; and (2) the results of the experiments in the Tidal Flume with a stratified tidal flow in the river were discussed for the same times.

5.2.1 Low tide

At low tide ($t = $ 9h10) the flow in the harbour is a combination of a density-driven exchange flow and a gyre driven by the ebb current in the river. The vertical distributions of the density at locations 1 and 2 in Fig. 5.3 show that the flow in the river is stratified. The water velocities in the saline wedge are very small. The river-discharge primarily occurs in the upper fresh layer. Consequently, only in the upper fresh layer in the harbour a gyre is driven by the ebb current, see Figures 5.4.a and b.
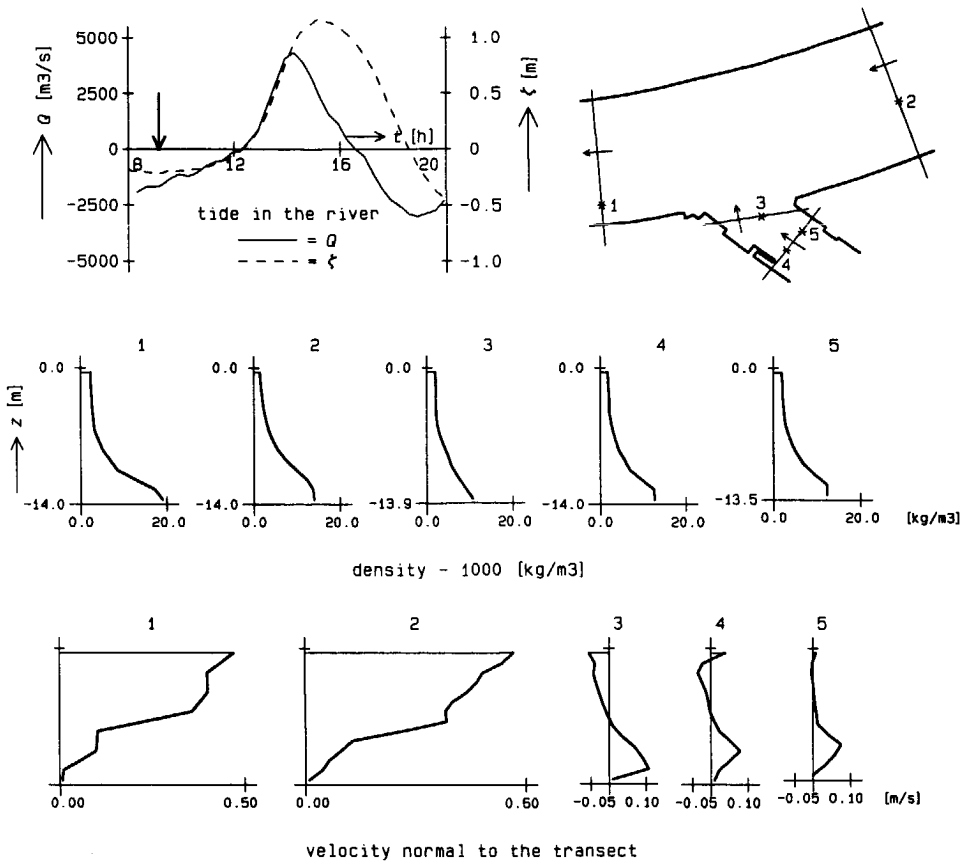
Figure 5.3 Vertical distributions of density and velocity in the 1st Petroleum Harbour at low tide ($t = 9h10$).

The velocity distributions at locations 3, 4 and 5, see Fig. 5.3, show the presence of a density-driven exchange flow with velocities of about 0.1 m/s. Denser water leaves the harbour near the bottom, see also Fig. 5.4.d. Besides the small velocity of the saline wedge, the outgoing denser water hinders the development of a gyre in the lower layer.

The fresh river-water enters the harbour mainly along its downstream sidewall. Along the upstream sidewall of the harbour the flow in the gyre and the density-driven exchange flow have opposite directions in the upper layer resulting in small water velocities, see Figures 5.4.a and b.
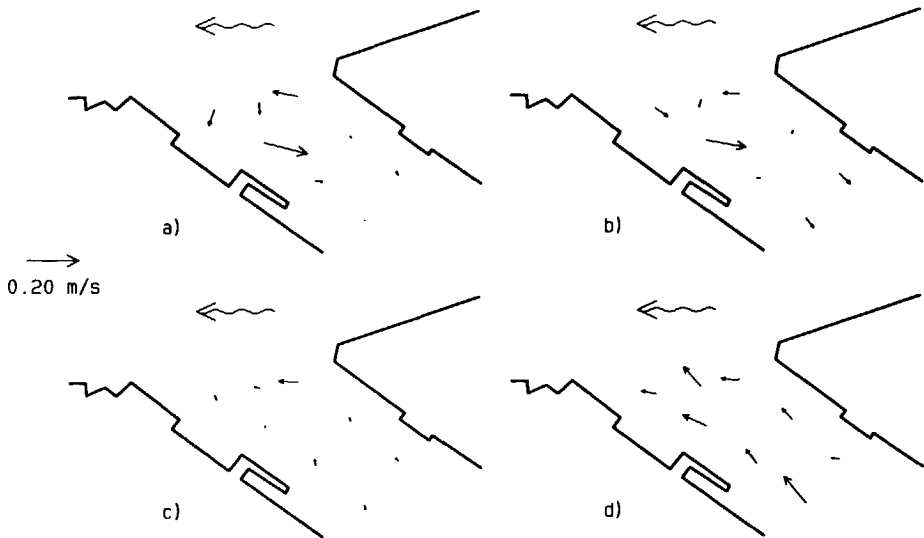
Figure 5.4 The flow in the harbour at low tide (t = 9h10) at four levels: a)
2 m, b) 5 m, c) 8 m, and d) 11 m below the free surface, respectively.

5.2.2 Slack water after low tide

At slack water after low tide (t = 12h20) the flow in the harbour is a combination of a net
flow caused by the filling of the basin, a density-driven exchange flow, and the remainder
of the gyre at low tide.

Figures 5.5.a and b show some circulation in the upper layer, which is the remainder
of the gyre at low tide. Figures 5.5.a and d show that the density-driven exchange flow is
still present. Because it is hindered near the bottom by the filling of the basin, the velocities
have decreased in the lower layer (cf. Fig. 5.4.d).

5.2.3 High tide

At high tide (t = 15h15) the flow in the harbour is a combination of a density-driven
exchange flow and a gyre driven by the flood current in the river.

Figure 5.5 The flow in the harbour at slack water after low tide (t = 12h20) at four levels: a) 2 m, b) 5 m, c) 8 m, and d) 11 m below the free surface, respectively.

The flow in the river at high tide is less stratified than that at low tide as can be observed from the vertical distributions of density and velocity in the river in Fig. 5.6. The river-discharge takes place over the entire water column. The flood current then will drive gyres in both the upper and lower layers, which is shown in Fig. 5.7. The gyre in the upper layer is pushed partly into the river by the outgoing fresh water of the density-driven exchange flow. The velocity of the density-driven exchange flow is about 0.3 m/s, which is three times as large as during low tide.

Near the bottom denser water is primarily entering the harbour along its downstream sidewall, see Figures 5.7.c and d. Along the downstream sidewall of the harbour the water velocities are small because the density-driven exchange flow and the flow in the gyre have opposite directions.
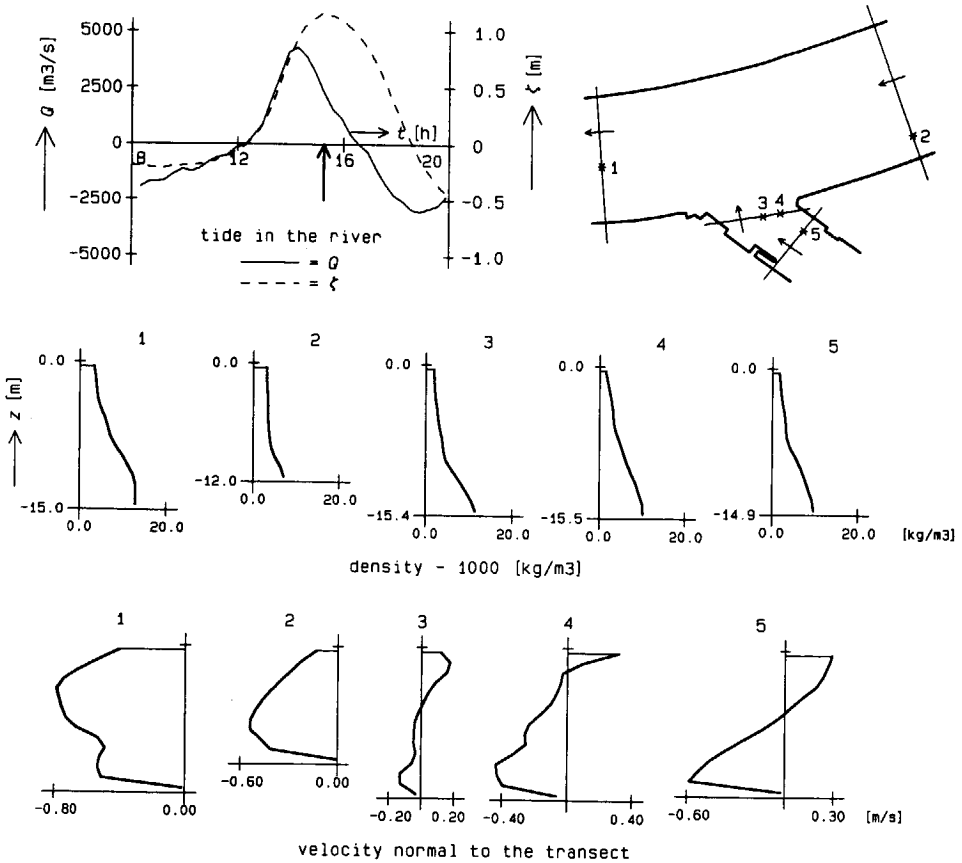
Figure 5.6 Vertical distributions of density and velocity in the 1st Petroleum Harbour at high tide (t = 15h15).

5.2.4 Slack water after high tide

At slack water after high tide (t = 16h35) the flow in the harbour is a combination of a net flow caused by the emptying of the harbour basin, a density-driven exchange flow, and a remainder of the gyre at high tide.

The presence of the density-driven exchange flow is shown in Figures 5.8.a and c, with denser river-water mainly entering the harbour along its sidewall on the right. The emptying of the harbour basin has decreased the water velocities in the lower layer.

At the transition from harbour to river the flow is almost the same from 5 m below
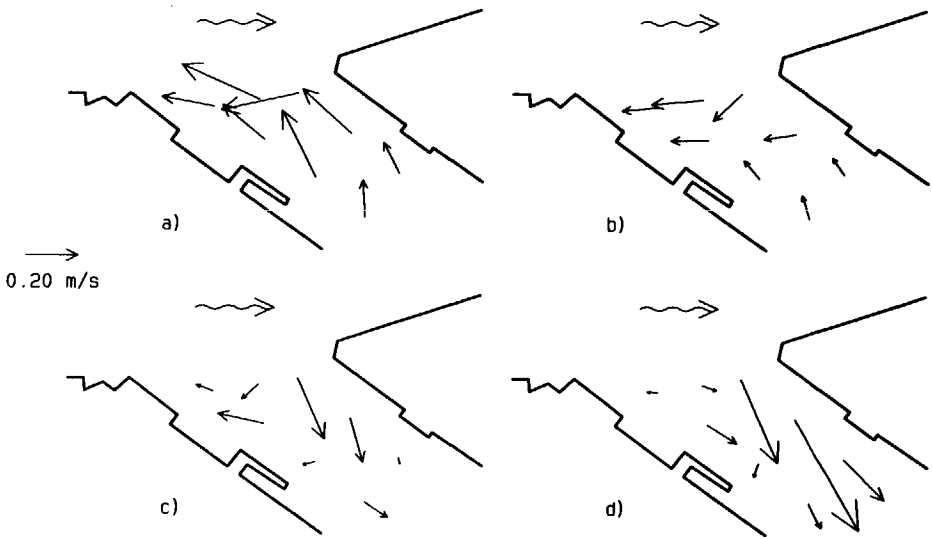
Figure 5.7 The flow in the harbour at high tide ($t = $ 15h15) at four levels:
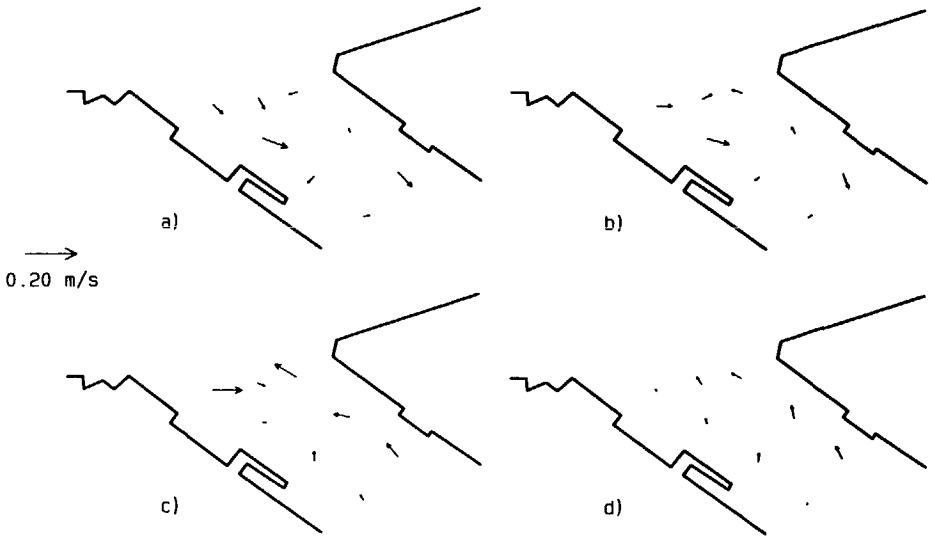a) 2 m, b) 5 m, c) 8 m, and d) 11 m below the free surface, respectively.
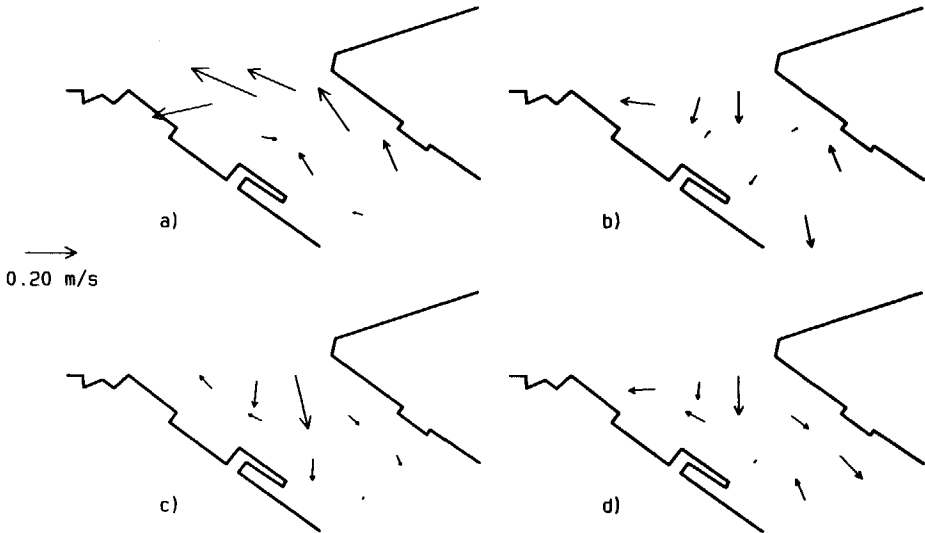
Figure 5.8 The flow in the harbour at slack water after high tide ($t = $ 16h35)
at four levels: a) 2 m, b) 5 m, c) 8 m, and d) 11 m below the free surface,
respectively.

the free surface down to close to the bottom, and represents the remainder of the gyre at high tide.

5.3 Comparison of the field measurement with the laboratory experiments

The geometry of the entrance of the 1st Petroleum Harbour is similar to that of model harbour 8, which is shown in Fig. 3.32 in section 3.4. Both entrances are oriented at an angle of 45 degrees to the river-axis. However, differences exist in the various parameters that influence the flow in the harbour and the exchange of matter between harbour and river. These parameters are listed for the 1st Petroleum Harbour in Table 5.1 and for model harbour 8 in Table 3.2 (section 3.4).

The ratio between the time scale of the tide and the time scale of the flow in the harbour is twice as large for model harbour 8, $t_t/t_g = 200$, as for the 1st Petroleum Harbour, $t_t/t_g = 95$. Consequently, more time is available for the gyre to develop in model harbour 8. The relative depth is twice as large for model harbour 8, $\overline{h}/B = 0.11$, as for the 1st Petroleum Harbour, $\overline{h}/B = 0.05$. The influence of the bottom, including bottom friction, therefore is larger for the 1st Petroleum Harbour. The relative variation of the tidal level is twice as large for model harbour 8 ($\hat{h}/h = 0.11$) than it is for the 1st Petroleum Harbour ($\hat{h}/h = 0.05$). The relative density difference between fresh river-water and salt sea water is the same in the field measurement and the laboratory experiment, $\varepsilon = 0.02$. The parameter T/t_i is about the same in the field measurement and the laboratory experiment. For model harbour 8 $T/t_i \approx 45$, and for the 1st Petroleum Harbour $T/t_i \approx 48$.

Two other quantities, which are not listed in both Tables, have a significant influence on the flow in the harbour: firstly, the phase difference between the tidal current and the tidal level; and secondly, the storage area of the harbour. Both quantities determine the influence of the emptying and the filling of the harbour basin on the flow in the harbour. The phase difference between the tidal current and the tidal level is about $0.1T$ in the field measurement and $0.15T$ in the laboratory experiment. The influence of the emptying and filling of the harbour basin on the initial evolution of the gyre in the harbour entrance then should be larger in the 1st Petroleum Harbour than in model harbour 8. The size of model harbour 8 is based on the nearby Botlek Harbour that has a storage area of 3.5 km^2. The 1st Petroleum

Harbour has a storage area of only 0.5 km^2. The influence of the emptying and filling of the basin with respect to that of the other flow mechanisms therefore is much larger for model harbour 8.

Furthermore, the tide in the Rotterdam Waterway was not exactly reproduced in the laboratory experiment. Fig. 5.2 shows that the ebb phase of the tide in the Rotterdam Waterway is much longer than the flood phase. Also the river-discharge during ebb is smaller than during flood. In the laboratory experiment a more or less sinusoidal tidal current was generated. As a result, the flow during ebb in model harbour 8 should differ both qualitatively and quantitatively from that in the 1st Petroleum Harbour. At high tide multiplying the water velocities in harbour 8 with the velocity scale 8.66 will lead to comparable magnitudes with the 1st Petroleum Harbour.

In the sequel of this section the flows in the upper and lower layers are compared for model harbour 8 (velocities not scaled up) and the 1st Petroleum Harbour at low tide, slack water after low tide, high tide, and slack water after high tide. The differences discussed above should be kept in mind when comparing the results.

Furthermore, a good comparison is hindered by the small spatial coverage and coarse resolution in the field observations.

5.3.1 Low tide

In Fig. 5.9 the flows in the upper and the lower layers are shown at low tide. At low tide the influence of the filling or emptying of the basin is negligible, and the flow in the harbour is a combination of a gyre driven by the ebb current in the river and a density-driven exchange flow.

The flow in model harbour 8 is primarily a density-driven exchange flow and a small gyre in the upper layer. The flow in 1st Petroleum Harbour is similar, although the gyre in the upper layer is somewhat larger. The phenomenon reported in section 3.4 of fresh water flowing downwards near the stagnation point at the downstream sidewall and leaving the harbour near the bottom cannot be observed in the 1st Petroleum Harbour.
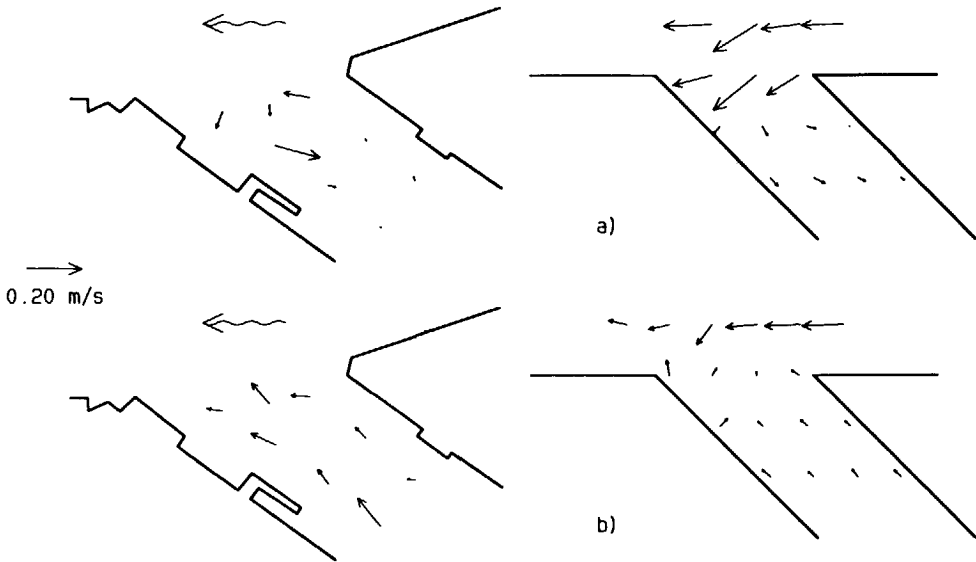
Figure 5.9 The flows in the 1st Petroleum Harbour and model harbour 8 at low tide in: a) upper layer, and b) lower layer.

5.3.2 Slack water after low tide

Fig 5.10 shows that the influence of the filling of the basin on the flow in the entrance is much larger in model harbour 8 than it is in the 1st Petroleum Harbour. Filling distinctly increases the water velocities in the upper layer, whereas in the 1st Petroleum Harbour the water velocities in the upper layer remain small.

The flow pattern in the lower layer is about the same for both harbours.

5.3.3 High tide

Fig. 5.11 shows a gyre spanning the entire entrance width in the upper layer in the 1st Petroleum Harbour, whereas in model harbour 8 only a small gyre at the upstream corner is present.

Near the bottom denser river-water is entering model harbour 8 over its entire width,

0.20 m/s

a)

b)
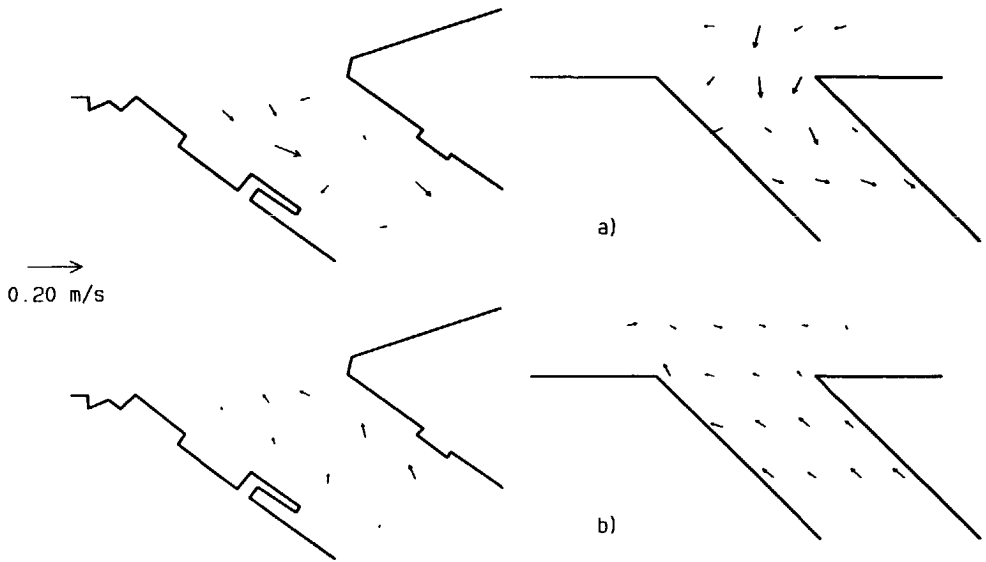
Figure 5.10 The flows in the 1st Petroleum Harbour and model harbour 8 at slack water after low tide in: a) upper layer, and b) lower layer.

0.20 m/s

a)

b)
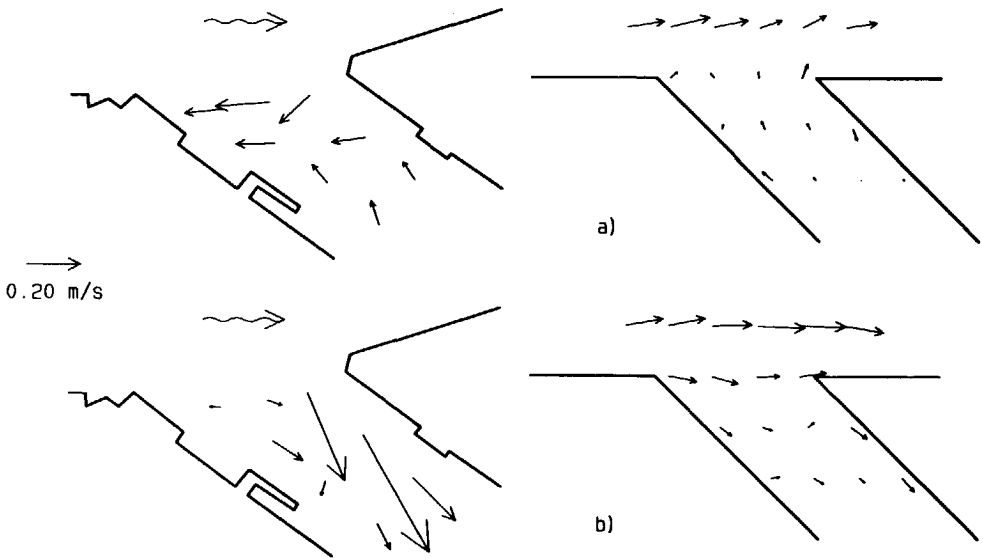
Figure 5.11 The flows in the 1st Petroleum Harbour and model harbour 8 at high tide in: a) upper layer, and b) lower layer.

whereas it is mainly entering the 1st Petroleum Harbour along its downstream sidewall.

5.3.4 Slack water after high tide

At slack water after high tide the flow patterns in model harbour 8 and in the 1st Petroleum Harbour are more or less similar, see Fig. 5.12. Gyres are present in both layers. The density-driven exchange flow in the 1st Petroleum Harbour is still quite strong, especially in the upper layer.

5.3.5 Conclusions

Generally, the flow patterns in model harbour 8 and in the 1st Petroleum Harbour are quite similar during a tidal cycle. During the flood phase the differences between them are basically differences in magnitudes of the water velocities, which are caused by the representation at reduced scale of the flow in harbour 8 (the velocity scale is 8.66).
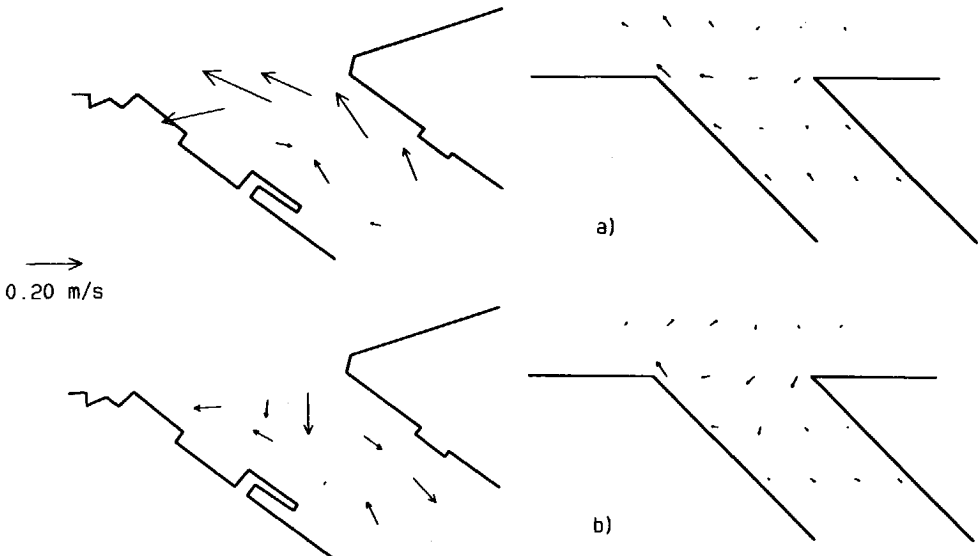
Figure 5.12 The flows in the 1st Petroleum Harbour and model harbour 8 at slack water after high tide in: a) upper layer, and b) lower layer.

Multiplying the water velocities with the velocity scale does not lead to comparable magnitudes of the velocities in harbour 8 and the 1st Petroleum Harbour during the ebb phase. The differences during low tide are caused by differences in tidal current and variation of the tidal water level. The ebb phase of the tide in the Rotterdam Waterway is longer than it is in the laboratory experiment. Furthermore, the water velocities in the Rotterdam Waterway during ebb, 0.35 m/s, are much smaller than the water velocities (multiplied by the velocity scale 8.66) in the laboratory experiment, 2.5 m/s.

Examining the flow patterns (Figures 5.3 to 5.8) in the 1st Petroleum Harbour it can be concluded that the density-driven exchange flow is the dominating flow mechanism causing exchange of water between harbour and river. Also it is observed that the density-driven exchange flow and the gyre interact as was the case in the laboratory experiments.

6 Summary and conclusions

The siltation of harbour basins is caused by the flow in the entrance of the harbour. In tidal harbours the flow in the entrance is a combination of unsteady gyres driven by the tidal current in the river, a net flow caused by changes in tidal level, and a density-driven exchange flow. These flow types are influenced by the geometry of the entrance. As a result, the flow pattern in the entrance can be very complex and difficult to model.

Former research showed that the exchange of matter between a harbour and a tidal river is influenced by the following parameters: the ratio, t_t/t_g, between the time scales of the flows in the river and in the harbour; the ratio, B/L, between the width and length of the harbour; the relative water depth h/B; the relative amplitude of the tidal level $\hat{h}/h$; the ratio, B_e/B, between the widths of the harbour entrance and the harbour; the orientation of the harbour, represented by its angle, α, with respect to the river; the ratio, T/t_i, between the tidal period and the time for internal waves to travel from the harbour entrance to the back of the harbour; the estuarine Richardson number Ri_E; and the phase difference between the tidal current and tidal level.

In this study the influences of these parameters on the flow in the harbour entrance and the exchange of water between harbour and river were examined by means of laboratory experiments and a field measurement. The data generated from these measurements were used to test and improve three computer models for the flow in harbour entrances and the exchange of matter between harbour and river.

Three series of experiments were carried out in the laboratory: (1) experiments with an oscillatory current in the river without variations in water level, (2) experiments with an oscillatory current in the river with variations in water level, and (3) experiments with a stratified tidal flow.

The conclusions drawn from experiment series 1 are:
- The flow in the harbour entrance and the exchange of matter between harbour and river depend markedly on the geometry of the entrance and the phase of the tide.

- For large enough values of t_t/t_g the flow in the harbour entrance is quasi-steady for some time during maximum current. The water velocities in a square harbour then equal those in an identical harbour on a river with a steady flow, with $\overline{u_{g,max}} \approx 0.25 u_r$ and $\overline{u_g} \approx 0.17 u_r$. The exchange of matter between harbour and river then takes place through the mixing layer, that is, it is primarily caused by turbulent motions.
- Narrowing the entrance width with 50 per cent decreases the velocities in the gyre with 40 per cent around maximum current.
- The orientation of the harbour influences both the behaviour of the mixing layer and the gyre. For an angle of 45 degrees between the downstream sidewall of the harbour entrance and the downstream river-bank the length of the gyre, the water velocities in the gyre, and the width of the mixing layer are much larger than for an angle of 135 degrees.
- A wider mixing layer is related to a larger exchange of momentum and matter between harbour and river.
- If the length to width ratio of the harbour is larger than 2, the harbour comprises several gyres, in which case the normalized exchange between harbour and river (the coefficient λ) is less because the secondary, tertiary, etc. gyres do not contribute to the exchange process.
- A quite strong secondary current is present in the primary gyre. The maximum velocity in the secondary current is, on the average, 15 per cent of the main velocity in the gyre.
- During slack water the flow in the harbour is unsteady. The gyre moves into the river and guides river-water into the harbour. A large increase in advective exchange then takes place.

The conclusions drawn from experiment series 2 are:

- Filling of the harbour basin accelerates the development of the gyre, whereas emptying of the harbour basin retards the development of the gyre.
- When the velocity of the net flow through the harbour entrance is smaller than approximately 5 per cent of the velocities in the gyre, emptying of the harbour

basin results in smaller velocities in the gyre and a smaller length of the gyre and filling of the harbour basin results in larger velocities in the gyre and a larger length of the gyre.

- If the water velocities in the entrance, caused by the emptying of the harbour basin, are larger than approximately 10 per cent of the velocities in the gyre of experiment series 1, no gyre will come into existence.

The conclusions drawn from experiment series 3 are:

- Density-driven exchange flow has a greater influence on the gyre than emptying and filling of the harbour basin caused by changes in tidal level, because of its larger velocities.
- The gyre reduces the exchange of water caused by the density-driven exchange flow by reducing the effective entrance width.
- Of the three flow mechanisms the density-driven exchange flow gives the largest exchange of water between harbour and river in the present study.

The flows in a square harbour and in an oblique harbour oriented at 45 degrees with respect to the river (surface area of both model harbours is 1 m^2) were simulated with depth-averaged and three-dimensional numerical models. From these simulations it can be concluded that:

- The depth-averaged flow is predicted well with a constant eddy viscosity based on the turbulence generated in the mixing layer, provided that the resolution of the grid in the harbour is sufficiently high to represent the gyres. At least 20×20 grid points are needed in the square harbour.
- Turbulence modelling is important to reproduce with some degree of accuracy the measured 3-D flow in the harbour with the TRISULA computer model. At least a Prandtl mixing-length model is needed.
- The results of the k-ε model are highly influenced by the boundary conditions of k and ε at closed walls. Conditions based on a local equilibrium between production and dissipation of turbulent kinetic energy are not suitable at the sidewalls of the harbour, particularly near the stagnation point. In this region the transport of

turbulent kinetic energy has to be included, a suitable boundary condition then is $\partial k/\partial n = 0$. The mixing length is prescribed as $L = \kappa \Delta n$, which yields for the local value of the rate of dissipation $\varepsilon = C_D k^{3/2}/\kappa \Delta n$.

- Although the Prandtl mixing-length model does not include transport of turbulent kinetic energy, it gives similar results as the k-ε model. The advantages of the mixing-length model are that less grid points are needed and no additional transport equations for k and ε have to be integrated. Consequently, the computation times and costs are far less.

- For the Prandtl mixing-length model an anisotropic eddy viscosity formulation, in which the horizontal exchange coefficient is based on turbulence generated in the mixing layer, gives better results than an isotropic eddy viscosity formulation.

- The maximal velocity of the computed secondary flow is about half that of the measured secondary flow.

- The 2-D transport model ESTRA predicts the exchange of matter between harbour and river well, provided that the mean velocity field is accurately reproduced both during maximum current and slack water. A velocity-dependent, anisotropic dispersion formulation according to $D_t = \gamma u_* h$, with $\gamma = 6$ in the streamwise direction and $\gamma = 1$ in the transverse direction, gives the most satisfactory results.

The TRISULA model is able to predict the mean flow in a harbour, with a simple geometry, due to an oscillatory current in the river. Further tests should be carried out with TRISULA in which variations in water level and density effects are included.

Further study is required concerning the turbulence model to be used. Appropriate turbulence modelling is especially important when the exchange of matter between harbour and river is dominated by the transport through a mixing layer at the transition from harbour to river. Measurements of turbulence quantities (k and ε) should be carried out to calibrate the k-ε model implemented in TRISULA to calculate the flow in harbour entrances.

A field measurement carried out in the 1st Petroleum Harbour in Rotterdam (The Netherlands) has shown that the phenomena observed in the laboratory experiments are also present, in a qualitative sense, in prototype harbours.

Notation

A	cross-sectional area of the harbour basin
A_e	cross-sectional area of the harbour entrance
A_h	storage area of the harbour basin
$\overline{A}$	tide-averaged cross-sectional area of the harbour entrance
B	width of the harbour
B_e	entrance width of the harbour
b	width of the mixing layer (as defined by Booij, 1986)
C	constant, Chézy coefficient
$C_{1,2,3}$	constants
c	concentration, specific heat
$\tilde{c}$	volume-averaged concentration in the harbour
$\tilde{c}_0$	initial volume-averaged concentration in the harbour at $t = 0$
c_D	constant
c_f	dimensionless friction factor
c_h	concentration at the boundary of the mixing layer located in the harbour
c_r	concentration at the boundary of the mixing layer located in the river
c_f	bed-friction coefficient
$c_{\mu,1\varepsilon,2\varepsilon,3\varepsilon}$	constants of the k-ε model
c'_μ	constant
D_t	eddy diffusion coefficient
d	bottom level
f_{ik}	coriolis coefficient
$G_{\eta\eta}, G_{\xi\xi}$	components of the covariant metric tensor
g	acceleration due to gravity
h	water depth
$\hat{h}$	amplitude of the variation in tidal level
$\overline{h}$	tide-averaged water depth
k	turbulent kinetic energy per unit mass
k_N	roughness height according to Nikuradse

L	length of the harbour, mixing length
L_g	length of the primary gyre
l_0	lateral length scale
M	mean value of a quantity, integral of the concentration over depth
m_0	scale of a quantity
n	direction normal to a boundary
P	production term
$\text{Pe}_{\Delta x}$	cell Peclet number
p	water pressure
p_a	atmospheric pressure divided by the density and the gravitation
p_{atm}	pressure at the free surface
Q	flow rate
Q_{ex}	rate of exchange between a harbour and a river
Q_f	fresh water discharge
Q_s	flow rate through entrance due to storage effects
Q_θ	heat transport through the harbour entrance
q_i	volume flux per unit width in x_i-direction
R	hydraulic radius
Re	Reynolds number
Ri_E	estuarine Richardson number
S	bed-friction number
S_i	transport of a material in x_i-direction
T	tidal period
t	time
$t_{1/2}$	half-life
t_g	time scale of the flow in the harbour
t_i	time scale of internal-wave propagation from the harbour entrance to the back of the harbour
t_t	time scale of the tide
U	velocity of the main flow
u,v	velocity components in (x,ξ)- and (y,η)-directions

$\hat{u}$	amplitude of the tidal current velocity
$\bar{u}$	depth-averaged velocity, tide-averaged velocity
u_d	velocity of the density-driven exchange flow
u_e'	rms velocity excess in the mixing layer
$\overline{u_g}$	average velocity of the gyre
$\overline{u_{g,\max}}$	maximum velocity of the gyre
u_h	water velocity in the harbour
u_i	velocity in x_i-direction
u_i'	velocity fluctuation in x_i-direction
u_r	water velocity in the river
$u_{r,\max}$	maximum water velocity in the river
u_s	velocity of the net flow through the harbour entrance
u_t	rms tidal velocity
u_*	bottom shear velocity
$u_{//}$	velocity parallel to a wall
ΔV	tidal prism
V_h	volume of the harbour
$\bar{V}_h$	tide-averaged volume of the harbour
v_s	velocity of the secondary flow
W	channel width
W_i	component of the wind stress on the surface in x_i-direction
w	velocity component in z-direction
$\bar{w}$	cross-sectional average mean lateral velocity in the harbour entrance
x,y,z	cartesian coordinates
$\Delta x,\Delta y$	mesh sizes
x^*	dimensionless coordinate
y_0	centre-line of mixing layer
α	angle at which the harbour is oriented with respect to the river axis
β	entrainment parameter
γ	proportionality coefficient

δ	width of the mixing layer (as defined by Brown & Roshko, 1974)
δ_h	boundary of the mixing layer that is located in the harbour
δ_r	boundary of the mixing layer that is located in the river
δ^*	dimensionless width of mixing layer
ε	relative density, dissipation of turbulent kinetic energy
ζ	water level elevation
η	dimensionless coordinate ($= y/l_0$)
η,ξ	curvilinear coordinates
η_0	centre-line of mixing layer
$\bar{\theta}$	volume-averaged excess temperature of harbour water with respect to river-water
κ	constant of Von Karman
$\varkappa$	proportionality coefficient
λ	relative velocity difference, normalized heat transport
λ_0	relative velocity difference at 0.01 m downstream of the separation point
μ	mass exchange coefficient
ν	kinematic viscosity coefficient
ν_t	eddy viscosity coefficient
$\hat{\nu}_t$	amplitude of the eddy viscosity
$\bar{\nu}_t$	average eddy viscosity in the mixing layer
ν_{t_0}	eddy viscosity at slack water
$\nu_{t,max}$	maximum eddy viscosity in the mixing layer
ν_t^h	horizontal eddy viscosity coefficient
ν_t^v	vertical eddy viscosity coefficient
Π_1,Π_2	dimensionless parameters
ρ	density
$\Delta\rho$	density difference
ρ_h	density of harbour water
ρ_r	density of river-water
$\bar{\rho_r}$	tide-averaged density of river-water
σ	dimensionless vertical coordinate
σ_k	turbulent Schmidt number for k

σ_t	turbulent Schmidt (or Prandtl) number
σ_ε	turbulent Schmidt number for ε
$\tau_b\cdot$	bottom shear-stress
Ω	boundary
ω	velocity component in σ-direction relative to a σ-plane

References

Bonnet, L. & Lamoen, J. (1949), "Model Experiments in Belgium Ports of the North Sea," *Dock & Harbour Authority*, Vol. 30; No. 348, pp. 169-174; No. 349, pp. 201-205; No. 350 pp. 237-243.

Booij, N. (1990), "User manual for the program DUCHESS," Department of Civil Engineering, Delft University of Technology.

Booij, N. & Sokolewicz, M. (1990), "Bridging the gap between hydrodynamic models and ecological models," in Hydraulic engineering software applications, Proc. of the third international conference on hydraulic engineering software, Massachusetts, USA.

Booij, R. (1986), "Measurements of the exchange between river and harbour" (in Dutch), Report No. 9-86, Department of Civil Engineering, Delft University of Technology.

Booij, R. (1987), "Report of a brief literature research concerning exchange processes between a harbour and a river" (in Dutch), Report No. 3-87, Department of Civil Engineering, Delft University of Technology.

Booij, R. (1991), "Eddy viscosity in a harbour," Proc. 24th IAHR Congress Madrid, Vol. C, Refined Flows Modelling, pp. 81-90.

Brinkmann, B. (1990), "A contribution to the determination of the exchange of water between a tidal river and harbour" (in German), Mitteilungen des Franzius-Instituts für Wasserbau und Küsteningenieurwesen der Universität Hannover, Heft 70, pp. 1-150.

Brown, G.L. & Roshko, A. (1974), "On density effects and large structure in turbulent mixing layers," *Journal of Fluid Mechanics*, Vol. 64, Part 4, pp. 775-816.

Christiansen, H. (1987), "New insights on mud formation and sedimentation processes in tidal harbours," Proc. of Coastal & Port Engineering in Developing Countries, Vol. 2, Group D, pp. 1332-1340.

Chu, V.H. & Babarutsi, S. (1988), "Confinement and bed-friction effects in shallow turbulent mixing layers," *Journal of Hydraulic Engineering*, Vol. 114, No. 10, pp. 1257-1274.

Delft Hydraulics (1975), "Influence of an air bubble curtain on the salt intrusion in the Rotterdam Waterway and the exchange flow rates Botlek" (in Dutch), Report M1319.

Delft Hydraulics (1977), "Harbour studies: study to the influence of a harbour on the state of salinity in the river and the exchange between harbour and river" (in Dutch), Report No. M896-36.

Delft Hydraulics (1986), "Description of the flow scheme of the Tidal Flume" (in Dutch), version 2, Z0017.

Delft Hydraulics (1988), "TRISULA, Volume III: The scientific background," Z-215-05.

Dursthoff, W. (1970), "On the quantative exchange of water between harbour and river" (in German), Mitteilungen des Franzius-Instituts für Grund- und Wasserbau der Technischen Universität Hannover, Heft 34, pp. 194-368.

Elder, J.W. (1959), "The dispersion of marked fluid in turbulent shear flow," *Journal of Fluid Mechanics*, Vol. 5, pp. 544-560.

Fischer, H.B., List, E.J., Koh, R.C.Y., Imberger, J. & Brooks, N.H. (1979), *Mixing in inland and coastal waters*, Academic Press.

Hensen, W. (1953), "Model Experiments for the Amerika Harbour in Cuxhaven" (in German), Mitteilungen des Franzius-Instituts für Grund- und Wasserbau der Technischen Universität Hannover, Heft 4, pp.113-172.

Kirby, R. (1991), "Flow modification at the bifurcation of a branch channel from a main channel carrying a water flow," Cohesive Sediments Research Newsletter, Vol. 1, No. 2, p. 7.

Langendoen, E.J. (1989), "Laboratory observations and calculations of the depth averaged flow patterns in a square harbor on a tidal river," Report No. 8-89, Department of Civil Engineering, Delft University of Technology.

Langendoen, E.J. (1990), "Laboratory observations of the velocity field in the entrance of a tidal harbor and the exchange of heat between harbor and river," Report No. 5-90, Department of Civil Engineering, Delft University of Technology.

Langendoen, E.J. & Karelse, M. (1990), "Laboratory observations of velocity and density fields in the entrance of a harbor on a stratified tidal river," Report No. 1-90, Department of Civil Engineering, Delft University of Technology.

Launder, B.E. & Spalding, D.B. (1974), *Lectures in mathematical models of turbulence*, Academic Press, New York.

Leendertse, J.J. (1967), "Aspects of a computational model for long period water wave propagation," Memorandum RM-5294-PR, RAND Corporation, Santa Monica, California.

Liepmann, H.W. & Laufer, J. (1947), "Investigation of free turbulent mixing," *N.A.C.A. Tech. Note*, no. 1257.

Magens, C. (1958), "Research into the causes of the siltation of the harbour of Brunsbüttelkoog" (in German), Mitteilungsblatt der Bundesanstalt für Wasserbau, Karlsruhe, Heft 10.

McGuirk, J. & Rodi, W. (1979), "Calculation of unsteady mass exchange between a main stream and a dead water zone," Proc. IAHR Congress on Hydraulic Engineering in Water Resources Development and Management, Cagliari, Vol. 3, Subject Ba, pp. 25-32.

Miles, J.B. & Shih, J. (1968), "Similarity parameter for two-stream turbulent jet-mixing region," *A.I.A.A. J.* 6, p. 1429.

Mills, R.D. (1968), "Numerical and experimental investigations of the shear layer between two parallel streams," *Journal of Fluid Mechanics*, Vol. 33, Part 3, pp. 591-616.

MKO (1983), "Siltation of harbours; part 1: water motion" (in Dutch), Report No. R 8307.

MKO (1987), "The gyre and silt concentrations in the Maashaven" (in Dutch), Report No. R 8701.

Nece, R.E. & Falconer, R.A. (1989), "Modelling of tide induced depth-averaged velocity distributions in a square harbour," Proc. of Int. Conf. on Hydraulic and Environmental Modelling of Coastal, Estuarine and River Waters, pp. 56-66, University of Bradford.

Patel, R.P. (1973), "An experimental study of a plane mixing layer," *A.I.A.A. J.* 11, p. 67.

Phillips, N.A. (1957), "A coordinate system having some special advantages for numerical forecasting," *Journal of Meteorology*, Vol. 14, pp. 184-185.

Pui, N.K. (1969), "The plane mixing layer between parallel streams," M.A. Sc. thesis, University of British Columbia.

Rodi, W. (1984), "Turbulence models and their application in hydraulics," A State of the Art Review, IAHR.

Roelfzema, A. & Os, A.G. van (1978), "Effect of harbours on salt intrusion in estuaries," Report No. 204, Delft Hydraulics.

Rohr, F. (1933), "Movement of water and sediment in harbours on rivers and seas" (in German), Ph.D. thesis, Technische Hochschule Karlsruhe.

Schijf, J.B. & Schönfeld, J.C. (1953), "Theoretical considerations on the motion of salt and fresh water," Proc. Minnesota International Hydraulics Convention, Minneapolis, Minnesota.

Schmucker, E.Gg. (1926), "Contribution to the understanding of the influences of siltation in harbours on estuaries, from research in the New Waterway from Rotterdam to sea" (in German), Ph. D. Thesis, Technische Hochschule München.

Spencer, B.W. & Jones, B.G. (1971), "Statistical Investigation of pressure and velocity fields in the turbulent two-stream mixing layer," *A.I.A.A. Paper*, no. 71-613.

Stelling, G.S. (1983), "On the construction of computational methods for shallow water flow problems," Ph. D. thesis, Delft University of Technology.

Sunyach, M. (1971), "Contribution to the study of the boundaries of free shear layers" (in French), D.Sc. thesis, University Claude Bernard, Lyon.

Townsend, A.A. (1976), *The structure of turbulent shear flow*, Cambridge University Press, Cambridge.

Uittenbogaard, R.E., Van Kester, J.A.Th.M. & Stelling, G.S. (1991), "Implementation of three turbulence models in 3D-TRISULA for rectangular horizontal grids," Project Z81, Delft Hydraulics.

Van Kester, J.A.Th.M. & Uittenbogaard, R.E. (1990), "The σ-coordinate transformation and the basic equations of TRISULA," Report Z81-21, Delft Hydraulics.

Van Kester, J.A.Th.M. & Stelling, G.S. (1992), "The acceleration of TRISULA-3D" (in Dutch), Project Z81, Delft Hydraulics.

Vollmers, H.J. (1963), "Systematics of the measures to decrease the sedimentation of suspensions in harbours on rivers" (in German), Ph.D. thesis, Technische Hochschule Karlsruhe.

Vollmers, H.J. (1976), "Harbour inlets on tidal estuaries," Proc. on Coastal Eng. Congress, Hawaii, Vol. 2, pp. 1854-1867.

Westrich, B. (1977a), "Exchange of mass in steady flows with dead water regions" (in German), SFB 80 ET/80, University of Karlsruhe.

Westrich, B. (1977b), "Water exchange in confined basins induced by unsteady main stream currents," Proc. IAHR Congress on Hydraulic Engineering for Improved Water Management, Baden Baden, Vol. 2, Subject Ad, pp. 461-468.

Westrich, B. & Clad, A. (1979), "Mass and heat exchange in flows with recirculating zones," Proc. IAHR Congress on Hydraulic Engineering in Water Resources Development and Management, Cagliari, Vol. 3, Subject Bb, pp. 269-276.

Winant, C.D. & Browand, F.K. (1974), "Vortex pairing: the mechanism of turbulent mixing layer growth at moderate Reynolds number," *Journal of Fluid Mechanics*, Vol. 63, Part 2, pp. 237-255.

Wygnanski, I. & Fiedler, H.E. (1970), "The two-dimensional mixing region," *Journal of Fluid Mechanics*, Vol. 41, Part 2, pp. 327-361.

Yule, A.J. (1972), "Two-dimensional self-preserving turbulent mixing layers at different free stream velocity ratios," *Aero. Res. Counc. R. & M.*, no. 3683.

Appendix A

The spreading rate of the shallow mixing layer as given by Chu & Babarutsi (1988) is

$$\frac{d\delta}{dx} = 0.36\lambda \left[1 - \frac{S}{0.09} \right], \qquad \text{for } S < 0.09 \qquad (A.1)$$

Writing equation (A.1) in the dimensionless variables $\delta^* (= c_f \delta / 2 h \lambda_0)$ and $x^* (= c_f x / h)$ gives:

$$\frac{d\delta^*}{dx^*} + \delta^* = 0.18 \frac{\lambda}{\lambda_0}. \qquad (A.2)$$

The ratio λ / λ_0 is obtained from the momentum equations in the ambient streams as, see Chu & Babarutsi (1988):

$$\frac{\lambda}{\lambda_0} = \left[\frac{u_{r_0} + u_{h_0}}{u_r + u_h} \right]^2 e^{-x^*}. \qquad (A.3)$$

Substituting equation (A.3) into equation (A.2) yields the following relation between δ^* and x^*:

$$\frac{d\delta^*}{dx^*} + \delta^* = 0.18 \left[\frac{u_{r_0} + u_{h_0}}{u_r + u_h} \right]^2 e^{-x^*}. \qquad (A.4)$$

Chu & Babarutsi (1988) solved equation (A.4) numerically with a Runge-Kutta method and $\left(u_{r_0} + u_{h_0} \right) / (u_r + u_h) = 1$. The virtual origin, where $\delta^* = 0$, was at $x^* = 0.025$. However, an exact solution of equation (A.4) is possible for $\left(u_{r_0} + u_{h_0} \right) / (u_r + u_h) = 1$, and is given by:

$$\delta^* = 0.18 e^{-x^*} (x^* - C).$$

Taking $\delta^* = 0$ at $x^* = 0$ then gives:

$$\delta^* = 0.18 e^{-x^*} x^*. \qquad (A.5)$$

Equation (A.5) is valid for $S < 0.09$, where S is defined as

$$S = \frac{c_f \delta}{4h} \frac{1}{\lambda} = \frac{c_f \delta}{2h\lambda_0} \frac{\lambda_0}{2\lambda} = \frac{1}{2} \delta^* \lambda_0 / \lambda = \frac{1}{2} \delta^* e^{x^*},$$

with $\left(u_{r_0} + u_{h_0} \right) / (u_r + u_h) = 1$. The condition $S < 0.09$ then yields $\delta^* < 0.18 e^{-x^*}$. From which follows that $x^* < 1.0$. If $S > 0.09$ or $x^* > 1.0$ then $d\delta^* / dx^* = 0$. This yields: $\delta^* = $ constant $= 0.18 e^{-1} = 0.066$.

Curriculum vitae

Eddy Johannes Langendoen werd geboren op 15 april 1964 te Oostvoorne. Hij volgde Atheneum-B onderwijs aan de Rijksscholengemeenschap te Brielle in de periode 1976-1982. Daarna studeerde hij Civiele Techniek aan de Technische Universiteit te Delft. Hij studeerde in 1987 af bij de sectie Vloeistofmechanica (vakgroep Waterbouwkunde). In hetzelfde jaar ving hij bij deze sectie een promotieonderzoek aan. Dit proefschrift bevat de bevindingen van dit onderzoek.

Sinds augustus 1992 is hij werkzaam als Post-Doctoral Research Associate bij het Center for Computational Hydroscience and Engineering van de University of Mississippi (USA). Hij houdt zich nu bezig met het ontwikkelen, verfijnen en toepassen van numerieke modellen betreffende de hydrodynamica en het sedimenttransport.